UNIVERSITY OF OKLAHOMA

GRADUATE COLLEGE

MULTISCALE MODELING OF FRACTURED RESERVOIR STIMULATION AND INDUCED SEISMICITY

A DISSERTATION

SUBMITTED TO THE GRADUATE FACULTY

in partial fulfillment of the requirements for the

Degree of

DOCTOR OF PHILOSOPHY

By

JIANRONG LU
Norman, Oklahoma
2020

MULTISCALE MODELING OF FRACTURED RESERVOIR STIMULATION AND INDUCED SEISMICITY

A DISSERTATION APPROVED FOR THE
MEWBOURNE SCHOOL OF PETROLEUM AND GEOLOGICAL ENGINEERING

BY THE COMMITTEE CONSISTING OF

Dr. Ahmad Ghassemi, Chair

Dr. Jean-Claude Roegiers

Dr. Mrinal Saha

Dr. Mashhad Fahes

Dr. Xingru Wu

Acknowledgements

I would like to express my sincere and deep thanks to my advisor Professor Ahmad Ghassemi for his funding and guidance during my Ph.D. studies. Professor Ahmad Ghassemi reshaped my motivation for researching rock mechanics. The purpose of university research is really an ongoing process of correcting and refining hypotheses based on the development of engineering practice. I hope to follow this principle in my own academic career.

Dr. Jean-Claude Roegiers, Dr. Xingru Wu, Dr. Mashhad Fahes, the late Dr. Thordur Runolfsson and Dr. Mrinal Saha are gratefully acknowledged for serving as my committee members.

I also benefited from the University of Oklahoma and made a lot of new friends in Norman. They brought me a lot of happiness and foods. I also want to thank our group members: Dr. Dharmendra Kumar, Dr. Qinglu Cheng and Dr. Zhi Ye, for the many technical discussions. Special thanks to Dr. Gensheng Qian, Dr. Lianbo Hu, Dr. Qian Gao, Dr. Kai Huang, Hao Xiong and many others for their supports in my life. I am proud to be a BOOMER SOONER.

I owe my great appreciation to my parents, Mr. Yuesheng Lu and Ms. Xiuyun Zhang, my mother-in law, Ms. Jinxia Xu, for their unconditional love and support.

I am deeply indebted to my wife, Dr. Jing Cao, and my son, Zikang Lu, for their love, support and the happiness they bring to my life.

出走半生，归来仍是最初的少年。

Table of Contents

List of Tables

List of Figures

Abstract

Natural fractures and fracture networks characteristics significantly influence the success of reservoir stimulations. Subsurface and surface investigations consider various geophysical techniques to probe and measure natural fracture characteristics at depth. However, the relationship between geophysical properties of a rock mass and its hydro-mechanical parameters is not unique. As a result, numerical modeling can be called upon to advance the characterization of fractured reservoir stimulation.

To simulate fractured reservoir stimulation (e.g., Enhanced Geothermal System), a fully coupled thermo-hydro-mechanical-seismic (THMS) finite element model with a dynamic 3D fracture network capability is further developed which incorporates the processes of fracture flow, poroelastic deformation, shear dilation, fracture network propagation and induced seismicity. A dual-scale semi-deterministic fracture network is generated using data from image logs, foliations/micro-fractures, intact and fractured core. Fracture network propagation under injection is considered using a rapid analytical approach. The induced stress field (stress shadow) caused by fracture pressurized is quantified using the Eshelby solution. The numerical model allows for multiple seismic events to occur on and around a fracture. The location, number and magnitude of seismic events are constrained in an effective physics-based, and conceptually rigorous manner.

Several verification and illustrative simulations are carried out. The model is also applied to a field case at intermediate scale (EGS Collab Testbed Experiment 1). The results demonstrate the effectiveness of the coupled thermo-hydro-mechanical-seismic model with a dynamic 3D fracture network in fractured reservoir stimulation and shed light on stimulation mechanisms and potential permeability creation and induced seismicity.

The spatial distribution of natural fracture roughness which plays a significant role in the patterns of seismic and aseismic slip on the fractures is considered in this dissertation. A novel approach is used to account for the spatial distribution of roughness on natural fractures. The approach utilizes the concept of Joint Roughness Coefficient (JRC) to obtain a shear stiffness distribution on the fracture surface. The spatial variability of the JRC is obtained through the concept of stochastic partitioning of the fracture plane which can be calibrated using laboratory and field data. The spatial distribution of JRC is then used to map the spatial distribution of fracture shear stiffness. A critical velocity as a function of fracture shear stiffness is defined to distinguish between the seismic/aseismic states. The technique is employed to simulate acoustic emission (AE) distribution during shearing of a rough fracture at laboratory scale.

To represent a large-scale real fracture roughness, synthetic anisotropic roughness is used. The synthetic anisotropic roughness is described by three parameters, including two fractal dimensions in perpendicular directions along the fracture, and amplitude elevation of scanning points on the fracture surface. These parameters are used as input for estimating JRC of a synthetic anisotropic roughness. A quadratic polynomial equation is derived to link the Hurst exponent with JRC covering its full spectrum (0-20). Such JRC-Hurst exponent relation is incorporated into the coupled thermo-hydro-mechanical-seismic model with a dynamic 3D fracture network to simulate a field case at a large scale (Utah FORGE). Also, the impact of cyclic injection on the stimulation is studied.

Finally, a Geomechanics-Based Stochastic Analysis of Microseismicity (GBSAM) is developed and applied to quantitatively estimate the natural fracture orientations in a reservoir from MEQs (induced seismicity) recorded during reservoir stimulation. This is

achieved by combining geomechanics and geostatistics to better constrain uncertainties in natural fracture orientations. The GBSAM is applied estimate the natural fracture orientations (dip and dip direction) in two case studies namely, the Newberry EGS and the Fenton Hill HDR. Results from the GBSAM are in very good agreement with results from boreholes image logs or previous studies in those case studies.

Chapter 1 Introduction

1.1 Background and Motivation

Fractured reservoirs present tremendous challenges to water, hydrocarbon and heat extraction. The existence of fractures primarily or perhaps dominantly affects hydraulic-mechanical properties of fractured reservoir and reservoir stimulation outcome. The effects of natural fractures on reservoir response is multiscale (i.e., fracture propagation, dilation and induced seismicity). Eight characteristics of natural fractures impact the success of reservoir stimulation at each scale: orientation, aperture, infilling, length, density, connectivity, planarity and roughness. Figure 1.1 shows a range of fracture characteristics that are addressed directly or indirectly by spatial scale (microscopic, mesoscopic, and macroscopic) (Interstate Technology & Regulatory Council 2017). Their relative importance for fluid flow varies depending on the scale of interest (Figure 1.1).

In-situ sampling methods provide direct measurement of fractured rock, however, the mapped zone is limited. Subsurface and surface investigations consider the geophysical techniques to probe and measure the fracture characteristics at depth. Geophysical techniques offer unique opportunities to mitigate some limitations of in-situ sampling methods. In recent years, these techniques have emerged as valuable tools for site characterization because the spatial continuity of fractured rock data is contained in the geophysical investigation. Despite these advantages, one critical issue in the geophysical characterization of fractured rock which needs be addressed is the relationship between geophysical properties of a rock mass and its hydro-mechanical parameters which is not unique. Furthermore, geophysical surveys rarely cover the details of fracture characteristics because of the low resolution. Therefore, geophysical techniques should

be strategically adopted in combination with in-situ measurements, numerical modeling, and mechanic learning. The value of a numerical model corresponds to the quality of the input parameters, and how well those parameters reflect the practical setting. Therefore, the synergistic coupling of geophysical technologies, in-situ measurements, machine learning and numerical modeling offers the greatest potential for advancing the comprehensive characterization of fractured reservoir stimulation.

The development of numerical models for fractured reservoir stimulation typically focus on the realistic representation of reservoir heterogeneity (e.g., fracture network). The generation of fracture network can be classified into two categories: a deterministic fracture network and a stochastic fracture network. In practice, details of the individual fractures are not always available so that various probabilistic frameworks have been utilized to stochastically characterize the distribution of fracture geometric features, such as asperity and length. This means that the results in each run can be different because of the variation in fracture properties. In addition, the degree of realism of synthetic fracture network in representing the realist fracture network remains an unresolved issue. Once the reservoir data is assessed, robust numerical simulation of reservoir stimulation at field scale, including the evolution of in-situ stress, fracture network behavior and induced seismicity are carried out. Numerical models applied to simulate fracture networks include generalized finite element, displacement discontinuity method, and the phase field model. Recent modeling of reservoir stimulation consider more physics to solve the problem (See e.g., Kumar and Ghassemi 2018, Kamali and Ghassemi 2020). Those works require less computation effort compared to FEM but still can be challenging for large-scale problems.

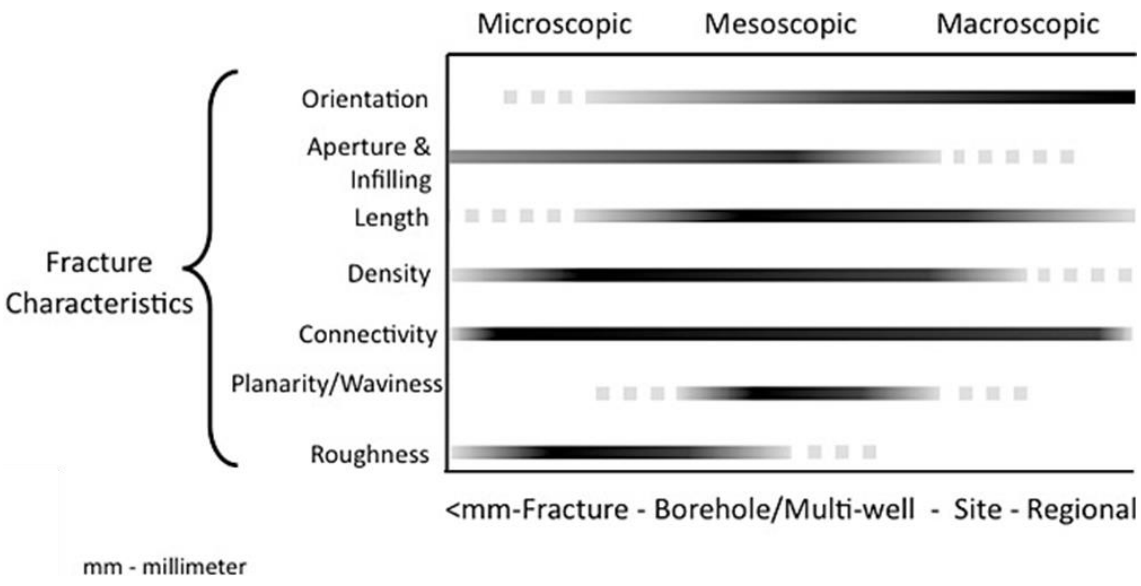

Figure 1.1 Range of fracture characteristics and their relative importance for fluid flow over the scale of interest (After Interstate Technology & Regulatory Council 2017).

1.2 Objectives and Significance of Research

The overall objective of this dissertation is to improve the state-of-the-art of fractured reservoir stimulation by developing an advanced numerical model with multiscale characteristics, and to apply the model to field-scale operations. The dissertation provides advancement in the following:

1. Estimating natural fracture orientation from MEQs recorded during stimulation

The natural fracture orientations are a critical feature that exerts a large control over network permeability tensor. Moment tensor inversion is widely employed to characterize natural fracture orientations in-situ away from the wellbore. However, the estimated fracture orientation is doubtful because of the low signal-to-noise ratio (SNR) of MEQs (induced seismicity) signal.

2. Consideration of the effects of fracture roughness on MEQs generation

The quasi-static model of simulating MEQs is by far the simplest and less time-consuming practical approach. In quasi-static models each failed fracture is assumed to

generate one seismic event which is always located at the center of the fracture. But in practice, a single slipped fracture may have multiple MEQs on/off the fracture. Furthermore, shear slip on a single fracture can have seismic and aseismic phases, which can be distributed both spatially and temporally. Thus, the location, number, and magnitude of MEQs generated by a slipped fracture are still not well constrained. The quantitative relationship between fracture roughness and the spatial distribution of seismic and aseismic slip on fracture has not been addressed. The transition between aseismic and seismic slip is still in debate.

3. Effective simulation of fracture network propagation

Most numerical methods applied to simulate fracture network propagation are based on generalized finite element, displacement discontinuity method, and phase field model. Recent studies on the modeling of fracture propagation consider more physics to solve the problem. Those works require less computational effort than FEM but still can be challenging for large-scale problems in an industrial setting. To date, all fracture network models are static.

4. Determination of Joint Roughness Coefficient (JRC) by fractal dimension of the fracture surface

Mechanisms of fracture shear slip strongly depends on the fracture roughness. In the rock mechanics discipline, fracture roughness is typically represented by the concept of Joint Roughness Coefficient (JRC). The JRC of fracture is commonly determined by using fractal dimension of the fracture surface. However, the connection between JRC and the fractal dimension of fracture surface is still in debate because of the calculation of fractal dimension and the fractal nature of the fracture surface.

1.3 Review of Literature and Previous Work

1.3.1 Coupled Thermo-Hydro-Mechanical-Seismic Model with a Dynamic 3D Fracture Network

The development of enhanced geothermal system (EGS) design must rely on effective stimulation of the hot fractured reservoir rock mass. Fluid injected into reservoir is intended to reactivate pre-existing fractures and create new ones to form a fracture network. This process is often manifested as multiple seismic events or micro-earthquakes (MEQs). Complications from reservoir heterogeneity and complexity of flow path may lead to channeling (Rawal and Ghassemi 2014), short-circuiting, and premature thermal breakthrough so that fracture network behavior is critical to the success of EGS. But there are still large uncertainties regarding the direct and indirect diagnostic technologies for imaging the flow path and fracture network. In general, geophysical surveys are the commonly used for probing the subsurface structures. However, imaging resolution is not high enough to identify the individual fracture. Numerical solutions provide a complementary method to predicate flow path and fracture network behaviors (e.g., dilation and propagation) and induced seismicity. Further, numerical solutions combined with field observations and geophysical surveys further elucidate the fundamental processes critical to EGS development.

EGS design typically needs to focus on: (1) description of the rock mass (rock matrix and 3D fracture network), (2) a representation of flow paths and rates in the reservoir, (3) geomechanical modeling to assess the fracture network responses to injection/production, and (4) seismic modeling to forecast the induced seismicity. An important challenge in modeling of EGS is whether to represent the fracture network explicitly (e.g., discrete

fracture network) (Ucar, Berre et al. 2018, Cheng, Wang et al. 2019) or implicitly (e.g., equivalent continuum model) (Pruess 1992). Numerical models with explicit representation of the fracture network have advantages over others since they can more readily handle the fracture network propagation, induced seismicity and transport phenomena. Continuum models are desirable because they are well-suited for simulating the fractured reservoir at larger field/basin scale. However, the latter leads to an over-simplistic fracture network response that is not representative of the realist reservoir. A hybrid method has been developed which combines the advantages from discrete fracture network and continuum model (Tezuka and Watanabe 2000, Cheng, Wang et al. 2019). Details of this hybrid method is presented in previous work (Cheng, Wang et al. 2019). The generation of fracture network can be classified into two categories: a deterministic fracture network and a stochastic fracture network. In practice, details of individual fractures are not always available so that various probabilistic frameworks have been utilized to characterize the stochastic distribution of fracture geometric features, such as asperity and length. This means that the results in each run can be different because of the variation in fracture properties. In this dissertation (presented in Chapter 2.2.1) we use a dual-scale semi-deterministic fracture network model that combines data derived from image logs, foliations/micro-fractures, core with fracture properties which follow a stochastic distribution. The variation of micro-fracture/foliations away from the fracture follow a stochastic distribution. An advantage of this fracture network model is that measurement data can be incorporated to constrain the uncertainties in the rock mass.

At least, two different stimulation mechanisms may occur concurrently during the development of EGS: (1) fracture shear slip and dilation and (2) fracture propagation

(Min, Zhang et al. 2010, Kamali and Ghassemi 2018, Kumar and Ghassemi 2018, Sesetty and Ghassemi 2018). The concept of fracture shear dilation has been called upon for EGS design, and several simplified fracture network models have been developed and used (Willis-Richards, Watanabe et al. 1996, Tezuka, Tamagawa et al. 2005, Cheng, Wang et al. 2019). Experimental works (Ye and Ghassemi 2018, Ye, Ghassemi et al. 2020) have shown that shear dilation could enhance permeability by up to 2-3 orders of magnitude. Further, a recent experimental study (Ye and Ghassemi 2019) has conclusively shown that fracture propagation by shearing of natural fractures can play a role in the development of fracture networks and permeability. Most numerical methods applied to simulate fracture network propagation are based on generalized finite element, displacement discontinuity method, and phase field model. Recent studies on the modeling of fracture propagation consider more physics to solve the problem (See e.g., Kumar and Ghassemi 2018, Kamali and Ghassemi 2020). Those works require less computation effort compared to FEM but still can be challenging for large-scale problems in an industrial setting. To alleviate such computational bottlenecks, analytical or semi-analytical approaches can be used. A major issue to be addressed in the framework of analytical approaches is the fracture propagation and the interaction between hydraulic fractures and natural fractures. In this context, the analytical methods with a sequential crack tip propagation algorithm can be adopted to model fracture propagation at much lower computation costs (Rahman, Hossain et al. 2000, Schwartzkopff, Xu et al. 2016). However, both of those works only considered single fracture propagation and did not address the interaction between hydraulic fracture and natural fractures. In this dissertation (presented in Chapter 2.2.3), we have mitigated these limitations and

developed a rapid analytical approach (Lu and Ghassemi 2019) to simulate the fracture propagation in a network of natural fractures.

Considering fracture propagation including non-planar and planar responses, is complex and challenging within an analytical framework. For instance, the stress intensity factor (SIF) of a non-planar fracture cannot be obtained accurately. Further, the pressure in the non-planar fracture needs be extracted from the current configuration of the fracture system. So, a dynamic fictitious equivalent plane is utilized to approximate the non-planar and planar fractures (Schwartzkopff, Xu et al. 2016). This 3D fictitious plane is formed to best fit to the tips of the penny shaped fractures used to represent the newly created surface resulting from a mixed-mode (I+II) propagation. Thus, the geometry of the fictitious plane is changed according to the evolution of the fracture during the propagation process. The fictitious plane is initially penny shaped and approximates the original fracture and the newly created non-planar surfaces. This is acceptable since the dimension of the newly created non-planar surfaces is small and often can be neglected (Kamali and Ghassemi 2018, Kumar and Ghassemi 2018, Sesetty and Ghassemi 2018). However, the fictitious plane is changed to elliptical shape later in the planar propagation stage. This is the relatively larger planar dimension of the fracture segment that becomes parallel to the maximum stress. It is assumed that the newly created fracture surfaces formed by the propagation process are on the fictitious plane. Another approximation is that a certain number (e.g., 20) of small penny fractures are used to best represent newly created surface. While the ratio between the total areas of these small penny fractures and the area of the newly created surfaces is close to 1 because the newly created surface is approximated by discrete penny fractures. This can be enforced by scaling the diameter

of discrete penny fractures. In addition, a hydraulic fracture (newly created surface) is very closed to a natural fracture. The newly created surface is represented by discrete penny fractures. The ratio between the total areas of these small penny fractures and newly created surface is required as 1. Thus, those discrete fractures may intersect with natural fracture and the connection of fracture network is changed and contradict with the numerical simulation outcome. So, the diameter of these penny fractures is scaled to maintain the connection of fracture network. Therefore, the ration between total areas of these small penny fractures and newly created surface is not 1.

Currently, the calculation of hydraulic and mechanical fields in the numerical system is only suited for penny shaped fractures. The kink angle is constant during the non-planar propagation stage which can reduce the complexity of simulation. A fracture starts to propagate in a planar fashion once the fictitious plane is perpendicular to the minimum principal stress direction and remains planar during the rest of the propagation stages as long as no stress perturbations are encountered. The stress changes caused by fracture propagation have limited effects on the propagation direction during the planar propagation stages as long as the fracture is in the opening mode (mode I). Most EGS testbeds consist of fractured rocks and a hydraulic fracture can be arrested when encroaching against a natural fracture during the stimulation. Multiple criteria (Gu and Weng 2010) can describe such complex interactions. In this dissertation (presented in Chapter 2.2.3), Renshaw and Pollard criterion (Renshaw and Pollard 1995) is utilized to evaluate the interaction between natural fractures and a hydraulic fracture.

The other aspect of our fracture network stimulation modeling is the simulation of micro-seismicity (induced seismicity). The generation of induced seismicity is believed to

evolve from shear slip on new or pre-existing fracture planes and rock failure and fracture propagation. The quasi-static model of simulating MEQ is by far the simplest and less time-consuming practical approach. The effective normal and shear stress on fractures are used to determine the occurrence of shear slip and potential seismic events. The magnitude of the seismic events is determined by the shear modulus, fracture slip distance, and the slip area. In quasi-static models each failed fracture is assumed to generate one seismic event which is always located at the center of the fracture. In practice, a portion of the fracture slip is aseismic, and one fracture may generate multiple seismic events located on or around the fracture. It is a major challenge to eliminate uncertainties in the number, magnitude and location of seismic events and the nature of the transition between aseismic and seismic slip is still unclear. However, the level of uncertainty can be reduced by using more realistic algorithms for MEQ generation as proposed herein. This issue is addressed by developing a new scheme for MEQ generation that can account for generation of multiple events and capturing the aseismic to seismic transition.

The numerical model presented in this dissertation (presented in Chapter 2), consists of four sub-models: 1) a coupled thermo-poroelastic model describing the coupling between rock deformation, fluid flow and heat flow in the fractured rock mass; 2) a dual-scale semi-deterministic fracture network describing the fracture network geometry and fluid transport within the fractures; 3) a fracture slip/dilation and propagation model to analyze fracture network deformation; and 4) a seismicity simulation model describing the events distribution and magnitudes. The latter distinguishes the transition between the aseismic and seismic slip. These aspects are described below, and the model is applied to the field test namely Collab. In this part of the dissertation (presented in Chapter 4), the EGS

Collab Testbed Experiment 1 namely Stim-II HF@164 Notch (Kneafsey, Dobson et al. 2018, Kneafsey, Dobson et al. 2018) carried out on May 24, 2018 is simulated. The simulations provide some insights on the mechanisms involved in the observed phenomena such as micro-seismicity, the resulting fracture network and the flow path as well as the injection pressure profile.

1.3.2 The Effects of Fracture Roughness on Seismicity Patterns

Numerical simulation of micro-seismicity is of significant to subsurface energy resource development and crustal dynamics. To date modeling approaches are inadequate and cannot capture many essential features of micro-seismicity which reflect the fracture/fault structure and surface characteristics. Also, laboratory and numerical studies have shown that the shear slip on a fracture can have seismic and aseismic phases, which can be distributed both spatially and temporally (Fournier and Morgan 2012, Ye and Ghassemi 2020). Capturing the existence of seismic and aseismic slip on fractures is central to simulation of micro-seismicity. Here, seismic and aseismic slip is understood to distinguish unstable and stable slip, respectively. The nucleation zone is a portion of fracture where rupture velocity accelerates from quasi-static to dynamic (Iio 2009). A seismic event occurs when the unstable region reaches the nucleation length (Mclaskey and Yamashita 2017). Note that the evolution of such seismic event is primary controlled by the rock itself (Mclaskey and Yamashita 2017). A parameter space that describes the fracture stability behavior can be found in (Mclaskey and Yamashita 2017). It is also known from laboratory tests that AE (micro-seismicity) distribution on a rough fracture can be heterogeneous. It is known (based on laboratory work e.g., Goebel, Kwiatek et al. 2017, Ye and Ghassemi 2020) that heterogeneous fracture roughness is essential to

aseismic to seismic transition and dynamic rupture. However, the quantitative relationship between fracture roughness and spatial distribution of seismic and aseismic slip has not been addressed. This is important in quantitative evaluation of the seismic potential of a given fracture, and in constraining the uncertainties in the relationship between shear slip and enhanced permeability. This issue is the focus of this dissertation (presented in Chapter 6).

1.4 Organization

This dissertation has nine chapters and each chapter contains its own focus, review of relevant literature, methodology, application, results, and discussion.

Chapter 2 addresses problems 2 and 3 mentioned in Chapter 1.2. A fully coupled thermo-hydro-mechanical-seismic (THMS) finite element model with a dynamic 3D fracture network is further developed which incorporates the processes of fracture flow, poroelastic deformation, shear dilation, fracture network propagation and induced seismicity. A dual-scale semi-deterministic fracture network is generated by combining the data from image logs, foliations/micro-fractures, core with properties of fractures (e.g., length and asperity) which follow a stochastic distribution. Fracture network propagation under injection is considered by an ultrafast analytical approach. The stress shadow caused by fracture pressurized is described by Eshelby solution. This model allows for multiple seismic events to occur on and around a fracture. The location, number and magnitude of seismic event clouds are constrained in an effective physics-based, and conceptually rigorous manner.

Chapter 3 presents several verifications and general examples for the coupled thermo-hydro-mechanical-seismic model (THMS) with a dynamic 3D fracture network. In

addition, the effects of poroelasticity on induced seismicity is examined by explicitly considering the poroelastic stress acting on a fracture subjected to injection. Also, the impact of thermal stress on the fracture network propagation is studied.

Chapter 4 applies the THMS with 3D fracture network to simulate the EGS Collab Testbed Experiment 1 namely Stim-II HF@164 Notch carried out on May 24, 2018.

Chapter 5 considers the fracture roughness in seismicity simulation. The numerical model proposed in Chapter 2 are extended to consider the effects of fracture roughness on reservoir stimulation. A JRC-Hurst exponents (H) relationship is derived by calculating the JRC values of synthetic roughness defined by Hurst exponents and root mean square (RMS) of height of the laser scan points. The linear Barton-Bandis model is employed to characterize the stability of the fracture. Therefore, problems 4 mentioned in Chapter 1.2 are presented. In addition, the spatial distribution of fracture shear stiffness is estimated by the spatial distribution of JRC so that problems 2 mentioned in Chapter 1.2 are treated.

Chapter 6 addresses the problem 2 mentioned in Chapter 1.2, i.e., studying the role of the spatial distribution of roughness on seismic events pattern on a fracture plane. The concept of joint roughness coefficient (JRC) is utilized to obtain a shear stiffness distribution on the fracture surface. The spatial variability of JRC is obtained through the concept of stochastic partitioning of the fracture plane. The spatial distribution of fracture shear stiffness as a function of the effective normal stress is mapped based on the spatial distribution of JRC. A critical velocity as a function of fracture shear stiffness is defined to distinguish between the seismic/aseismic states. The method is first applied to simulate acoustic emission (AE) distribution during shearing of a rough fracture at laboratory scale.

A case study of the Utah FORGE is presented in Chapter 7. The extended numerical model from Chapter 5 is employed to optimize the well trajectories in Utah FORGE EGS. Chapter 8 responds to the first problem mentioned in Chapter 1.2. A Geomechanics-Based Stochastic Analysis of Microseismicity (GBSAM) is proposed to constrain the natural fracture orientations by combining a geomechanics and geostatistics model to interpret microseismic data. The GBSAM is applied to extract information about natural fracture orientations (dip and dip direction) in two case studies, i.e., the Newberry EGS and the Fenton Hill HDR. Results from GBSAM are in very good agreement with results from boreholes image logs or previous studies in those case studies.

Finally, Chapter 9 includes a brief summary of this dissertation's findings and provides recommendations for future research.

Chapter 2 Coupled Thermo-Hydro-Mechanical-Seismic Model with a Dynamic 3D Fracture Network

2.1 Coupled Thermo-Poroelastic Model

Coupled process involving poroelastic deformation, fluid flow and heat transfer occur in EGS where fractures are the primary pathways for fluid migration and production. Thus, convective heat transfer in the low permeable matrix is often insignificant (Delaney 1982) and is not considered. The heat transfer in the reservoir is assumed to occur via fracture flow and heat conduction between rock matrix and fracture fluid. The coupled thermo-poroelastic processes in the rock matrix can be described in the following constitutive equations (McTigue 1986):

$$\dot{\sigma_{ij}} = 2G\dot{\varepsilon}_{ij} + \left(K - \frac{2G}{3}\right)\dot{\varepsilon}_{ij}\delta_{ij} - \alpha\dot{p}\delta_{ij} - K\alpha_m\dot{T}\delta_{ij} \tag{2.1}$$

$$\dot{\xi} = \alpha\dot{\varepsilon}_{kk} + \left(\frac{\alpha-\phi}{K_{sk}} + \frac{\phi}{K_f}\right)\dot{p} - \left[\alpha\alpha_m + (\alpha_f - \alpha_m)\phi\right]\dot{T} \tag{2.2}$$

Where $\dot{\sigma}_{ij}$ is the increment of the total stress components; $\dot{\varepsilon}_{ij}$ is the increment of the strain components; $\dot{\xi}$ is the change of fluid volume per unit reference pore volume; $\dot{p}$ and $\dot{T}$ are pore pressure change and temperature change, respectively; α is the Biot's coefficient; K is the bulk modulus; G is shear modulus; ϕ is porosity; K_{sk} and K_f are bulk modulus of rock skeleton and fluid and matrix, respectively. The conservation equations for momentum, mass and energy are shown as:

$$\sigma_{ij,j} = 0 \tag{2.3}$$

$$\frac{\partial\xi}{\partial t} = \kappa p_{,jj} \tag{2.4}$$

$$\rho_t C_t \frac{\partial T}{\partial t} = -h_{i,i} - C_f T q_{i,i} \tag{2.5}$$

From the above constitutive equations and conservation equations, the coupled thermo-poroelastic field equation can be derived (McTigue 1986):

$$Gu_{i,jj} + \left(K + \frac{G}{3}\right) u_{j,ji} - \alpha p_{,j} - \gamma_1 T_{,j} = 0 \tag{2.6}$$

$$\alpha \frac{\partial \varepsilon_{kk}}{\partial t} + \beta \frac{\mathrm{d}p}{\mathrm{d}t} - \kappa p_{,jj} - \gamma_2 \frac{\mathrm{d}T}{\mathrm{d}t} = 0 \tag{2.7}$$

$$\frac{\partial T}{\partial t} - c^T T_{,jj} - \left(\kappa^T T p_{,i}\right)_{,i} = 0 \tag{2.8}$$

A finite element method is developed for solving Equation 2.6, 2.7 and 2.8. The details of the mathematical formulation can be found in (Zhou and Ghassemi 2009). It can be shown (Cheng, Wang et al. 2019) that after spatial discretization using Galerkin method and Crank-Nicolson approximation in the time domain, the finite element matrix formula of the above equations is written as:

$$\begin{bmatrix} K_u & -C_{up} & -C_{uT} \\ C_{pu} & C_{pp} + \Delta t\theta C_{pp} & -C_{pT} \\ 0 & 0 & C_{TT} + \Delta t\theta (K_{cdT} + K_{cvT}) \end{bmatrix} \begin{bmatrix} \Delta u \\ \Delta p \\ \Delta T \end{bmatrix} = \begin{bmatrix} \Delta t \dot{F}_u \\ \Delta t F_{qin} - \Delta t K_p p_{t-\Delta t} \\ \Delta t F_{hin} - \Delta t (K_{cdT} + K_{cvT}) T_{t-\Delta t} \end{bmatrix} \tag{2.9}$$

Where $\Delta u, \Delta p$ and ΔT are the vectors of unknowns variables; $\Delta t = t_n - t_{n-1}$ is the time step size; θ is a scalar parameter and set to be 1.0 in this work; F_u, Fq and F_h are the external load, fluid and heat source terms; $p_{t-\Delta t}$ and $T_{t-\Delta t}$ is the pore pressure and temperature of the previous time step. Other matrix are described in (Cheng, Wang et al. 2019). By solving the Equation 2.9 with initial and boundary conditions, the primary unknowns of displacement u, pore pressure p and temperature T can be resolved directly.

2.2 Fracture Network Model

2.2.1 Fracture Network Generation

A dual-scale semi-deterministic fracture network is generated by combining data from image logs, core and stochastic fracture properties (e.g., length and asperity). Fracture networks can be extremely variable and difficult to detect in the subsurface. As a result,

stochastic models are often used to describe the fracture network geometry (Willis-Richards, Watanabe et al. 1996, Rahman, Hossain et al. 2002). In generating a stochastic fracture network, the fractures can be treated as penny-shaped and their radii are assumed to follow a log normal distribution (Long, Remer et al. 1982, Dershowitz and Einstein 1988) which is also used in this work. Furthermore, fracture apertures are assumed to follow a power law distribution (Laubach, Hooker et al. 2014). Geophysical surveys, as well as core and outcrop studied, provide some valuable information to constrain the uncertainties in the generation of fracture network. For instance, fracture orientation can be extracted from the borehole image logs and core (Figure 2.1). Of course, some bias is introduced when the hole is parallel to a particular fracture set. The fracture network realizations are thus inherently non-unique and inevitably impact the results in each run. Although borehole imaging and core only map a small zone around the wellbore, they are still useful as a reference for fracture orientation. In the intermediate-scale (e.g., decameter scale) experiments, the number and location of detected fractures from image logs and core are considered the same as the real system (Ulrich, Dobson et al. 2018, Kneafsey, Dobson et al. 2019). However, there are still foliations/micro-fractures surrounding the fracture (Figure 2.1) which affect the rock mass response to injection (Cavailhes, Sizun et al. 2013). The micro-fracture density in the rock matrix increases dramatically toward the fracture surfaces (Moore and Lockner 1995, Sagy, Reches et al. 2001) and can be fitted well by a power law relation (Anders, Laubach et al. 2014, Meng, Wong et al. 2019). Some studies suggest two specific formulas (e.g., $\rho = 0.953d^{-0.391}$ for cracks where d ranges from 1 to 10 mm, and $\rho = 47d^{-0.214}$ for cracks where d ranges from 10 to 100 m, where ρ is the crack density and d is the distance from

the natural fracture/fault center) (Meng, Wong et al. 2019). For instance, the density of micro-fractures and macro-fractures near Muddy Mountain fault has been shown to decrease with distance from the fault planes (Brock and Engelder 1977) and can be fitted by a power law relation. Further, micro-fracture density is higher in a shear dilatational zone than on a compressional zone (Moore and Lockner 1995).

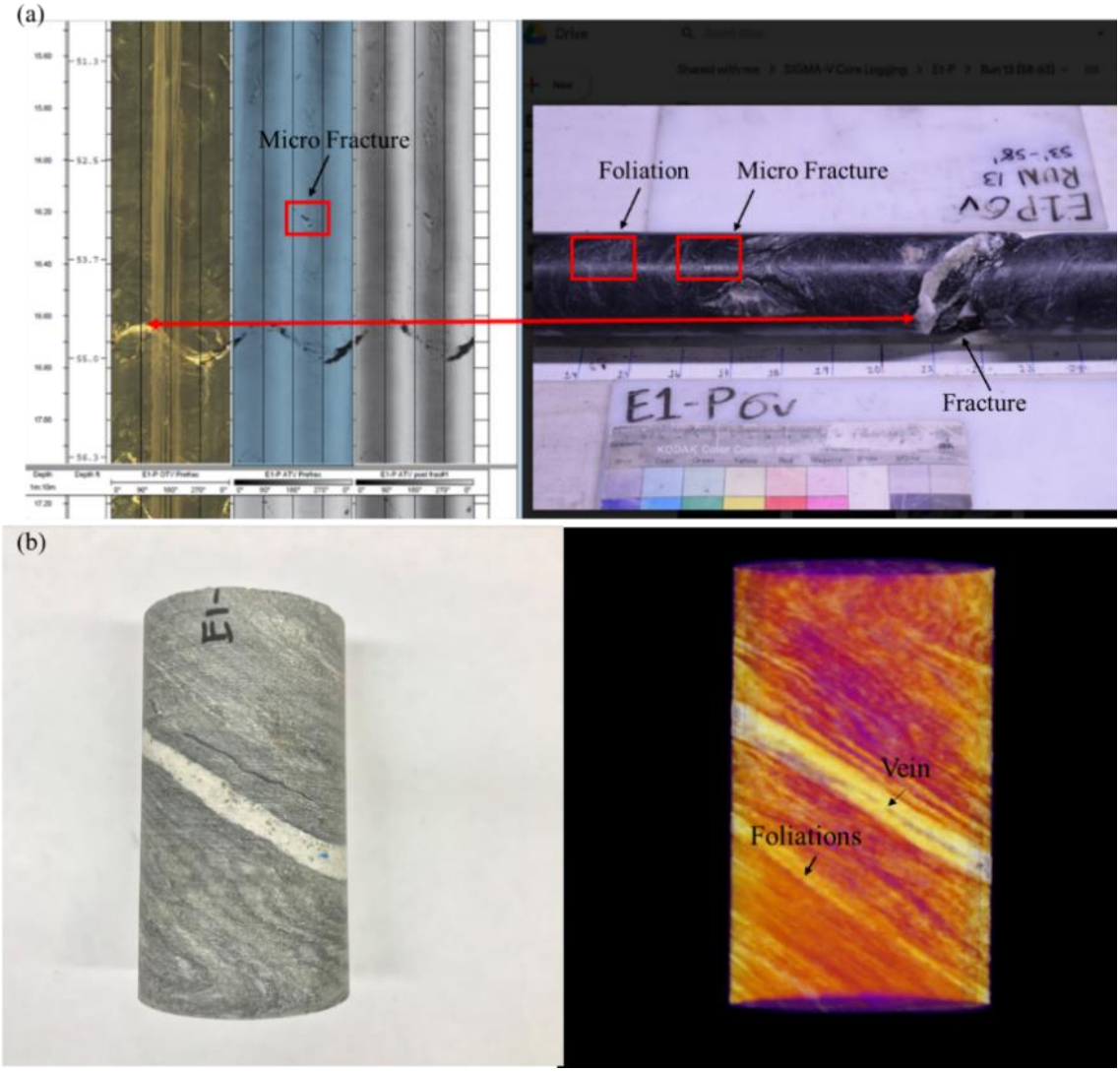

Figure 2.1 (a) Acoustic televiewer log showing the fracture orientation, foliation and micro fracture in borehole E1-P from EGS Collab. (b) Poorman Schist sample from E1-PDT 99.3~100.25 ft and CT scanning image of the sample (the sample was CT scanned at Berkeley Lab). The rock sample is from EGS Collab and diameter is 61 mm and length is 110 mm.

The distribution of foliation in the Collab rock mass is very irregular and may not follow a certain type of stochastic distribution. However, the micro-foliation density surrounding the fractures is considered to follow the same power law relation as the micro-fractures in this work to make it possible to construct a less complex numerical system. Thus, micro-foliation and micro-fractures are treated similarly in this work. The major foliations are accounted for by the heterogeneity in the reservoir properties (e.g., in Young modulus) or discrete fracture. So, to account for the natural fracture, micro/macro-foliation, and microcrack populations we use a dual-scale approach.

In our approach, the rock mass is viewed to consist of a population of large-scale facture (derived from the borehole image logs and core) and a population of small-scale fractures representing the micro-fracture/foliation population. Note that the major fractures and foliations are in the major fracture category. While micro-fractures and micro-foliations are in the micro-fracture group. Micro-fractures are assumed to accompany each major fracture and are located around them. The Young's modulus of finite elements follows the Log Normal distribution to implicitly represent the distribution of micro-fractures. The mean and std of this Log Normal distribution can be determined by measuring Young's modulus of multiple core samples. Further, micro-fractures are treated as mass points in the FEM for the purpose of stress calculations on them. The major fractures are explicitly represented in the model so that their deformation and pressure can be explicitly simulated. The micro-fracture density away from a major fracture is described by a power law. This is justified in view of the study in (Anders, Laubach et al. 2014). Specifically, the shortest distance between micro-fractures and the parent major fracture is described

by a power law. Here a simple method is used to generate desired micro-fractures population surrounding the major fracture.

To generate the micro-fracture population, a density of micro-fracture N is assumed ($500/m^3$) over the entire system. They are then distributed in a cubic around the major fractures. The length of the cubic is assumed as the three times radius of major fracture. Here major fracture PDT-114 is utilized to illustrate the generation of micro-fracture population. The information of PDT-114 can be found in EGS Collab site. In the first step, the radius of PDT-114 is $R = 3$ m and the volume of this cubic contained PDT-114 is 729 m^3. The number of micro-fractures in this cubic is $729\ m^3 \times 500/m^3 \approx 3.6 \times 10^5$. Note that field studies suggest that the density of micro-fracture can be larger than $10{,}000/m^3$ (Anders, Laubach et al. 2014). Here the density of micro-fracture N of $500/m^3$ is adopted to lower the computation costs. Figure 2.2 shows a histogram plot of the shortest distance between micro-fractures and the major fracture. So far, those micro-fractures are randomly distributed.

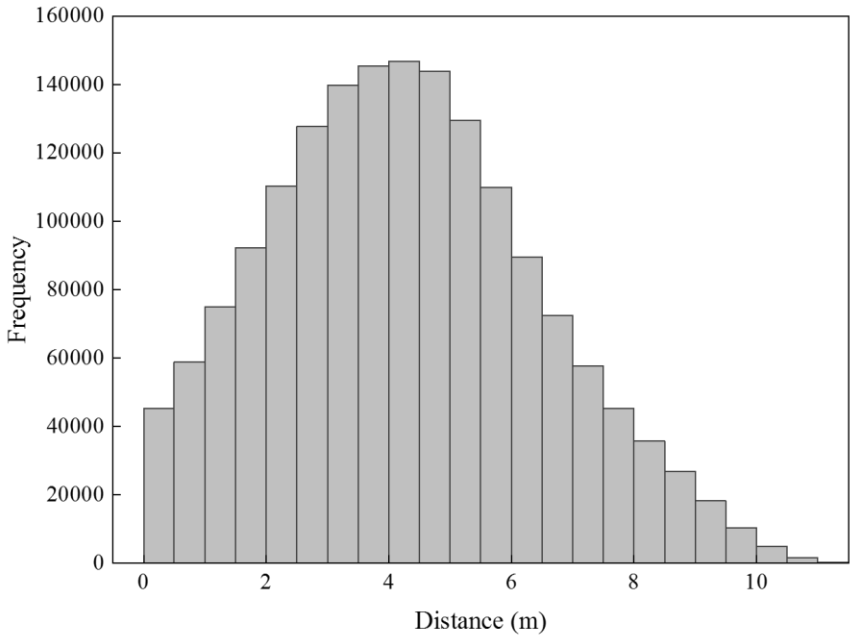

Figure 2.2 The histogram plot of the shortest distance between micro-fractures and major fracture.

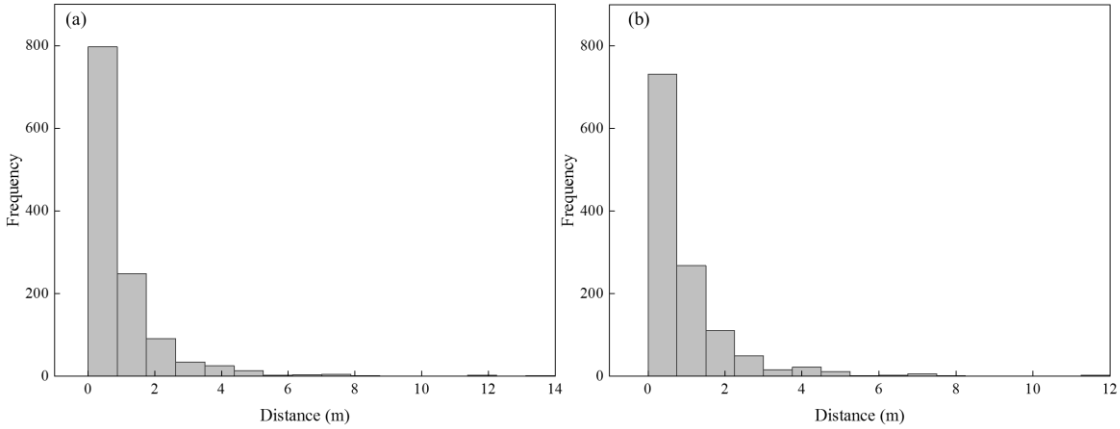

Figure 2.3 The distribution of distances. (a) the distribution of desired distances generated by a power law ($k = 4$ and $a = 5$ and $T_{mic} = 1223$). (b) the distribution of shortest distance between desired micro-fractures and the major fracture.

In the second step, the number of accompanying micro-fracture of each major fracture is identified. Field data (Mitchell and Faulkner 2009, Anders, Laubach et al. 2014) suggested that most micro-fractures are located within a zone surrounding a major fracture which extends nearly 1 m from the major fracture. The volume of surrounding zone (ellipsoid shape) of this major fracture can be calculated as: $4/3 \cdot \pi \cdot 1[\mathrm{m}] \cdot (1+R)[\mathrm{m}] \cdot (1+R)[\mathrm{m}]$ where R is the radius of the major fracture. In this case, the total volume of surrounding zone (ellipsoid shape) of PDT-114 is $4/3 \cdot \pi \cdot 1[\mathrm{m}] \cdot (1+3)[\mathrm{m}] \cdot (1+3)[\mathrm{m}] = 67\ \mathrm{m}^3$. Therefore, the number of accompanying micro-fractures of PDT-114 is $N \times 67\ \mathrm{m}^3 = 500/\mathrm{m}^3 \times 67\ \mathrm{m}^3 = 33{,}500$.

The density of micro-fractures is usually identified by SEM for example. Thus, the minimum size of micro-fracture is very small (~1 μm-mm). It is believed that detectable seismicity cannot occur on such small size micro-fracture in-situ. Here, we define an effective micro-fracture size for seismicity generation. In the third step, we require the

radius of the micro-fracture to be larger than a threshold value for Collab fracture (here we use 30 mm which is two orders less than the radius of major fracture). The micro-fracture size commonly follows a power law distribution (Anders, Laubach et al. 2014, Laubach, Hooker et al. 2014).The cumulative power law distribution is (Laubach, Hooker et al. 2014) is given as $F = a \cdot X^{-b}$. F is the fracture cumulative frequency and X is the fracture radius (mm). Here a = 2.4x10^{-2} and b=0.1 based on the observation of sandstone from field data (Laubach, Hooker et al. 2014). Therefore, the number of effective (following power law distribution with radius > 30 mm) micro-fractures around PDT-114 is 1223.

In the fourth step, a power law is determined based on field observations or estimation of micro-fractures density within the surrounding zone of each major fracture. Such power law (Pareto distribution, PDF $= a \cdot k^a/x^{a+1}$) could be described by two numbers: $k > 0$, the location parameter and $a > 0$, the shape parameter. Thus, the mean of power law distribution is $k \cdot a/(a-1)$ and the variance is $k^2 \cdot a/\big((a-2) \cdot (a-1)^2\big)$ and assume $k = 4$ and $a = 5$. In this case, PDT-114 have 1223 micro-fractures which is defined in the third step. Figure 2.3a shows the power law distribution ($k = 4$, $a = 5$ and $T_{mic} = 1223$.) of desired micro-fractures population in FEM. The micro-fractures generated in first step is selected when the shortest distance between this micro-fracture and major fracture is best to fit the power law. The shortest distance between selected micro-fractures and major fracture is shown in Figure 2.3b. Such distribution of distance fits the power law very well. The selected micro-fractures will be considered in FEM (Figure 2.4). In the fifth step, the selected micro-fractures around the major fractures are assigned orientations. Micro-fractures in granite exhibits no strongly preferred orientation (Tuttle

1949). It mostly depends on the its slip direction (Anders, Laubach et al. 2014). In this work, micro-fracture orientation is assumed to follow by lognormal distribution. For instance, the dip of the selected micro-fractures around PDT-114 is followed the lognormal distribution (mean is 58^o and std is 10^o) and the value of mean is the same as dip of PDT-114. While the strike of the selected micro-fractures is also followed the lognormal distribution (mean is 11^o and std is 50^o) and the value of mean is the same as the strike of PDT-114. Figure 2.4 shows the orientation of the selected micro-fractures surrounding of PDT-114.

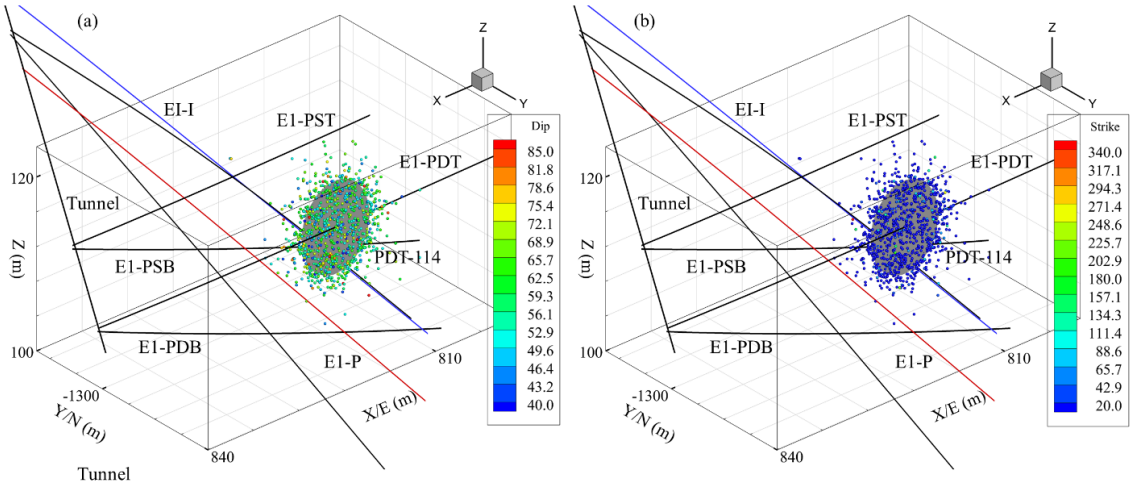

Figure 2.4 Orientation of selected micro-fractures. (a) the dip of selected micro-fractures and (b) the strike of selected micro-fractures.

In the sixth step, the selected micro-fractures are submitted into FEM to calculate the Coulomb failure function (CFF). The stress and pore pressure fields of micro-fractures can be obtained by interpolating the stress and pressure distribution on the finite elements. The larger the CFF, the larger the event magnitude may occur on this micro-fracture. The CFF is defined as CFF $= \tau_s - \mu \cdot \sigma_n$. τ_s and σ_n is the shear stress and normal stress on

fracture, respectively. μ is friction coefficient which is the same as the major facture. The cohesive strength is assumed as zero.

2.2.2 Fluid Flow in Fracture

After a 3D dual-scale semi-deterministic fracture network is generated, a fracture flow model is defined for the major fractures. The fracture permeability is defined using the cubic law and the overall rock mass permeability is calculated using the equivalent permeability concept. Here the contribution of micro-fractures is included in the rock matrix permeability. The intersection line between the fractures and finite elements (Hexahedrons) faces are calculated based on a geometric surface-surface intersection algorithm (Wang 2014, Cheng, Wang et al. 2019). The permeability tensor on a finite element can be calculate as (Wang 2014, Cheng, Wang et al. 2019)

$$k_i = \sum_{j=1}^{n_{fi}} \frac{a_j^3 l_{ij}}{12 A_i}, i = x, y, z \tag{2.10}$$

Where n_{fi} is the total number of fractures in the volume (finite) element; a_j is the aperture of the j^{th} fracture; l_{ij} is the length of intersection line on the element interface; A_i is the cross-section area in the corresponding i direction (Figure 2.5). k_i $(i = x, y, z)$ is represent the permeability of a finite element in x, y and z direction (local coordinate system), respectively.

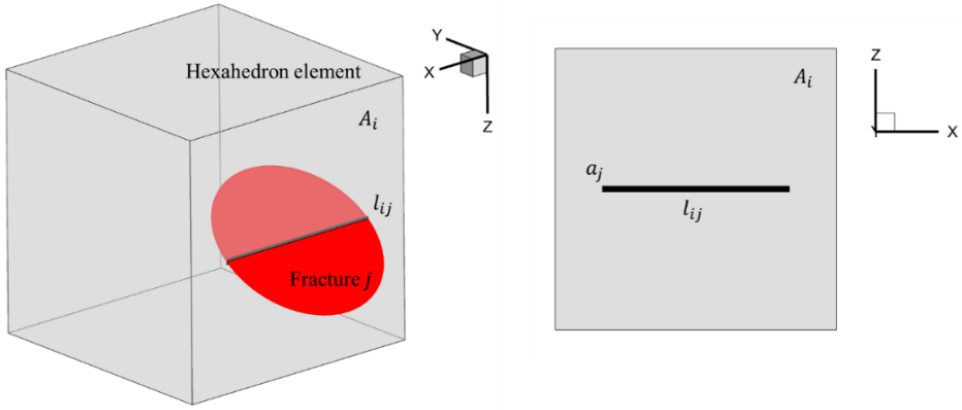

Figure 2.5 The contribution of one fracture permeability to equivalent permeability of a finite element (reproduced from Wang and Ghassemi 2013)

During injection, the effective normal stress on a fracture can change so that its aperture and permeability would also change and would influence the variation of permeability tensor in the finite element. Therefore, the fluid pressure, displacement and temperature of the fractures has to be integrated with those of the equivalent porous medium. The pore pressure, displacement and temperature within the equivalent medium are calculated by the thermal-hydrological-mechanical model (Chapter 2.1) at each time step. The fluid pressure within a fracture is approximated by averaging the pressure values of all finite elements intersected by it. The heat transport within the fracture network is obtained by utilizing the method from (Bruel and Cacas 1992). Fluid flow and heat transfer occurs in the connected fracture network. The fluid and heat transfer within the fracture network is simulated by assuming a 3D flow channel consists of 1D flow pipes (Cheng, Wang et al. 2019). Such 1D pipes link the fracture centers with the mid-point of intersection line of adjacent fractures. The temperature of fluid in the fracture and rock matrix are assumed continuous at the fracture well (Cheng, Wang et al. 2019). Thus, the heat transfer model of fracture network is assumed as 1D steady state. The energy conservation of each fracture should be balanced so the convective heat transport from fluid flow should equal the sum of the heat conduction between adjacent rock matrix and fluid in the fracture, and the change of energy retained by the volume of the fluid within the fractures. Details of the energy conservation in each fracture can be found in (Cheng, Wang et al. 2019). The changes of fluid pressure and temperature within the fracture network are substituted into the Equation 2.9 for next time step. Thus, the stress changes around the fractures due to

the changes in fracture network are considered. The normal and shear stress, σ_n, τ_n on a fracture are calculated depending on the pore pressure and in-situ stress. Patton's saw tooth fracture model is used to estimate the fracture shear strength, τ_p (Patton 1966):

$$\tau_p = \sigma_{eff} \tan\left(\phi_{basic} + \phi_{dil}^{eff}\right) \tag{2.11}$$

$$\phi_{dil}^{eff} = \frac{\phi_{dil}}{1+9\sigma_{eff}/\sigma_{neff}} \tag{2.12}$$

Where $\sigma_{eff} = \sigma_n - p$ is the effective normal stress on fracture; ϕ_{basic} is the basic friction angle; ϕ_{dil}^{eff} is the effective shear dilation angle; ϕ_{dil} is the experimentally measured dilation angle and σ_{neff} is the effective normal stress required to cause 90% reduction in the natural fracture aperture. Once the Mohr-Coulomb failure criterion is met, the fracture will slip. The shear displacement U_s of a fracture is given by (Hicks, Pine et al. 1996):

$$U_s = \frac{\tau_n - \tau_p}{K_s} \tag{2.13}$$

Where K_s is the fracture shear stiffness (e.g., $K_s = 7\pi/24 \cdot G/r$ for penny shaped crack (Eshelby and Peierls 1957), r is the fracture radius and G is shear modulus); The total stimulated fracture aperture is written as (Willis-Richards, Watanabe et al. 1996):

$$a = \frac{a_0}{1+9\sigma_{eff}/\sigma_{nref}} + a_s + a_{res} \tag{2.14}$$

Where a_0 is the initial effective aperture; a_s is the aperture change due to shear displacement; In general, a_s is proportional to the fracture shear displacement U_s (e.g., $a_s = U_s \tan\left(\phi_{dil}^{eff}\right)$). a_{res} is the residual aperture at high effective stress which can cause 90% reduction in fracture aperture; The residual aperture a_{res} is assumed to be zero in this work. If the effective normal stress σ_{eff} is become negative, fracture will be fully open. The fracture aperture is given by the aperture-to-length scaling law:

$$a = \frac{K_{Ic}(1-v^2)}{E\sqrt{\pi/8}}\sqrt{2r} \tag{2.15}$$

Where K_{Ic} is the fracture toughness; The fluid leak-off rate v_L can be described by the Darcy's law as (Valko and Economides 1995):

$$v_L = -\frac{k}{\mu}\frac{\partial P_f}{\partial n} \tag{2.16}$$

where *k* is the matrix permeability, μ is the fluid viscosity, $\partial P_f/\partial n$ is the fluid pressure gradient normal to the fracture surface. The fracture aperture can be calculated by Equation 2.14 or 2.15 and used as input for the next time step. Induced stress caused by fractures also affect the fluid flow and induced seismicity. Since fracture network are embedded into mesh of rock matrix, the induced stress may not comprehensively consider. Thus, the induced stress is calculated based on the Sneddon solution (Sneddon 1946) or Eshelby solution (Eshelby and Peierls 1957). The total induced stress field is obtained as the superposition of induced stress of each fracture. The total induced stress field caused by fracture network are substituted into the Equation 2.9 for next time step.

2.2.3 Fracture Propagation

The processes of fracture propagation when the fracture is not parallel to a principal stress, usually has two stages: a non-planar stage and a planar propagation. The geometry of the initial fracture is circular so that the stress intensity factors for mode I, II and III for an internally pressurized by a fluid pressure P_f is (Schwartzkopff, Xu et al. 2016):

$$K_I(\varphi) = 2\sqrt{\frac{r}{\pi}}\sigma_{n(eff)} \tag{2.17}$$

$$K_{II}(\varphi) = -\frac{4\cos(\varphi-\omega)}{2-v}\sqrt{\frac{r}{\pi}}\tau_{eff} \tag{2.18}$$

$$K_{III}(\varphi) = \frac{4(1-v)\sin(\varphi-\omega)}{2-v}\sqrt{\frac{r}{\pi}}\tau_{eff} \tag{2.19}$$

Where r is the radius of the initial fracture; σ_{neff} and τ_{eff} are the effective normal stress and shear stress. ω is the shear angle (form by the angle between shear stress direction and reference direction) and φ is the fracture front angle (Figure 2.6); the edges of each fracture can have multiple tips and 20 tips are used in this work. Note that 20 tips on the edges can ensure the effective and accurate of the program. Those tips are uniformly located on the edges of fracture and are used to extend a fracture.

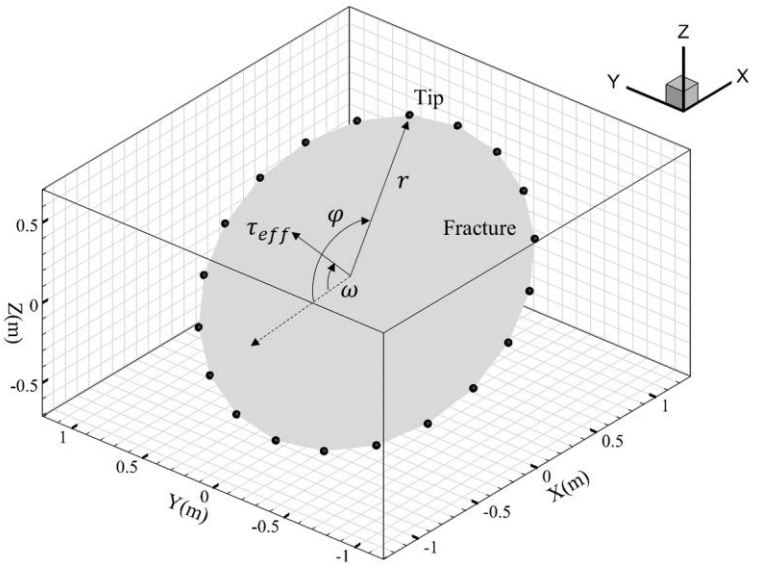

Figure 2.6 The definition of tips, fracture radius, shear angle ω, fracture front angle φ and shear stress τ_{eff}. The direction of dot arrow is obtained by projecting the dip direction on the fracture (Schwartzkopff, Xu et al. 2016).

The method for calculating the above parameters (e.g., shear angle ω) can be found in (Schwartzkopff, Xu et al. 2016). The kink angle $\theta_0(\varphi)$ at the non-planar propagation stage can be evaluated by:

$$\theta_0(\varphi) = \begin{cases} 0^o & \text{if } K_{II}(\varphi) = 0 \\ 2\tan^{-1}\left[\dfrac{K_I(\varphi) \mp \sqrt{K_I^2(\varphi)+8K_{II}^2(\varphi)}}{4K_{II}(\varphi)}\right] & \text{if } K_{II}(\varphi) \neq 0 \end{cases} \tag{2.20}$$

In order to simplify the complexity of the computation, the kink angle $\theta_0(\varphi)$ during the non-planar propagation stage is assumed to remain constant. According to the maximum

tensile stress criterion, a fracture propagates along $\theta_0(\varphi)$ during the non-planar propagation stage if:

$$K_{eq} = \cos\frac{\theta_0(\varphi)}{2}\left(K_I(\varphi)\cos^2\frac{\theta_0(\varphi)}{2} - \frac{3}{2}K_{II}(\varphi)\sin\theta_0(\varphi)\right) \geq K_{Ic} \tag{2.21}$$

Where K_{eq} is the equivalent stress intensity factors; For a fracture not aligned with the maximum stress, the newly created crack tips will not be the on the same plane after fracture propagation because of the different kink angle $\theta_0(\varphi)$ value for a new different φ. To represent the newly formed fracture segment, a certain number of penny fractures is inserted to best represent the newly created surface (Figure 2.7). The number of inserted penny fractures is assumed the same as the number of propagating tips "nodes."

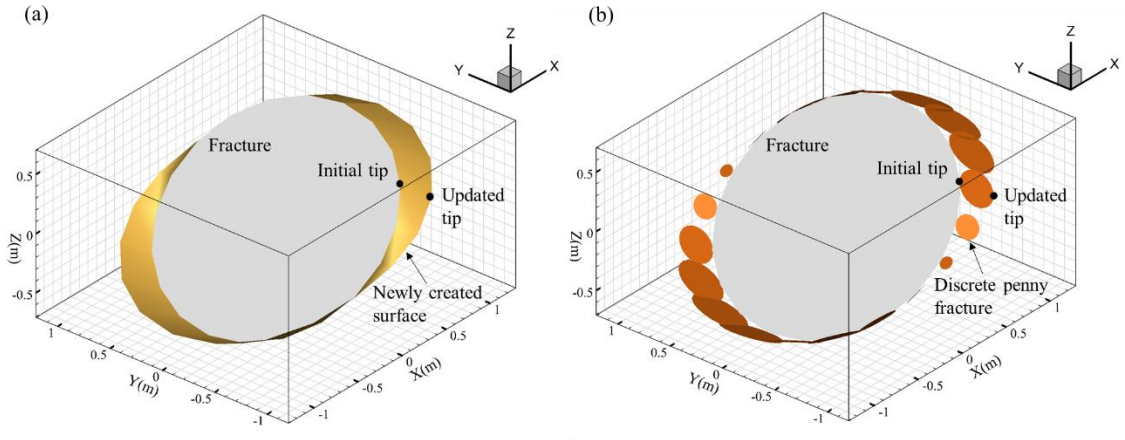

Figure 2.7 The representation of newly created surface and updated tips. (a) the newly created surface. (b) the newly created surface is represented by 20 discrete penny fractures.

Penny-shaped fractures are used because the calculation of the hydraulic field in current numerical system assumed penny shape fractures. Also, if the subsequent fracture front is nonplanar, the SIF for the next step cannot be calculated analytically for other shapes aside from elliptical. It is, therefore, necessary to consider a dynamic "fictitious" penny shape plane which best fits the updated tips because the dimension of non-planar

propagation is usually small compared to the original fracture (Figure 2.8). l is the diameter of "fictitious" plane. It is a plane fitted by the updated tips using least squares method. The pressure in the fictitious plane is considered the same as that of the propagated fracture because those two are very close. The normal and shear stress of fictitious plane is calculated based on the procedures in Chapter 2.1 using its geometric properties.

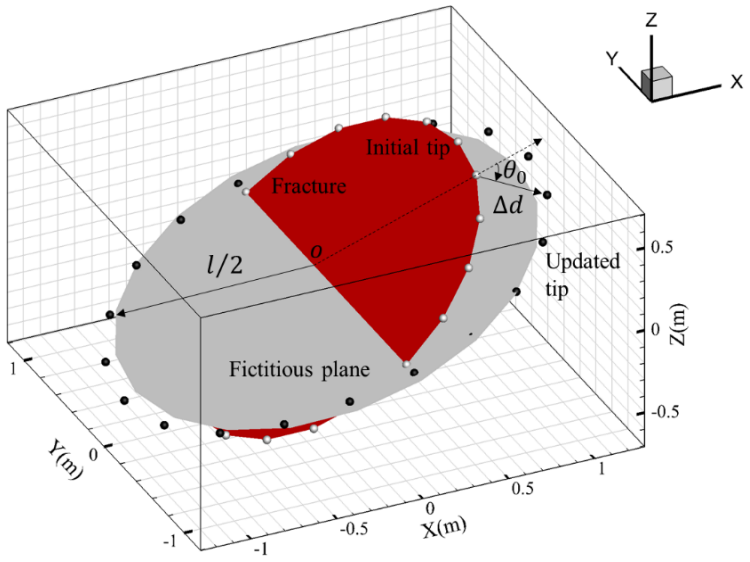

Figure 2.8 The definition of the fictitious plane (grey), the kink angle θ_0 and the propagation increment, Δd. l is the length of the fictitious plane. o is the center of initial fracture center. The fictitious plane is bested fitted by the updated tips.

The SIF of the "fictitious" penny plane can be calculated by the Equation 2.17-2.19. As the fracture continues to propagate, the fictitious plane becomes perpendicular to the direction of minimum principal stress and tends to propagate in a planar manner. Here, during the planar propagation stage (usually a few steps), an elliptical fictitious plane is used to best fit the fracture tips by least-squares criterion because the crack tips are usually distributed in a wing manner (for mechanical analysis). The propagation length of the planar propagation would be larger than those of non-planar propagation because fracture

is more likely to propagate in mode I. Once the fictitious plane is propagated, the pressure drop, ΔP_f in the fictitious plane can be calculated (Rahman, Hossain et al. 2002):

$$\frac{\Delta P_f}{\Delta l} = \frac{64\mu q}{\pi l a^3} \tag{2.22}$$

Where $\Delta l = l_{j+1} - l_j$ and j is the j^{th} iteration step. q is the flow rate in this fracture and a is the fracture aperture and μ is the fluid viscosity; The SIF of a fictitious elliptical fracture during the planar propagation stage determined by as (Kachanov, Shafiro et al. 2013):

$$K_I(\varphi) = \frac{\sigma_{n(eff)}\sqrt{\pi}}{E(k)}\left(\frac{b}{a}\right)^{0.5}(a^2\sin^2\varphi + b^2\cos^2\varphi) \tag{2.23}$$

$$K_{II}(\varphi) = 0 \tag{2.24}$$

Where a and b are the major and minor axis of the fictitious plane. The newly created surface should be perpendicular to the minimum principal stress direction. Thus, the shear stress on this fictitious plane is zero and $K_{II}(\varphi)$ and kink angle are also zero. Equation 2.23 and 2.24 are substituted into Equation 2.21 to calculate the equivalent stress intensity factors, K_{eq} which are defined by Equation 2.21. The magnitude of fracture propagation at tips can be given by scaling law (Mastrojannis, Keer et al. 1980):

$$\Delta d^i = \begin{cases} 0 & K_{eq}^i < K_{Ic} \\ \Delta d_{\max}\left(\frac{K_{eq}^i - K_{Ic}}{K_{eq}^{\max} - K_{Ic}}\right)^m & K_{eq}^i \geq K_{Ic} \end{cases} \tag{2.25}$$

Where Δd_i is the growth rate of the i^{th} tip, m is the index and is generally assumed as 1, $\Delta d_{\max}$ is the maximum propagation length (e.g., 10% of initial fracture radius); In this work, the propagation scheme is based on the suggestion from (Rahman, Hossain et al. 2000, Rahman, Hossain et al. 2002, Schwartzkopff, Xu et al. 2016). An algorithm describing the propagation scheme is given below.

Algorithm 1. An algorithm for fracture network propagation.

while current time step < total time step **do**

Current time step size Δt

Compute primary variables (e.g., displacement, pressure using FEM)

for each fracture **do**

Outline fictitious plane

Determine θ_0 and K_I^{eq} (Equation 2.20 and 2.21)

while $0 < \frac{K_I^{eq} - K_{Ic}}{K_{Ic}} < \varepsilon_{SIF} = 10\%$ **do**

Propagate the fracture by Δd (Equation 2.25) in direction θ_0 (fracture tips are updated)

Outline fictitious plane based on newly created tips

Calculate the pressure drop by Equation 2.22.

Calculate SIF and K_I^{eq} (Equation 2.17-2.19/2.23-2.24, 2.21)

end

if $\frac{K_I^{eq} - K_{Ic}}{K_{Ic}} \geq \varepsilon_{SIF} = 10\%$ **then**

Redefine time step size $\Delta t := \Delta t/2$

return (Re-run current time step)

end

if $K_I^{eq} - K_c < 0$ **then**

continue (Skip to next fracture**)**

end

end

Insert penny fractures to represent newly created surfaces of propagated fractures.

End

2.2.4 Eshelby Solution for Fracture Pressure Induced Stress Field (Stress Shadow)

Eshelby solution was first introduced to formulate the elastic stress field surrounding and insider an inclusion in an isotropic elastic infinite medium (Eshelby and Peierls 1957, Eshelby and Peierls 1959). Since 1960's, Eshelby solution has been applied to solve complicate problems, such as faulting (Rudnicki 1977), deformation in reservoir undergoing production (Guido, Antonellini et al. 2015). The details of Eshelby solution for induced stress field can be found in (Meng, Heltsley et al. 2012) or Appendix A. Note that the solution only describes the induced stress field of an inclusion. The superposition principle is applied to calculate the total stress field of fracture network. However, because in most applications the number of fractures in our applications is more than several thousands and the density of fracture is relatively high, there are two limitations in the analysis: (1) the magnitude of total induced stress field may exceed the matrix strength (i.e., tensile strength); (2) the computational cost is generally high. Thus, some assumptions are adopted for addressing these two limitations. The induced stress field of the region close to a fracture is considered which can save lots of computational time. The distance between this region and fracture is less than 0.25 times the fracture radius. For example, for areas beyond 0.25 times the fracture radius, the induced stress field is ignored, because the magnitude of induced stress is relatively small. In addition, the magnitude of total induced stress filed may exceed the rock matrix strength at crack tips. Thus, the magnitude of total induced stress filed should not exceed the threshold values (i.e., rock tensile strength). Therefore, the excess portion of total induced stress field is not considered.

2.2.5 Simulation of Induced Seismicity

Slip on fractures is believed to induce seismic events. In-situ (Scotti and Cornet 1994, Amann, Gischig et al. 2018) and lab experiments (Ye and Ghassemi 2018, Ye and Ghassemi 2019, Ye and Ghassemi 2020) indicate that injection-induce fracture slip can enhance the permeability by up to 2-3 orders of magnitude, and a large portion of slip can be aseismic. We argue that aseismic-seismic transition exhibits a dependence on the slip rate and slip distance. Motion (e.g., aseismic-seismic transition) can be described by the dynamic equations of motion where velocity/slip rate and displacement/slip distance are the primary variables. Some studies have attempted to employ the spring system (Figure 2.9a) to represent the instability of faults (Marone 2019, Scholz 2019) and a threshold velocity was derived (Im, Marone et al. 2019). Such a spring system can be exactly described by the dynamic equations of motion. When either the fracture slip distance, or the fracture slip rate, or both are larger than threshold values in a cycle, slip will become unstable (seismic). Or, when the critical stiffness, K_c, is larger than fracture shear stiffness, K, slip will become unstable (seismic) (Scholz 2019):

$$K_c = \frac{(b-a)\cdot\sigma_n}{D_c}\left[1 + \frac{M\cdot V^2}{\sigma_n\cdot a\cdot D_c}\right] \tag{2.26}$$

$$K = \frac{7\pi}{24}\frac{G}{r} \tag{2.27}$$

Where a, b and D_c are the experimentally measured parameters of rate-state friction law (Figure 2.9b). M is the mass per unit area of fracture $(\mathrm{kg/m^2})$. σ_n is the effective normal stress and V is the slip rate; D_c is a distance for the evolution to steady state. Equation 2.26 can be found in (Gu, Rice et al. 1984, Im, Marone et al. 2019). In practice, K represents elastic properties of the rock surrounding the fracture/fault and the size of

the latter. Equation 2.27 describes the penny shape fracture shear stiffness (Eshelby and Peierls 1957); r is the fracture radius.

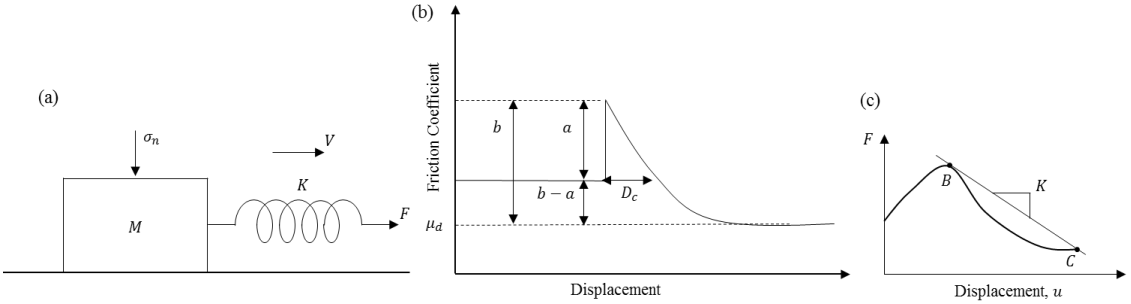

Figure 2.9 Schematic diagram shows the definition of spring system and rate and state friction law. (a) is spring system, σ_n is the effective normal stress, K is the stiffness of spring, F is loading force and V is the slip rate. M is the mass of system. (b) is the rate and state friction law. μ_d is the experimentally measured dynamic friction coefficient. (c) is Force-displacement diagram in the vicinity of the fracture.

By submitting Equation 2.27 into Equation 2.26 ($K_c = K$), the threshold slip rate V_c for penny fracture is given by:

$$V_c = \sqrt{\frac{\sigma_n \cdot a \cdot D_c}{M}\left(\frac{7\pi \cdot G \cdot D_c}{24(b-a)\cdot \sigma_n \cdot r} - 1\right)} \tag{2.28}$$

For example, if fracture radius $r = 10$ m, rock mass per unit area of fracture $M = 5600$ kg/m^2, Young's modulus $E = 40$ GPa, Poisson's ratio is 0.22, a=0.003, b=0.006, $D_c = 10$ μm, effective normal stress is $\sigma_n = 2$ MPa, the threshold slip rate is $V_c = 4$ mm/s according to Equation 2.28. The rate-state friction parameters are defined according to the (Im, Marone et al. 2019). Note that very few works can reliably and explicitly present the threshold slip rate for penny fracture. It suggests that if the loading slip rate of fracture is larger than $V_c = 4$mm/s, fracture slip is eventually unstable. If the spring reaches a tangent point (point B), $\partial F/\partial u$ will decrease faster than K (Figure 2.9c). It suggests that the surrounding rock is no longer capable of absorbing the energy released

during deformation on the fracture and seismic slip occurs on the fracture. Seismic slip may occur after sufficient aseismic slip is accumulated (Dobroskok and Ghassemi 2005). Some previous self-weight sliding tests indicated that if the shear slip distance is larger than the peak displacement δ_p, the fracture becomes unstable (Barton and Bandis 1982, Barton, Bandis et al. 1985):

$$\delta_p = \frac{l}{500}\left(\frac{JRC}{l}\right)^{0.33} \tag{2.29}$$

Where l is the length of fracture; JRC is the joint roughness coefficient. The fractures length in the experiments was in the range of 0.3 m to 12 m. Equation 2.29 is an empirical formula based on the analysis of 650 tests at low normal stress. However, Equation 2.29 is not dependent on normal stress which is not always realistic. Recently, another empirical formula was derived based on 358 direct shear tests where the length of fracture are range from 0.05 to 3 m. (Asadollahi, Invernizzi et al. 2010, Rashidian and Chang 2012):

$$\delta_p = 1.925 \cdot l^{0.09} \cdot JRC^{-0.97} \cdot JCS^{-1.19} \cdot \sigma_n^{0.24} \tag{2.30}$$

Where JCS is the joint compressive strength and σ_n is the normal stress acting on it; Equation 2.30 describes the peak displacement of rough $(JRC > 5)$ and hard $(JCS > 50\ \text{MPa})$ fractures. For example, if fracture (e.g., granite) length $l = 10\ \text{m}$, $JRC = 6$, $JCS = 230\ \text{MPa}$, $\sigma_n = 45\ \text{MPa}$, the peak displacement is $\delta_p = 0.017\ \text{m}$ according to Equation 2.29. The peak displacement is $\delta_p = 0.0016\ \text{m}$ according to Equation 2.30. It seems that the Equation 2.30 is more realistic for calculating the peak displacement of fractures in our application. Equation 2.29 and 2.30 attempts to scale δ_p from laboratory to field and so they may not map the full nonlinear features of the rock mass. But it still provides a straightforward method to distinguish between the seismic

and aseismic slip. So, we use them as a convenient modeling approach, i.e., if the slip rate is larger than the threshold slip rate (from Equation 2.28) or the slip distance is larger than the threshold slip distance (from Equation 2.30), shear stiffness K is less than the critical stiffness K_c. So, the threshold slip displacement and slip rate are utilized to distinguish between the aseismic and seismic slip. In our simulation, the slip rate is more likely to reach the threshold slip rate.

It is generally accepted that fracture failure and the onset of slip is governed by the Mohr-Coulomb failure criterion. Commonly, one event is then generated at failure on the fracture faces. In practice, one fracture may generate multiple events (Ye and Ghassemi 2019) on or in the fracture surrounding volume. Numerical generation of induced seismicity has been intensely studied (Hazzard and Young 2004, Baisch, Vörös et al. 2010, Segall and Lu 2015), yet few models exist capable of achieving induced seismic events with realistic quantitative output. Those simulations cannot resolve the number and location and magnitude of multiple seismic events caused by fracture failure. Other studies (McClure 2012, McClure 2015) also use one event whenever the slip rate of an element is larger than an arbitrarily chosen value. Event hypocenters were defined as the location of failure elements and the event hypocenters were relocated randomly to approximate the effect of relocation error. Failed elements were randomly assigned a certain number of events. However, in these works, the seismic energy of the event cloud is not consistent with the seismic energy of the failed element, i.e., energy conservation is not enforced. It is known that most seismic events in the fields are made up of many smaller-scale ruptures of one major fracture and surrounding micro-fractures (Ye and Ghassemi 2019, Hu, Ghassemi et al. 2020). Those multiple events occur close to each

other in space and time. In this work, we propose a new model of seismic generation. A micro-fractures population is defined following Chapter 2.2.1 and is used to generate multiple events. Multiple micro-fractures (Figure 2.10b) are located on or around the major fracture (Figure 2.10a). The contour of Figure 2.10b shows the shortest distance between micro-fractures and a major fracture. Micro-fractures located on the major fracture are treated as the contact points between the top and down surfaces of major fractures. The shear slip of the major fracture is assumed to be reflected on the shear slip of micro-fractures, because the micro-fractures are located in the perturbed region of the major fracture. Thus, seismic events may occur on a major portion of the fracture area as well as in its surroundings (e.g., Figure 2.10d).

The seismic source parameter such as the magnitude, location and number of events in the cloud needs to be defined properly. Here a new method is proposed to constrain the uncertainties of the events cloud. In the first step, the major fracture will slip during the injection based on Mohr-Coulomb failure criterion and one fictitious event occurs at the center of the major fracture (e.g., Figure 2.10c). The seismic moment of this fictitious event is calculated as (Hanks and Kanamori 1979, McGarr, Spottiswoode et al. 1979):

$$(M_0)_1 = \int_{\Sigma} GU_s \mathrm{d}A \tag{2.31}$$

Where $(M_0)_1 (\mathrm{N \cdot m})$ is the seismic moment; G is the shear modulus and U_s is shear displacement (seismic). A is the slip area and here is treated as the area of the fracture. In simulation, the seismic moment from Equation 2.31 consists of the seismic moment from all the slip events (on/off a fracture). Because those events are all associated with this major fracture slip. Thus, the fictitious event should be representative of the events cloud (e.g., Figure 2.10d) from energy conservation perspective.

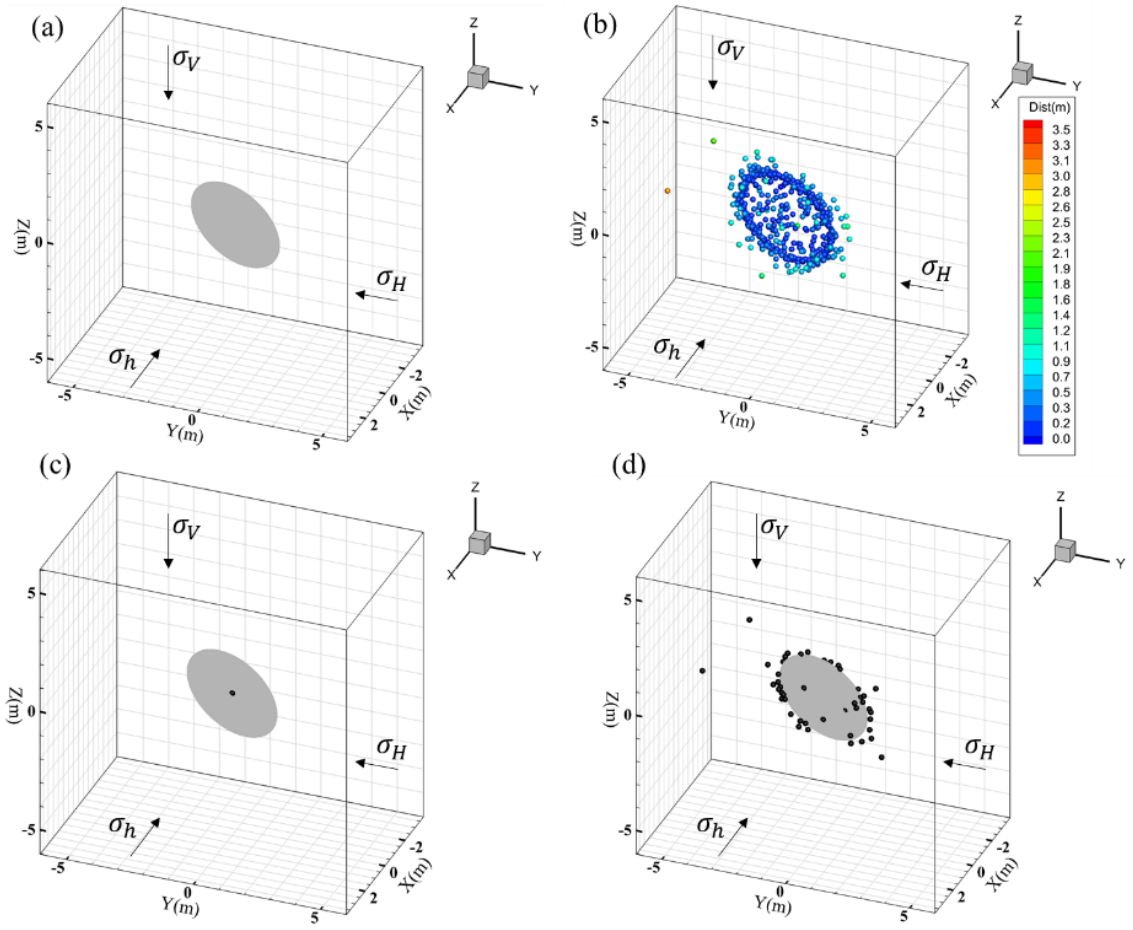

Figure 2.10 Schematic diagram shows the procedures of events cloud generation. (a) is major fracture. (b) is the distribution of micro-fractures. (c) is the fictitious event. (d) is the events cloud.

The moment magnitude of the fictitious event $(M_w)_1(\mathrm{N}\cdot\mathrm{m})$ generated by shear slippage can be estimated as:

$$(M_w)_1 = \frac{2}{3}\log_{10}(M_0)_1 - 6.07 \tag{2.32}$$

The seismic energy of the fictitious event $(E_R)_1(\mathrm{Joule})$ can be calculated as:

$$\log_{10}(E_R)_1 = 4.8 + 1.5\cdot(M_w)_1 \tag{2.33}$$

The seismic energy $(E_R)_1$ is the lumping of all seismic energy. Next, we calculate the shear stress and normal stress on the micro-fractures (the orientation of micro fractures

may follow a randomly distribution or a certain stochastic distribution (e.g., Log normal distribution). In this work, the orientation of micro-fractures follows the Log normal distribution. The mean of Log normal distribution is the same as the orientation of major fracture and standard deviation is set to zero. The micro-fractures friction angle is treated the same as the major fracture and micro-fractures cohesion is set to zero in this work. There is one potential seismic event on each failed micro-crack based on the Mohr Coulomb failure criterion. Thus, there may have an event cloud surrounding a major fracture (e.g. Figure 2.10d). However, the number of seismic events on or surrounding a major fracture has to be constrained. It is known that Gutenberg-Richter law expresses the relationship between the magnitude and the total number of events in any given region. Thus, events should follow the Gutenberg-Richter law suggesting that event clouds have the same b-value as the fictitious events because those events occur in the same region. Here a-value is used as a fitting constant. The Gutenberg-Richter law on a failure fracture can be represented as:

$$\log_{10} N = a - b \cdot M \tag{2.34}$$

Where N is the number of events having a magnitude larger or equal to the magnitude M; b value can be obtained from the field observation; a is the fitting number, and is calculated based on the information of numerically generated fictitious event:

$$a = b \cdot (M_w)_1 \tag{2.35}$$

Where $(M_w)_1$ the moment magnitude of fictitious event and obtained from Equation 2.32; The event cloud is assumed to be exactly fitted by the Gutenberg-Richter law (i.e., R-squared is equal to one). The moment magnitude of nth event is calculated as:

$$(M_w)_n = \frac{a - \log_{10} n}{b} \tag{2.36}$$

Where $(M_w)_n$ is the moment magnitude of nth event and a is from Equation 2.34; The seismic energy of nth event $(E_R)_n$ is calculated as:

$$(E_R)_n = 10^{(4.8+1.5\cdot(M_w)_n)} \tag{2.37}$$

If n is equal to one, Equation 2.36 attempts to calculate the seismic energy of fictitious events. Equation 2.37 can theoretically be used to generate an infinite number of events and some constrains are needed to limit the number of events. The first prescribed condition is the energy conservation i.e., the total seismic energy of the real event cloud should be less than the seismic energy of the fictitious event. While the seismic energy of fictitious event is defined according to Equation 2.31. In practical, Equation 2.31 can describe the seismic moment from all the slip events (on/off a fracture). Thus, Equation 2.31 in numerical model is supposed to already consider seismic moment from all the slip events (on/off a fracture):

$$\sum_{j=2}^{n}(E_R)_j \leq (E_R)_1 \tag{2.38}$$

Where $\sum_{j=2}^{n}(E_R)_j$ is the total seismic energy of the event cloud; $(E_R)_1$ is the seismic energy of the fictitious event defined in Equation 2.33. Another condition is that the receivers cannot detect very small-magnitude events. So, there is a threshold magnitude imposed. Such a threshold on moment magnitude of event M_{th} is set as -3 in this work which is the same as the magnitude of the background seismicity in the regions of our application:

$$(M_w)_n \geq M_{th} = -3 \tag{2.39}$$

These two conditions (Equation 2.38 and 2.39) constrain the number of generated events in the model. The stress and pore pressure fields of micro-fractures can be obtained by interpolating the stress and pressure distribution on the finite elements. The contribution

of micro-fracture to matrix permeability have been contained through the concept of the equivalent matrix permeability. Micro-fractures failure is assessed based on the Mohr-Coulomb failure criterion. In general, the number of failing micro-fractures is larger than the number of events. Each failing micro-fracture is assumed to have one event. Multiple events can occur on the same location over time on fracture. But we only consider the cumulated MEQs at the same location. Therefore, the CFF of each selected micro-fracture is calculated. The large CFF, the larger of magnitude of event occurred on this micro-fracture. While other failing micro-fractures could be considered as aseismic.

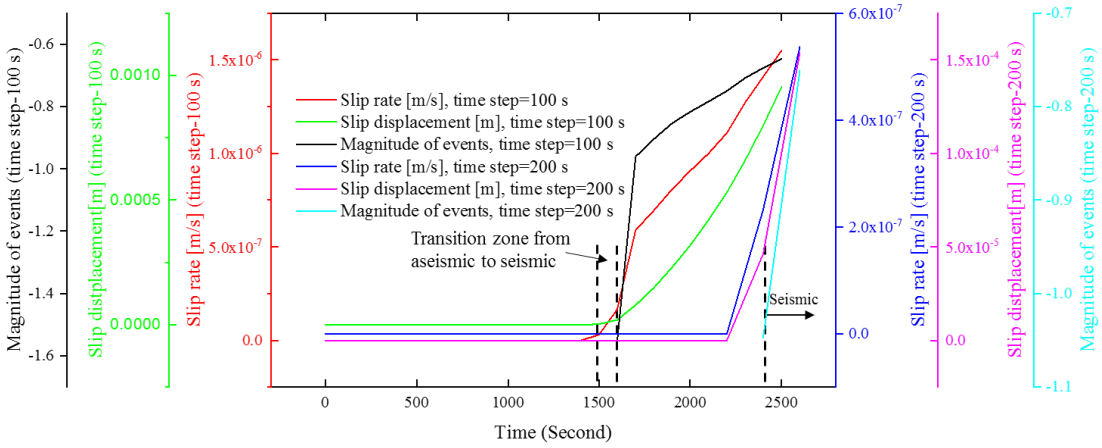

Figure 2.11 The evolution of slip rate, displacement and magnitude of events occurred on fracture 101 (of Collab) over time. Slip rate, time step =100s (red line), slip displacement, time step=100 s (green line), magnitude of events, time step=100s (black line). Slip rate, time step =200s (blue line), slip displacement, time step=200 s (pink line), magnitude of events, time step=200s (cyan line).

In addition, the time step in FEM may have effects on the generation of MEQs, specially on the transition between aseismicity and seismicity. For instance, if the time step is large and the increases of stress on fracture is large, the increases of slip rate is thus large and the transition from aseismicity to seismicity will not be reflected in FEM and only the seismic phase will be observed. For example, the threshold slip rate and threshold slip

displacement is $1x10^{-7}$ m/s and $1x10^{-5}$ m, respectively. Such threshold slip rate and threshold displacement is employed to distinguish between aseismic and seismic state. The simulation settings can be found in Chapter 4. The time step is 100 second and 200 second, respectively. Figure 2.11 shows the evolution of slip rate, displacement and magnitude of events occurred on fracture 101 over the times. There is a transition zone from aseismic to seismic when the time step of simulation is 100 second. It is in the range from 1500 second to 1600 second. While none of transition zone from aseismic to seismic when the time step of simulation is 200 second. A good time step could be set based on the maximum slip velocity of fracture. But this suggestion is not working well in field case (e.g., Utah FORGE). Because 64 fractures are slipped in Utah FORGE. Each slipped fracture has a maximum slip velocity. Therefore, a good time step is set based on the minimum value of those 64 maximum slip velocities. So, the only effective way of mapping the transition between aseismicity and seismicity is by reducing the time step.

2.3 Integration of the 3D Fracture Network with the Coupled FEM

The dual-scale semi-deterministic fracture network model is integrated with the coupled thermo-poroelastic FEM by linking the permeability change, responding to fracture shear dilation and propagation. Fracture network geometry (i.e., aperture and radius) are submitted to FEM for equivalent permeability calculations at each time step. The stress and fluid pressure of fracture are calculated from the FEM solutions. According to the failure criterion, fracture may experience the transition between aseismic and seismic state during the stimulation. If fluid pressure is high enough to make the fracture network propagate, an ultrafast analytical approach is utilized to simulate fracture propagation. Once fractures deform and extend (i.e., dilation and propagation), the geometry of the

fracture network are updated, the solution proceeds to the next time step. The flowchart of the integrated model is shown in Figure 2.12 and Appendix B.

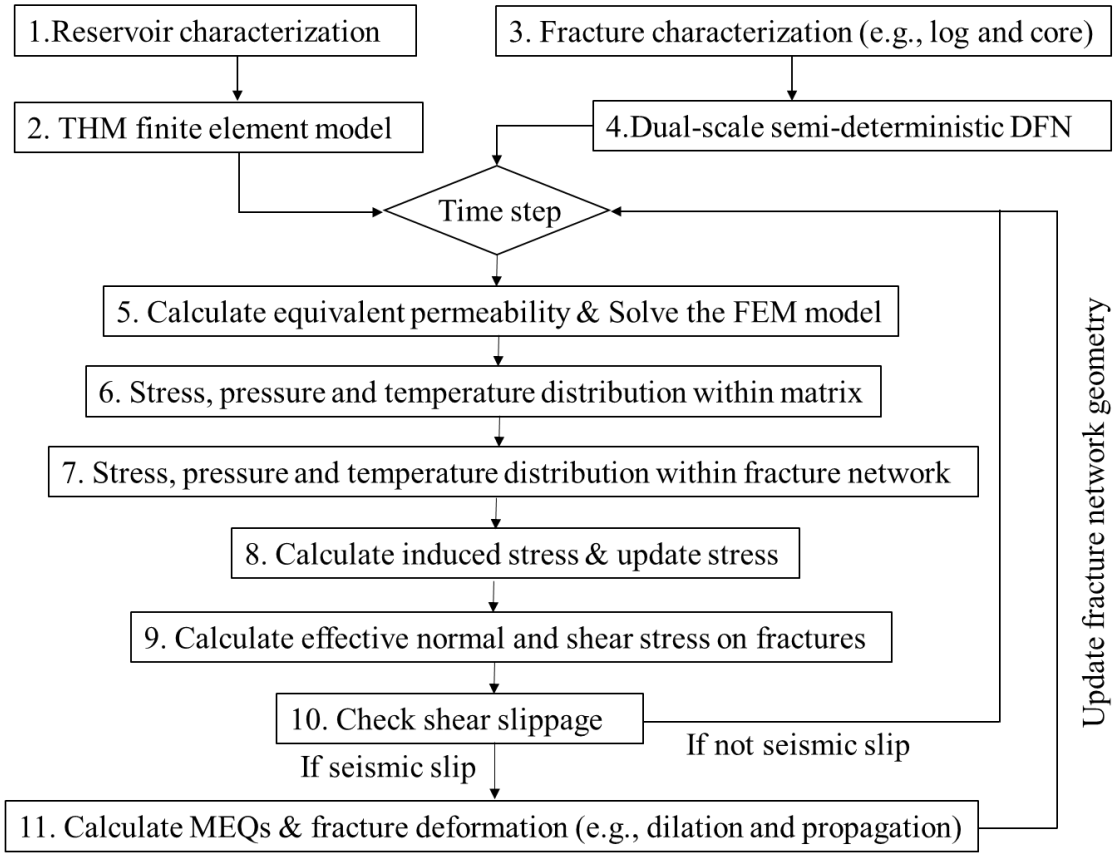

Figure 2.12 The flowchart of the integrated model.

2.4 Conclusions

In this chapter, a coupled Thermo-Hydro-Mechanical-Seismic Model with 3D fracture network has been further developed to simulate the response of EGS to water injection. The coupling process between behavior of fracture network, fracture flow, fracture dilation and propagation, and induced seismicity is described using a hybrid EPM/DFN. A dual scale semi-determinist fracture network generated by combining data derived from

imaging logging and core with fracture properties which follow a stochastic distribution. An advantage of this semi-determinist fracture network model is that measurement data can be incorporated to constrain the uncertainties in the rock mass. Another advantage of this network model is that micro-fractures are also considered. Integration between the coupled finite element model and the dual scale semi-determinist fracture network model is achieved by linking permeability change with fracture deformation (e.g., dilation and propagation). A stress dependent fracture deformation model with a shear dilation model is utilized to account for shear dilation. An ultrafast analytic approach for fracture propagation is applied using the maximum tensile stress criterion. Stress shadow caused by fracture pressurized is described by Sneddon solution or Eshelby solution. The induced seismicity during injection process are also evaluated. A seismic model is developed which allow for multiple seismic events to occur on and around a fracture. Two conditions are imposed to constrain the number and magnitude of events. The switching conditions between aseismic slip and seismic slip are also resolved.

Chapter 3 Verifications and General Examples for Coupled Thermo-Hydro-Mechanical-Seismic Model with a Dynamic 3D Fracture Network

3.1 Introduction

This Chapter presents several comparison studies between the predications from Coupled Thermo-Hydro-Mechanical-Seismic model with 3D fracture network and published results. In addition, several general examples are also presented.

3.2 The Distribution of Pore Pressure Surrounds Fracture

The first considers the pore pressure surrounding a fracture. A penny shape fracture is suddenly pressurized by a 25 MPa for 10 hours. The radius of this fracture is 10.5 m. The permeability of rock matrix is 0.01 mD and initial pore pressure is 20 MPa. The numerical domain is 100 × 100 × 100 m. The results of the pore pressure distribution are shown in Figure 3.1a. A comparison of the numerical results for pore pressure $(X, Z = 0\ \mathrm{m})$ surrounds fracture with the analytical solution from (Warpinski, Wolhart et al. 2004). The red zone in Figure 3.1a is asymmetrical because the meshes cut by fracture is asymmetrical. A very good agreement between numerical results and analytical solution is observed (Figure 3.1b).

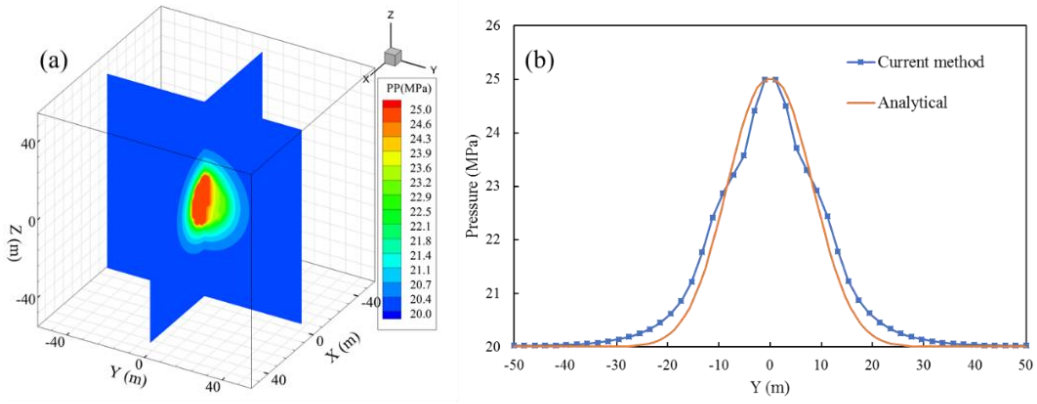

Figure 3.1 The distribution of pore pressure surrounds fracture. (a) is the pore pressure distribution after 10 hours pressurization. (b) is the comparison between the numerical results from current method and analytical solution.

3.3 Frictional Slip of a Single Fracture

For another comparison, frictional slip of a penny fracture is considered. The dip direction of fracture is zero and dip angle of the fracture are 60° and 75°, respectively. The fracture diameter *L* is 10 m. The friction coefficient of the fracture is 0.6. The numerical domain is subjected to remote uniaxial compression (Figure 3.2a). The value of uniaxial stress σ is 41.8 MPa. Young's modulus is 71 GPa and Poisson's ratio is 0.219. Figure 3.2b and 3.2c shows compare numerical results with analytical solution (Phan, Napier et al. 2003, Kaven, Hickman et al. 2012). An acceptable difference (24.4% at the location of maximum slip distance) is observed between the slip distance from current method and analytical solution (Figure 3.2b). The slip distance of fracture in current method is uniformly distributed because normal and shear stresses on fracture are uniformly assigned in the model. Figure 3.2c indicates that the normal stress on fracture from current method and analytical solution match very well.

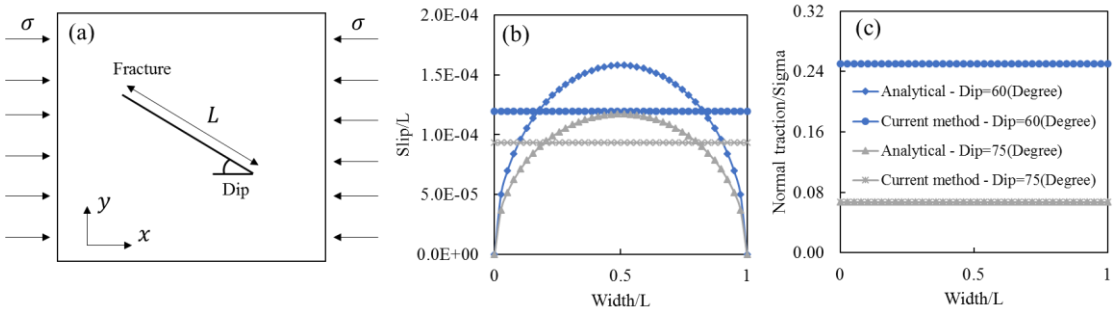

Figure 3.2 Frictional slip of a single fracture. (a) is the boundary conditions and fracture geometry in numerical model. (b) is the dimensionless slip distance alone the fracture width. (c) is the dimensionless normal traction along the fracture width.

3.4 Fracture Propagation

The next comparison study is to investigate the fracture propagation aspect of the model. The geometric and mechanical properties of fracture in this comparison are from (Rahman, Hossain et al. 2000, Schwartzkopff, Xu et al. 2016). The fracture only twists in the vertical direction ($z-$axis) and realigns to the horizontal plane ($xy-$plane). Figure 3.3a is the fracture (dip=45^o, dip direction=0^o) propagation surface. One must keep in mind that the newly created surface is approximated by one continuous surface rather than discrete fracture (e.g., Figure 2.7b) when post-processing to more readily display the geometry. The propagation profile in xz cross section follows the same trend as that of published results (Figure 3.3b, 3.3c, 3.3d). Figure 3.3b indicates that the fracture (dip=15^o, dip direction=0^o) propagation path from current method is lower than others because the calculation of the kink angle in the current method is based on an initial fracture (penny-shape). The value of kink angle is kept constant during the non-planar propagation stage in current method. The kink angle from published results is updated in each step and this is more realistic to represent the actual situation, but higher computational power is required. Figure 3.3c suggests that fracture (dip= 30^o, dip direction=0^o) propagation paths defined by the current method are lower than the results from published works, the differences are not significant. It suggests a trend where the difference is smaller for fractures with higher dip. For the fracture (dip= 45^o, dip direction=0^o) with a higher dip, the results from the current method align closely with the published results (Figure 3.3d). Further, the height of the fracture (the distance between x-axis and fracture tip) propagation is underestimate, especially for fractures with lower dip (Figure 3.3b).

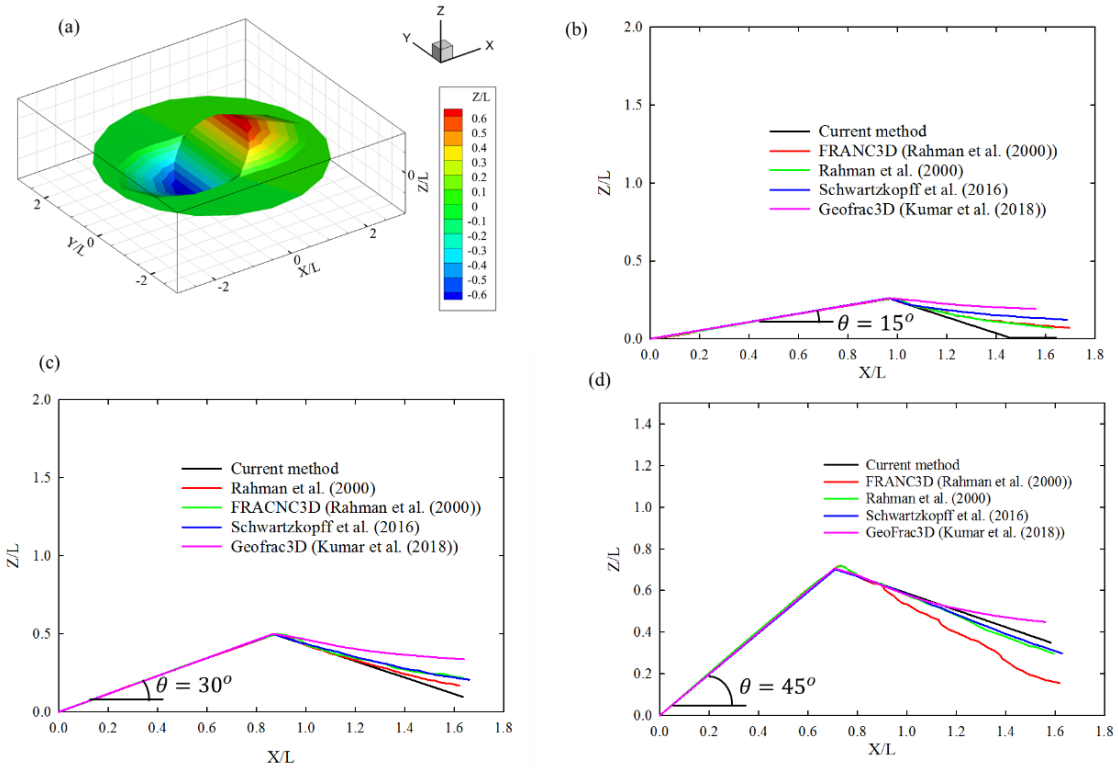

Figure 3.3 Comparison between current results and published results. $L = 0.1$ m is the initial fracture radius. (a) is the fracture (dip=45^o , dip direction=0^o propagation surface. (b) is the cross section along $Y = 0$ of fracture (dip= 15^o , dip direction= 0^o) propagation surface compare with published results. (b) is the cross section along $Y = 0$ of fracture (dip=30^o , dip direction=0^o) propagation surface compare with published results. (b) is the cross section along $Y = 0$ of fracture (dip= 45^o , dip direction= 0^o) propagation surface compare with published results.

3.5 Seismicity Generation

The next study is to explore the generation of event cloud surrounding a fracture. Fracture radius is 5 m and dip is 61° and strike is 89°, friction coefficient of fracture is 0.61. This fracture is subjected to constant injection rate of $4.5 \cdot 10^{-5}$ m^3/s. The injection time is 510 seconds. The permeability of rock matrix is 0.1 mD. The vertical stress is 41.8 MPa and the maximum, and minimum horizontal stresses are 35.5 MPa and 21.7 MPa , respectively. The b-value is given as 0.8. Figure 3.4 shows the distribution of events. At the final time step, 147 events are generated. Those events are located on or around the

fracture (Figure 3.4a), the black spheres are considered as aseismic while the others are seismic. The magnitude of the events (Figure 3.4a) ranges from -0.66 to -3. Such events cloud can be well fitted ($R^2 = 1$) by Gutenberg-Richter law with a= -0.23 and b=0.8.

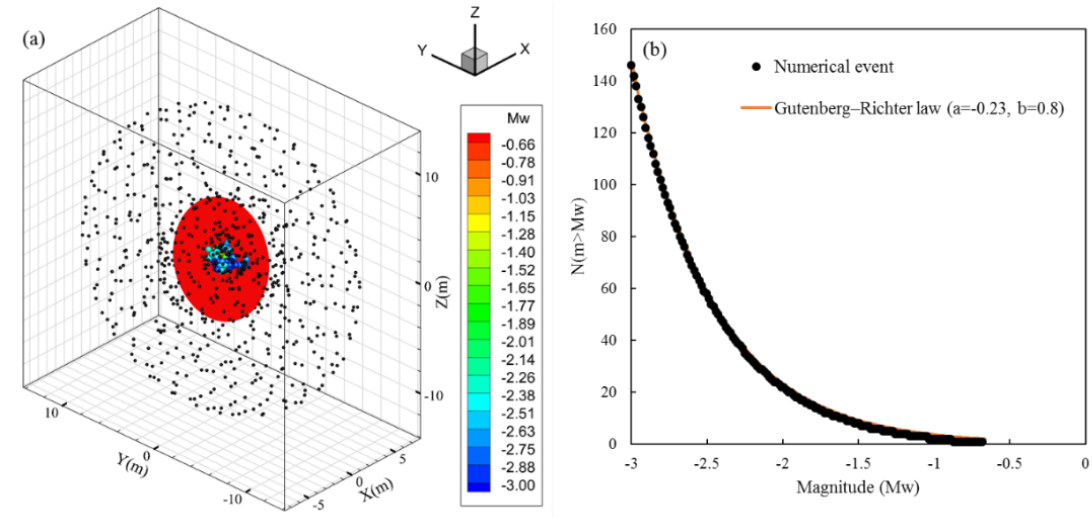

Figure 3.4 The events cloud and magnitude of events. (a) the events cloud is located on/surround the fracture. The black spheres are considered as aseismic while others are seismic. (b) indicates that the events cloud can be well fitted by Gutenberg-Richter law (a=-0.23 and b=0.8).

3.6 Eshelby Solution for Fracture Pressure Induced Stress Field (Stress Shadow)

The next comparison study is to explore the fracture pressure induced stress field using Eshelby solution. In this study, the length of fracture is 2 m and the inner pressure is loaded as 1 MPa. Both dip and strike of the fracture is zero. Figure 3.5 indicates that the stress field from Eshelby solution used in this work can match the publish results.

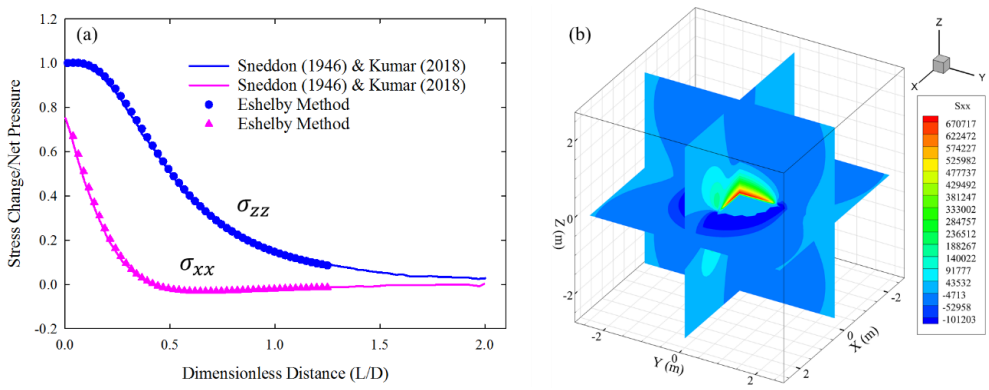

Figure 3.5 The stress field within the zone surrounding the fracture. (a) the σ_{zz} and σ_{xx} comparison between Eshelby method and Sneddon solution. *D* is the fracture length. (b) the distribution of σ_{xx}. The unit is Pa.

3.7 The Effects of Thermal Stress on Fracture Propagation

In this study, the effect of thermal stress on fracture propagation is examined. A low temperature water is injected into the high temperature rock to stimulate the reservoir. The thermal stress resulted by the temperature gradient influences the fracture network propagation. It is known that the increasing temperature gradient can reduce the breakdown pressure. Here a numerical simulation is designed to map interaction between temperature gradient and fracture propagation. The numerical setting is the same as the numerical setting in Chapter 4 except the injection fluid and reservoir temperature. Here the injection fluid temperature is fixed as 50^oC and reservoir temperature is 150^oC. The other numerical settings can be found in Chapter 4. Figure 3.6b shows the distribution of matrix temperature at 2600 seconds injection. It seems that the cooling zone is relatively large. Fracture 100 and 101 of Collab testbed) are propagated at 2600 seconds injection but the fracture initial pressure is decreased approximately 8% as compared to results from Chapter 4 (fracture initial pressure is 4289 psi). The propagation length for fracture 101 at 2600 seconds injection is approximately 0.62 m (Figure 3.6a) while the

propagation length of fracture 101 at 2600 seconds injection is approximately 0.50 m (caused by fluid injection) without considering the effects of thermal stress. The fracture pressure at 2600 seconds injection is shown in Figure 3.6a. In this example, the influence of thermal stress on fracture propagation is generally large because the cooling zone is generally large (Figure 3.6b). The thermal stress can cause the development of fracture network when the injection time is large (e.g., order of weeks to years) (Tarasovs and Ghassemi 2011). The cooling zone could be large enough to stimulate reservoir because of the thermal stress during the EGS development.

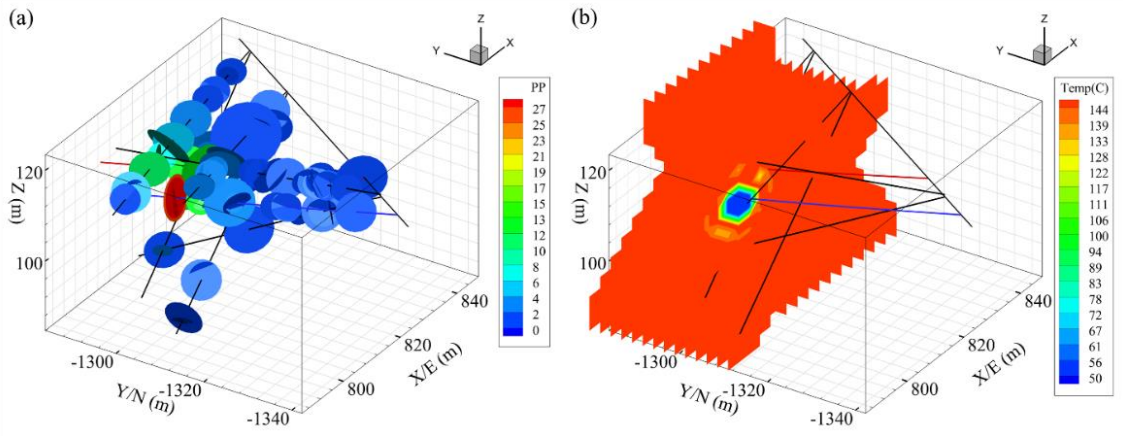

Figure 3.6 The distribution of fracture pressure and matrix temperature after 2600 second injection. (a) distribution of fracture pressure after 2600 seconds injection time and (b) distribution of matrix temperature after 2600 seconds injection.

3.8 The Effects of Poroelasticity on Induced Seismicity

Fluid injection can cause seismicity via pore pressure increase, and total stress changes due to poroelasticity. Increasing the pressure in a fracture lowers the effective normal stress reducing the fracture shear strength and increasing slip potential (e.g., Mohr Coulomb). The poroelastic stresses due to the pore pressure change can result in total stress variations on the fractures. The magnitude of the direct pressure effect is controlled

by the rock diffusivity (involving elastic stiffness, matrix and fracture permeability, fluid viscosity) and the injection rate. The magnitude of the poroelastic stress due to pore pressure change is controlled by Biot's coefficient α and bulk modulus (Cheng 2016). However, there appears to be some level of opacity in the literature regarding the role of poroelastic stress on induced seismicity. A recent paper (Alghannam and Juanes 2020) describes the impact of poroelastic stress in the mass-spring system for rate-state friction law. We re-examine this issue by explicitly considering the poroelastic stress acting on a fracture subjected to injection.

The Coupled Thermo-Hydro-Mechanical-Seismic Model with the 3D fracture network (with rate state friction law) is used to assess the effects of fluid diffusion and poroelastic stress on induced seismicity. Two types of injection scenarios are designed in the numerical simulations to distinguish and to underscore the contributions of fluid diffusion and poroelastic stress to the fracture stability and induced seismicity.

We consider a circular fracture of radius 3 m. The fracture dip and strike are 81^o and 66.2^o, respectively. A rate-state friction law is employed to describe the evolution of the fracture friction coefficient ($D_c = 20 \times 10^{-6}$ m, a=0.011, b=0.015 and $V_0 = 1 \times 10^{-12}$m/s). The reservoir rock properties are listed in Table 3.1 and represent a sandstone. The injection rate and injection time are also found in Table 3.1.

In the first scenario, water is injected at entire surface of the fracture and two numerical simulations are carried out with different Biot's coefficient (e.g., 0.0 and 1.00). Therefore, any element intersected with entire surface of the fracture is considered as injection elements. The injection rate at every nodes of injection elements have the same value and total injection rate is 3×10^{-5} (m^3/s) (Table 3.1). The sphere represents the center of the

fracture (Figure 3.7a). The second scenario involves fluid injection some distance away from the fracture (Figure 3.7b). The grey sphere represents the injection points located at $[x, y, z]$= [817.6142 m, 1296.63 m, 105.2805 m] and distance between injection points and fracture center is 6 m. Three numerical simulations are carried out with different Biot's coefficient (e.g., 0.1, 0.90 and 1.00) in the second injection scenario. These two injection scenarios are designed to investigate the effects of poroelastic and fluid diffusion on induced seismicity. The fracture pressure, effective normal stress, shear stress and magnitude of numerically generated seismic events are monitored during the simulation.

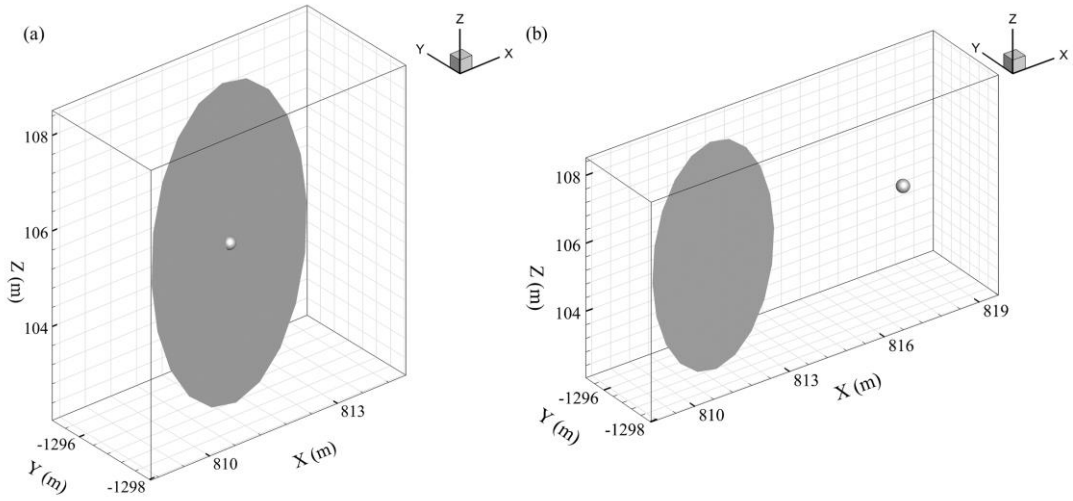

Figure 3.7 The set-up of two different injection scenarios. Both injection scenarios have the same fracture geometry. The coordinate of center of fracture is [811.6142, 1296.63, 105.2805]. fracture radius is 3 m. Fracture dip and strike is 81 and 66.2 degree, respectively. The grey sphere represents the injection points in both two simulations. (a) fluid injection occurs on entire surface of fracture. (b) fluid injection occurs away from the center of fracture. Here the coordinate of injection point is $[x, y, z]$ = [817.6142, 1296.63, 105.2805]. In case (b) an instantaneous poroelastic stress and late time pore pressure effect is active.

Table 3.1 Rock and Fluid Data Used in Simulation (Chang and Segall 2016)

Parameter value	**Values**	**Source/Comments**
Young's Modulus	25.5 GPa	Assumed
Drained Poisson's Ratio	0.22	Assumed
Undrained Drained Poisson's Ratio	0.46	Assumed
Biot's Coefficient	0.0/1.0, 0.1/0.9/1.0	Three different Biot's coefficient are tested.
Vertical stress S_V	22.0 MPa	Z-axis
Maximum horizontal stress $S_{\mathrm{h}max}$	39.0 MPa	X-axis
Minimum Horizontal stress $S_{\mathrm{h}min}$	13.0 MPa	Y-axis
Initial pore pressure	3.0 MPa	Assumed
Matrix Permeability	1 mD	Assumed
Dilation angle	0.035 rad	Assumed
Fracture radius	3 m	Assumed
Cohesive	0	Assumed
Frictional angle	0.6	Assumed
Fracture aperture	0.1 mm	Assumed
Injection rate	3×10^{-5} $(\mathrm{m}^3/\mathrm{s})$	Assumed. Constant injection rate.
Injection time	4000 seconds	Injection shut in at 4000 seconds.

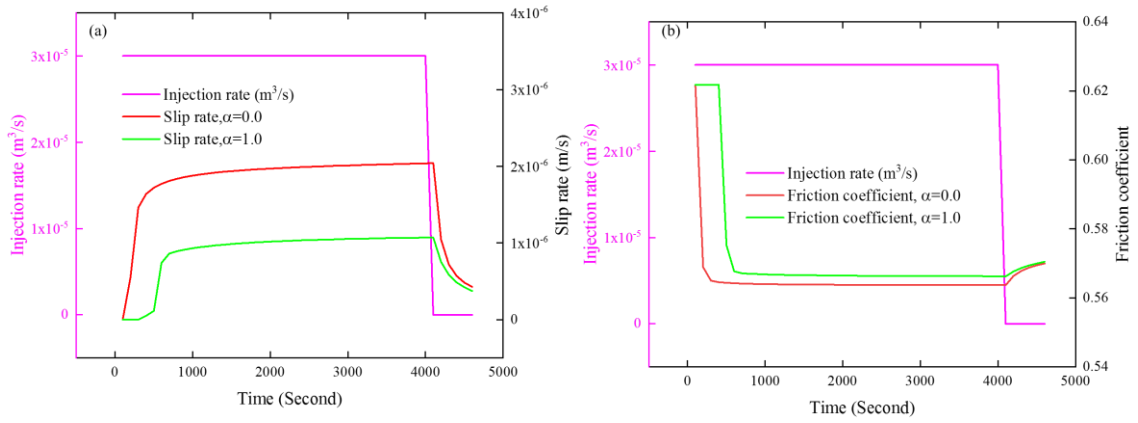

Figure 3.8 The evolution of fracture slip rate and friction coefficient at first injection scenario with different Biot's coefficient. (a) the evolution of fracture slip rate due to the injection occurs on the fracture. (b) the evolution of friction coefficient due to the injection occurs on the fracture.

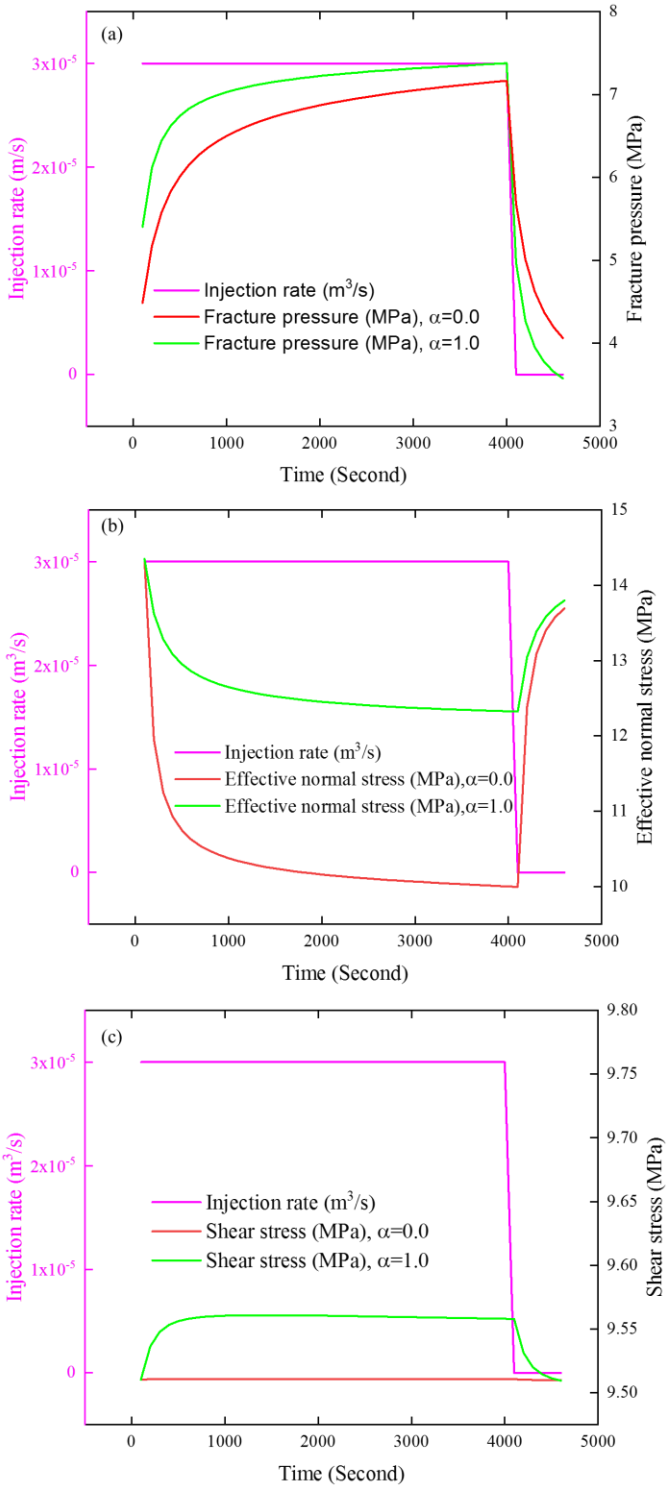

Figure 3.9 The evolution of fracture pressure, effective normal stress, shear stress at first injection scenario with different Biot's coefficient. (a) the evolution of fracture pressure; (b) effective normal stress, (c) shear stress due to the injection occurs on the fracture.

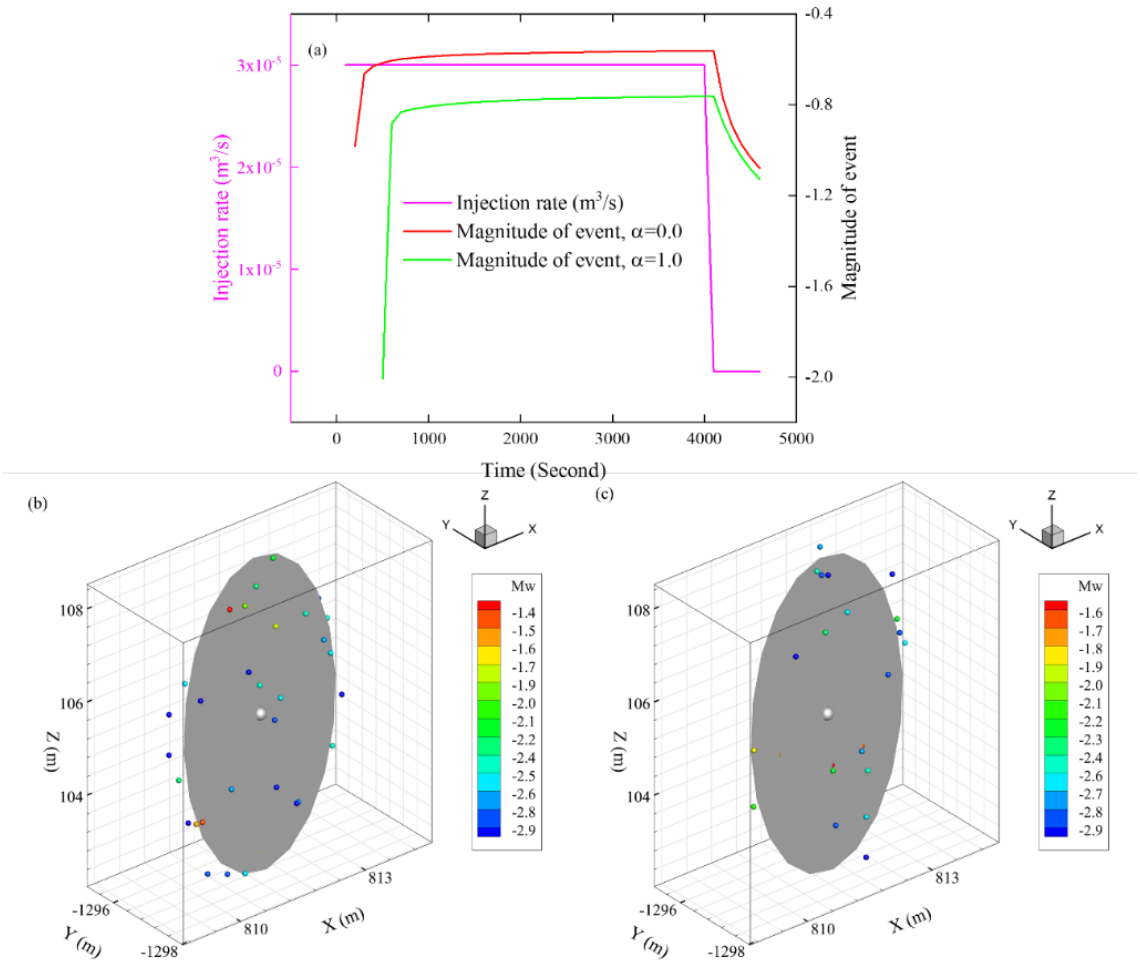

Figure 3.10 The evolution of magnitude of event due to the injection occurs on the fracture in the first scenario with different Biot's coefficient. (a) the evolution of magnitude of event due to the injection occurs on the fracture in the first scenario with different Biot's coefficient. (b) the distribution of event at 4100 seconds in the first scenario with Biot's coefficient is 0.0. The number of MEQs is 49. (c) the distribution of event at 4100 seconds in the first scenario with Biot's coefficient is 1.0. The number of MEQs is 35.

Figure 3.8 shows the fracture slip rate and friction coefficient in the first injection scenario. Fracture pressurization reduces the effective stress on the fracture causing shear slip. Injection has stopped at 4000 seconds. The maximum slip rate is reached at 4100 seconds and is equal to 2.039×10^{-6} m/s and 1.072×10^{-6} m/s for Biot's coefficient of 0.0 and 1.0, respectively. At 4000 seconds shut-in, the slip rate is 2.037×10^{-6} m/s and 1.070×10^{-6} m/s when the Biot's coefficient is 0.0 and 1.0, respectively. Therefore, the slip rate increased

at 4100 seconds i.e., shut-in by approximately 0.1% of the slip rate at 4000 seconds. Figure 3.9 shows the evolution of fracture pressure, effective normal stress and shear stress due to the injection into the fracture for the two different Biot's coefficients. As the fracture is pressurized by fluid injection, the fluid diffuses into the rock matrix cause the expansion of zone surrounding the fracture. Note that fracture is mechanically closed during the injection (i.e., a closed natural fracture) and the fracture aperture is 0.1 mm (Table 3.1).

As the fluid diffuses into the rock matrix, the poroelastic effect causes the total normal stress acting on the fracture to increase, contributing to fracture stability. This is because the surrounding zone of the fracture experiences compression due to the poroelastic effect in response to pore pressure buildup. In contrast, fracture pressure significantly increases when injecting into the fracture. Therefore, the effective normal stress is decreased (Figure 3.9b). The total normal stress will go down when the injection is shut-in because the poroelastic stress is reduced. However, the fracture pressure is also significantly decreased, so the effective normal stress increases as time increases after injection shut in.

Figure 3.10a shows the evolution of magnitude of event. Injection has stopped at 4000 seconds. The maximum magnitude of the simulated event is reached at 4100 seconds and is -0.562 and -0.7622 when Biot's coefficient is 0.0 and 1.0, respectively. As the 4000 injection seconds, the magnitude of simulated event is -0.5624 and -0.7626, respectively. Therefore, the increases of magnitude of simulated event at 4100 seconds is approximately 0.07% of magnitude of simulated event at 4000 seconds.

Figure 3.10b and 3.10c show the distribution of seismic events for injection in the fracture. Figure 3.10b is the distribution of seismic events after 4100 seconds injection for Biot's coefficient of 0.0, and the number of events is 49. The magnitude of events ranges from -1.4 to -3.0. Figure 3.12c is the distribution of seismic events after 4100 seconds of injection with Biot's coefficient of 1.0, and the number of events is 35. The event magnitudes range from -1.6 to -3.0. Strong compression develops within a zone surrounding the fracture due to poroelastic effects. Such poroelastic compression leads to the stability of the fracture. Therefore, the number of events in the simulation with Biot's coefficient of 0.0 is larger than the number of events in the simulation with Biot's coefficient of 1.0.

Figure 3.11 shows the fracture slip rate and friction coefficient for the second injection scenario. In this case, the fracture stability is also affected by the poroelastic stress in addition to pore pressure. Injection is continued for 4000 seconds and is then shut-in. The maximum slip rate is reached at 4100 seconds and is 3.036×10^{-6} m/s and 3.568×10^{-6} m/s when Biot's coefficient is 0.9 and 1.0, respectively. Note that no fracture shear slip occurred on the fracture for Biot's coefficient of 0.1. As the 4000 injection seconds, the slip rate is 3.029×10^{-6} m/s and 3.560×10^{-6} m/s when the Biot's coefficient is 0.9 and 1.0, respectively. Therefore, the increases of slip rate at 4100 seconds due to injection shut-in is approximately 0.2% of the slip rate at 4000 seconds.

Figure 3.12 shows the evolution of fracture pressure, effective normal stress, shear stress in the second injection scenario with different Biot's coefficient. Figure 3.13a shows the evolution of event magnitudes. Injection has stopped at 4000 seconds. The maximum magnitude of the simulated events is reached at 4100 seconds and the maximum

magnitude of simulated event is -0.7772, and -0.7290 when Biot's coefficient is 0.9 and 1.0, respectively. At 4000 seconds, the magnitude of the simulated event is -0.7778, and -0.7296, when Biot's coefficient is 0.9 and 1.0, respectively. Therefore, the increases in magnitude of the simulated event at 4100 seconds is approximately 0.07% of the magnitude of simulated event at 4000 seconds.

Figure 3.13b, 3.13c show the distribution of seismic events. Figure 3.13b is the distribution of seismic events after 4100 seconds injection with Biot's coefficient is 0.9; the number of events is 34. The event magnitudes range from -1.6 to -3.0. Figure 3.13c is the distribution of seismic events after 4100 seconds injection with Biot's coefficient is 1.0; the number of events is 37. The magnitude of events ranges from -1.5 to -3.0. The poroelastic effects can perturb the stress field in the vicinity of the injection location and gives rise to extension/compression zones. The distribution of extension and compression stress state will be determined by the fracture location, orientation, injection location, as well as permeability and fracture connectivity in reservoir. Therefore, the number of events in the simulation with Biot's coefficient of 1.0 are larger than the number of events in the simulation with Biot's coefficient of 0.9.

In addition, the effect of fluid diffusion on induced seismicity depends on the diffusion time. In the first injection scenario, the diffusion time is very small, and the seismic event occurs at 200 and 500 seconds when Biot's coefficient is 0.0 and 1.0, respectively (Figure 3.12a). In the second injection scenario (Figure 3.15a), the diffusion time is relatively large, and the seismic events occur at 1200 seconds (Biot's coefficient=0.9) and 600 seconds injection (Biot's coefficient=1.0), respectively. Because fracture is favored to slip due to increased tensile stress because of poroelastic effects. Further, the magnitude

of events in the first injection scenario is larger than the magnitude of events in the second injection scenario.

In a recent work (Alghannam and Juanes 2020), applied the spring-slider model considering fluid flow to investigate the effects of the injection rate on induced seismicity. In their work, the poroelastic stress was not included and the contributions because in the 1D spring-slider model the diffusion length is zero and stress perturbation zone in the vicinity of the injection cannot be developed. In addition, the '1D poroelastic spring-slider model' in their work cannot consider the influence of poroelastic effects on induced seismicity. In general, the poroelastic response to injection depends on the distance between injection and fracture, facture location and orientation, stress regimes (e.g., normal faulting), as well as the matrix permeability and fracture hydraulic connectivity. Therefore, 1D model (e.g., spring-slider model) is not well suited for investigating the poroelastic effects on induced seismicity. However, a critical stiffness as the function of pore pressure rate is derived, and this critical stiffness may be useful since current critical stiffness does not consider the pressure rate.

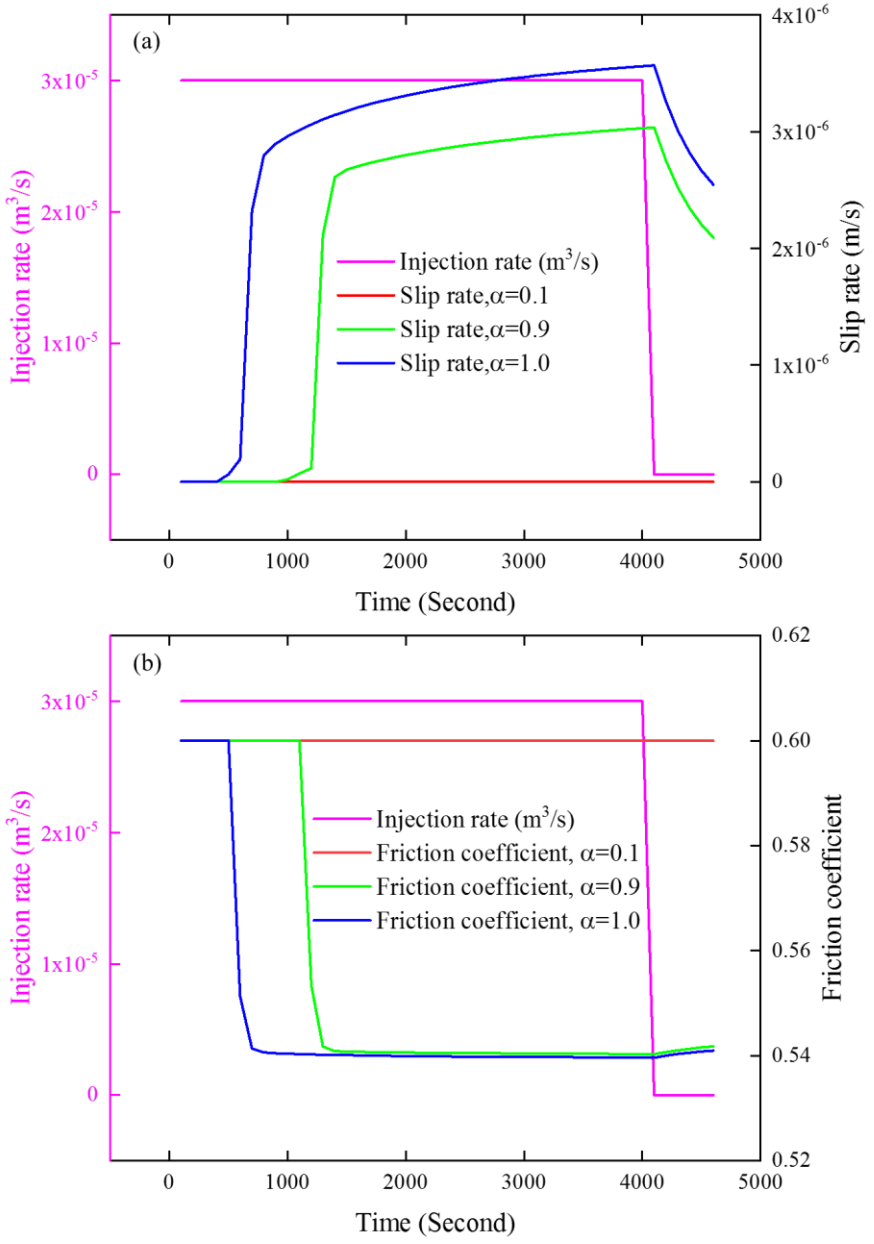

Figure 3.11 The evolution of fracture slip rate and friction coefficient at second injection scenario with different Biot's coefficient. (a) the evolution of fracture slip rate due to the injection occurs far from the center of fracture. (b) the evolution of friction coefficient due to the injection occurs far from the center of fracture.

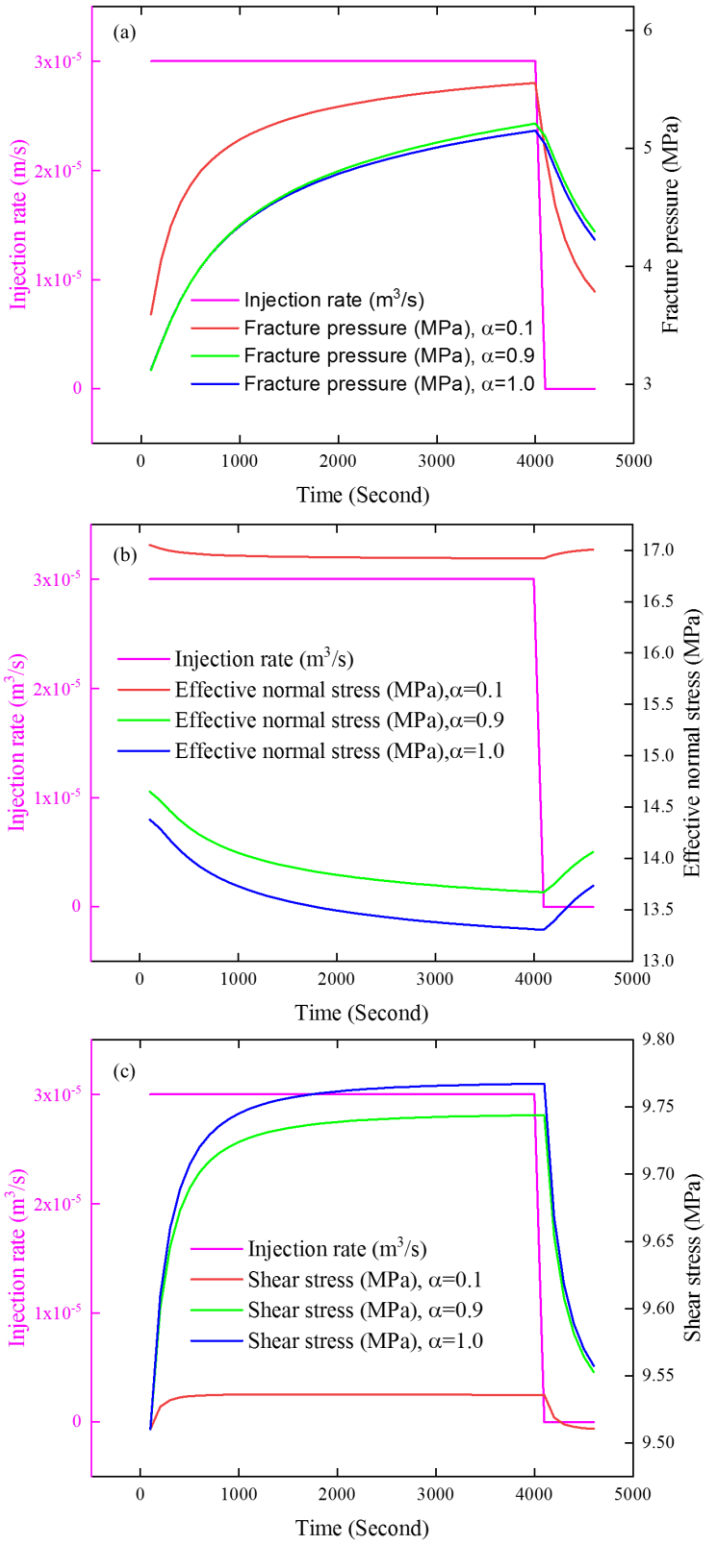

Figure 3.12 The evolution of fracture pressure, effective normal stress, shear stress at second injection scenario with different Biot's coefficient. (a) the evolution of fracture pressure; (b) effective normal stress, (c) shear stress due to the injection occurs far from the center of the fracture.

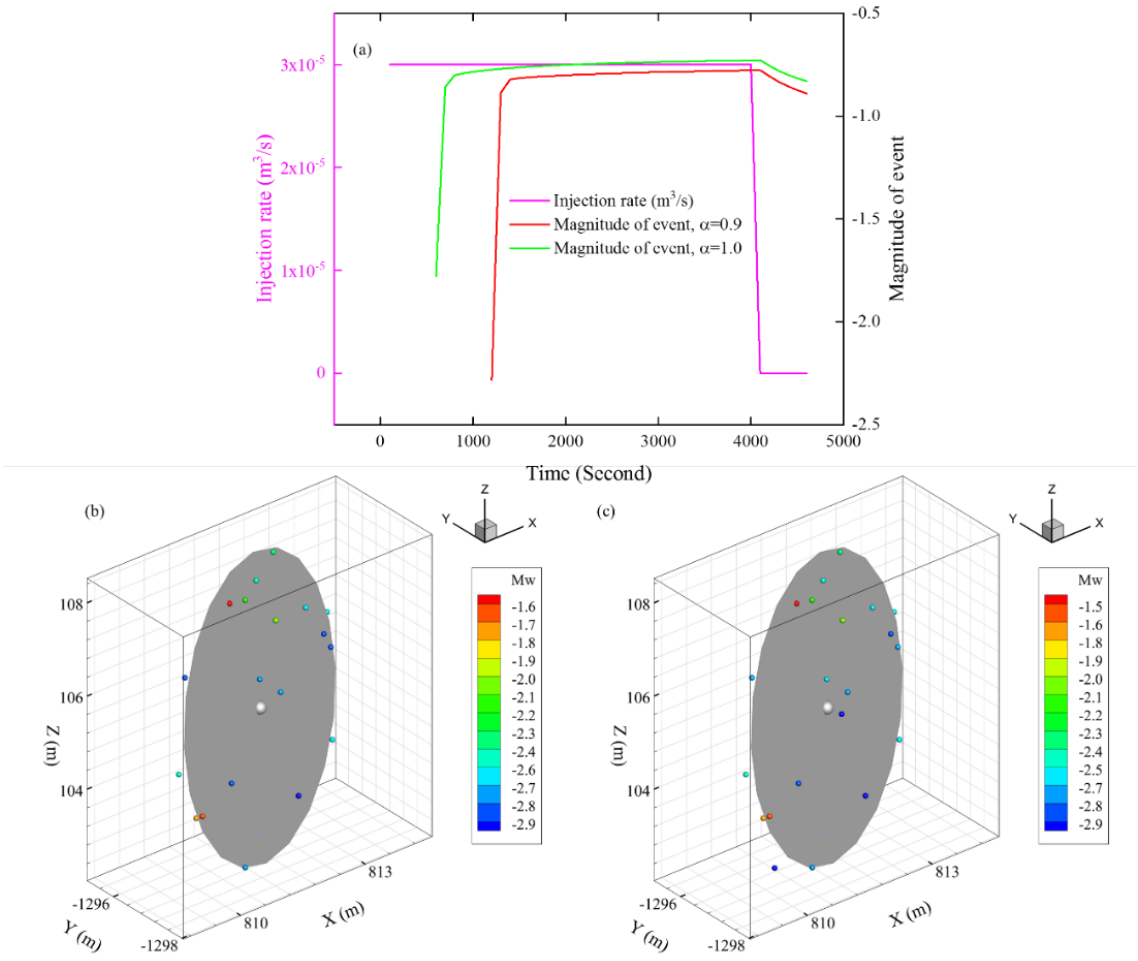

Figure 3.13 The evolution of magnitude of event due to the injection occurs far from the center of the fracture in the second scenario with different Biot's coefficient. (a) the evolution of magnitude of event due to the injection occurs far from the fracture in the second scenario with different Biot's coefficient. Note that none of MEQs are generated when Biot's coefficient equal to 0.1. (b) the distribution of event at 4100 seconds in the second scenario with Biot's coefficient is 0.9. The number of MEQs is 34. (c) the distribution of event at 4100 seconds in the second scenario with Biot's coefficient is 1.0. The number of MEQs is 37.

3.9 Conclusions

In this Chapter, several comparison studies and general examples are presented. The results from coupled thermo-hydro-mechanical-seismic model with 3D fracture network matches the published results. It demonstrates the effectiveness of our coupled thermo-

hydro-mechanical-seismic model with 3D fracture network in fractured reservoir stimulation (e.g., EGS development).

Chapter 4 An Application for EGS Collab

4.1 Introduction

EGS Collab Project has been launched by DOE-GTO to simulate a decameter scale reservoir to enhance the understanding of rock mass respond to stimulation. The focus of the EGS Collab Project is to control the permeability enhancement under complex in-situ stress conditions and heterogeneous rock mass properties. The EGS Collab site is hosted in the Sanford Underground Research Facility (SURF). Four rock formations are present in this location: the Poorman Formation, the Yates amphibolite, the Homestake Formation, and the Tertiary Rhyolite dikes (Figure 4.1a). EGS Collab testbed 1 is entirely located within the Poorman Formation which shows intense multiscale fold. The rock consists of graphitic sericite-biotite phyllite/schist with local interlayers of quartz, and calcite veins. The detailed geologic descriptions of those formations can be found elsewhere (Stanton W. Caddey, Richard L. Bachman et al. 1992).

The EGS Collab consists of eight HQ-diameter holes (hole diameter is 96 mm and core diameter is 63.5 mm) with approximately equal lengths (about 61.0 m) (Figure 4.1b). Each hole is steel-cased from the top (collar) to a depth of 6.1 m. Six of the holes (E1-OT/OB, E1-PST/PSB and E1-PDT/PDB) are monitoring wells, while other two holes (E1-I and E1-P) are injection well and production well, respectably. Geophysical monitoring is via a dense 3D sensor array including 24 hydrophones (Sensor 1), 18 accelerometers (Sensor 2), 4 geophones (Sensor 3), 17 continuous active sources seismic monitoring (Sensor 4), 96 thermistors (Sensor 5), 123 seismic shot (Sensor 6) and 96 ERT electrode (Sensor 7) (Figure 4.1b). Six radial notches (~ 8.89 mm radially from the hole) were created along the injection well E1-I as marked in Figure 4.1b. The coordinate

system used in this work is the local Homestake Mine Coordinate system from an old gold mine that was in operation for over 100 years.

The purpose of the layout of the holes is to create connected flow path (connector) between the injection well E1-I and production well E1-P. The E1-I and E1-P were drilled (azimuth = 356˚ and inclination = 12˚) approximately parallel with the trend of minimum horizontal stress (azimuth = 2º and plunge = 9.3˚). The distance between injection well E1-I and production well E1-P is approximately 10 m. Stress measurements as part of kISMET have indicated the S_{hmin} is about 21.7 MPa, and the S_{Hmax} is about 35.5 MPa. The vertical stress is lithostatic and equal to 41.8 MPa. The initial pore pressure is set to zero in this work since no direct measurements are available and there are no observed major flows from the rock matrix. E1-OT and E1-OB are intended to intersect with potential hydraulic fracture. Other four holes (E1-PST/PSB, and E1-PDT/PDB) are designed to be paralleled with the potential hydraulic fracture.

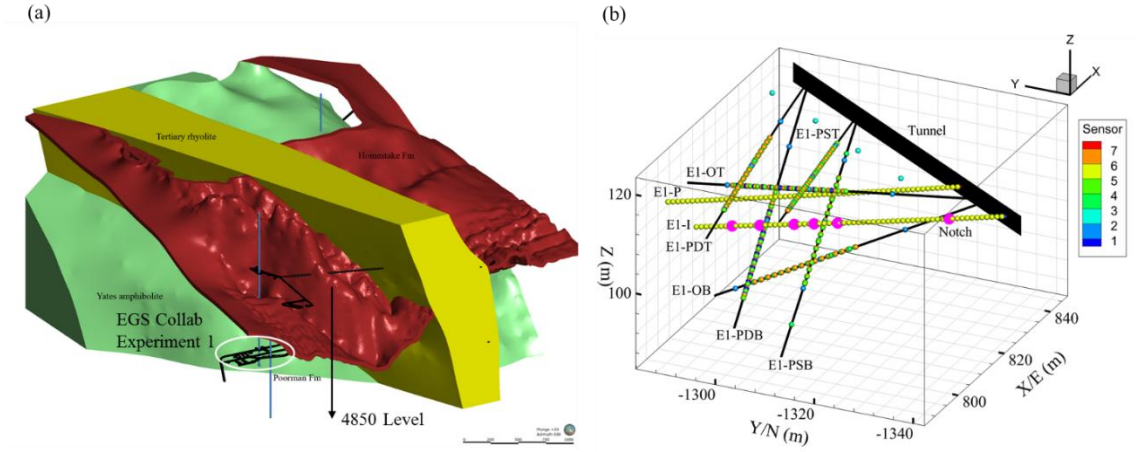

Figure 4.1 Geological model and layout of holes of EGS Collab testbed. (a) EGS Collab testbed is entirely located within Poorman Formation at 4850 ft depth. (b) Six holes (E1-OT/OB, E1-PSB/PST and E1-PDT/PDB) are used as monitoring wells. E1-I and E1-P are injection well and production well, respectively. The six pink spheres along E1-I are notches. The contour represents different types of sensor. For example, Sensor 1 is the 24 hydrophones, Sensor 2 is the 18 accelerometers, Sensor 3 is the 4 geophones, Sensor 4 is the 17 continuous active sources seismic monitoring, Sensor 5 is the 96 thermistors, Sensor 6 is the 123 seismic shot and Sensor 7 is the 96 ERT electrode.

Three multi-test experiments were planned and performed: (1) a hydraulic fracturing test at Notch@142 occurred during May 21-22, 2018 and Notch@164 occurred during May 22-24, 2018 referred to as Stim-II HF@164 Notch; (2) hydraulic characterization test at Notch@164 conducted from October 24 to November 20, 2018; and (3) hydraulic characterization tests at Notch@164 conducted in February-March 2019. The experiment 1 was intended to induce controlled fracture propagation (presumably a penny-shaped one) to connect the injection well E1-I with the production well E1-P. Figure 4.2 shows the injection profile of the Stim-II HF@164 Notch in Experiment 1. As shown in Figure 4.2a, pressure drop was very small and indicated that the length of hydraulic fracture was very small and hydraulic fracture have intersected natural fractures (Kneafsey, Blankenship et al. 2020). Figure 4.2b is the injection profiles of the test on May 24 and the pressure drop was very small. However, the injection rate was relatively high, and it suggested that fracture propagation started from natural fractures.

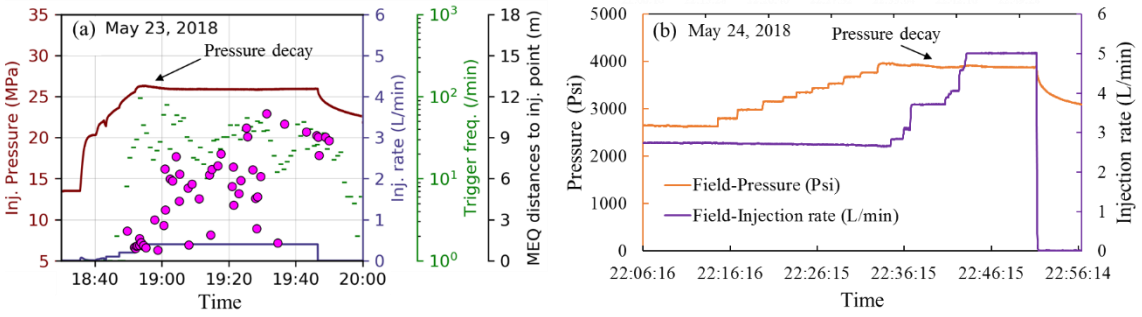

Figure 4.2 Injection profiles and induced seismicity of Stim-II HF@164 Notch. (a) the injection profiles of the test on May 23, 2018. The green dots represent the micro-seismic events triggers per minutes. The pink dots represent the distance between events and the Notch@164. (b) the injection profiles (SNL14) of the test on May 24, 2018.

Two direct observations of the first hydraulic fracture's (Stim-II HF@164 Notch) manifestations have been suggested by the Collab team to be: (1) temperature anomalies

at T22:43 of 2018/05/24 in well E1-OT (Figure 4.3a) and (2) visible fluid flow out of the production well E1-P in fluid test on 2018/05/25 (Figure 4.3b). Figure 4.3 illustrates a hydraulic connection between the E1-I and E1-P. Most studies of the data have speculated that the propagation length of the hydraulic fracture in Stim-II HF@164 Notch is approximately 12 m and more (Wu, Fu et al. 2019, Fu, Wu et al. 2020, Makedonska, Jafarov et al. 2020), concluding that the outflow in the production well E1-P is due to an interesting hydraulic fracture(s). On the other hand, it seems that the pressurized fluid is jetting into the hole via veins (Ye and Ghassemi 2019) from a pressurized zone or natural fractures in the vicinity of the production well. It is worth noting that two natural fractures namely I-164a/b (at 164.4 and 164.6 ft depths along E1-I, respectively) are very close to the Notch@164 (164.24 ft depth) (Figure 4.4). The length of isolated zone is 64.8 inches and is located from 163.918 ft to 169.318 ft depths along E1-I. Thus I-164a/b is in this isolated zone. The injection rate in the May 22 test was small (maximum flow rate of 0.2 L/min and duration was 10.5 minutes) during the early stage "breakdown" and propagation so that it likely yielded only a very small hydraulic fracture at Notch@164. The length of hydraulic fracture is only 0.25 m based on the model described in the previous sections. Therefore, it is more likely that the hydraulic fracture linked up with either or both natural fractures I-164a/b (Figure 4.5) prior to extending far into the rock mass towards the production well. The injection rate in the test of May 23 was small (maximum flow rate of 0.4 L/min and duration was 65.2 minutes) during the early stage of breakdown and propagation and may have resulted in limited propagation. And it is likely that the hydraulic fracture intersected one or both natural fractures observed near the notch (Kneafsey, Blankenship et al. 2020) (Figure 4.5). The pressure decay following

the test of May 23 indicates that the fluid may have leaked from natural fractures I-164a/b to the rock matrix or other small cracks and void (Figure 4.2). The injection rate in the test of May 24 was later increased to a much higher value (maximum flow rate is 5 L/min and duration was 31.7 minutes). A higher injection rate likely dilated natural fractures I-164a/b intersected by the hydraulic fracture and propagated them to intersect E1-P. This is supported by the fact that a temperature increase was detected at E1-OT at T22:53 (Figure 4.3a) and water was produced in E1-P in fluid test on May 25 (Figure 4.3b). In this work, we provide simulation results to assess the likelihood of this sequence of events and to suggest that the pressurization and/or propagation of I-164a/b is responsible for the observed water jets rather than a direct hydraulic fracture from Notch@164 connecting with the E1-I with E1-P. In essence, we provide a fracture network conceptual model of the Experiment 1.

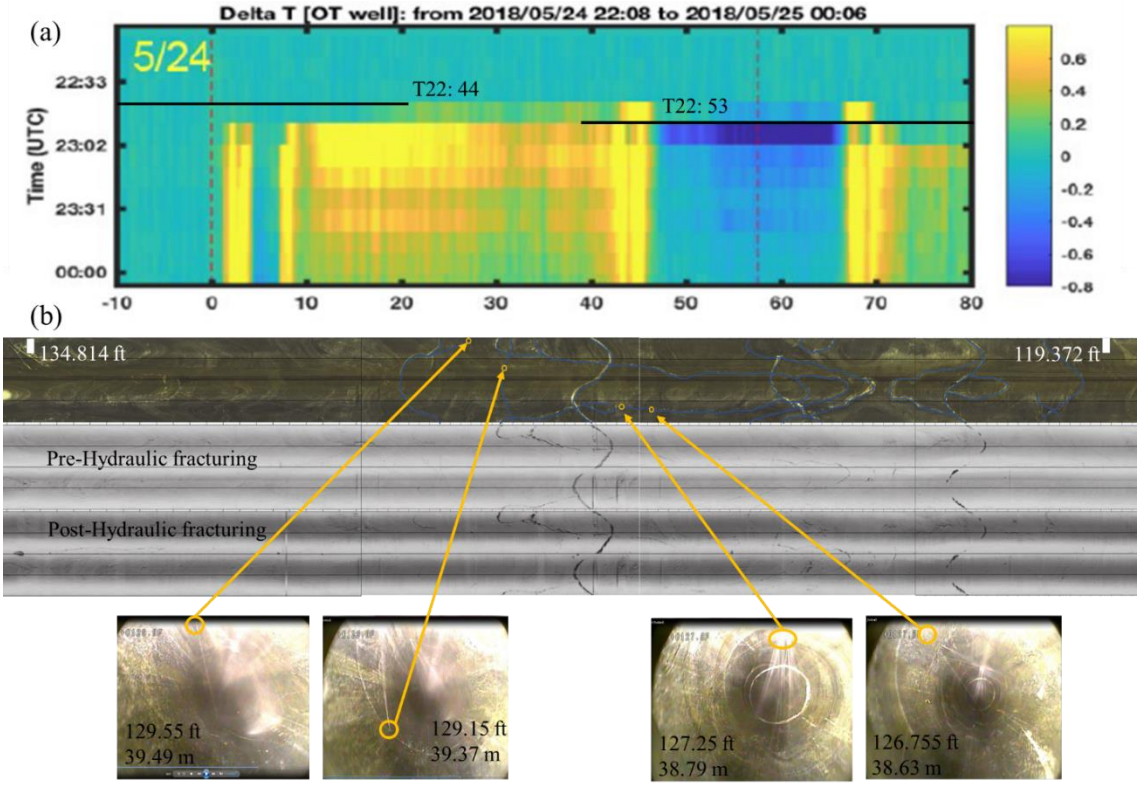

Figure 4.3 Field observation at E1-OT and E1-P caused by injection. (a) the temperature perturbations along E1-OT on May 24. (b) water jet occurs in E1-P at 126 ft and 129 ft depth. The water jetting was detected at May 25.

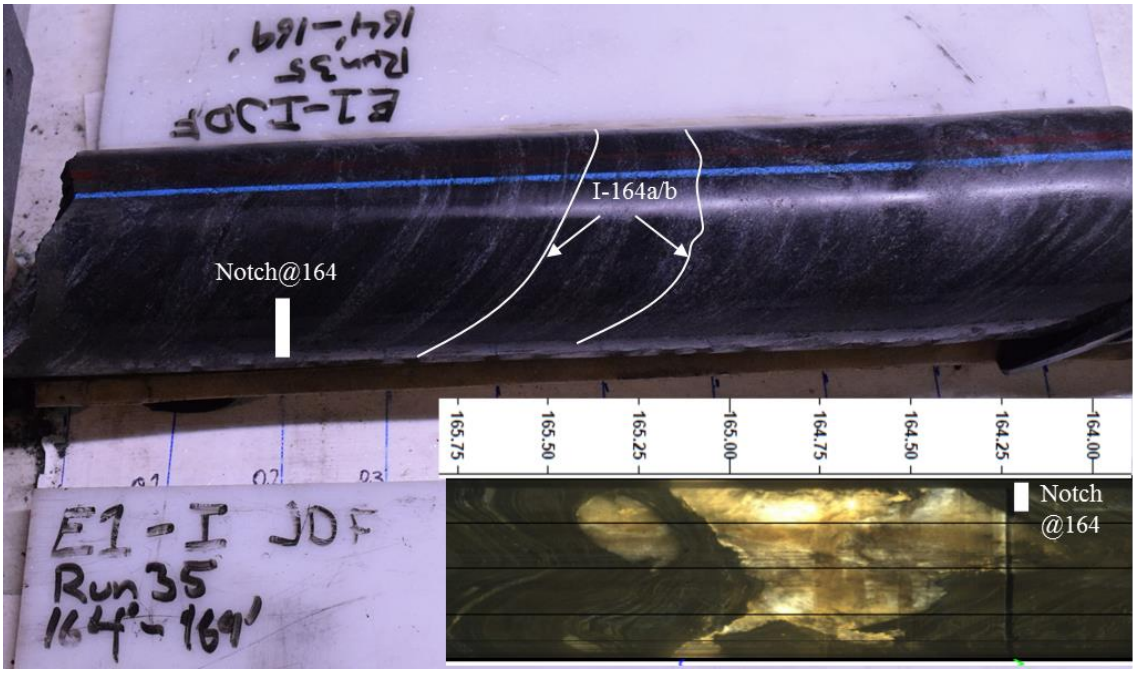

Figure 4.4 Core and acoustic televiewer log showing the fractures in E1-I (at 164 ft to 169 ft depth).

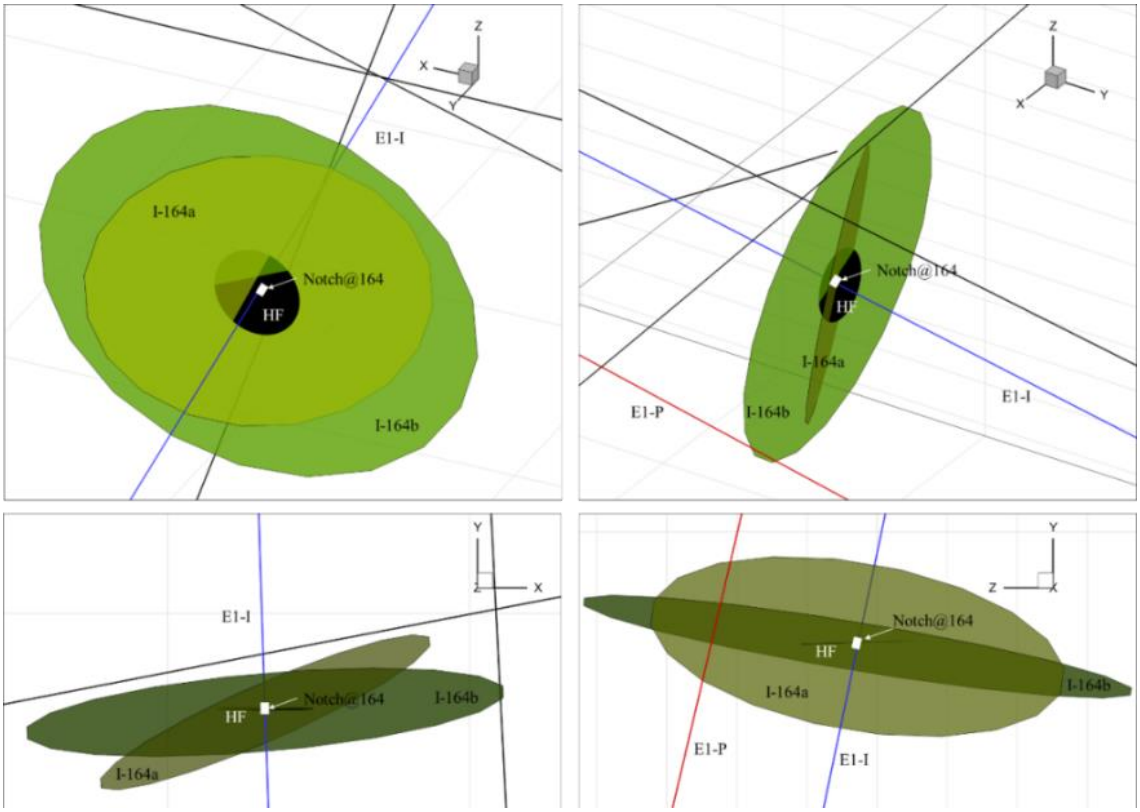

Figure 4.5 A schematic of hydraulic fracture intersecting NFs I-164a/b. The generation of the hydraulic fracture is assumed to be due to the injection into Notch@164. Note that the hydraulic fracture almost overlaps with I-164b.

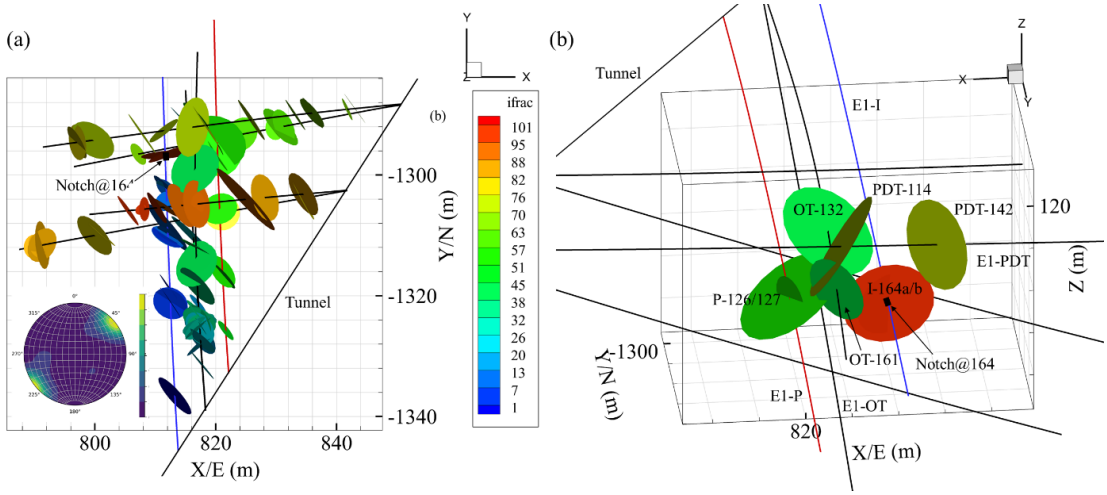

Figure 4.6 The configuration of major fractures and orientation of fracture. (a) There are 101 major fractures in this configuration. Most fractures are steeply dipping. (b) Some major fractures surround the Notch@164. An OT-PDT-P connection can be extracted: E1-OT → OT-161→PDT-114→E1-PDT→P-122/126 →E1-P or E1-OT→OT-161→P-126/127 →E1-P. Such connection partly matches the field observation during the fracture mapping exercise (Ghanashyam, Robert et al. 2019).

In this work, Stim-II HF@164 Notch is simulated using the model described in the previous sections. The injection began on May 24, 21:00 and ended on May 24, 22:53. The detailed injection profile is illustrated in Figure 4.2b. Image logs and core data have shown 101 major fractures in the EGS Collab Testbed 1 and most of the fractures steeply dip (see stereographic plot in Figure 4.6a) (EGS Collab Team 2020). There are likely small-sized fractures and micro-cracks present near major fractures, but they are not shown in the Figure 4.6a. The color represents the major fractures index as described in the geological survey of the site. For example, the name of fracture 44 is OT-132, denoting the location of the center of fracture 44 (OT-132) at 132.4 ft along the hole E1-OT. Two main natural fractures I-164a/b intersects the E1-I at 164 ft (Figure 4.6b). The centers of fractures I-164a/b and the Notch@164 nearly share the same location. Thus, it is likely that NFs I-164a/b are the primary connections from 164@Notch to the rest of the reservoir rock mass because of the low permeability of the rock matrix. An OT-PDT-P connection can be extracted from Figure 4.6b: E1-OT→OT-161→PDT-114→E1-PDT→P-122/126 →E1-P or E1-OT→OT-161→P-122/126 →E1-P. Such connection partly matches the field observation during the fracture mapping exercise (Ghanashyam, Robert et al. 2019).

The rock mechanical properties have been measured by various groups including the University of Oklahoma and various compilations can be found in (Kneafsey, Dobson et al. 2019, Ye and Ghassemi 2019, EGS Collab Team 2020, Ye, Ghassemi et al. 2020). The temperature of injection and rock matrix is 20^oC and 30^oC, respectively. In the current modeling we disregard the difference between the injected water temperature and rock temperature. This is because as shown in (Ghassemi and Zhang 2006) thermal

stresses develop much slower than the fracture propagation time scale. Although, there could be some impact on the injection temperature at the wellbore, however, in view of the small temperature differences the impact is likely small. Here, the initial time step in the finite element model is 100 seconds. Such time step may be changed during the iteration of fracture propagation (see Algorithm 1 in Chapter 2.2.3). Thus, the time step size may impact the quasi-static behavior (e.g., transition between aseismic and seismic state). In this work, Crank-Nicolson method is applied to discrete the time domain and it is unconditionally stable. The wellbore boundary condition is rate control. All unknowns and induced micro-seismicity are calculated at the end of each time step. The input parameters are shown in Table 4.1.

Table 4.1 Reservoir properties used in the model.

Parameter value	**Values**	**Source/Comments**
Young's Modulus (Lognormal distribution)	$mean = 71$GPa $variance = 5$	Oldenburg et al. 2016
Drained Poisson's Ratio	0.22	Oldenburg et al. 2016
Undrained Drained Poisson's Ratio	0.46	Assumed
Biot's Coefficient	0.52	Assumed
Vertical stress S_V	41.8 MPa	Oldenburg et al. 2016
Maximum horizontal stress $S_{\mathrm{h}max}$	35.5 MPa	Oldenburg et al. 2016
Minimum Horizontal stress $S_{\mathrm{h}min}$	21.7 MPa	Oldenburg et al. 2016
Initial pore pressure	0.0 MPa	EGS Collab 2020
Matrix Permeability	0.05 mD	Ye, Ghassemi et al. 2016
Dilation angle	0.035 rad	Assumed

Fracture radius (Lognormal distribution)	$mean = 3(\text{m})\ \ variance = 0.75$	Estimating from Oldenburg et al. 2016
Fracture asperity (Lognormal distribution)	$mean = 4 \cdot 10^{-5}(\text{m})$ $variance = 10^{-9}$	Assumed
Cohesive (Lognormal distribution)	$mean = 0$ MPa $variance = 0$	Assumed
Frictional angle (Lognormal distribution)	$mean = 0.6(\text{rad})$ $variance = 0.01$	Assumed
Mode I fracture toughness	$2\ \text{MPa}\sqrt{\text{m}}$	Morris et al. 2016

4.2 Numerical Results

Based on the natural fracture data, E1-I and other wells are not connected prior to stimulation. Fracture PDT-142, OT-132 and P-129 are close to I-164a/b, but they do not intersect each other (Figure 4.6b). The zone surrounding the 164@Notch is isolated prior to injection. In our simulation, I-164a/b and the Notch@164 share the same location. Thus, I-164a/b are the primary conduits from the 164@Notch to the reservoir (i.e., HF not involved). Water enters the system at Notch@164 in E1-I and then flows to I-164a/b, pressurizing them. In the simulation, none of the natural fractures (I-164a/b and OT-132) show any propagation before T22:43. But field observations (Figure 4.3a) indicate a temperature change at T22:43 along a short section of E1-OT. This hydraulic communication signature in E1-OT is likely caused because I-164b is very close to OT-132 so the former can feed the latter. So, numerical results (Figure 4.9c/d) seem to match the field observations. The calculated fluid pressure distribution within the reservoir and the fracture network at time steps T22:36 and T22:43 are shown in Figure 4.7. The natural fractures surrounding I-164a/b are pressurized, and weeps zones may be activated during the injection.

As injection continues, fracture I-164a/b start to open and propagate (non-planar) at approximately T22:44. The natural fractures (e.g., PDT-142, OT-132) surrounding I-164a/b continue to be pressurized likely by matrix diffusion because fractures I-164a/b are isolated. Figure 4.8a/b shows the calculated fluid pressure distribution within the reservoir and the fracture network at T22:44 and the propagation length is only approximately 0.5 m (Figure 4.9a/b). Such a small propagation of natural fractures I-164a/b is not sufficient to yield an effective flow path between E1-I and E1-P because I-164b only intersects with OT-132 and the length at intersection is only 0.1 m (Figure 4.9b).

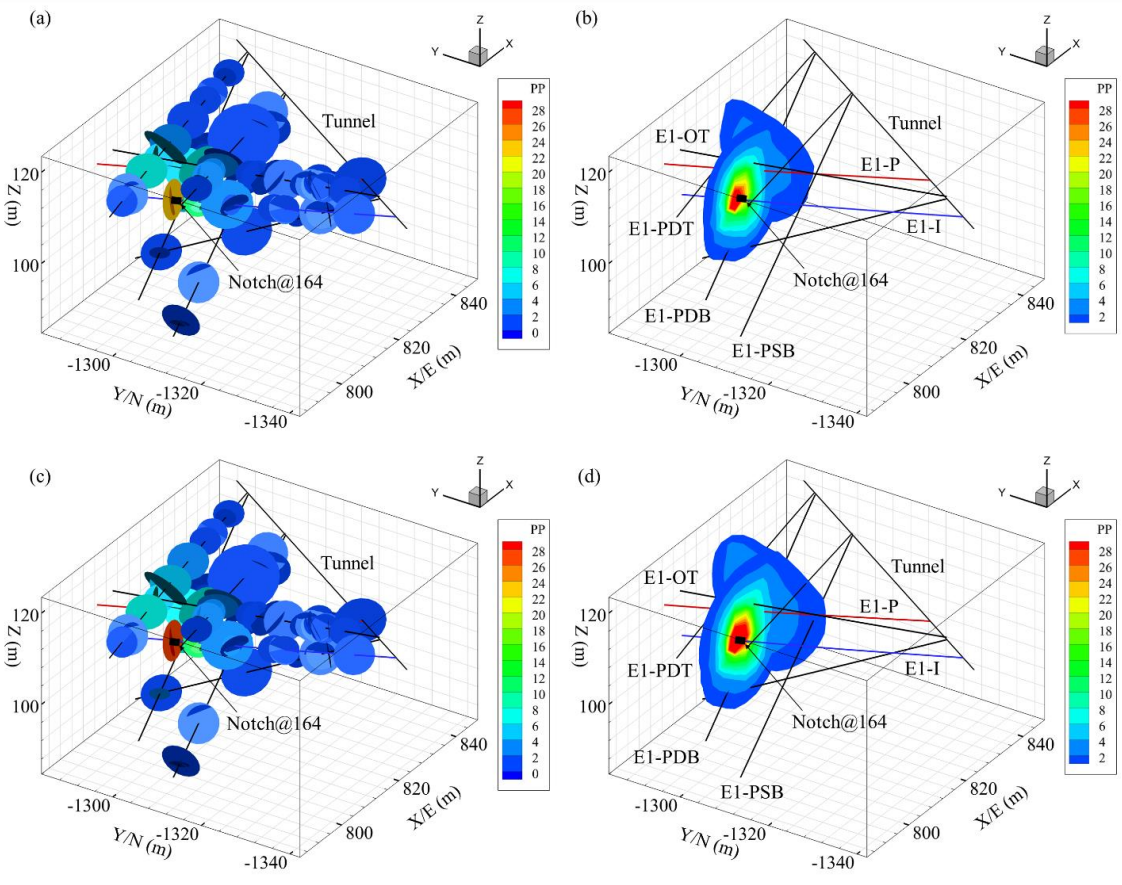

Figure 4.7 Fracture and matrix pressure at different times. Unit: MPa. (a) and (b) show the fracture and matrix pressure at time T22:36, respectively. (c) and (d) show the fractures and matrix pressure at time T22:43. The slices locations in (b) and (d) are X=823 m and Y=-1296.5 m, respectively.

The geometry of fracture propagation from numerical results seems to reflect the variation of temperature in E1-OT from the field observation (Figure 4.3a). Because field observation indicates a temperature changed at T22:44 detected in a large zone surrounding the E1-OT which suggest injection fluid flowing to E1-OT by hydraulic fracture (Figure 4.3a). But the values of temperature changes in E1-OT was not high, suggesting that E1-I and E1-OT are partially connected.

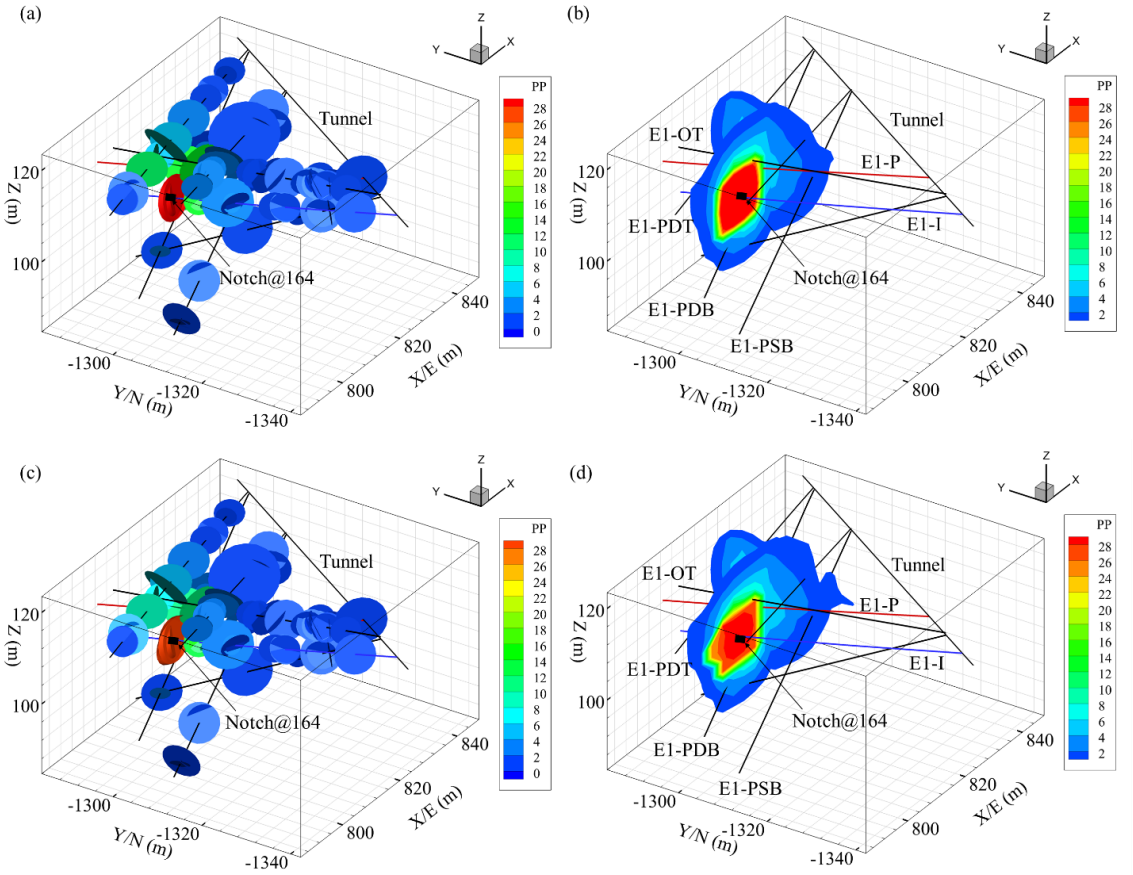

Figure 4.8 The results from numerical simulation. Unit: MPa. (a) and (b) show the fractures and matrix pressure at T22:44. (c) and (d) show the fractures and matrix pressure at T22:45.

As the injection continues, I-164b starts to propagate along the maximum stress direction fashion while I-164a remains stationary (Figure 4.9a/b). The propagation length of I-164b at T22:45 is approximately 0.6 m. Figure 4.8c/d show the calculated fluid pressure

distribution within the reservoir and the fracture network. Fracture I-164b starts to intersect with P-129 at T22:45, however the intersection length is approximately 0.1 m (Figure 4.9c/d). The planar propagation length of I-164b at T22:52 becomes relatively large (~9 m) which is shown in figure 4.10c/d. Figure 4.10a/b shows the calculated fluid pressure distribution within the reservoir and the fracture network. The natural fractures surrounding I-164a/b is pressurized and yet show no propagation (Figure 4.10c/d) in the model. Few fractures (e.g., PDT-114) will slip after injection shut in. The newly created fractures segment of I-164b form an effective flow path which tends to connect E1-I, E1-OT, E1-PDT and E1-P. The length of the planar propagation segment is larger than the length of non-planar propagation segment, and I-164b fully intersects with the OT-132, P-122/126/127/129 and E1-P.

Several potential connection paths can be envisioned from the fracture network after propagation and intersection, such as, injection well E1-I to production well E1-P, monitoring well E1-PDT to monitoring well E1-PST and production well E1-P to monitoring well E1-PST. The first potential connection path (Figure 4.11a): from injection well E1-I to Notch@164, from Notch@164 to fracture I-164b, from I-164b to OT-132, from OT-132 to P-122/126/127/129, from P-122/126/127/129 to production well E1-P. Thus, E1-I and E1-P are effectively connected. The second potential connection path (Figure 4.11b): from monitoring well E1-PDT to PDT-142, from ODT-142 to I-164a/b, from I-164a/b to OT-132, from OT-132 to monitoring well E1-OT/PST-56, from PST-56 to monitoring well E1-PST. The third potential connection path (Figure 4.11b): from monitoring well E1-P to P-126/129, from P-126/129 to I-164b, from I-164b to OT-132, from OT-132 to PST-56, from PST-56 to E1-PST. The uncertainties in

connection paths will need be reduced with additional data. The pressure and rate of Notch@164 (SNL14) is recorded during the injection. Figure 4.12 shows the comparison between numerical results at Notch@164 and field data. It seems that numerical results and field data show a reasonable match.

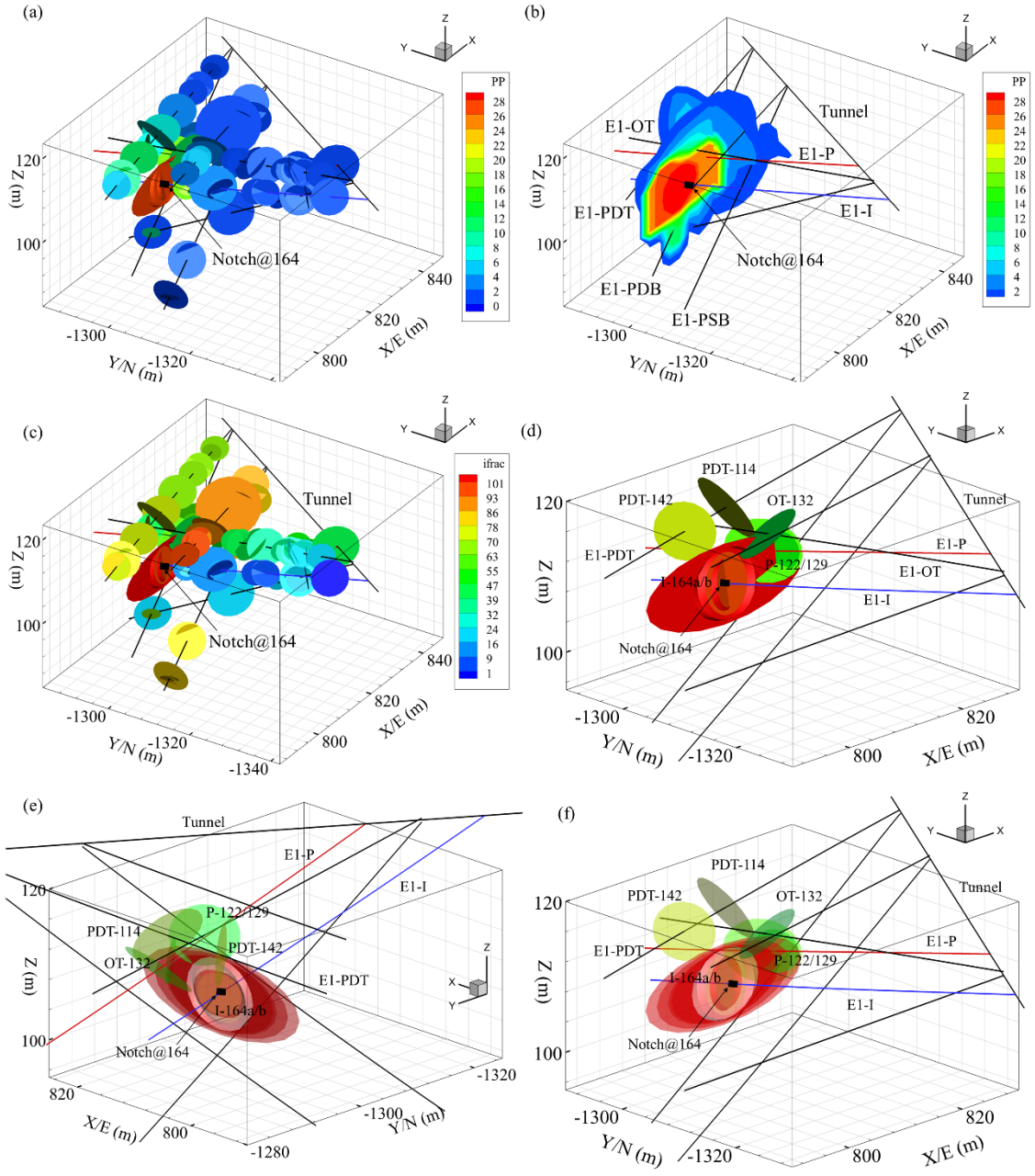

Figure 4.9 The results from numerical simulation. (a) and (b) show the propagation of I-164a/b at T22:44. The length of intersection between I-164b and OT-132 is relatively small (0.1 m). (c)

and (d) is the propagation of I-164b at T22:45. The length of intersection between I-164b and P-129 is relatively small (~0.1 m). Injection well E1-I partly connect with production well E1-P. (e) and (f) is the transparent view of fracture network.

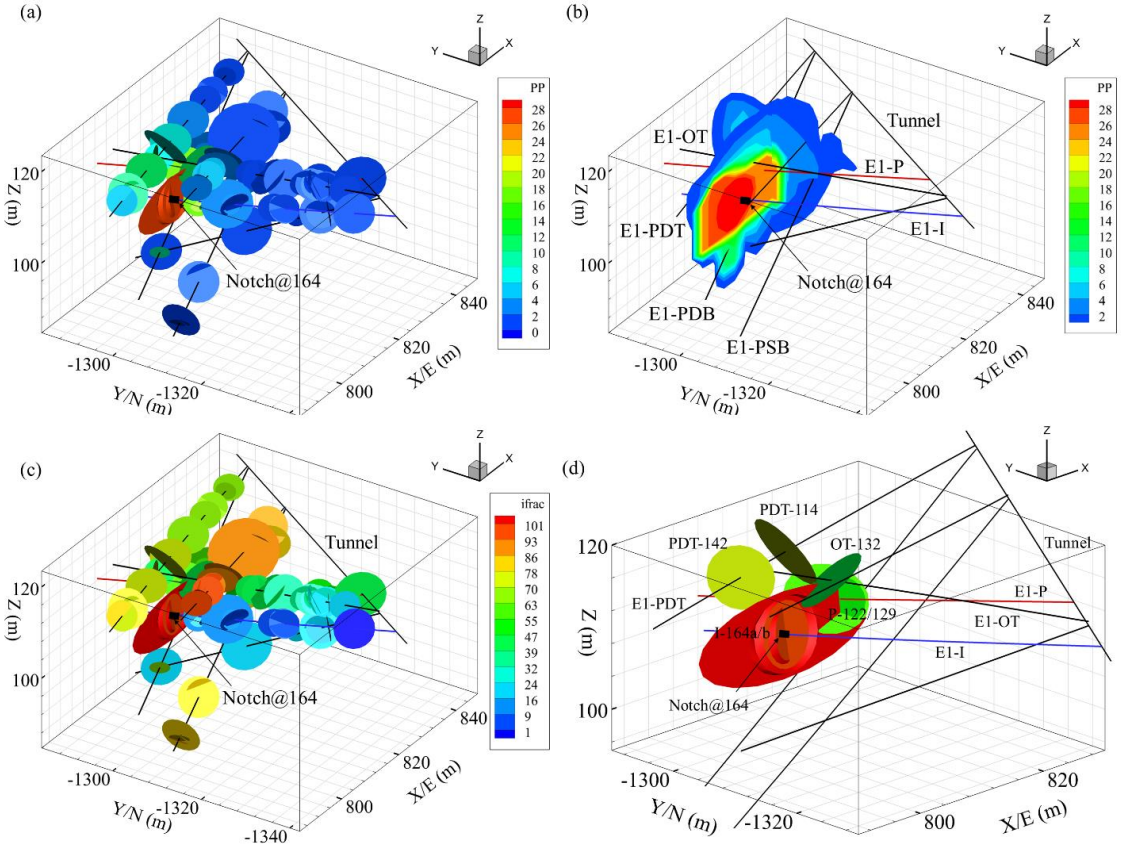

Figure 4.10 The results from numerical simulation. (a) and (b) show the fracture and matrix pressure at T22:52. (c) and (d) is the propagation of I-164b at T22:52. I-164b fully intersect with the OT-132, P-122/126/127/129 and E1-P. Injection well E1-I fully connect with production well E1-P.

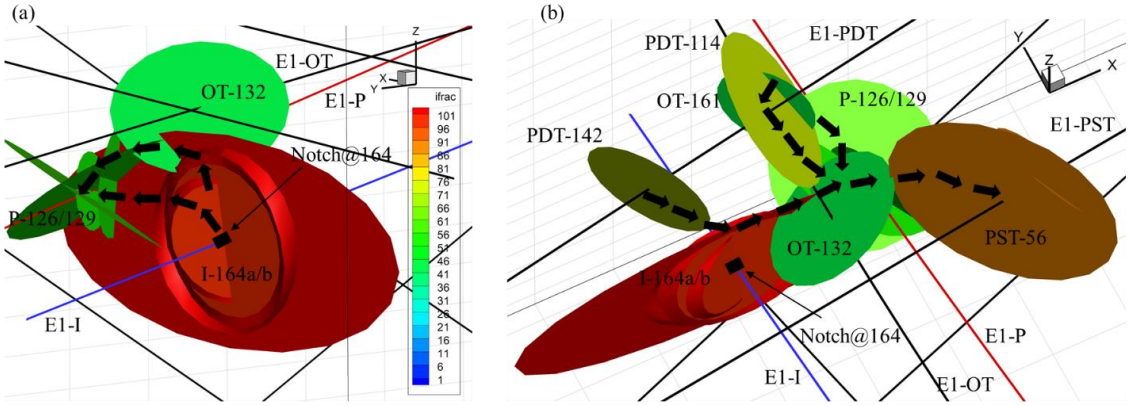

Figure 4.11 Three connectors are yielded during the injection. (a) show the connector between E1-I and E1-P. (b) show the connector between E1-PDT and E1-PST and the connector between E1-P and E1-PST.

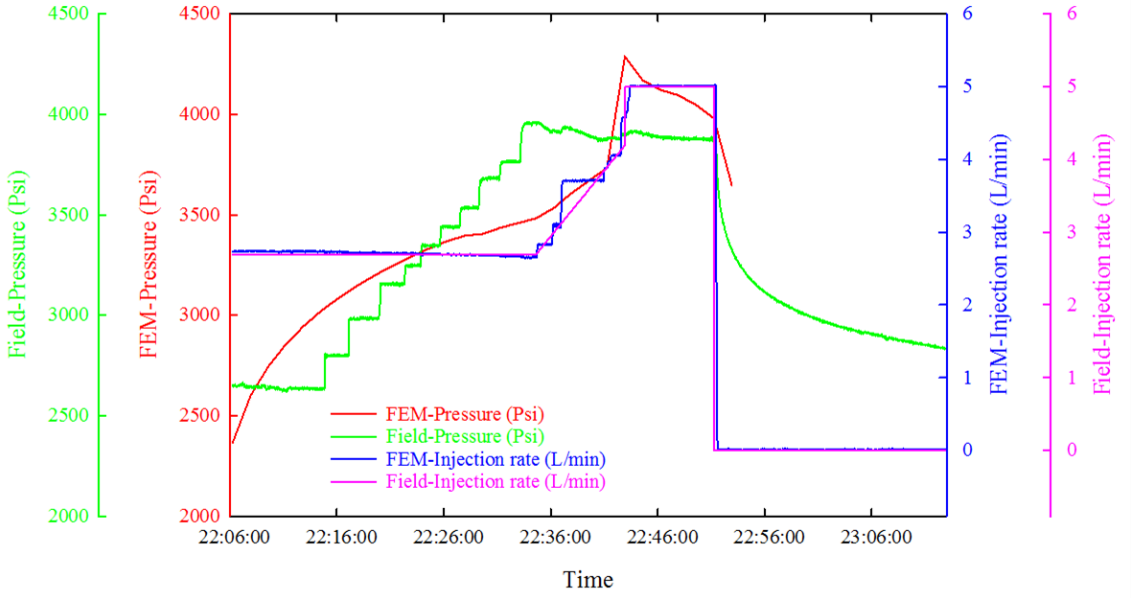

Figure 4.12 The pressure and injection rate at 164@notch (SNL14). The resulting pressure trend generally agrees with field measured values.

In this simulation, three factures slipped namely, I-164a/b and PDT-114. The number of simulated MEQ events was numerically obtained and is plotted in Figure 4.13 for comparison with the field-observed events. The number of the simulated events and field observed events are 298 and 245, respectively. Figure 4.13d is the magnitude-frequency distributions of the simulated events. The b-value is model predefined based on the field studies, and the a-values is fitting number. The evolution of effective principal stress is shown in Figure 4.14.

Most field-observed events are distributed in the zone between the E1-I and E1-P. The location of simulated events matches the field-observed events in this zone very well

because the newly create fractures I-164b penetrates this zone and perpendicular with S_{Hmax}. It suggests that the geometry of newly created fractures from numerical model may match the realist hydraulic fractures. In addition, the differences between the distribution of field-observed MEQs and simulated MEQs may provide valuable information about the geometry of foliation.

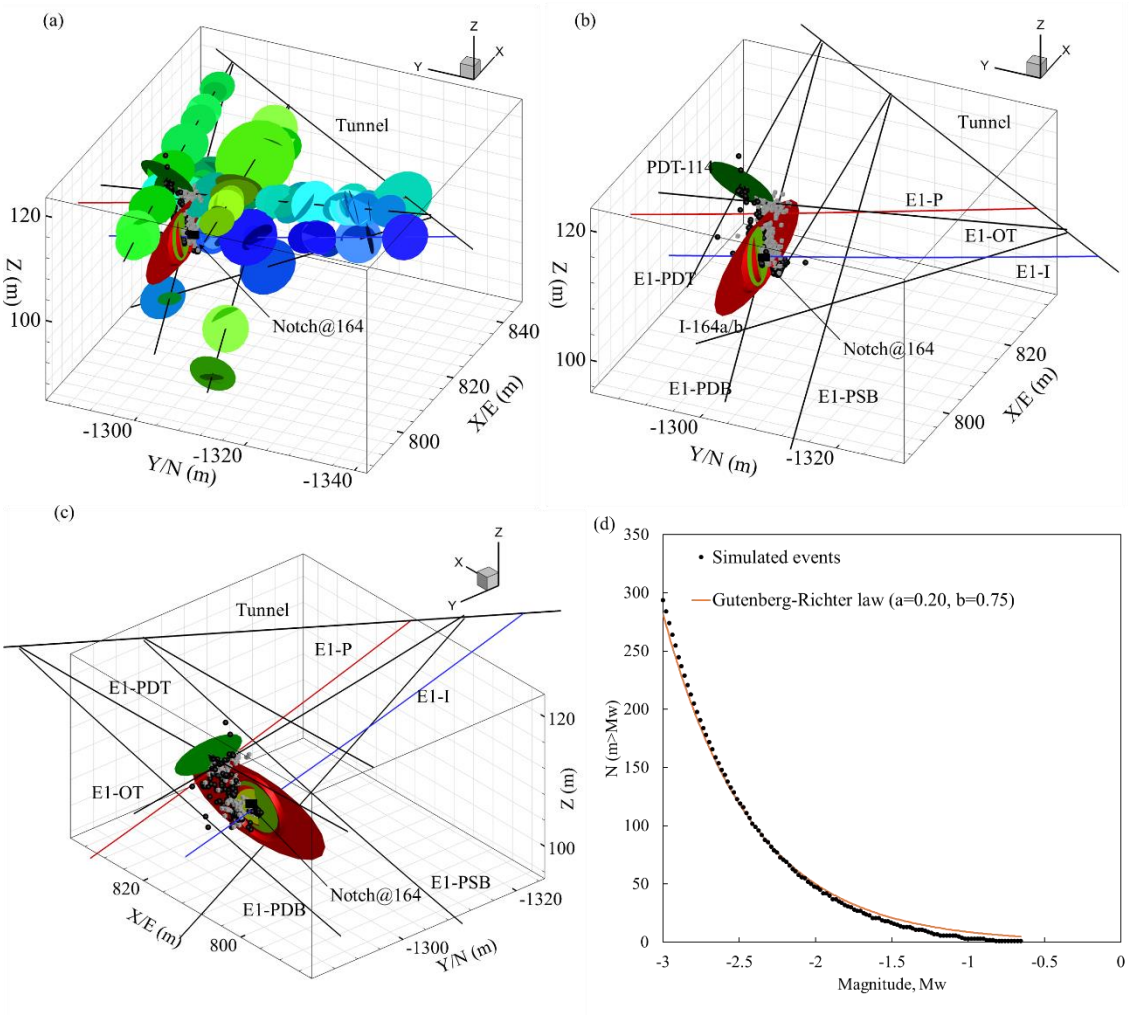

Figure 4.13 Comparison between simulated events with field-observed events. Black sphere represents field-observed MEQs and grey cube represent the simulated MEQs. (a)~(c) the distribution of simulated events and field-observed events. (d) The magnitude-frequency distributions and seismic b-values for simulated MEQs. b-values is predefined, and a-values is a fitting number.

These differences can be attributed to the activation of foliation which are not included in dual scale semi-determinist fracture network (Figure 4.15). The four foliations can be estimated from field observations (e.g., seismicity, ERT).

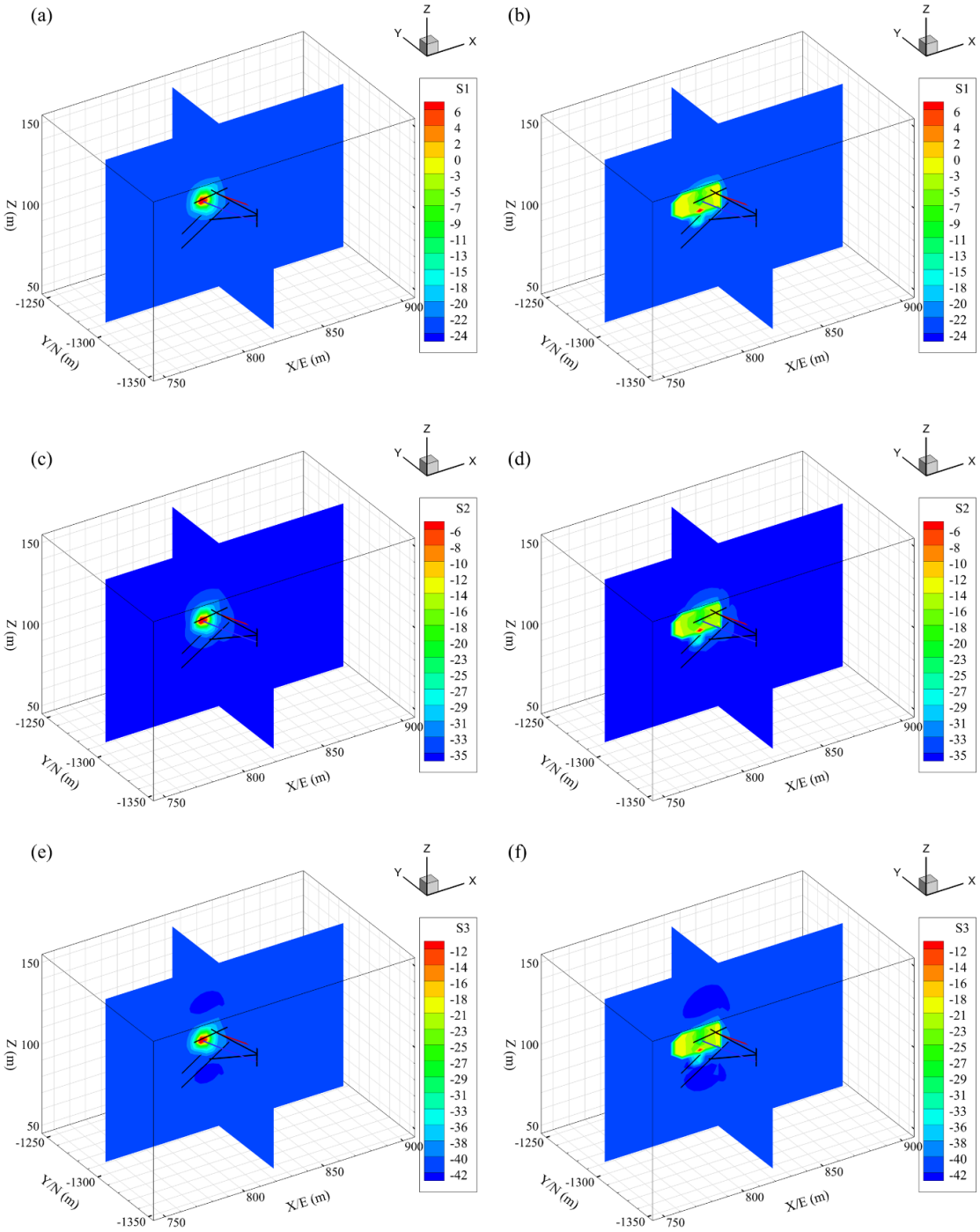

Figure 4.14 The evolution of effective principle stress over times. Unit: MPa. (a) and (b) show the effective minimum principle stress distribution at T22:43 and T22:53, respectively. (c) and (d) show the effective intermediate principle stress distribution at T22:43 and T22:53, respectively. (e) and (f) show the effective maximum principle stress distribution at T22:43 and T22:53, respectively.

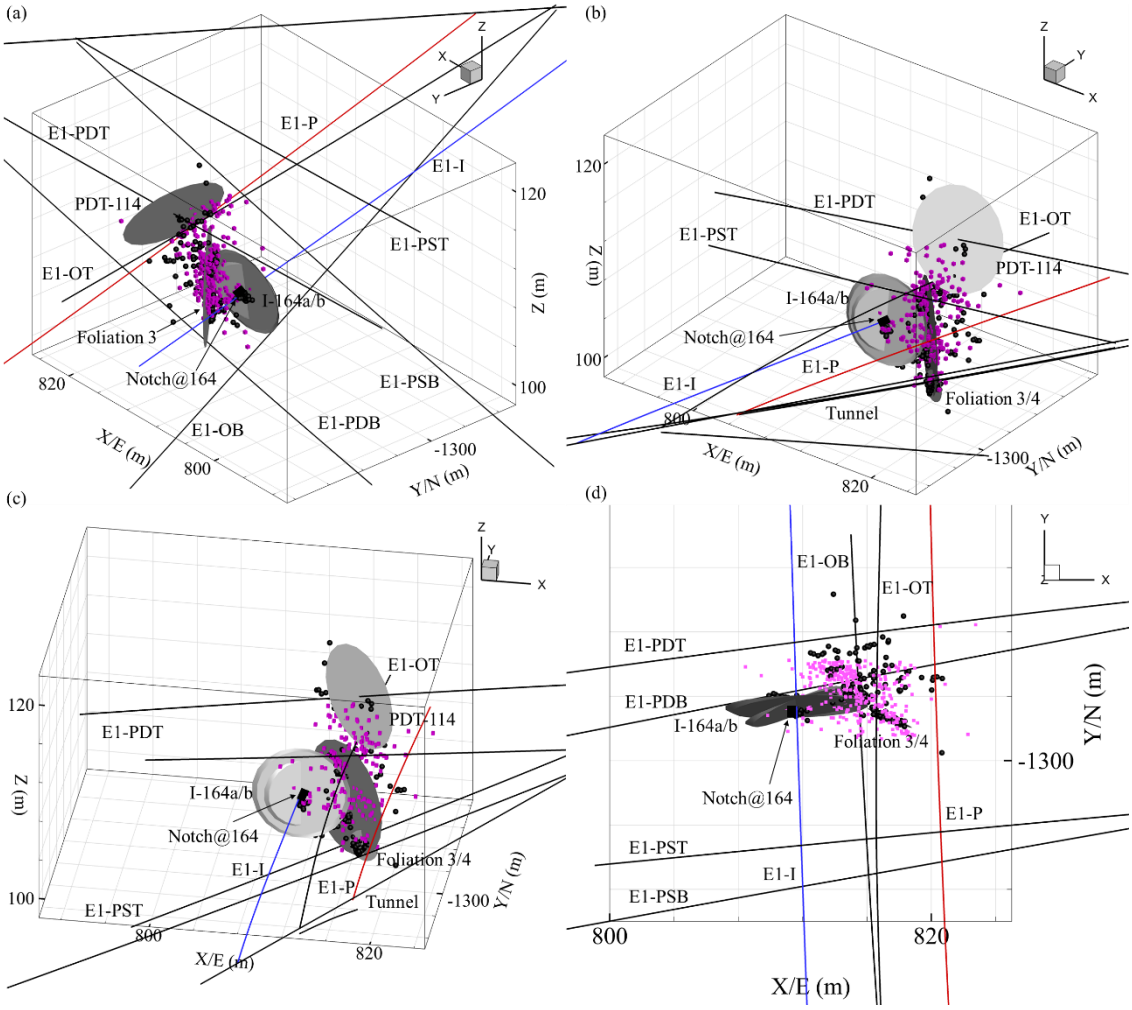

Figure 4.15 Four foliations are estimated from field observation (e.g., seismicity and ERT). Black sphere represents the field-observed MEQs. Pink cube represents the simulated MEQs. Foliation 3&4, I-164-a/b and PDT-114 are slipped. The simulated MEQs generally match the field-observed MEQs.

Further, the detail of reactivated foliations can be treated as complementary data to constrain the uncertainties in dual scale semi-determinist fracture network. Those four foliations are inserted into the fracture network and numerical simulations are performed

while numerical parameters are not changed. The results show that I-164a/b, foliation 3/4 and PDT-114 are slipped. The distribution of simulated and field-observed MEQs are shown in Figure 4.15. It seems that the simulated MEQs generally match the field-observed MEQs. Thus, the heterogeneity of reservoir may not capture by those four foliations. Further studies need to constrain the uncertainties.

4.3 Conclusions

In this chapter, the Coupled Thermo-Hydro-Mechanical-Seismic Model with 3D fracture network is used to simulate EGS Collab. The simulation results (e.g., injection profiles, induced seismicity and fracture propagation) of the Stim-II 164@notch on May 24 show match with field observations.

Chapter 5 Considering Fracture Roughness in Seismicity Simulation

5.1 Introduction

Conventional simulation of micro-seismicity does not account for the fracture roughness. In addition, Mohr-Coulomb failure criterion is commonly employed to characterize the stability of fracture. However, fracture roughness is not considered in Mohr-Coulomb failure criterion. These limitations are relaxed in this chapter by developing advanced techniques for their consideration.

5.2 The Effects of Spatial Distribution of Fracture Roughness on Seismicity Patterns

The spatial distribution of seismic and aseismic slip on a fracture can be hypothetically correlated with the spatial distribution of fracture roughness. Both fracture roughness and distribution of seismic and aseismic slip are highly heterogeneous in a practical setting. The techniques of tectonic geodesy have been used to determine the distribution of seismic and aseismic slip (Avouac 2015), but it is not obvious how slip and roughness are manifested at depth. On the other hand, laboratory experiments that produce seismic and aseismic slip can be directly correlated with a quantified measure of fracture roughness. However, care should be practiced eliminating the effects of boundary conditions during the experiment. For example, direct shear tests are widely used to describe the fracture friction behavior while the distribution of stress along the fracture is not uniform. Also, the constant piston displacement loading condition more realistically captures the subsurface conditions and the stress drop (Ye and Ghassemi 2020) .

Numerical models can consider multiscale fracture roughness and non-linear frictional law (Tal and Hager 2018, Lu and Ghassemi 2019). However, the fully dynamic simulation of shear rupture on a fracture in 3D is computationally expensive. So that simplifications are often made which can result in some bias. For example, fracture roughness is implicitly represented in some numerical models by using a spatial distribution of the parameters of the rate-state friction law (Hillers, Ben-Zion et al. 2006, Richards‐Dinger and Dieterich 2012). And model calibration is difficult because of the absence of direct field observations. Another limitation is the difficulty in capturing the seismic and aseismic slip in a fully dynamic simulation. It is necessary to artificially predefine a critical velocity to distinguish seismic and aseismic slip (Tal, Hager et al. 2018). In other words, a fully dynamic model would need to switch between quasi-static and dynamic time integration schemes when the slip rate on nodes on the fracture becomes larger than the critical velocity. This is because aseismic slip only occurs during the quasi-static stage of a fully dynamic model while seismic slip only occurs in dynamic stage. Thus, this type of fully dynamic model cannot reproduce seismic and aseismic slip on the fracture surface simultaneously.

The unstable slip of fracture occurs when the elastic stiffness is less than critical stiffness (Rice and Ruina 1983). Slip at a certain velocity is aseismic when the elastic stiffness (fracture shear stiffness) is larger than the critical stiffness (Im, Marone et al. 2019). The critical stiffness corresponds to rate-state friction parameters (e.g., a and b), mass and velocity. Elastic stiffness is treated as fracture shear stiffness (Mclaskey and Yamashita 2017). Therefore, it is of interest to establish how one can link the fracture shear stiffness with fracture roughness. This is because the Joint Roughness Coefficient (JRC) is well

accepted parameter to determine fracture shear behavior (e.g., fracture shear stiffness and aperture) in the rock mechanics discipline (International Society for Rock Mechanics 1978). The ability to do so could be instrumental to numerical simulation of micro-seismicity. While fracture roughness can be related to the JRC which accounts for the wavelength and frequency of the surface profile on the entire fracture surface. However, JRC can provide information on the spatial distribution of roughness, however, there is no effective way to measure the *local roughness* via JRC. The JRC is considered uniform on a natural fracture (or at least on a large portion of it).

Thus, first a stochastic partition method is used to divide the contour of laser scan points into multiple patches. The details of stochastic partition method can be found in Appendix C. This provides a local measurement of roughness at every laser scan point on patches. The spatial distribution of JRC are usually heterogeneous on a fracture so the second step is to figure out a robust, physically sound quantitative correlation between the spatial distribution of JRC and the spatial distribution of fracture shear stiffness. This can be achieved by applying an empirical formula on every laser scan points to enable linking the JRC with fracture shear stiffness (Barton and Choubey 1977):

$$K_s = \frac{\Delta\tau}{d} = \frac{100}{L} \cdot \sigma_n \tan\left[JRC\ \log_{10}\left(\frac{JCS}{\sigma_n}\right) + \phi_r\right] \tag{5.1}$$

Where L is the equivalent length which can be considered as length of fracture or a patch of fracture; σ_n is the effective normal stress; JCS is compressive strength of the fracture surface and ϕ_r is the residual friction angle. In this case, $\Delta\tau$ is the shear stress change from initial state to peak shear strength state and d is the peak shear displacement of rock fracture. That is estimate the spatial distribution of fracture shear stiffness K_s the spatial distribution of JRC.

A critical velocity is defined as (Im, Marone et al. 2019),

$$V_c = \sqrt{\frac{\sigma_n a D_c}{M}\left(\frac{K_s D_c}{(b-a)\sigma_n} - 1\right)} \tag{5.2}$$

Where a, b and D_c are rate state friction law parameters; M is mass per unit area at facture depth ($\mathrm{kg/m^2}$); σ_n is the effective normal stress and K_s is fracture shear stiffness. Because the critical velocity corresponds to a given effective normal stress and fracture shear stiffness, the spatial distribution of critical velocity is also not uniform on a fracture. As a result, different patches may experience aseismic and seismic slip simultaneously. The distribution of seismic and aseismic slip can be described by the spatial distribution of critical velocity and nucleation length (Dieterich 1992, Im, Marone et al. 2019). The effect of nucleation length is considered because seismic events only occur when the length of the unstable zone is larger than nucleation length. How the rate of loading (m/s) of fracture influence the moment magnitude of events and distribution of aseismic and seismic slip on fracture are also investigated.

5.3 The Relation between Joint Roughness Coefficient (JRC)-Fractal Dimension

In Chapter 5.2, the concept of JRC is employed to describe the spatial distribution of fracture shear stiffness. In the rock mechanics discipline, fracture roughness is typically represented by JRC (Barton 1973, International Society for Rock Mechanics 1978, Magsipoc, Zhao et al. 2020). The shear stress-shear displacement curve from millimeter-scale direct shear tests provide an accurate way to calculate JRC. For instance, Barton 1973 recommended that JRC could be determined from laboratory direction shear test with a constant normal stress. The JRC can be expressed as:

$$\mathrm{JRC} = \frac{\tan^{-1}(\tau/\sigma_n) - \phi_b}{\log_{10}(\sigma_c/\sigma_n)} \tag{5.3}$$

Where σ_n is the normal stress, τ is the peak shear strength for the normal stress; ϕ_b is the basic friction angle and σ_c is the rock compressive strength. While such procedure is neither feasible nor possible in EGS project. In practical, JRC is commonly determined by a visual comparison of fracture roughness and ten standard profiles (Barton and Choubey 1977). However, this framework is not practically feasible because biases are introduced in the process of the visual estimation of JRC (Beer, Stead et al. 2002, Grasselli and Egger 2003, Alameda-Hernández, Jiménez-Perálvarez et al. 2014). The visual estimation of JRC is strongly subjective and thus not suitable for engineering projects. In practical, roughness is likely anisotropic, which is rarely addressed by the visual comparison method (Barton and Quadros 2014).

Since 1980's, numerous studies attempted to correlate JRC against roughness parameters derived by statistical and fractal, and directional roughness methods (Grasselli 2006, Jang, Kang et al. 2014, Ünlüsoy and Süzen 2020). Note that fracture surface exhibit self-affine fractal properties instead of self-similar fractal properties (Mandelbrot 1985, Renard, Voisin et al. 2006, Candela, Renard et al. 2012, Magsipoc, Zhao et al. 2020). The fractal properties of self-similar surface are exactly or approximately like a part of itself. While the fractal properties of self-affine surface are different with a part of itself. The different between and self-affine and self-similar is scaled differently. The self-similar surface has the equal scales in both x and y direction of surface. The self-affine surface has different scales in different scales in different direction of surface.

Pre-existing JRC-roughness parameters relationships have their own advantages and drawbacks. The JRC-statistical roughness parameters relationship (i.e., JRC-Z_2) are the widely used in practical because of simplicity and efficiency (Myers 1962, Sayles and

Thomas 1978, Yu and Vayssade 1991). But the results are sensitive to the sampling interval because of the nature of self-affine fractals (Stigsson and Mas Ivars 2019). In addition, the sampling interval may influence the scale effects of JRC (Yong, Qin et al. 2019) and the value of fracture roughness parameters (e.g., JRC, Z_2) (Kulatilake and Um 1999). The JRC-fractal dimension relationship (e.g., JRC-D, D is the fractal dimension) are attractive because this method requires less engineering judgement and practical experience (Lee, Carr et al. 1990). But the calculation of D may generate conflicting results because of the error in utilizing fractal concepts (Stigsson and Mas Ivars 2019). For example, divider method, compass walking and h-l method are applied to determine the D of fracture roughness. However, those methods are only applicable to self-similar fracture roughness rather than self-affine fracture roughness. Therefore, the results from those works are very doubtful (Stigsson and Mas Ivars 2019). In addition, a positive correlation between JRC and D is not reflected in some JRC-D relationships. For example, a JRC-D(H) model (JRC$\sim 4.3H$) is developed to estimate JRC (Stigsson and Mas Ivars 2019). H is the Hurst exponent and $H = 2 - D$ for curves or $H = 3 - D$ for surface. This JRC-H model implies that JRC have a positive correlation with H, which contradicts with common sense. Because the higher value of H indicates the surface with a smoother trend, with less volatility and less roughness (Mandelbrot 1985). For example, the JRC of a smooth surface (H = 0.9 & $\sigma\delta h(1\text{ mm}) = 0.2$) is 10.5 and JRC of rough surface (H=0.7 & $\sigma\delta h(1\text{ mm}) = 0.2$) is 9.6 according to (Stigsson and Mas Ivars 2019). $\sigma\delta h(1\text{ mm})$ is the standard deviation of asperity difference of points 1 mm apart.

In addition, the value of D mostly range from 1 to 1.1 in those JRC-D relations (See Table 5.1 or Li and Huang 2015). While the value of D typically is in 1~1.5 for fracture profiles

and 2~2.5 for fracture surface (Brown 1987, Magsipoc, Zhao et al. 2020). Table 5.1 shows the previous relations of JRC-fractal dimension (D or H) (Li and Huang 2015). Note that C-W is compass walking and B-C is Box counting and PSD is power spectral density. St. profiles is the 10 standard profiles.

Table 5.1 Literature review of relation between JRC-fractal dimension (After Li and Huang 2015).

No.	Equation	Method	D/H range	St. Profiles	Reference
T1	JRC=-1138.6+1141.6D		1.0-1.0149	Y	Turk et al, 1987
T2	JRC=-1022.55+1023.92D		1.0–1.0182	Y	Carr and Warriner,1987
T3	JRC=209.7517$D-204.1486$		1.0–1.0686	N	Qin et al,1993
T4	JRC=172.206$D-167.2946$		1.0–1.0876	Y	Zhou and Xiong,1996
T5	JRC=7811778.928D^3 $-23723041.6842D^2$+24014672.3562D -8103409.7809		1.0–1.0144	Y	Bae et al, 2011
T6	JRC=1000$(D-1)$		1.0–1.0200	Y	Carr and Warriner,1987
T7	JRC=1870$(D-1)$		1.0–1.0107	Y	Maerz and Franklin,1990
T8	JRC=1647$(D-1)$		1.0–1.0121	N	Liu,1993
T9	JRC=1195.38$(D-1)$	C-W	1.0–1.0167	Y	Lamas,1996
T10	JRC=479.396$(D-1)^{1.0566}$		1.0–1.0495	Y	Zhou and Xiong,1996
T11	JRC=29.35$(D-1)^{1.0566}$		1.0–1.4343	N	Jia et al.2011
T12	JRC=150.5335$(D-1)^{0.46}$		1.0–1.0177	Y	Wakabayashi, Fukushige,1992
T13	JRC=-0.87804+27.7844$(D-1)/0.015$ $-16.9304[(D-1)$ $/0.015]^2$		1.0005–1.0113	Y	Lee et al,1990
T14	JRC=28.5-33.18/$[1+150(D-1)]$		1.0011–1.0194	N	Xu et al,2012
T15	JRC=100$(D-1)^{0.4}[1$ $-1/\exp(300(D-1))]$		1.0–1.0181	N	Xu et al,2012
T16	JRC=60$(D-1)^{12}/[0.006+(D-1)]$		1.0–1.0177	N	
T17	JRC=15179$W_d(D-1)^{1.46}$	B-C	-	Y	Chen,2012
T18	JRC=53.7031$(D-1)^{0.3642}$	h-L	1.0–1.0664	N	Askari and Ahmadi,2007
T19	JRC=85.2671$(D-1)^{0.5679}$	h-L	1.0–1.0778	Y	Xie and Pariseau,1994
T20	JRC=50$(D-1)$		1.0-2.0	N	Ficker, 2017
T21	JRC=1.319(1+2.862 tan $\beta)D_f$	B-C	2-3	N	Wang et.al, 2017
T22	JRC=-4.3+54.6$\sigma\delta h(1\ mm)+4.3H$	PSD	0-1	N	Stigsson and Ivars, 2019

It seems that the empirical equations in Table 5.1 are only corrected over specific ranges of JRC and D/H. Thus, the full spectrum of fractal dimension is not covered. It is suspected that amplitude parameters (e.g., absolute height and RMS of height) of scan

points on fracture are not contained in those JRC-D relationships (Table 5.1). This is because a natural fracture surface has self-affine fractal properties fully defined by the fractal dimension and amplitude parameters of laser scan points on the fracture surface. Therefore, some researchers concluded that none of methods can accurately describe the JRC of fracture (Hsiung, Ghosh et al. 1993, Ünlüsoy and Süzen 2020) and there is still no universally accepted method for reliably and accurately estimating the JRC of a fracture (Ünlüsoy and Süzen 2020). The JRC-directional roughness parameters relationship (Grasselli and Egger 2003) considers three-dimensional surface, which is rarely applied in practical.

In Chapter 5.4, a self-affine anisotropic roughness is constrained by three parameters, including fracture dimension (Hurst exponent) in perpendicular directions (x direction/East and y direction/North) and amplitude parameter of scan points on fracture. Fractal dimension D is directly connected to Hurst exponent H. In the case of our work, H is equal to $3 - D$ for fracture surface and H typically ranges from 0.5 to 1.0 because D is generally in 2~2.5 for surface. Therefore, H and JRC present a negative correlation. The amplitude parameter of scanning points on fracture can be complemented by the Root-mean-square (RMS) of height of scan points on fracture. The JRC-H relationship could be derived by calculating the JRC of synthetic anisotropic roughness which is defined by Hurst exponent and RMS. The advantage of synthetic anisotropic roughness compared to realist fracture in studying the relationship between the JRC-fractal dimension is that they allow the independent study of the effects of surface morphology on JRC. Note that the synthetic anisotropic roughness only captures the real fracture

roughness to a finite degree of accuracy within a finite range of scales (Candela, Renard et al. 2009).

5.4 The JRC-Hurst Exponent (H) Empirical Relation

The JRC-H empirical relation is used for characterization of a self-affine anisotropic surface, which is considered to be a realist fracture surface representation. In addition, the fracture samples from subsurface projects are limited and the full spectrum of fractal dimension (i.e., D or H) may not be covered. The nature of generating a surface is to use equations to interpret the multiscale structures of fracture surfaces as mathematic-based structures. There are a number of ways to generate fractal surface, including random midpoint displacement (Fournier, Fussell et al. 1982), Fourier transform (Candela, Renard et al. 2009). The random midpoint displacement and Fourier transform could be the most common in practical settings. The random midpoint displacement method uses the modified fractal Brownian motion to generate a self-affine surface. This method is commonly applied because it is simple to generate a large fractal surface. The Fourier transform method is used to describe fracture profiles by an infinite superposition of sine functions and in practice the number of functions could be set to half the number of points use to define the synthetic surface (Stigsson 2016). The method was further developed to be able to generate anisotropic surface with different fractal dimensions in two perpendicular directions (Candela, Renard et al. 2009). But the amplitude of height of laser scan points are not constrained. Because both fractal dimension and amplitude parameter of height of laser scan points are required for the definition of self-affine surface (Stigsson and Mas Ivars 2019).

In this work, extended Fourier transform method is developed with consideration of amplitude of height of laser scan points. The extended Fourier transform method uses two Hurst exponents and amplitude parameters (RMS) to constrain the self-affine anisotropic surface. The method first generates a mesh grid of desired dimension and a random Gaussian noise (vibration considered as asperities) is assigned to all coordinates of the grid. Such Gaussian noise field is decomposed using Fourier transform and the frequencies are scaled by the scaled anisotropic matrix E to match the desired fractal dimension. The anisotropic matrix E is defined as (Candela, Renard et al. 2009):

$$E = \begin{bmatrix} 1/H_x & \\ & 1/H_y \end{bmatrix} \tag{5. 4}$$

In the next step, an inverse Fourier transform is performed to populate each coordinate of the surface. In the final step, the fracture surface is rescaled according to the value of RMS. Appendix D provides the MATLAB program for extended Fourier transform method. Self-affine surface can scale differently in different directions because of the decoupling of the different axis (Stigsson 2016). Therefore, self-affine surfaces can more realistically represent real fracture surfaces, underscoring the point that fracture roughness is scale dependent (because the self-affine surface is scaled differently in different direction of surface). Figure 5.1 shows the geometry of two synthetic self-affine surfaces. The Hurst exponent in x- and y-directions, H_x and H_y , are both 0.6 (isotropic- Figure 5.1a) and the RMS is 0.002 m in Figure 5.1a. Two representative fracture profiles are extracted in two perpendicular direction of the surface (Anisotropic- Figure 5.1b). Figure 5.1c shows the anisotropic surface with the Hurst exponent in x and y direction, H_x and H_y , being 0.6 and 0.8, respectively with RMS of 0.002 m. Two representative fracture 1D profiles are extracted in two perpendicular directions of the surface (Figure

5.1d). This method is verified by comparison between the input parameters (H_x=H_y) of the synthetic isotropic surface and the evaluated H of this isotropic surface obtained from power-spectral-density (PSD) analysis on this surface. The statistical properties of the surface can be extracted from power spectrum $C(q)$, q is the wavevector obtained by PSD analysis over surface. The power spectrum $C(q)$ is the function of Fourier transform of the autocorrelation function of $h(x)$ where $h(x)$ is the height of surface (asperity) at position x. The effects of sampling interval (resolution) on the value of evaluated H are considered.

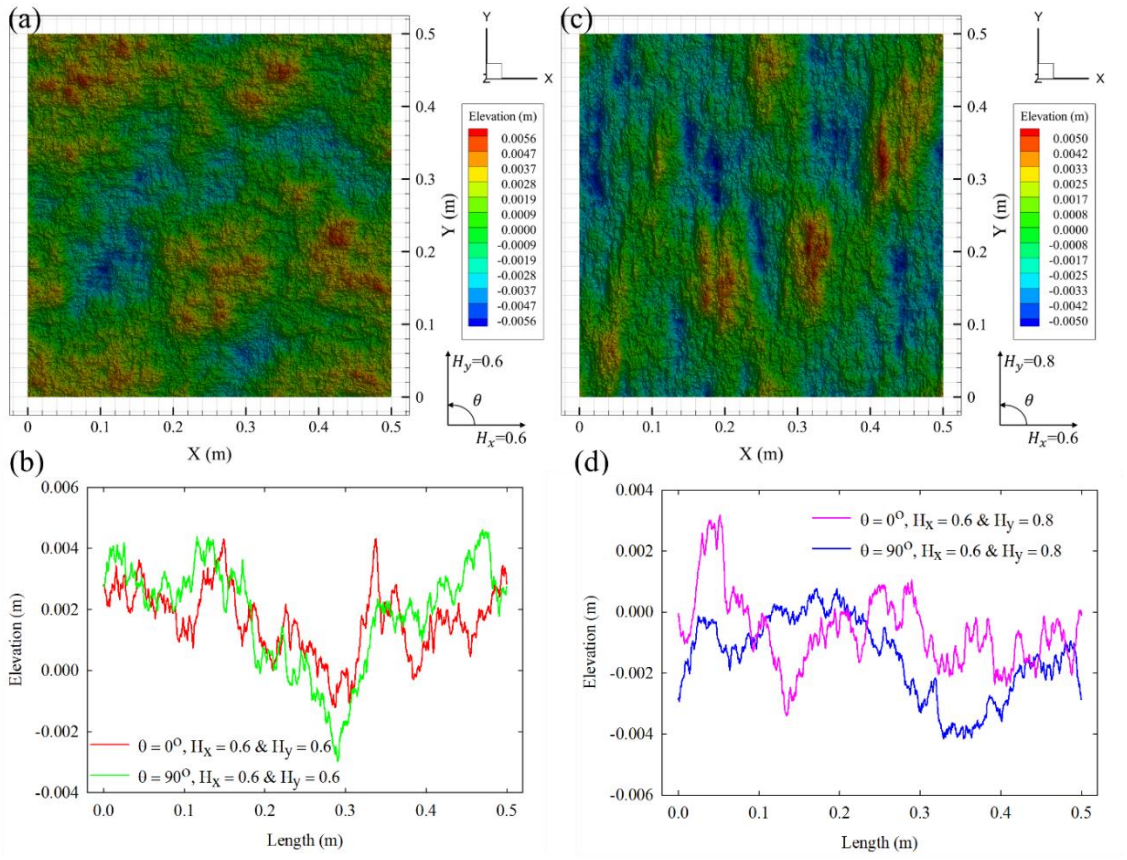

Figure 5.1 The geometry of two self-affine surface. (a) isotropic self-affine surface with $H_x = 0.6$ & $H_y = 0.6$ and $RMS = 0.002$ m. (b) the representative profiles extracted in $x = 0.0$ m and $y = 0.024$ m direction of the surface (a). (c) An anisotropic self-affine surface with $H_x = 0.6$ & $H_y = 0.8$ and $RMS = 0.002$ m . (d) the representative profiles extracted in $x = 0.366$ m and $y = 0.048$ m direction of surface (c). The method can generate isotropic and anisotropic surface based on Hurst exponent and RMS.

Figure 5.2 shows the comparison between input parameters (H_x=H_y) and evaluated H at different sampling intervals (distance between neighboring points, resolution), because the sampling interval has a large influence on the value of the fracture roughness (e.g., Z_2, R_p and SF). If the sampling interval is less than 1 mm, the evaluated H are very close to input parameters (H_x=H_y) (Figure 5.2). In this work, the sampling interval is regarded as 0.5 mm. Therefore, the extended Fourier transform method is effective to generate surface and PSD is robust and accurate to calculate H over the synthetic surface.

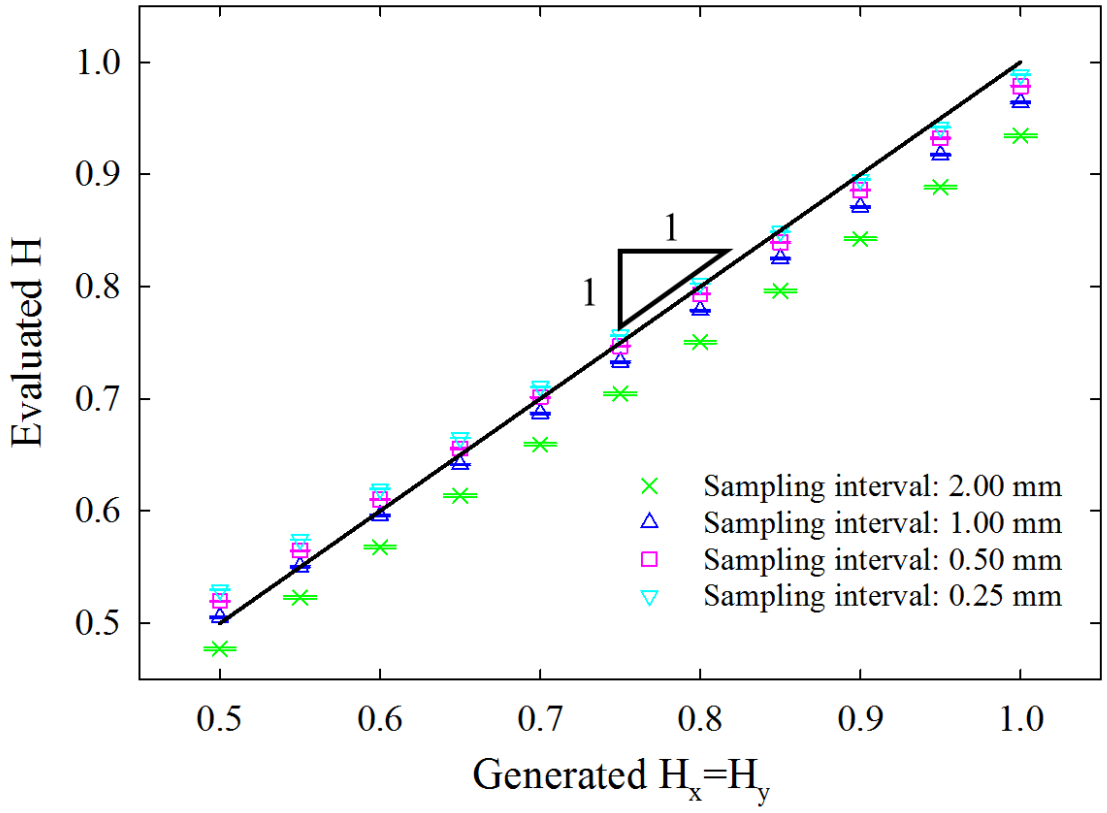

Figure 5.2 The comparison between input parameters (H_x=H_y) of the synthetic isotropic surface and the evaluated H of this isotropic surface. The slope of black line is 1. The green thin ×, blue triangle up, pink square and cyan triangle down are the evaluated H from synthetic isotropic surface with sampling interval 2.00 mm, 1.00 mm, 0.50 mm and 0.25 mm, respectively. Sampling interval (the distance between scan points on fracture) have large influence on the value of fracture roughness (Z_2, Rf, D, H, et.al). This plot shows that the sampling interval have less influence on the value of fracture roughness when the sampling interval is large than 1 mm.

The JRC-H relations can be estimated by evaluating the JRC over a self-affine synthetic isotropic/anisotropic roughness described by two the Hurst exponents H_x, H_y and the RMS. Based on previous work (Brown 1987, Akarapu, Sharp et al. 2011, Magsipoc, Zhao et al. 2020) the H value is assumed to be in the ranged of 0.5-1.0. Further, The JRC value is commonly in the range 0-20. H and JRC are negatively correlated, and the RMS of asperities elevation is chosen as $2x10^{-3}$ m. Because the JRC of synthetic surface (with $H_x = H_y = 0.5$, RMS=$2x10^{-3}$ m) is 19.9 (approximately 20). The JRC of synthetic surface (with $H_x = H_y = 1.0$, RMS=$2x10^{-3}$ m) is 0.3 (approximately 0.0). Therefore, the value of RMS (equal to $2x10^{-3}$ m) is reasonable because the limit values of Hurst exponent and JRC are mapped during the analysis of self-affine surface. Those two conditions act as input for estimating the JRC-H relations. Note that the effects of distribution of elevation of laser scan points on JRC is not included and would be considered in future work. Thus, the self-affine synthetic anisotropic surface could be fully constrained by the two Hurst exponents and RMS because of the nature of self-affine surface (Stigsson 2016). The measurement of JRC is based on the value of Z_2 over a synthetic surface and details can be found in some previous works (Jang, Kang et al. 2014). In most previous work, the JRC-H (D) relation is derived by the standard profiles (the ten profile types from (Barton and Choubey 1977)). One limitation of those works is that each trace (1D) is regarded as the representative trace of the fracture surface (2D). However, the uncertainties of this procedure cannot be justified. For example, ten type traces from (Barton and Choubey 1977) and seven type traces from (Bakhtar and Barton 1984) are analyzed by power spectral density (PSD) and Hurst exponent calculated from the slope of the PSD in a log-log coordinate system. Note that the slope of PSD in log-log

coordinate system equals $(-2-2H)$ for the fracture surface and $(-1-2H)$ for fracture profiles. Figure 5.3a shows the distribution of H with JRC for those seventeen fracture traces and the relation between H and JRC is not clear. For example, H positively correlates with JRC when JRC is in the range from 1 to 5, while H negatively correlates with JRC when JRC is in the range from 15 to 19. Common sense would indicate the higher values of H correspond to a smoother surface and smaller JRC. This expected phenomenon is also found in (Stigsson and Mas Ivars 2019).

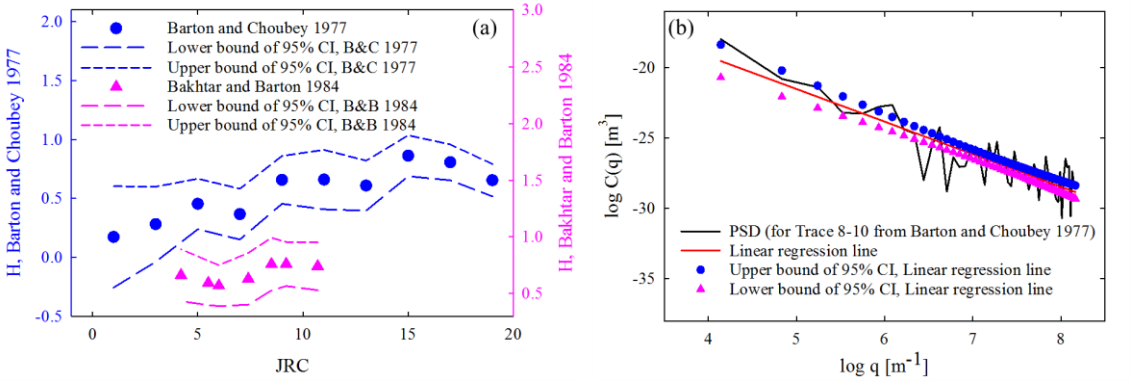

Figure 5.3 The distribution of JRC and H for the ten type traces from Barton and Choubey 1997 and seven type traces from Bakhtar and Barton 1984. (a) the distribution of JRC and H with the lower and upper bound of 95% of CI. (b) the PSD plot for the Trace 8-10 from Barton and Choubey 1977. The dots and triangles in represent the upper and lower bound of 95% CI of the linear regression line respectively.

In addition, the slope of PSD in log-log coordinate system is also highly uncertain. Figure 5.3b shows the PSD plot for the Trace 8-10 from Barton and Choubey 1977. The dot and triangle in Figure 5.3b represent the upper and lower bound of 95% CI of the linear regression line, respectively. The variation of slope of linear regression line could result in high uncertainties in the relation between JRC-H (Figure 5.3a). It is speculated that the ten type-traces from Barton and Choubey 1997 may not be suitable for the derivation of JRC-H relation. Thus, it is better to derive the relation between JRC-H by calculating the

JRC of a synthetic surface defined by Hurst exponents and RMS of height of the scan points on fracture (asperity heights).

The processes of deriving JRC-H relation in this work follow four steps: (1) generate self-affine synthetic surface by extended Fourier transform method with the value of H_x & H_y (0.5 to 1.0) and RMS; RMS is fixed as 0.002 m; Here the length of surface is 0.5x0.5 m; (2) evaluate the surface asperity height at a length scale of 10 cm and use it to calculate the distribution of JRC for the synthetic surface. Note that the JRC is determined by a widely acceptable empirical formula ($JRC=51.16\cdot(Z_2)^{0.531}-11.44$) (Jang, Kang et al. 2014). A bias will be introduced because such JRC-Z_2 empirical formula is not suited for determining the JRC of an anisotropic surface. A lognormal distribution is recommended to fit the distribution of JRC. The mean of the lognormal distribution is considered the JRC of this entire synthetic surface at 10 cm scale; (3) repeat step (1) and (2) multiple times (i.e., 1000 times in this work) by keeping the H_x and H_y are the same as before while changing the geometry of synthetic surface by the random Gaussian noise (vibration considered as asperities) used to assign asperities to all the points on the entire surface. Note that each time will generate a different JRC values. Therefore, there are 1000 JRC values are generated because we repeat step (1) and (2) 1000 times. (4) a Lognormal distribution is applied to fit the 1000 JRC values generated in Step 3. The mean of this Lognormal distribution is the taken as the final JRC value of the self-affine synthetic surface for the given H_x and H_y and RMS. (5) change the value of H_x and H_y and repeat step (1), (2), (3) and (4). So, the full spectrum of JRC-H relations is covered (because JRC is in 0-20 range and H is in 0.5 to 1 are utilized to describe the JRC-H relation). Figure 5.4 shows the results. Because we use RMS=0.002 m and H_x=H_y=0.5 to

generate a synthetic surface (JRC=20). we use RMS=0.002 m and H_x=H_y=1 to generate a synthetic surface (JRC=0). In addition, H is located [0.5, 1] and JRC is located [0,20]. Figure 5.4 shows the evolution of JRC with the variation of H_x and H_y with RMS is fixed as 0.002 m. A quadratic polynomial equation is employed to fit the simulation results. The empirical JRC-H relation is given as:

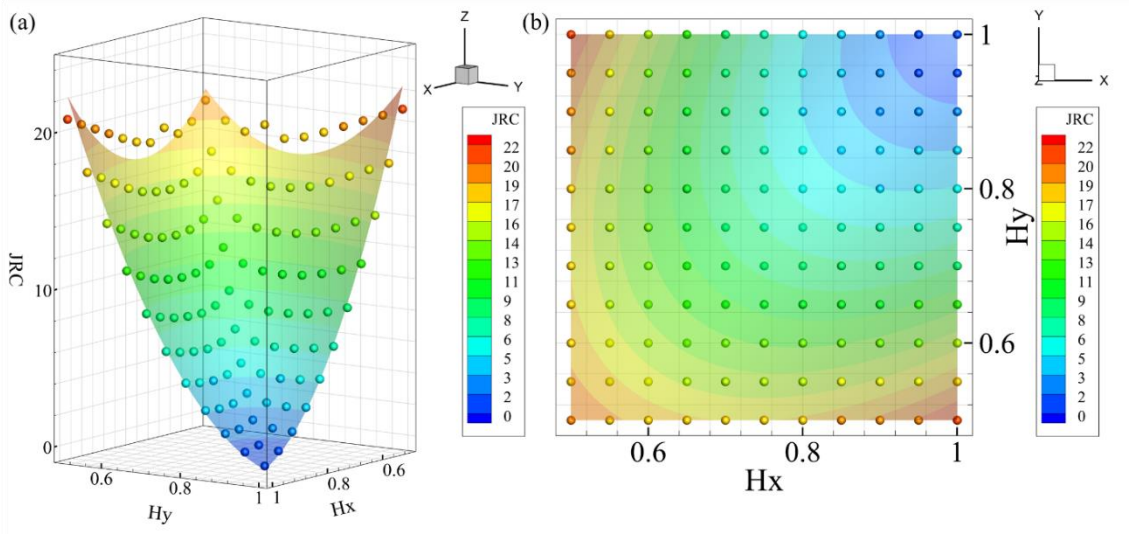

Figure 5.4 JRC-H relationship. The color dots are the results from evaluation of JRC over a self-affine synthetic surface. The color contour is the quadratic polynomial equation function (Equation 5.5) which fits the values of color dots.

$$\mathrm{JRC}(H_x, H_y) = 61.32 - 50.73H_x - 50.73H_y + 68.01H_x^2 - 95.81H_xH_y + 68.01H_y^2 \quad (5.5)$$

Where H_x and H_y is the Hurst exponent along the x- and y-axis, respectively. Both H_x and H_y are in the ranged from 0.5 to 1.0. Note that Equation 5.5 has a predefined condition of RMS fixed at 0.002 m. Further, Equation 5.5 is formulated at the decimeter scale (~10 cm) and upscaling law is necessary for field studies. For example, $H_x = 0.6$ and $H_y = 0.7$ are measured over the fracture surface at 10 cm scale. The JRC of this surface is 13 according to Equation 5.5. The JRC of large-scale fracture at 100 m scale can be obtained from (Barton and Bandis 1982) scaling: $\mathrm{JRC}_0(L_n/L_0)^{-0.02\mathrm{JRC}_0} =$

$13(100/0.1)^{-0.02\cdot13}$= 2.2. A brief introduction on elementary upscaling law can be found in Chapter 7.1. Figure 5.4 implies that JRC and H are negatively correlated which match previous studies (Li and Huang 2015, Ficker 2017) and common sense. The advantage of Equation 5.5 over others is that the full spectrum of H with JRC are covered and effects of anisotropic roughness on JRC are also considered. Note that the direction angle of self-affine synthetic anisotropic surface is 90^o in this work. The direction angle, different from 90^o would be considered by rotated surface upon. The synthetic JRC-H relation can accelerate our numerical model for fracture network simulation.

5.5 The Linear Barton-Bandis Model

In our previous work (Chapter 2), fracture failure was evaluated by Mohr-Coulomb failure criterion with Patton's saw-tooth fracture model (Cheng, Wang et al. 2019, Lu and Ghassemi 2019). Patton's model is very simple, however the effects of increasing normal stress in changes of shear strength and fracture roughness are not fully reflected. While Barton-Bandis model can capture the most realist of fracture nonlinear shear behavior. The parameters in Barton-Bandis model have physical background and is easily determined by simple lab tests. In the reality, Mohr-Coulomb failure criterion is widely used for fracture stable analysis. Our fracture network model can be benefitted from the link between existing Mohr-Coulomb failure criterion and Barton-Bandis model. This can be achieved by calculating Mohr-Coulomb failure criterion parameters by "multi-linearization" Barton-Bandis model (Prassetyo, Gutierrez et al. 2017). A linearized of Barton-Bandis model is given as (Prassetyo, Gutierrez et al. 2017):

$$\tau_t = c_t + \sigma_n \tan(\phi_t) \tag{5.6}$$

Where τ_t is equivalent peak shear strength, c_t is the equivalent peak cohesion, σ_n is the normal stress on fracture, ϕ_t is the equivalent peak friction angle; The ϕ_t and c_t are given by the slope and intersect of the tangent to the failure surface at the current normal stress, respectively. ϕ_t is the equivalent peak friction angle gave as:

$$\phi_t = \psi_t + \phi_r = JRC \log_{10}\left(\frac{JCS}{\sigma_n}\right) + \phi_r \tag{5.7}$$

In Equation 5.7, JRC , JCS and ϕ_r are the parameters of Barton-Bandis model. ψ_t is the equivalent dilation angle and ϕ_r is residual angle; The details of the linearized of Barton-Bandis model can be found in (Prassetyo, Gutierrez et al. 2017).

5.6 Integration of the JRC-H Relation with FEM with 3D Fracture Network

Fracture roughness have large influence on fracture deformation. In the rock mechanics discipline, JRC is commonly applied to describe the fracture roughness. However, the calculation of JRC is still in debated because of the measurement of JRC and scaling effects of JRC. Since only rock samples with small size (~10 cm) are available in projects. Here we propose a new method to relax these limitations. The flowchart of this method is shown in Figure 5.5. The details of this flowchart can be found in Appendix E.

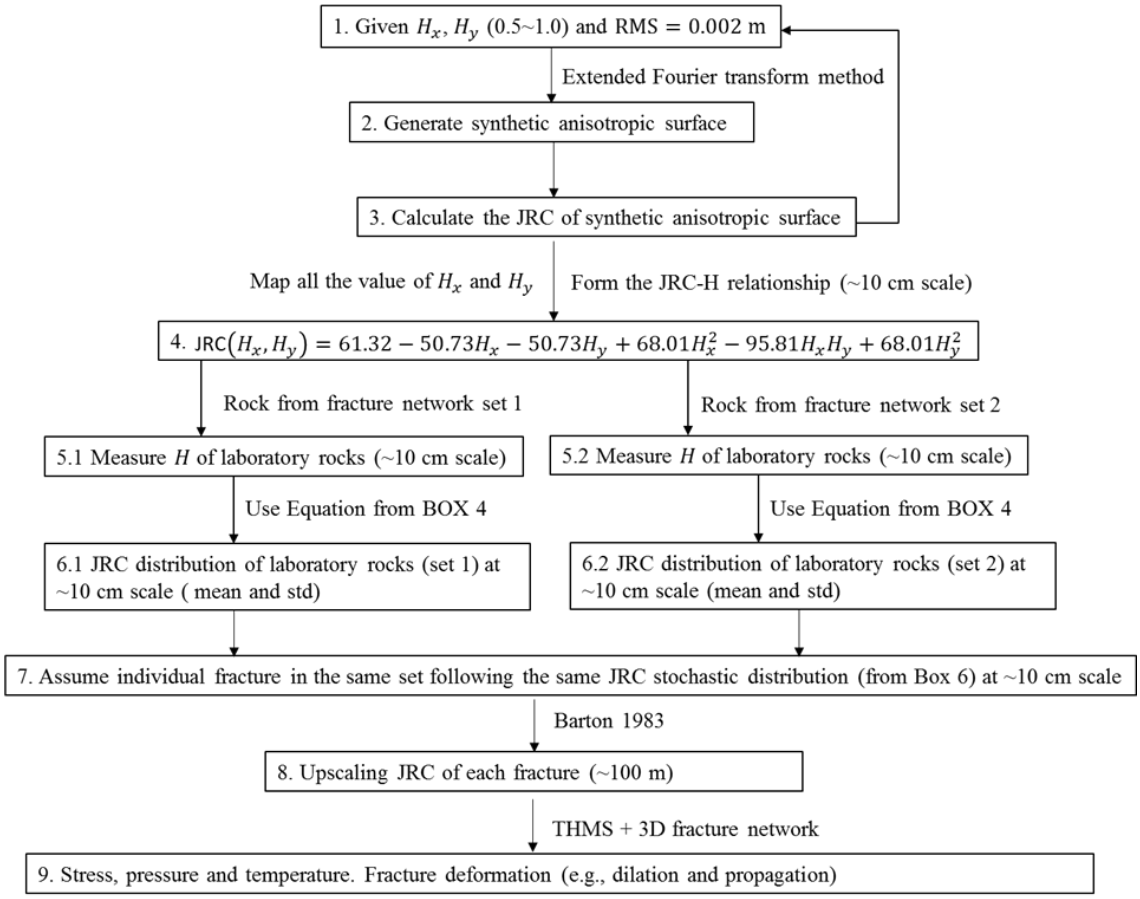

Figure 5.5 The flowchart of integration of the JRC-H relation with FEM with 3D fracture network

5.7 Conclusions

In this chapter, several techniques are introduced to investigate the effect of fracture roughness on micro-seismicity and fracture failure criterion. This can be achieved by applying the concept of stochastic partition and JRC to the reservoir simulation. The spatial distribution of fracture shear stiffness can be described. The occurrence of micro-seismicity depends on the ratio between critical stiffness and fracture shear stiffness. Our previous fracture network model is extended to consider the fracture roughness and fracture pressure induced stress field. A framework of synthetic anisotropic surface is developed, and the geometrical structures of synthetic roughness is fully controlled by

two Hurst exponents in perpendicular direction and RMS of height of scan points on fracture. A JRC-Hurst exponent relation is proposed by calculating the JRC value of synthetic anisotropic surface which is defined by two Hurst exponents and RMS. Therefore, the linear Barton-Bandis model can be used in numerical simulation.

Chapter 6 An Application for Triaxial Injection Laboratory Tests

6.1 Introduction

Ye and Ghassemi 2020 studied the effects of fracture roughness on the distribution of AE (seismic events) during frictional slip due to injection. The rock sample was a cylindrical (length are 106 mm and diameter are 50 mm) Sierra White granite with a tensile rough fracture (of elliptical shape with major axis of 43 mm and minor axis of 24 mm). The inclination angle of fracture is 36^o and this work focus on the top fracture surface because the top and bottom fracture surfaces are fully mated (Figure 6.1a) and would be the same. The geometrical properties of the rock sample are shown in Figure 6.1a. The initial axial load is 170 MPa. A 3D laser scan system (B&H Machine Company) with 0.5 mm resolution laser beam was used to measure the topography of the top fracture surface before test. Figure 6.1b shows the asperity height of the top fracture surface and the AE events distribution due to shear slip by injection. The asperity height is defined relative to the lowest plane of the fracture surface. Laboratory observations of the triaxial shear test (Ye and Ghassemi 2020) suggest that the fracture is in the seismic stage when the slip rate of fracture is larger than 1.9×10^{-5} m/s (at an effective normal stress of 44 MPa). The loading (increasing injection pressure) time was approximately 400 seconds and in view of the smallness of fracture surface area, the slip velocity and normal stress can be considered to be uniform on the fracture plane. The effects of heterogeneous variables (i.e., slip velocity and normal stress) on AE are not considered in this work to enable comparison with analytical treatment (the 1D mass-spring system). Further, 1D mass-spring system is not a necessary part of our framework and it is only used here to show that the numerical model can produce similar results (Chapter 6.2). Most seismic events

are clustered and located in a specific zone. It suggests that seismic slips occur in that zone, while aseismic slips occur on other zone of the fracture. A question that arises is why AE (seismic events) occur on that zone and how roughness impacts the partition of seismic slip and aseismic slip zones.

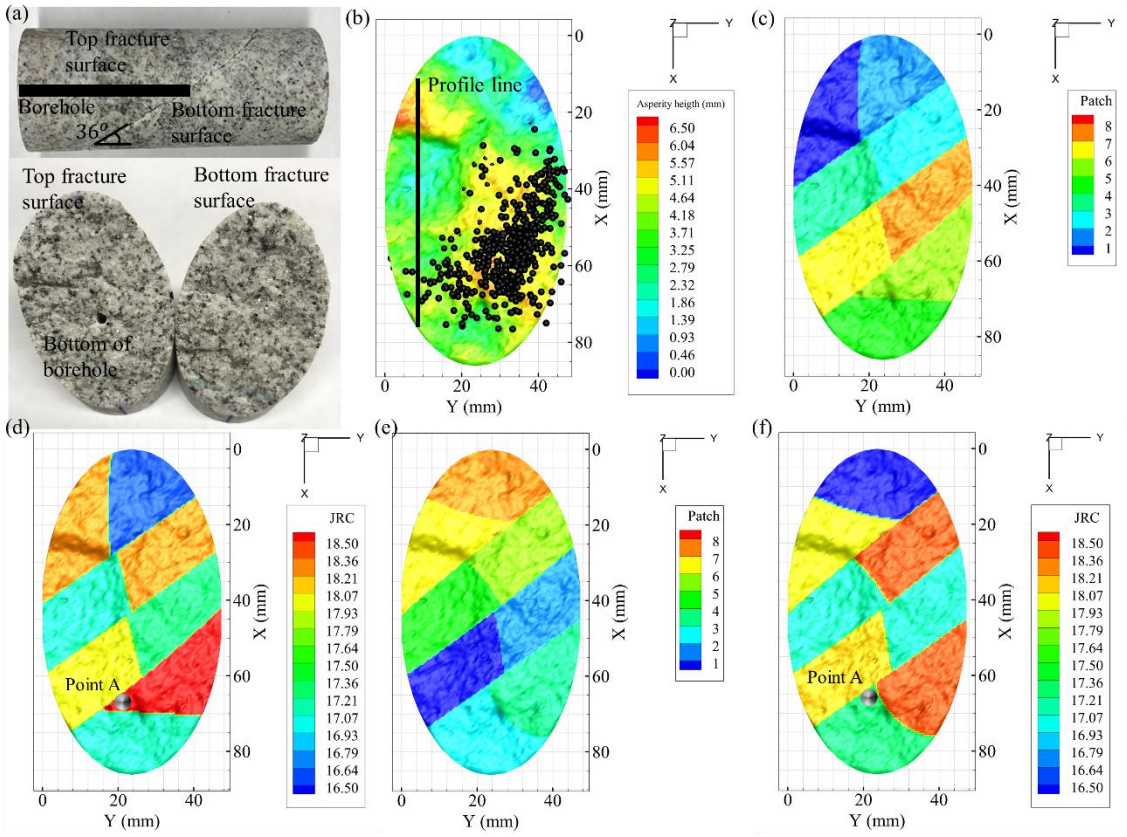

Figure 6.1 The geometry and partition of fracture surface. (a) the geometry of rock sample. (b) profile line, fracture asperity height and black sphere represent the seismic events from the lab test (Ye and Ghassemi 2020). (c) and (d) is one of partition of fracture and JRC, respectively. The JRC at point A is 18.5. (e) and (f) is another partition of fracture and JRC, respectively. The JRC at point A is 17.2.

There are a variety of roughness measurements (e.g., maximum height, autocorrelation length and root mean square gradient), partly because there are many geometric features to describe surface characteristics. The measurements can be categorized into three groups: statistical (e.g., RMS, Z_2, SF, R_p, PSD), fractal (fractal dimension), and

directional roughness methods ($A_0\theta^*_{\max}/(C+1)$) (Magsipoc, Zhao et al. 2020). RMS (root mean square) deviation corresponds to the standard deviation of the height distribution. Z_2 is the RMS of the average local slope. Power spectral density (PSD) represents the amplitude of roughness as a function of the spatial frequency of the roughness. A_0 is the total area fraction facing queried analysis direction which provides a measure of contact area and $\theta^*_{\max}/(C+1)$ is directional roughness metric; The details of roughness parameters can be found in (Magsipoc, Zhao et al. 2020). The roughness in the statistical methods is measured either along a single line profile or along a set of parallel line profiles or area on the surface (Figure 6.1b). The statistical methods are standardized by the International Standardization Organization (ISO).

The fractal dimension suggests the complex nature of surface topography; the degree of variation of a curve/surface from its topological ideal (Mandelbrot 1967, Brown 1987). The obtained values from fractal methods (e.g., roughness-length method, PSD and root-mean-square correlation function) are very sensitive to the methods used in characterizing the fractal. The source of such limitation is from the inaccurate surface measurement or errors in utilizing fractal concept (Kulatilake, Shou et al. 1995).

The directional roughness methods ($A_0\theta^*_{\max}/(C+1)$) are kind of 3D methods to measure the roughness. It starts with the geometry of triangular mesh which are formed by the laser scan points and considers the magnitude of potential contact area. It has is still limited in industry because directional roughness methods are far complex than statistical methods and fractal methods. The directional roughness methods are far complex than statistical methods and fractal methods. The detail of those methods can be checked in the review (Magsipoc, Zhao et al. 2020).

In this work, Z_2, SF and R_p are selected to characterize the roughness because they are standardized by the ISO and have greater relevance to the industry. The Z_2, SF and R_p correspond with roughness slope, degree of change in roughness height and actual length of the profile, respectively (Jang, Kang et al. 2014). It should be notes that Z_2, SF and R_p are measured along a single line profile. Z_2, SF and R_p on a fracture are calculated using the following equations (Jang, Kang et al. 2014):

$$Z_2 == \left[\frac{1}{L}\int_{X=0}^{X=L}\left(\frac{\mathrm{d}Z}{\mathrm{d}X}\right)^2 \mathrm{d}X\right]^{1/2} = \left[\frac{1}{L}\sum_{i=1}^{n-1}\frac{(Z_{i+1}-Z_i)^2}{X_{i+1}-X_i}\right]^{1/2} \quad (6.1)$$

$$\mathrm{SF}=\frac{1}{L}\int_{X=0}^{X=L}[f(X+\mathrm{d}X)-f(X)]^2\mathrm{d}X = \frac{1}{L}\sum_{i=1}^{n-1}(Z_{i+1}-Z_i)^2(X_{i+1}-X_i) \quad (6.2)$$

$$\mathrm{R_p} = \frac{\sum_{i=1}^{n-1}\left[(Z_{i+1}-Z_i)^2+(X_{i+1}-X_i)^2\right]}{L} \quad (6.3)$$

Where Z_i is the height of a single line profile at X_i and L is the length of the line profile; Each row and column of the laser scan points are located on a line profile. The final values of Z_2, SF and R_p of the fracture are the average of the values of Z_2, SF and R_p from all the line profiles. Previous works reported that the Z_2, SF and R_p correlated well with the JRC and have proposed multiple empirical formulas between these variables (Tatone and Grasselli 2010, Jang, Kang et al. 2014):

$$\mathrm{JRC}=51.16\cdot(\mathrm{Z_2})^{0.531}-11.44 \quad (6.4)$$

$$\mathrm{JRC}=121.13\cdot\sqrt{\mathrm{SF}}-3.28 \quad (6.5)$$

$$\mathrm{JRC}=92.07\cdot\sqrt{\mathrm{R_p}-1}-3.28 \quad (6.6)$$

Note that the derivation of Equations 6.4-6.6 is based on the experimental data. The major barriers in surface contact mechanics stems from the multiscale nature of phenomena

occurring during the fracture deformation. This is partly attributed to a larger number of asperities over a wide range of length scales. For example, it is widely recognized that fracture roughness contains a large-scale waviness component and a small-scale unevenness component (International Society for Rock Mechanics 1978). Such multiscale properties of fracture roughness need to be considered during the calculations. Based on the literature review, none of formulas can be applied to measure the multiscale properties of fracture roughness. Current analysis of Z_2, SF and R_p are usually sufficient to measure the entire surface rather than spatial variation of roughness.

In this work, a stochastic graph partition method (Gilbert, Miller et al. 1995) is utilized to partition the meshed fracture surface into multiple patches (i.e., Figure 6.1c or 1e). The details of such graph partition method can be found in (Gilbert, Miller et al. 1995) or Appendix C. After dividing the fracture surface into a number of patches assumed to have a uniform JRC, Z_2, SF and R_p are measured in each patch according to Equation 6.1-6.3. Then JRC of each patch is obtained based on the Equation 6.4-6.6. This provides a local measurement of JRC at every point on the surface and multiscale nature of fracture roughness could be accessed. In the case of a patch, the JRC of a point depends on the geometry of the rest of the points of this patch. This is very important since in previous work consideration of 'surrounding points' at local scale was not reasonably included (Fardin, Stephansson et al. 2001, Tatone and Grasselli 2013). In their works, fracture surface was artificially divided into multiple squares of desired windows sizes. The measurements of local roughness were performed on the points in each square and thus, JRC of a point depend on the geometry of the rest points of this square. Such windowing strategy rarely map the possible range of geometry of surrounding points. In our work, it

is obvious that JRC of a point is different in different runs because of the variation of geometry of surrounding points of this point on a patch as different patching scheme is simulated. Thus, the surrounding points of a point at local scale are stochastically defined. For example, Figure 6.1c/e show two realizations of the partition form in two different runs, respectively. Each realization has eight patches and area of each patch is approximately 405 mm^2 (equivalent length scale is approximately 20 mm). The equivalent length of a patch is defined as the square root of area of a patch. The Z_2 of each patch is measured by Equation 6.1 and JRC of each patch is obtained according to the Equation 6.4. The JRC of point A is 18.5 in the first realization (Figure 6.1d). The JRC of point A is changed from 18.5 to 17.2 in the second realization (Figure 6.1f). This is because the patch contains point A in different runs has a different shape covering an area that is different.

If a vest number of runs (greater than 1000 in this work) are performed to partition the fracture surface at the same equivalent length scale (the same number of patches), each point will have multiple JRC values. It is supposed that the stochastic properties of JRC at each point can be outlined after multiple runs are performed at the same equivalent length scale by fitting the JRC values of each point by a normal distribution. The mean of the normal distribution is then assumed to represent the true JRC of the point. In addition, fracture surfaces exhibit roughness at all scales and Equation 6.1-6.3 (Equation 6.4-6.6) are not designed to measure the multiscale roughness. Those formulas measure the roughness over different length scales according to average strategy. Figure 6.2a shows the JRC at point B with coordinate $[X, Y] = [65.12\ \mathrm{mm}, 25.12\ \mathrm{mm}]$ are measured over a wide range of equivalent length scales (57~ 5 mm, 1~128 patches) after 1000 runs

are performed. The JRC are calculated by the Z_2, SF and R_p through the Equation 6.4-6.6. Those calculations may show multiscale nature of the fracture roughness. As the equivalent length scale decreases (or the number of patches increases), the JRC value at point B derived from Equation 6.4-6.6 decrease by ~12% and the multiscale effects of roughness are not pronounced in this case. The length of error bars is very small and slightly increases when the equivalent length decreases from 57 mm to 5 mm (1 to 128 patches). The error bar represents the variation in JRC values after 1000 runs are performed. The multiscale nature of fracture roughness leads to the variation of JRC over the length scales (number of patches). It seems that the Equation 6.4-6.6 both captures the trend of roughness over the length scales. The histogram in Figure 6.2a shows the distribution of JRC (based on Equation 6.4) at point B after 1000 runs over the length scale (5 mm, 128 patches). The normal distribution curve show that the mean is 15.7 and std is 2.0. The std is relatively small and it suggests that our method can effectively capture the true JRC at point B at the equivalent length scale of 5 mm.

The results from Figure 6.2a demonstrate the effectiveness of our method to determine the JRC at different length scale because the JRC values of points after 1000 runs can be well fitted by a stochastic distribution (normal distribution). The focus of this dissertation is not the effects of the multiscale nature of roughness on seismicity. The roughness measurements are performed at equivalent length of 5 mm and are assumed to cover the mechanical properties of interest. Further, equivalent length is only 5 mm which is much smaller than the nucleation length (24.2 mm in this case which is defined by Equation 6.9). Figure 6.2b shows the distribution of JRC (mean of normal distribution) after 1000 runs are performed according to Equation 6.4 at the equivalent length scale of 5 mm.

Figure 6.2c is the distribution std (std of normal distribution). Each point on the fracture has a JRC and the std is relatively small. The local zones with high asperity height have large JRC which match the observations from visual inspection. It suggests that our method can map the spatial variation of fracture roughness and spatial distribution of JRC at equivalent length of 5 mm. Figure 6.2d is the relation between distribution of seismic events from lab test (Ye and Ghassemi 2020) and spatial distribution of JRC. It seems that most events are located over the smoother zone of fracture (lower JRC).

Fracture shear stiffness can be experimentally measured but and the spatial variability of fracture shear stiffness has not been investigated well. Some experiments tried to map the spatial distribution of fracture shear stiffness by acoustic methods (Acosta-Colon, Pyrak-Nolte et al. 2009). The transmission of P- and S- waves (of each sensor pair-source and receiver) across a fracture were recorded and fracture shear stiffness can be determined from seismic wave attenuation and velocity. Although, the fracture shear stiffness of the zones under sensors are mapped, it still demonstrates that fracture shear stiffness spatially changes across the fractures. It is found that local fracture roughness influences the magnitude of the local shear stiffness (Choi 2013). In this work, the spatial distribution of JRC are determined (Figure 6.2b) and it reflect the distribution of local fracture roughness. Thus, the spatial distribution of fracture shear stiffness can be derived from the spatial distribution of JRC.

For most practical purposes, fracture shear stiffness K_s can be estimated by $\Delta\tau/d$ where $\Delta\tau$ is the shear stress change and d is the shear displacement (Mclaskey and Yamashita 2017). Note that this calculation includes the contribution of stiffness of loading machine.

Empirical Equation 6.7 from JRC-JCS strength model is adequate as a basis for calculating the fracture shear stiffness (Barton and Choubey 1977):

$$K_s = \frac{\Delta\tau}{d} = \frac{100}{L} \cdot \sigma_n \tan\left[JRC\ \log_{10}\left(\frac{JCS}{\sigma_n}\right) + \phi_r\right] \tag{6.7}$$

Where L is the equivalent length; σ_n is the effective normal stress and is fixed at 44 MPa based on the our experiment data (Ye and Ghassemi 2020); JCS is compressive strength of the fracture surface and ϕ_r is the residual friction angle. In this case, $\Delta\tau$ is the shear stress change from initial state to peak shear strength state and d is the peak shear displacement of rock fracture. The parameters in Equation 6.7 are fixed at $JCS = 173$MPa and $\phi_r = 30^o$C which generally typify granite surface (Grasselli and Egger 2003). Figure 6.3a shows the distribution of fracture shear stiffness K_s and local zones with high JRC value have large fracture shear stiffness. A critical velocity is defined as (Im, Marone et al. 2019):

$$V_c = \sqrt{\frac{\sigma_n a D_c}{M}\left(\frac{K_s D_c}{(b-a)\sigma_n} - 1\right)} \tag{6.8}$$

where a, b and D_c are the rate state friction law parameters; RSF parameters are set at $a = 0.004$, $b = 0.006$ and $D_c = 0.15$ μm which analog the values from (Im, Marone et al. 2019). M is mass per unit area at facture depth ($\mathrm{kg/m^2}$); In this case, M can be approximately defined as $\rho \cdot \pi \cdot r^2 \cdot h/(\pi \cdot r^2) = 1.8 \times 10^7$ ($\mathrm{kg/m^2}$) where $\rho = 2800\ \mathrm{kg/m^3}$ is the density of granite and r is the half of equivalent length and $h = 6300$ m is the depth of fracture which derived from laboratory settings (the magnitude of axis load) (Ye and Ghassemi 2020). Lab work suggest that the critical velocity is 19 $\mu\mathrm{m/s}$, therefore, the critical JRC is 16.5 according to Equation 6.7-6.8 so that, if the

JRC of the point is less than 16.5 and the friction of this point will be eventually unstable at the loading velocity (critical velocity). Conversely, if the JRC of this point is large than 16.5, the friction of this point will be eventually stabilized at the loading velocity (critical velocity). Thus, the unstable laser scan points form clusters and there are six clusters in Figure 6.3b. While the rest of the points (blue color in Figure 6.3b) are stable. The unstable length in Figure 6.3b is defined as the square root of the area of each cluster. The unstable length of zero represent those points that are stabilized during the fracture slip. Seismic events occur on the unstable clusters when the unstable length of this cluster is larger than the nucleation length. The nucleation length h^* is defined as (Harbord, Nielsen et al. 2017):

$$h^* = C\frac{GD_c}{\sigma_n(b-a)} = 24.2 \text{ mm} \tag{6.9}$$

Where C is the dimensionless shape factor (Rubin and Ampuero 2005) and is assumed as 0.56, $G = 25.4$ GPa is the shear modulus according to the lab data (Ye and Ghassemi 2020); In this case, seismicity occur on one unstable clusters because its unstable length is larger than h^* and the unstable length is 24.2 mm (Figure 6.3c). The AE events from the laboratory are also plotted in Figure 6.3c; it seems that most events are located in the seismicity zone (green zone in Figure 6.3c) which is the relatively smoother (lower JRC) portions of the fracture (Figure 6.2d). We claim that seismic slip on this zone (green zone in Figure 6.3c) set in motion the process of AE generation. In contrast, slip on the rougher portions of fracture may results in large area of newly created surface and fracture energy would be very high but the radiated seismic energy may be low from energy conservation perspective. This case study shows that our simulation results match the lab data and the modeling framework can capture the slip pattern of realist fracturs.

6.2 Model Verification

In order to verify the numerical approach and the model calculation, the spring slider model is simulated to check the effects of JRC on the instability of laser scan points under the same lab observed loading velocity (Ye and Ghassemi 2020). Each laser scan point is considered as a spring slider with the same rate and state friction law (RSF). The RSF parameters are defined in previous calculations and are homogenous over the fracture plane. The mechanical interaction between each laser scan points are ignored. Note that spring slider model can only be applied conceptually to nature and can span the full inertial spectrum from stable sliding to unstable motion. Previous works (Im, Marone et al. 2019) established the spring slider model to mimic earthquake occurrence and mechanisms realistically. In a one-dimensional spring-slider system, the Newtonian force balance governing motion is defined as:

$$M\ddot{u} = K_s(u_{lp} - u) - \mu\sigma_n \tag{6.10}$$

Where u_{lp} is the displacement of a load point, u is the displacement of the slider and μ is the friction coefficient; The evolution law of the state variable θ is defined as:

$$\frac{\mathrm{d}\theta}{\mathrm{d}t} = 1 - \frac{V\theta}{D_c} \tag{6.11}$$

Where θ is the state variable and V is slip velocity; Rate and state friction law is defined as:

$$\mu = \mu_0 + a\ln\left(\frac{V}{V_0}\right) + b\ln\frac{V_0\theta}{D_c} \tag{6.12}$$

Where μ_0 is a reference friction coefficient which defined at reference slip velocity V_0; The stick slip motion on each laser scan points can be captured by Equation 6.10~6.12. The numerical details can be found in (Im, Marone et al. 2019) or Appendix F. Two

simulations are performed but the loading velocity are both 20 $\mu m/s$ which slightly larger than critical velocity (19 $\mu m/s$). The numerical simulation time is 10 seconds which is obtained from the Lab test (Ye and Ghassemi 2020). Other parameters (e.g., RSF) are all the same. Therefore, the effects of JRC on velocity and friction evolution over time and displacement are checked. The velocity, displacement and friction coefficient from the simulations are shown in Figure 6.3e and 6.3f. In the first simulation, Figure 6.3e shows that the velocity variation of point (with JRC=16.5) as the displacement is increased. In addition, the variation of the friction coefficient of point (with JRC=16.5) is shown with time (Figure 6.3f). Therefore, the point (JRC=16.5) is in unstable state (oscillating states) in the first simulation which match our previous calculation. In the second simulation, Figure 6.3e shows that the velocity of point (with JRC=20.0) becomes eventually constant with increasing the displacement. In addition, the friction coefficient of point (with JRC=20.0) becomes constant with increasing the time (Figure 6.3f). Therefore, the point with JRC=20.0 is in a stable state in the second simulation which matches our previous calculation. It can be concluded that numerical results from these two simulations match our previous calculations so that the calculations are verified using the spring-slider model. In previous works, fracture shear stiffness in spring-slider model are artificially defined (Im, Marone et al. 2019). Fracture shear stiffness were derived by shear stress-shear displacement curve in lab tests (Mclaskey and Yamashita 2017) or simple plane strain analysis (Tal, Goebel et al. 2020). To the author's knowledge, none of these works can give the spatial distribution of fracture shear stiffness on fracture.

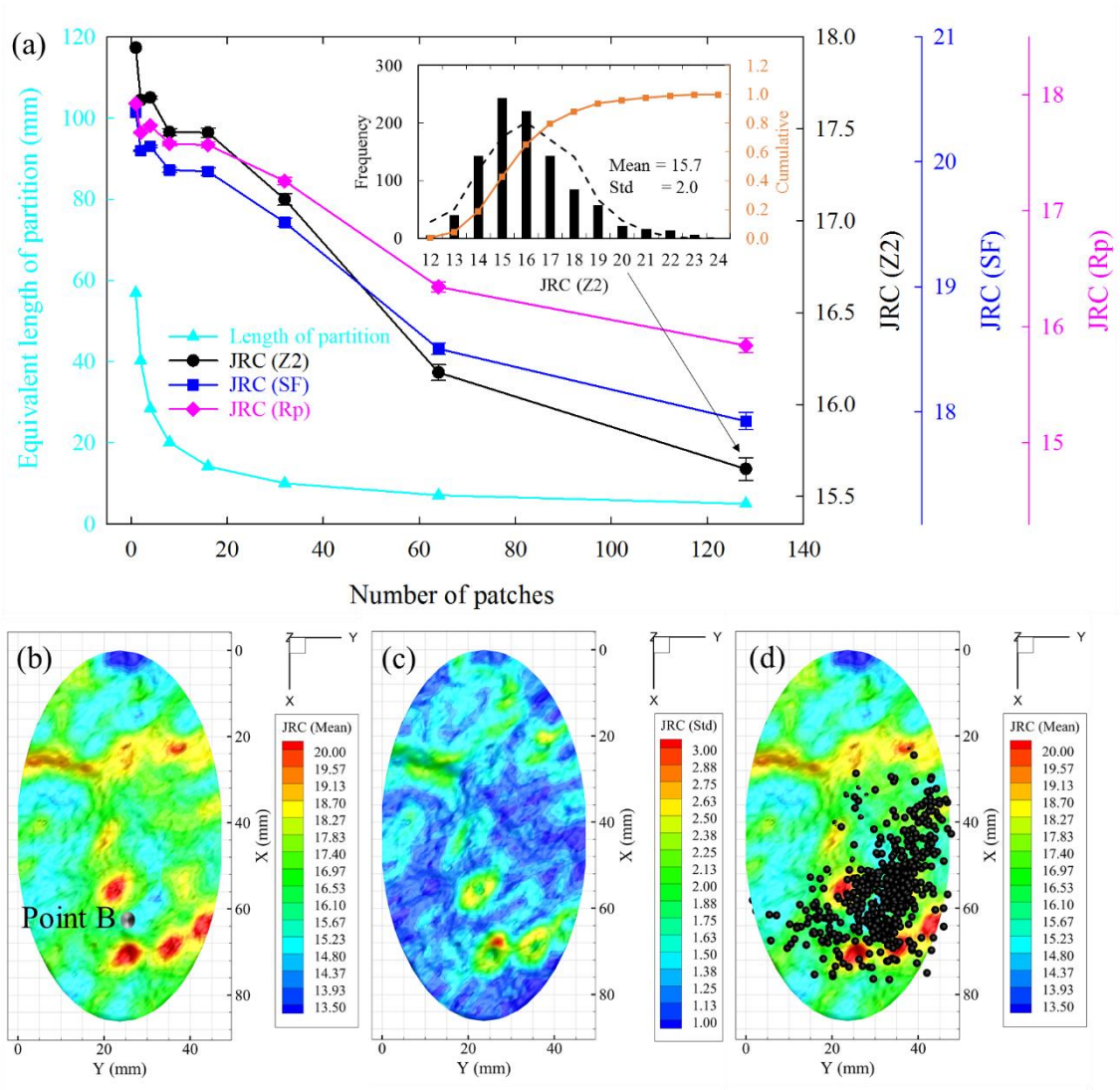

Figure 6.2 The spatial distribution of JRC. (a) JRC are measured by Z_2, SF and R_p over a wide range of equivalent length scale (5 mm ~ 57 mm). The JRC from all the runs is fitted by a normal distribution (inserted histogram). The mean of this normal distribution is considered as the true JRC at this point. (b) the spatial distribution of JRC at equivalent length scale (5mm). (c) the spatial variation of std of normal distribution at equivalent length scale (5mm). (d) The relation between spatial distribution of JRC and seismic events from the lab test (Ye and Ghassemi 2020). Most events are located in the smoother zone (low JRC).

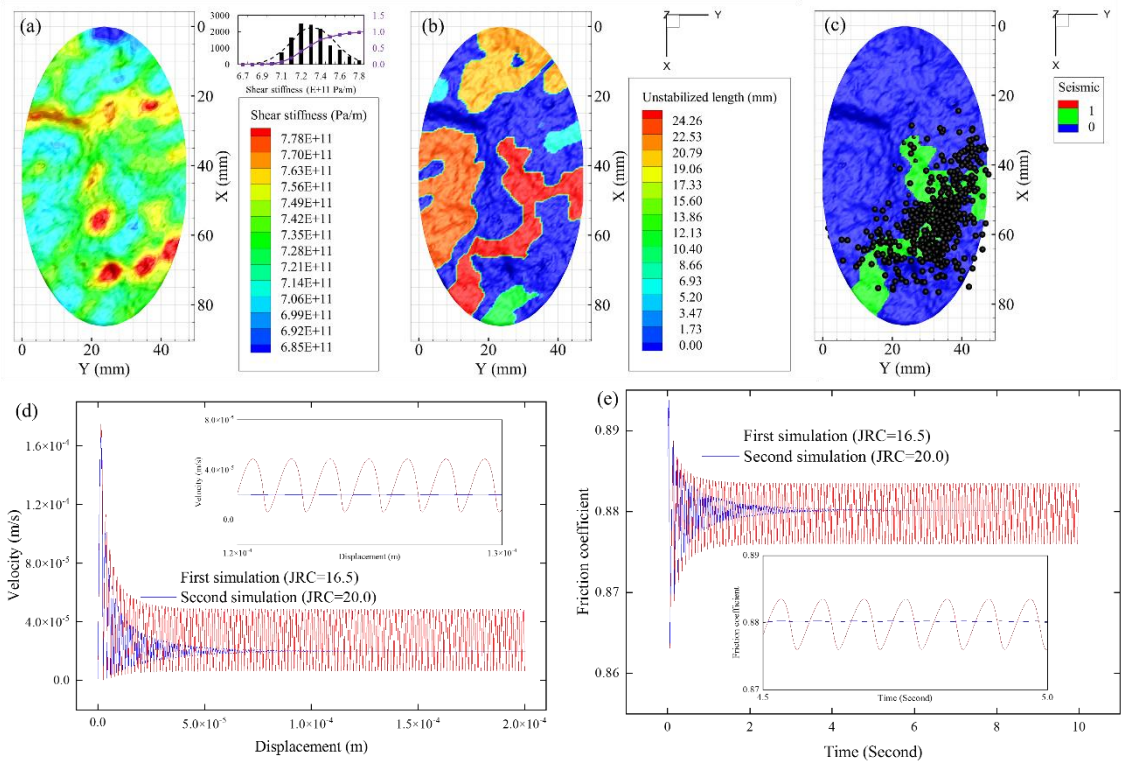

Figure 6.3 The seismicity pattern on fracture surface. (a) the fracture shear stiffness at equivalent length scale (5 mm). The inset plot indicates the distribution of shear stiffness. (b) the distribution of unstabilized clusters on fracture surface. Stable zone (blue) and unstable zone (every color except for blue). (c) seismic pattern on fracture surface and black sphere represents the events from lab test (Ye and Ghassemi 2020). Seismic (green) and aseismic (blue). (d) and (e) are the evolution of friction coefficient and slip velocity of two points. The JRC of those two points are 16.5 and 20, respectively.

6.3 The Effects of Loading Rate on Moment Magnitude and Seismicity Patterns

In Chapter 6.2, the effects of fracture roughness on seismicity pattern have been investigated. The loading rate (m/s) in Chapter 6.2 was kept constant. While the loading rate can significantly affect seismicity (Mclaskey and Yamashita 2017). In this section, the effects of loading rate on the distribution of aseismic and seismic slip on fracture and moment magnitude of seismic event at different nucleation lengths will be investigated and other settings are the same as in the Chapter 6.2. The seismic slip displacement D is 0.63 mm which can be derived from our lab test (Ye and Ghassemi 2020). The seismic

moment can be calculated as $M_w = G \cdot D \cdot A$. A is the source area (seismic area) and G is shear modulus; Three simulation tests are performed to investigate the effects of loading rate on moment magnitude of seismic event and the distribution of aseismic and seismic slip on fracture with different nucleation lengths. The nucleation length in the first, second and third simulation are 0.000 m, 0.008 m and 0.015 m, respectively.

The loading rate in those three simulations is increased from 1.40×10^{-5} m/s to 2.69×10^{-5} m/s. The processes of simulation follow three steps. In the first step, the critical velocity of every points (laser scan points) on fracture surface is calculated according to Equation 6.7 and 6.8. If the loading velocity is larger than the critical velocity of points, those points are in an unstable state. In the second step, the distribution of unstable clusters on the fracture surface is reconstructed. In the third step, if the length of unstable clusters is larger than nucleation length, those clusters (patches) are considered as seismic patches. Figure 6.4a shows the moment magnitude is increase as the loading rate increase under different nucleation length. As the loading rate increases, the seismic area also increases. therefore, the magnitude also increases. When the loading rate is less than 1.53×10^{-5} m/s, seismicity does not occur on the fracture in any of the three simulations because the fracture shear stiffness is larger than the critical stiffness. In the first simulation, seismicity would occur on the fracture when the loading rate reaches 1.56×10^{-5} m/s. In the second simulations, seismicity will occur on the fracture when the loading rate reach 1.70×10^{-5} m/s. In the third simulations, seismicity will occur on the fracture when the loading rate reaches 1.80×10^{-5} m/s. If the loading rate continues to increase, the moment magnitude in three simulations increase rapidly until the loading rate reach 2.37×10^{-5} m/s because the entire fracture surface is in seismic state. Figure 6.4b/c/d shows the seismic

areas (distribution) at different loading late in the second simulations. Figure 6.4b shows the loading late is $1.72x10^{-5}$ m/s and seismic area is 82.40 mm^2. Figure 6.4c shows the loading rate is 1.78x10-5 m/s and seismic area is 311.48 mm^2. Figure 6.4d shows the loading late is $1.91x10^{-5}$ m/s and seismic area is 1827.20 mm^2. The topological evolution of seismic patches under the increasing loading rate may reflect the transition from aseismic to seismic phase on fracture surface.

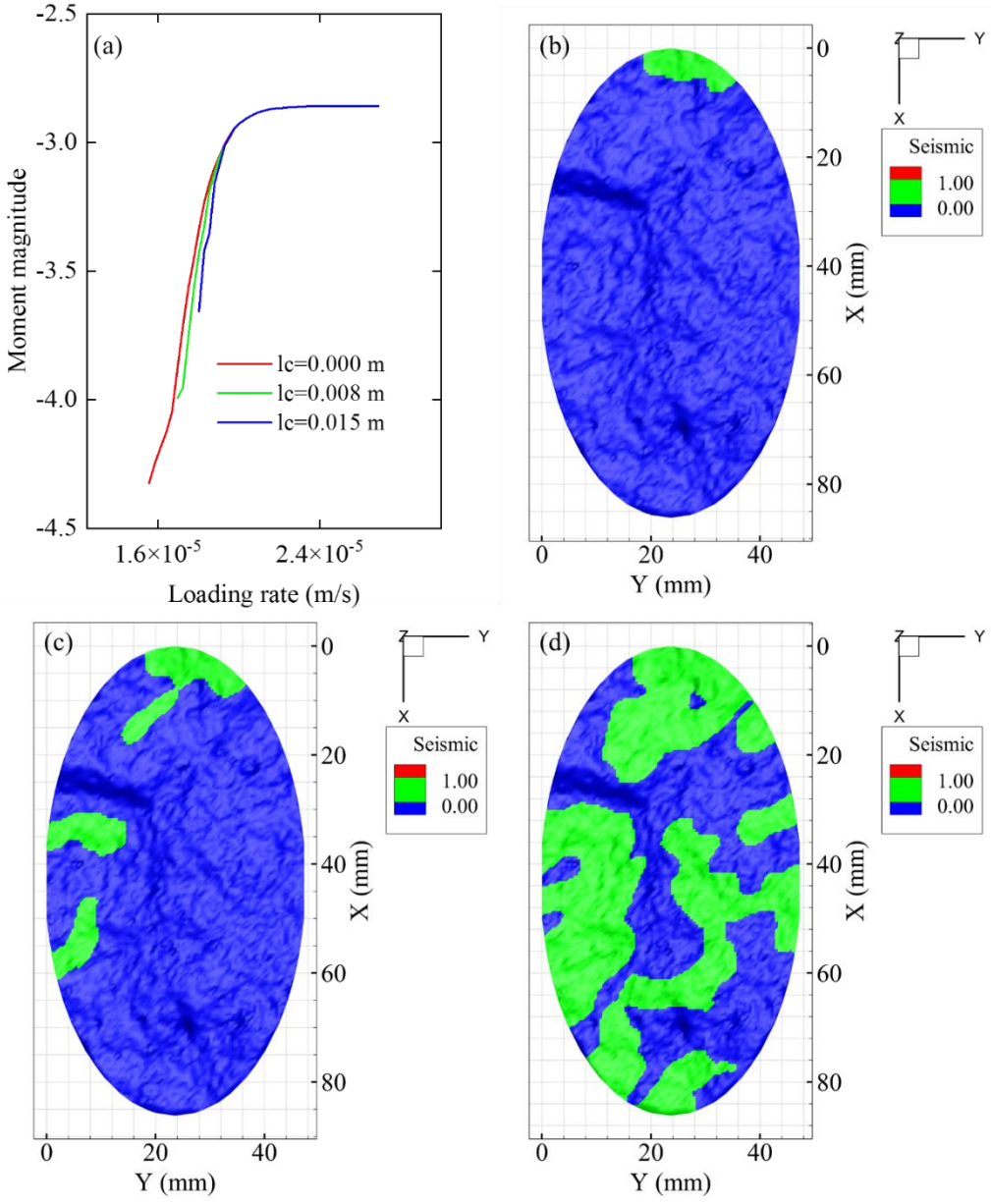

Figure 6.4 Three simulations are performed while the nucleation length are 0.000 m, 0.008 m and 0.015 m, respectively. The other settings are all the same. (a) the moment magnitude is increased as the loading velocity is increased. (b), (c) and (d) are shown the seismic pattern under loading velocity 1.72×10^{-5} m/s, 1.78×10^{-5} m/s and 1.91×10^{-5} m/s in test 2, respectively. Seismic slip (green) and aseismic slip (blue). The seismic area in (b), (c) and (d) are 82.40 mm^2, 311.48 mm^2 and 1827.20 mm^2, respectively.

6.4 Conclusions

By setting the stochastic partition on laser scan points and mass spring model, the effects of fracture roughness on seismicity has been investigated. Our previous laboratory injection test is conceptually simulated, and the simulated seismicity generally matches laboratory observations. Previous methods only cover the fracture roughness over the entire surface rather than the spatial distribution of fracture roughness. This limitation is relieved here by applying a stochastic partition on the laser scan points and relating the roughness to JRC. Each laser scan points have a JRC based on the patch it falls on. Further, an empirical formula is employed to link the JRC with fracture shear stiffness. Spring slider model is implemented to study the effects of JRC on the instability of laser scan points on a fracture surface. Such framework is applied to a current laboratory test and the simulated seismicity generally matches the lab observation. The simulated results show that the lower JRC (roughness), the higher opportunity seismicity occurs on fracture when the length of unstable zone is larger than nucleation length. Finally, the effects of loading rate on seismic pattern are also investigated with different nucleation length. It indicates that the lower nucleation length, the seismicity occur on fracture is earlier. But the nucleation length cannot affect the moment magnitude if the loading rate is large enough.

Chapter 7 Application to Utah FORGE

7.1 Introduction

Chapter 5 propose a fractured network model which include the effects of fracture roughness on fracture deformation and stress shadow caused by fracture pressurization. Specifically, the stress shadow caused by fracture pressurization is described by Eshelby solution. The JRC of lab rock fracture is determined by the proposed JRC-Hurst exponent relation. The linear Barton-Bandis model is employed to characterize the stability of fracture in this fracture network model. In this Chapter, such fracture network model is applied to the Utah FORGE to identify the best potential well trajectories in terms of the potential SRV.

The optimal well trajectories are assumed to correspond to the maximum SRV. The Utah FORGE (Frontier Observatory for Research in Geothermal Energy) is the testbed for enhancing the EGS technologies that significantly accelerate renewable energy production. The Utah FORGE site is located 322 km south of Salt Lake City and 16 km north-northeast of Milford, Utah, the area of this site is about 5 km^2 (Figure 7.1a/b). Utah FORGE reservoir consists of crystalline (granitic) rocks of > 1 km^3, with temperature ranging from 175^o C to 225^o C at the depth of 1.5-4 km (Simmons, Kirby et al. 2019, Moore, McLennan et al. 2020). The geothermal gradients of Utah FORGE site at shallow (~<500 m) is 200^oC/km and 70^oC/km at depth (~>1500 m) (Allis, Gwynn et al. 2018) (Figure 7.2). The granitoid typically includes all plutonic rocks, ranging from diorite to granite. Utah FORGE site have four faults and faults system that are detected by geological survey, seismic migration and logs (Simmons, Kirby et al. 2019). They are Mineral Mountains West fault system, Opal Mound and Negro Mag faults and unnamed

fault. While Opal Mound and Negro Mag faults are the primary faults in this region (Figure 7.1c/d). The opal mound fault act as a hydraulic barrier separating the Roosevelt Hot Springs geothermal system from the low permeability thermal region. The subsurface structures of Utah FORGE site are shown in Figure 7.1c/d. Note the Utah FORGE EGS reservoir is located between 175^{o} and 225^{o} isothermal surface

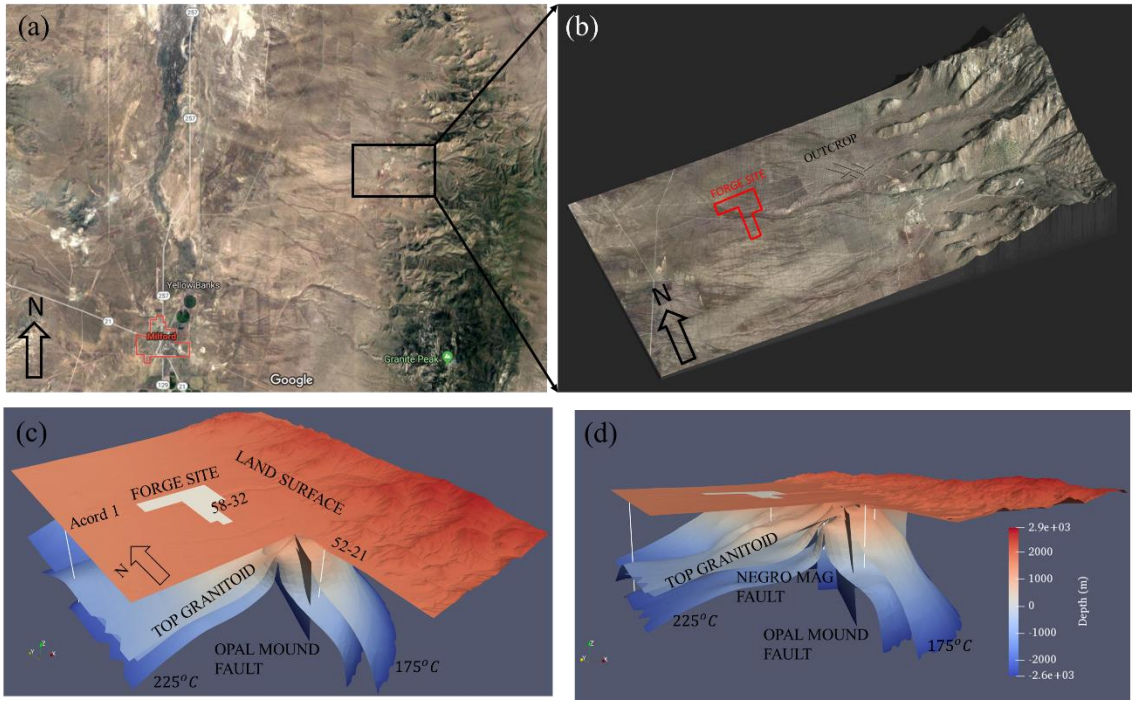

Figure 7.1 The location of geological map of Utah FORGE SITE. (a) and (b) Land surface in the region surrounding the Utah FORGE site. (c) and (d) Geological map of the Utah FORGE site. Opal mound and Negro mag fault are the primary faults in this region. The contour represents the depth.

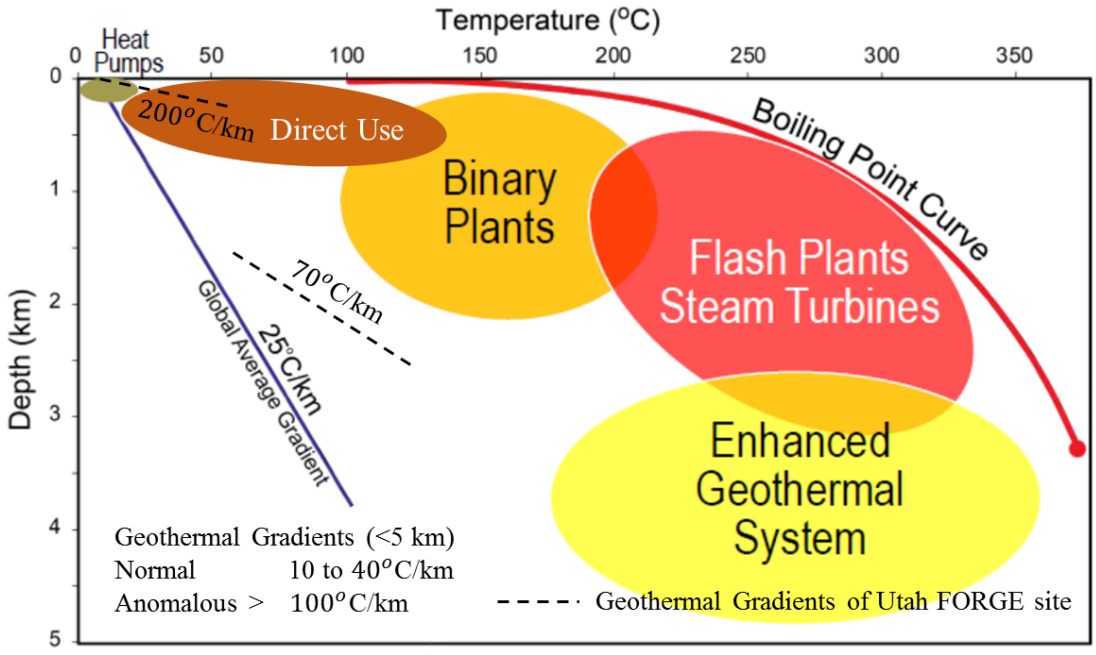

Figure 7.2 Temperature distribution at depths for different application. Geothermal gradient of Utah FORGE site is 200° C/km at shallow and 70° C/km at depth (Adapted from Moore and Simmons 2013).

During Phase 2b of the Utah FORGE project, well 58-32 was drilled, completed and stimulated to measure reservoir properties, including temperature, fracture, rock type, permeability and in-situ stress at depths. The vertical stress gradient is found from the density log while both minimum and maximum horizontal stress gradient were obtained by microhydraulic fracturing and DFIT (Moore, McLennan et al. 2020). The orientation of horizontal stress is measured by FMI log. Figure 7.3 shows the distribution of in-situ stress, pore pressure in Utah FORGE site. Utah FORGE team generated the discrete fracture network in a stochastic manner according to the observation of outcrop and fracture data measured by the FMI in well 58-32 (Finnila, Forbes et al. 2019, Nadimi, Forbes et al. 2020).

The number of discrete fractures is 6184 and fracture radius is ranged from 80 m to 150 m. Thus, such discrete fracture network is assumed to be a good representation of the fracture network in Utah FORGE site.

In this work, a sample from the core extracted from the well 58-32 (at 7443.78 ft depth) is used to measure the fracture roughness (Figure 7.4a). This core is split in tension, and its roughness is then evaluated. Fracture roughness (with length is ~0.06 m) rarely display anisotropic properties by visual estimation in Figure 7.4b, thus, fracture is regarded as isotropic. The Hurst exponent is 0.61 obtained by performing a PSD analysis on the real fracture surface (Figure 7.4c). Note that the slope of PSD in Figure 7.4c is much easier to calculate than the slope of PSD in the Figure 5.3b because a radially averaged technique is employed for PSD analysis on fracture surface. Here, 'radially averaged' means that power spectrum for equal lengths of the wavevector are averaged over a length from the fracture center (Maus and Dimri 1996). The JRC_0 is 14.6 at the scale of (~0.06 m) according to the Equation 5.5. Further, the JRC of the fracture network at centimeter scale (JRC_0) are assumed to follow the lognormal distribution with a mean 14.6 and std of 1. In addition, the JCS of the fracture network at centimeter scale (JCS_0) are assumed to follow the lognormal distribution with mean 173 MPa and std 10 MPa which are from the lab test data (Asadollahi 2009). Residual angle ϕ_r is also followed the lognormal distribution with mean 27^o and std 1^o which are also from the lab test data (Asadollahi 2009). The JRC and JCS of large-scale fracture (i.e., 100 m) are rarely measured because field fracture roughness is limited and laboratory direct shear test for large scale fracture is neither feasible nor possible.

The scaling law should be applied for identifying the realist fracture JRC_n and JCS_n because both JRC and JCS are scale dependent parameters. Barton and Bandis proposed a widely used scaling law:

$$\mathrm{JRC}_n = \mathrm{JRC}_0 \left(\frac{L_n}{L_0}\right)^{-0.02\mathrm{JRC}_0} \tag{7.1}$$

$$\mathrm{JCS}_n = \mathrm{JCS}_0 \left(\frac{L_n}{L_0}\right)^{-0.03\mathrm{JRC}_0} \tag{7.2}$$

Where JRC_n is the JRC value of fracture at length scale L_n. JRC_0 is the JRC value of fracture at length scale L_0 (~0.01 m). The generalized scaling law for JRC and JCS can be expressed as follow (Du, Gao et al. 2015)

$$\mathrm{JRC}_n = \mathrm{JRC}_0 \left(\frac{L_n}{L_0}\right)^{-D_{JRC}} \quad \text{and} \quad \mathrm{JCS}_0 \left(\frac{L_n}{L_0}\right)^{-D_{JCS}} \tag{7.3}$$

D_{JRC} is the fractal dimension of JRC scale effect, which is defined the velocity rate of JRC_n decreases as increasing L_n . The concept of D_{JCS} is defined in the same manner as D_{JRC}. The D_{JCS} is $1.5D_{JRC}$ according to the Equation 7.1 and 7.2. The processes of generally deriving D_{JRC} follow four steps: (1) synthetic a large scale fracture (~100 m) based on H_x, H_y and RMS. The details of synthetic surface can be found in section 5.1. (2) perform the measurement of JRC_0 at length scale $L_0 = 0.1$ m. (3) perform the measurement of JRC_n at different length scale (i.e., L_n = 0.15 m, 0.5 m,1 m,10 m,100 m). (4) the fractal dimension D_{JRC} can be defined as (Du, Gao et al. 2015)

$$D_{JRC} = \frac{\lg(\mathrm{JRC}_n/\mathrm{JRC}_0)}{1-\lg(L_n)} \tag{7.4}$$

In this work, D_{JRC} is assumed as 0.292 which is an analogy to the lab test data from (Du, Gao et al. 2015).

In phase 3, an injection well will be developed and used for EGS research. The Utah FORGE team provided three potential wells and required us to determine which well is the best for injection. Those three potential wells 3-1a, 3-1b and 3-1c are shown in Figure 7.3. Both three wells have 60 m open hole from the toe. Thus, the injection occurs on the open hole section. In this work, numerical simulation is performed to test the injection of each well. The injection rate is 20 BPM and injection time is 6900 seconds. Reservoir properties in numerical model are shown in Table 7.1. The pressure of fracture 806, 361 and 1520 are monitored during the simulation when the injection occurs on wells 3-1a, 3-1b and 3-1c, respectively.

7.2 Numerical Simulation for Optimizing Wellbore Trajectories

Figure 7.5a shows the evolution of MEQs during the numerical simulation. The number of MEQs increases as the injection continues and the number of MEQs still increases when the injection is stopped at 6900 seconds. This is because pressure continues to propagate even if the injection is shut down. Thus, fracture network continues to be stimulated. Both injection of well 3-1a, 3-1b and 3-1c are generated the largest number of MEQs at 7200 seconds. For example, the maximum number of MEQs for well 3-1a injection is 2058, for well 3-1b injection is 2260 and for well 3-1c injection is 3401. While the number of MEQs at 6900 seconds is 1991, 2179, and 3358, for well 3-1a, well 3-1b, and well 3-1c, respectively (Figure 7.5c). The increases in MEQs due to shut in is not large because the fracture network is fully connected, and the increased pressure can easily diffuse into other fractures. The magnitude distribution of MEQs can be found in Figure 7.10.

Table 7.1 Reservoir properties are used in numerical model

Parameter value	**Values**	**Source/Comments**
Young's Modulus	61 GPa	OU lab test
Drained Poisson's Ratio	0.26	OU lab test
Undrained Poisson's Ratio	0.35	Assume
Biot's coefficient	0.5	Assumed
Porosity	0.005	OU lab test
Initial pore pressure	22.0 MPa	Field observation
Matrix permeability	0.001 mD	OU lab test
Vertical stress, σ_V	25.5 KPa/m	Density log
Maximum horizontal stress, σ_{Hmax}	13.1-14.2 KPa/m	FMI data. Orientation: Trend - 30^o Plunge - 2^o
Minimum horizontal stress, σ_{hmin}	15.6-18.3 KPa/m	FMI data. Orientation: Trend - 120^o Plunge - 2^o
Vertical stress at toe, σ_V	58.0 MPa	Stress in east and north direction are obtained by rotating maximum and minimum horizontal stress.
horizontal stress in east (X-axis) direction at toe, σ_x	36.8 MPa	
horizontal stress in North (Y-axis) direction at toe, σ_x	38.8 MPa	
Fracture asperity (Lognormal)	$\mu = 1 \cdot 10^{-4}$ m, $s = 10^{-8}$ m	Assumed
Cohesion (Lognormal)	0 MPa	Assumed
JRC_0 at scale (~0.06 m) (Lognormal)	$\mu = 14.6$, $std = 1$	OU lab test
JCS_0 at scale (~0.06 m) (Lognormal)	$\mu = 173$ MPa , $std =$ 10 MPa	JCS_0 is analogy to the JCS of typical granite.
Mode I fracture toughness	1.5 MP$\sqrt{\text{m}}$	OU lab test

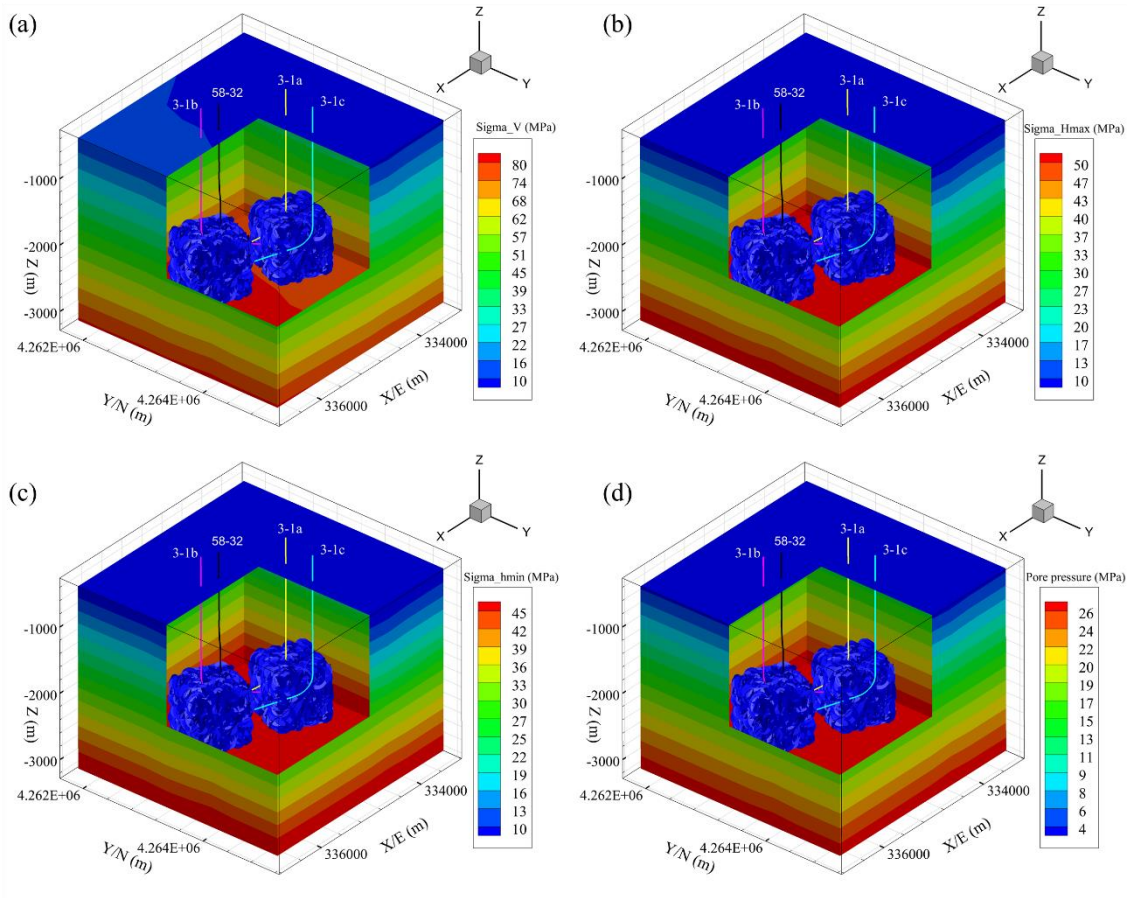

Figure 7.3 Reservoir properties of Utah FORGE site. (a) in-situ stress in vertical direction. (b) and (c) are the σ_{HMAX} and σ_{hmin} , respectively. (d) the distribution of pore pressure. Well 58-32 is the test well. Discrete fracture network is calibrated by Utah FORGE team. 3-1a, 3-1b and 3-1c are the potential well trajectories.

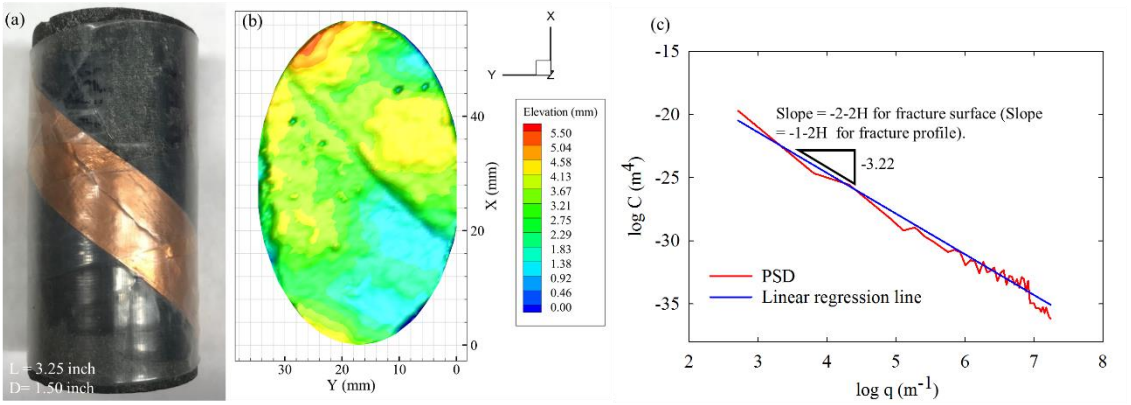

Figure 7.4 Fracture roughness. (a) core from well 58-32 (at 7443.78 ft). the length of core is 3.25 inch and diameter are 1.5 inch. (b) fracture elevation. (c) the PSD analysis on fracture surface.

Thus, Hurst exponent H is 0.61 and $H_x = H_y = 0.61$ because fracture surface rarely shows the anisotropic properties by visual inspection.

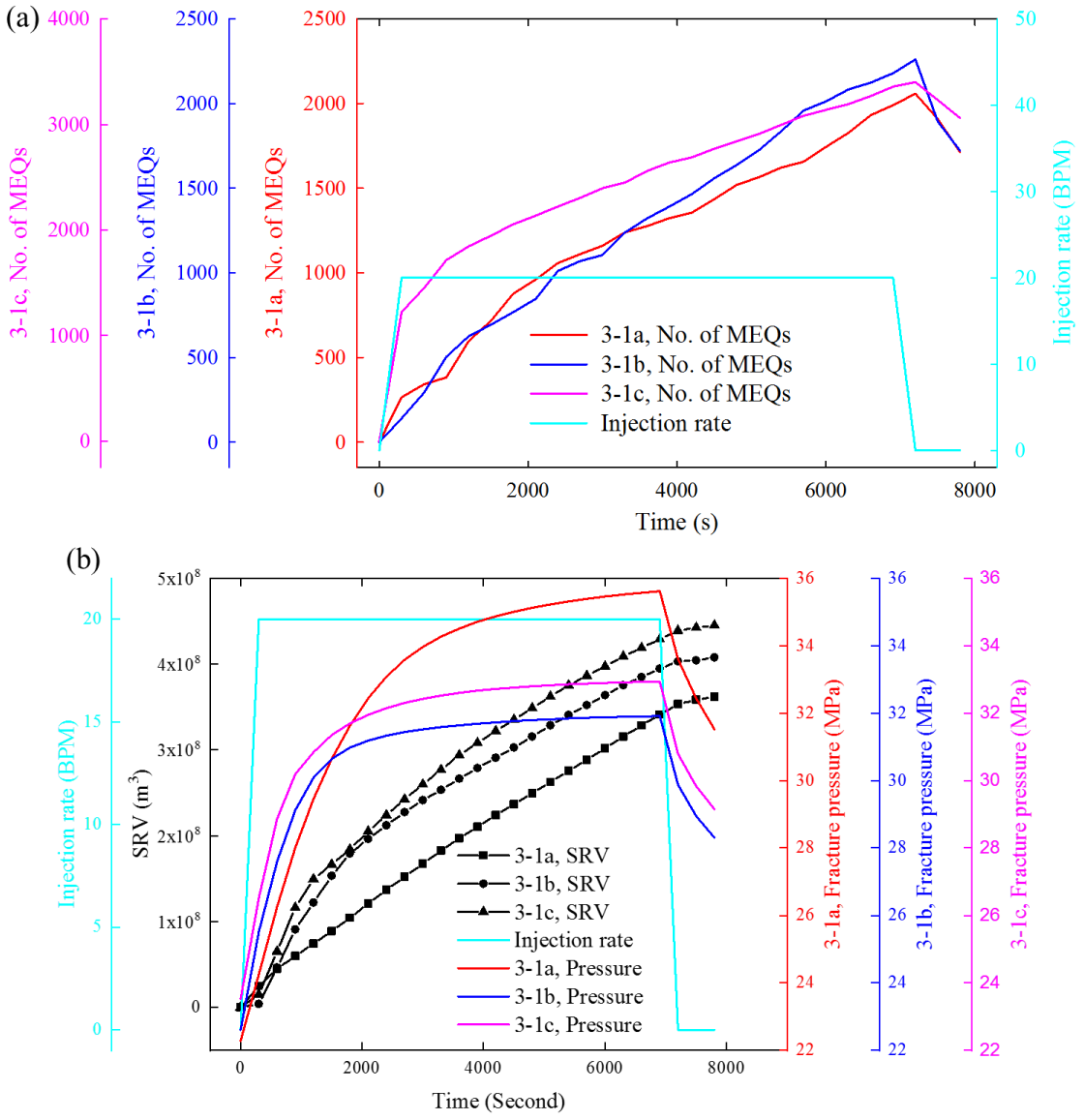

Figure 7.5 The evolution of MEQs, pressure and SRV during the numerical simulation for well 3-1a, 3-1b and 3-1c. (a) injection rate (cyan), the temporal evolution of MEQs for 3-1a (red), the temporal evolution of MEQs for 3-1b (blue), the temporal evolution of MEQs for 3-1c (pink). (b) injection rate (cyan), the temporal evolution of pressure (fracture 806) for 3-1a (red), the temporal evolution of pressure (fracture 361) for 3-1b (blue), the temporal evolution of pressure (fracture 1520) for 3-1c (pink). the temporal evolution of SRV for 3-1a (square-line), the temporal evolution of SRV for 3-1b (sphere-line), the temporal evolution of SRV for 3-1c (upper triangle-line).

After 7200 seconds, the number of MEQs is reduced for both well 3-1a, 3-1b and 3-1c injection. Because the pressure of the fracture network is decreased, and fracture network trend to gradually become stable. It seems that well 3-1c could be the best one because the number of MEQs is larger than others. Figure 7.5b shows the evolution of SRV and fracture pressure during the simulation. The pressure of fracture 806, 361 and 1520 is monitored during the simulation. Both fracture 806, 361 and 1520 pressure increase as the injection continues and decrease as the injection shut down. While the maximum pressure within fractures does not exceeded the in-situ minimum stress (36.8 MPa). The SRV increases as the injection continues and interestingly, it continues to increase for some time after shut-in at 6900 seconds. This is because the pressure continues to propagate. After 7200 seconds, the fracture network pressure is decreased and the increases of SRV become smaller. The increases of SRV due to shut in is approximately 3% for both three wells (Figure 7.5d).

Figure 7.6 shows the pore pressure distributions after 1500 and 6900 seconds of well 3-1a, 3-1b and 3-1c injection. In general, the pore pressure distribution is mostly controlled by the fracture network connectivity. In the case, the number of fractures is 6,184 and the fracture radii ranged from 80 m to 150 m. Thus, those fracture are fully intersected, and the pore pressure distribution depends on the distance between fracture and open hole section of injection wells. The injection fluid mainly pressurizes the fractures that intersect the open hole section of wells and the nearby fractures. Figure 7.7 show the fracture pressure distributions after 1500 and 6900 seconds of well 3-1a, 3-1b and 3-1c injection.

During injection, some fractures tend to slip and have increased aperture and permeability. Figure 7.8 and 7.9 show the evolution of equivalent permeability and fracture permeability at 1500 seconds and 6900 seconds of injection, respectively. Some fractures have experience shear slip to enhance the fracture and equivalent permeability during the well 3-1a, 3-1b and 3-1c injection. For example, 36 fractures slip for the well 3-1a injection, 37 fractures for the well 3-1b injection, and 64 fractures for the well 3-1c injection. After shut-in well 3-1a injection, two fractures (fracture 272 and 618) start to slip. After shut-in well 3-1b injection, two fractures (fracture 635 and 1182) start to slip. However, none of fractures start to slip after shut-in well 3-1c injection. The equivalent permeability increases approximately 20 times the initial equivalent permeability while the fracture permeability increases approximately 15 times that of the initial fracture permeability. Figure 7.10 shows the simulated injection induced MEQs at 7200 seconds. During the well 3-1a injection, 2058 MEQs are generated and the magnitude of those events ranges from -3 to 1.2. During well 3-1b injection, 2260 MEQs are generated with magnitude ranging from -3 to 1.2. During well 3-1c injection, 3401 MEQs are generated with magnitude ranging from -3 to 1.2. In the case of this work, the principal stress tensor is also monitored due to the well 3-1a, 3-1a and 3-1c injection. Figure 7.11 indicates that the direction of the principal stress tensor is not changed much because the pore pressure is less than minimum principal stress (36.8 MPa) during the injection and differential stress is more than 20 MPa and the maximum increases of pore pressure is 14 MPa (Figure 7.12). In conclusion, the well 3-1c should be the best one for Utah FORGE EGS because of the largest SRV and maximum number of MEQs.

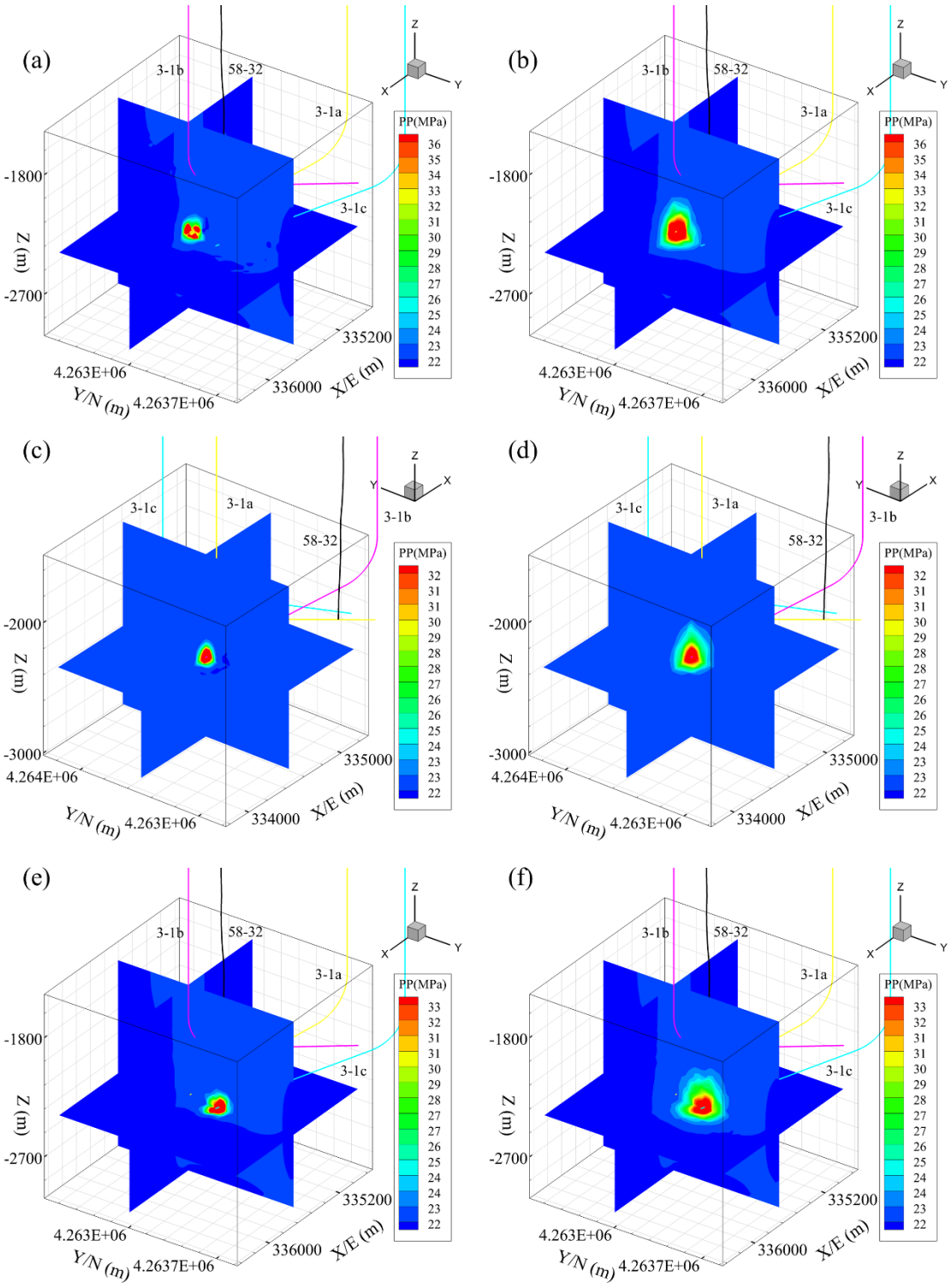

Figure 7.6 The evolution of pore pressure within reservoir due to the well 3-1a, 3-1b and 3-1c injection. (a) and (b) pore pressure due to well 3-1a injection at 1500 seconds and 6900 seconds, respectively. (c) and (d) pore pressure due to well 3-1b injection at 1500 seconds and 6900 seconds, respectively. (e) and (f) pore pressure due to well 3-1c injection at 1500 seconds and 6900 seconds, respectively.

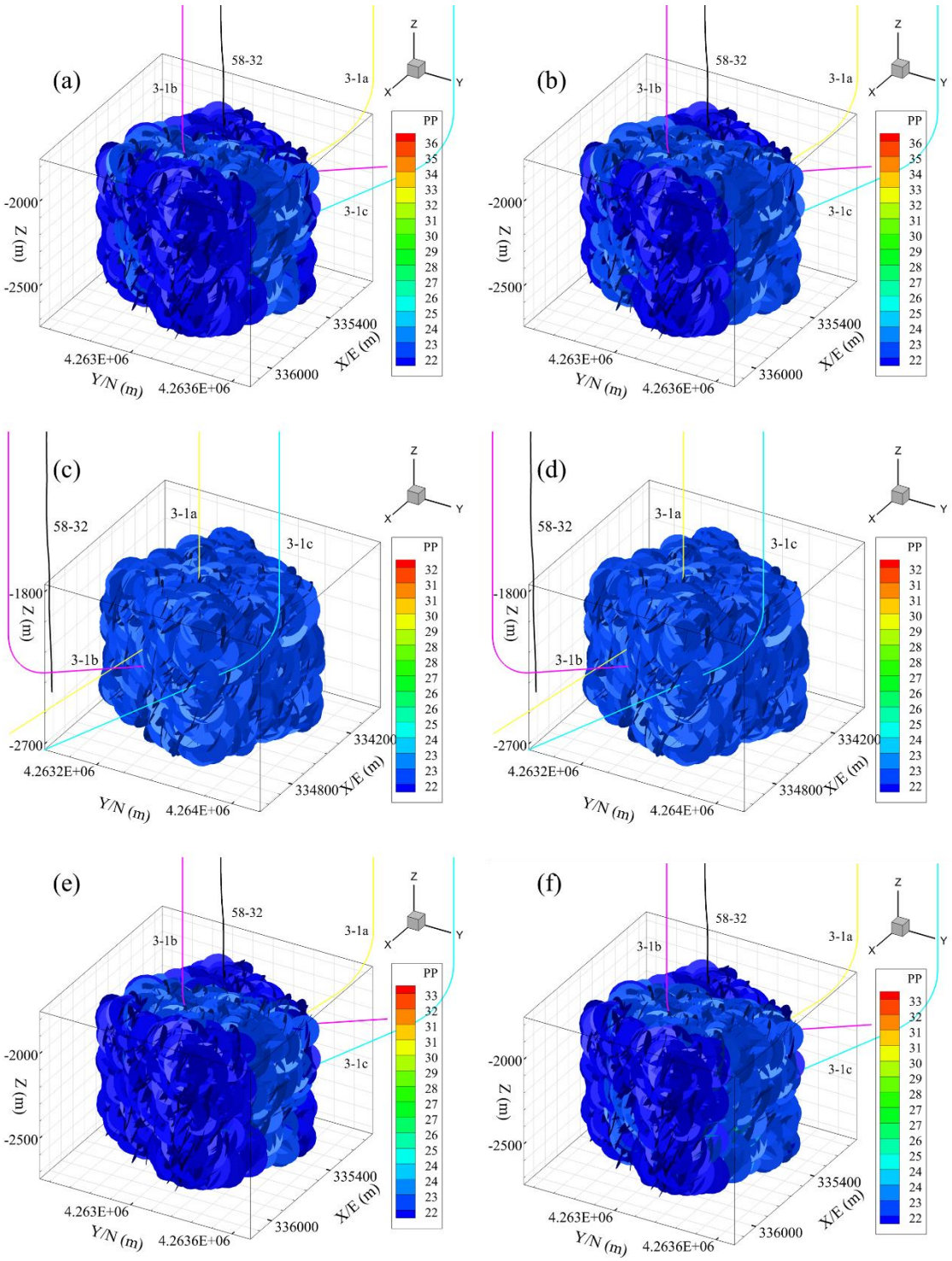

Figure 7.7 The evolution of fracture pressure due to the well 3-1a, 3-1b and 3-1c injection. (a) and (b) fracture pressure due to well 3-1a injection at 1500 seconds and 6900 seconds, respectively. (c) and (d) fracture pressure due to well 3-1b injection at 1500 seconds and 6900 seconds, respectively. (e) and (f) fracture pressure due to well 3-1c injection at 1500 seconds and 6900 seconds, respectively.

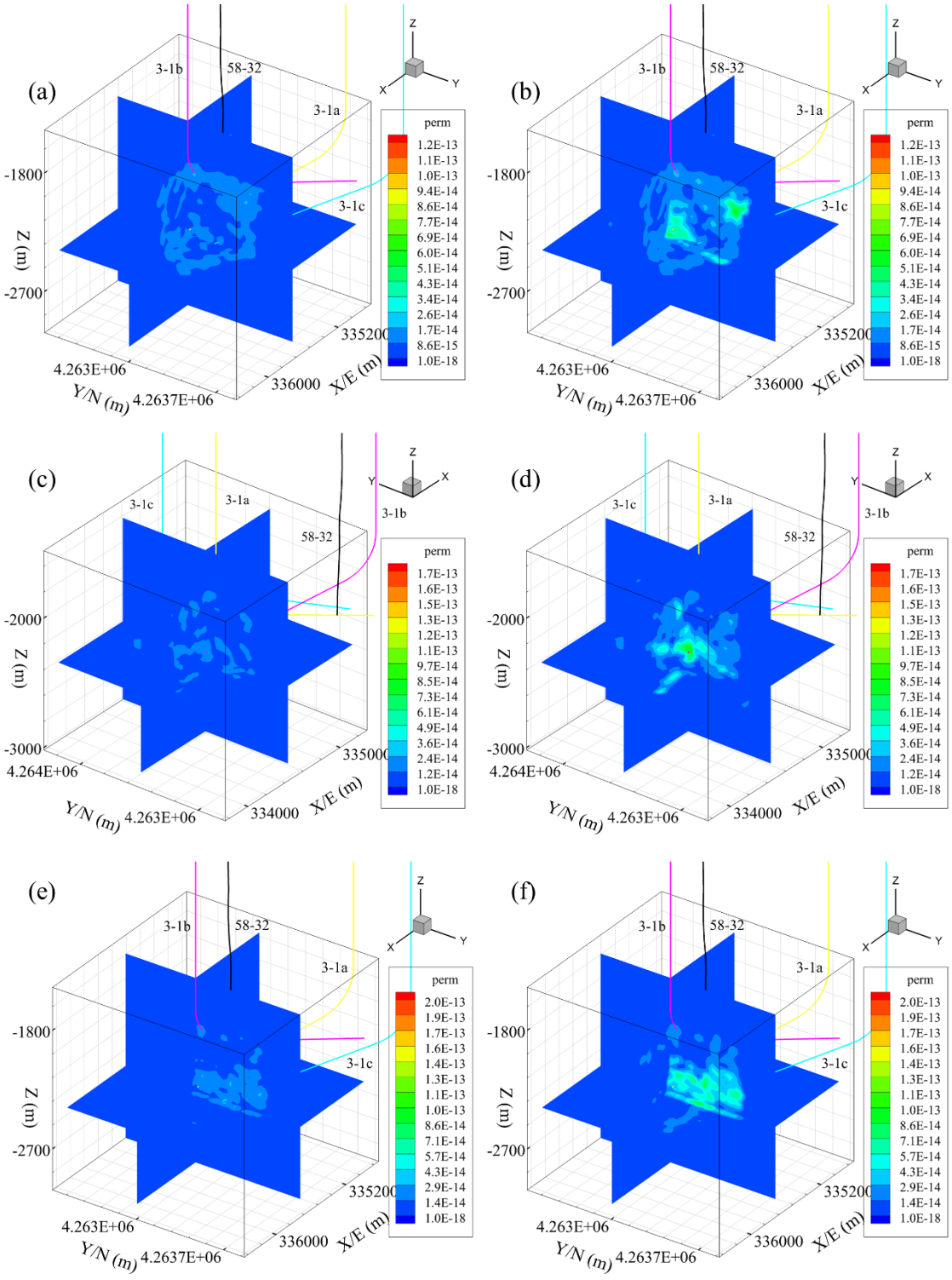

Figure 7.8 The evolution of matrix permeability during the injection. (a) and (b) matrix permeability due to well 3-1a injection at 1500 seconds and 6900 seconds, respectively. (c) and (d) matrix permeability due to well 3-1b injection at 1500 seconds and 6900 seconds, respectively. (e) and (f) matrix permeability due to well 3-1c injection at 1500 seconds and 6900 seconds, respectively.

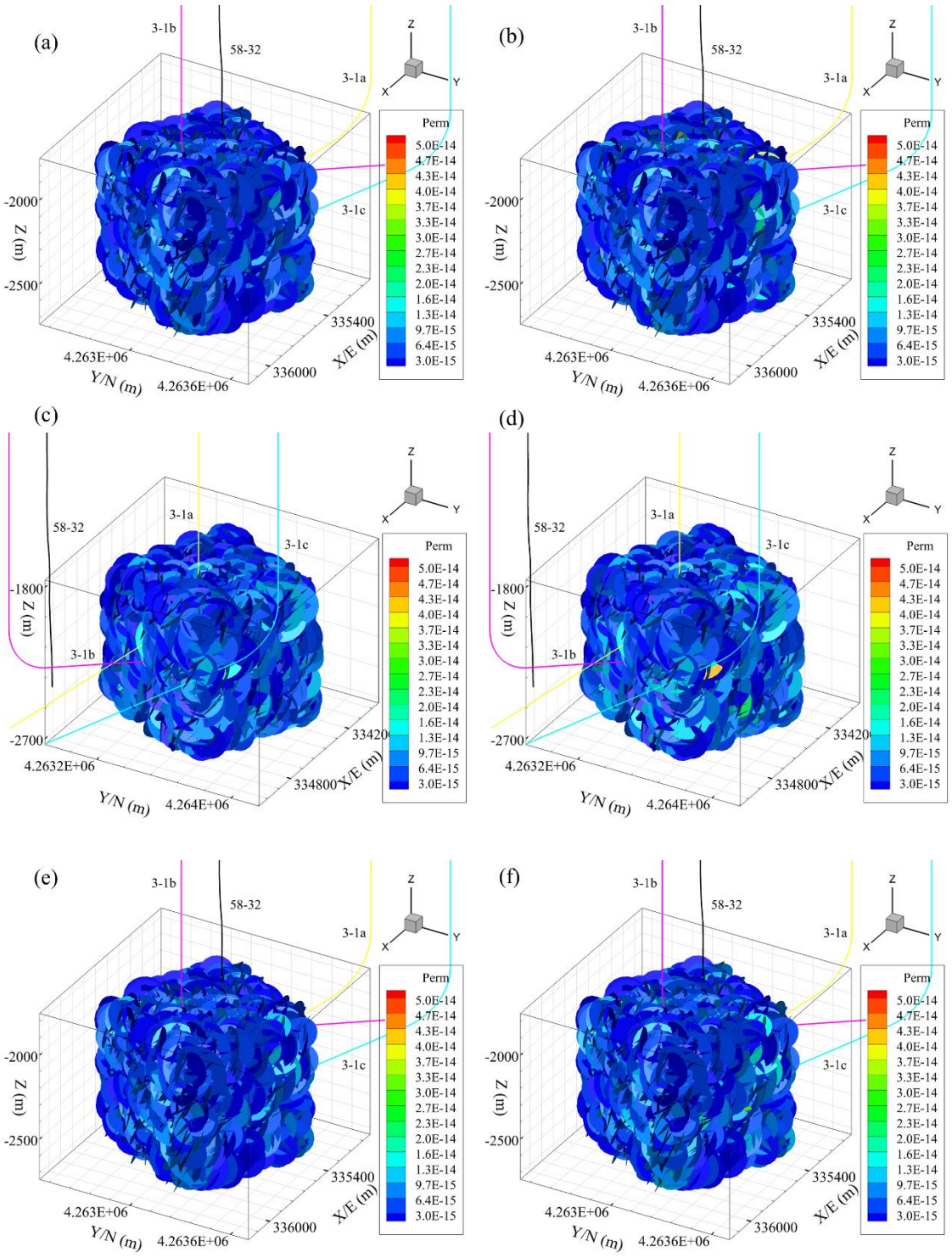

Figure 7.9 The evolution of fracture permeability during the injection. (a) and (b) fracture permeability due to well 3-1a injection at 1500 seconds and 6900 seconds, respectively. (c) and (d) fracture permeability due to well 3-1b injection at 1500 seconds and 6900 seconds, respectively. (e) and (f) fracture permeability due to well 3-1c injection at 1500 seconds and 6900 seconds, respectively.

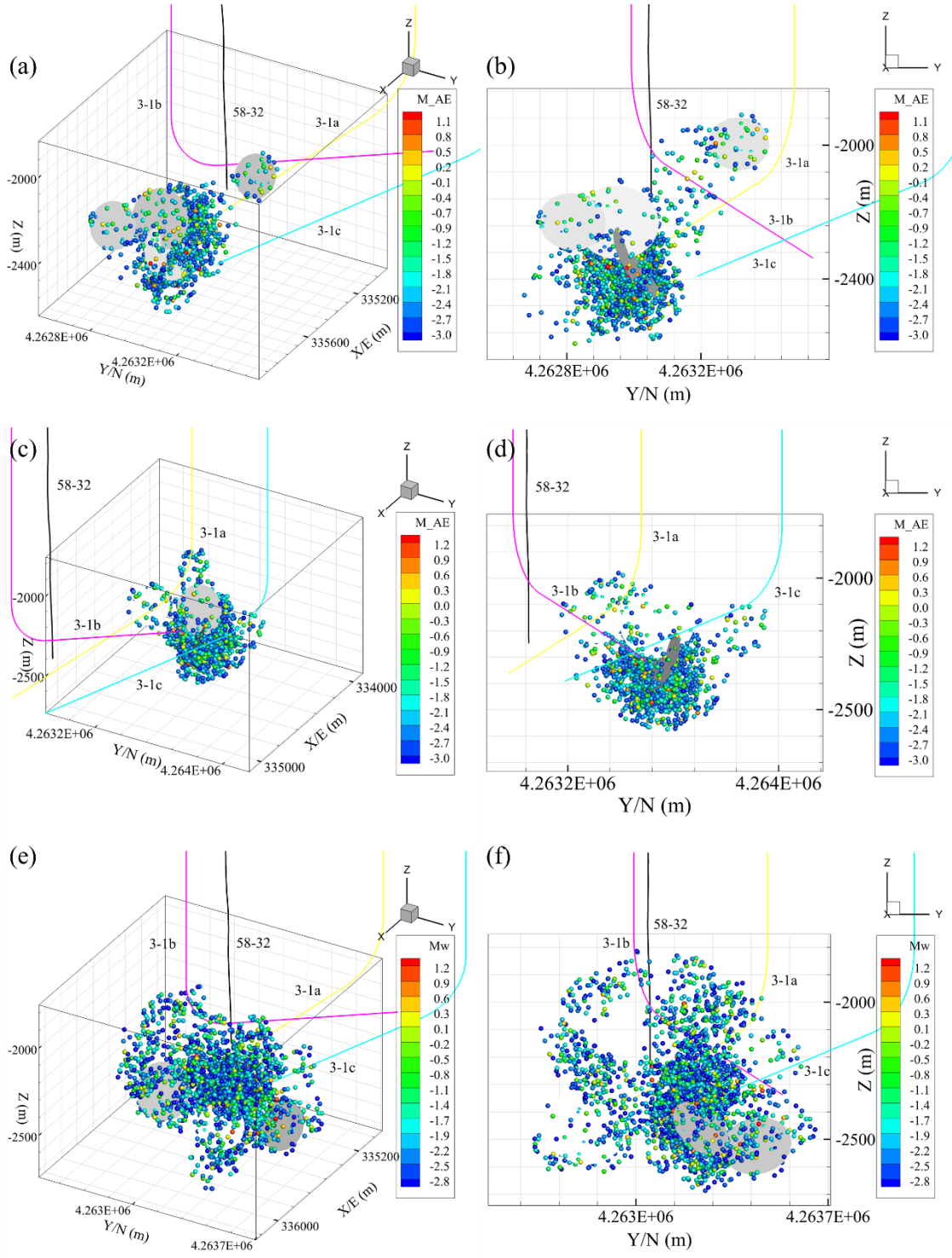

Figure 7.10 The distribution of MEQs during the injection. (a) and (b) distribution of MEQs due to well 3-1a injection at 7200 seconds. (c) and (d) distribution of MEQs due to well 3-1b injection at 7200 seconds. (e) and (f) distribution of MEQs due to well 3-1c injection at 7200 seconds.

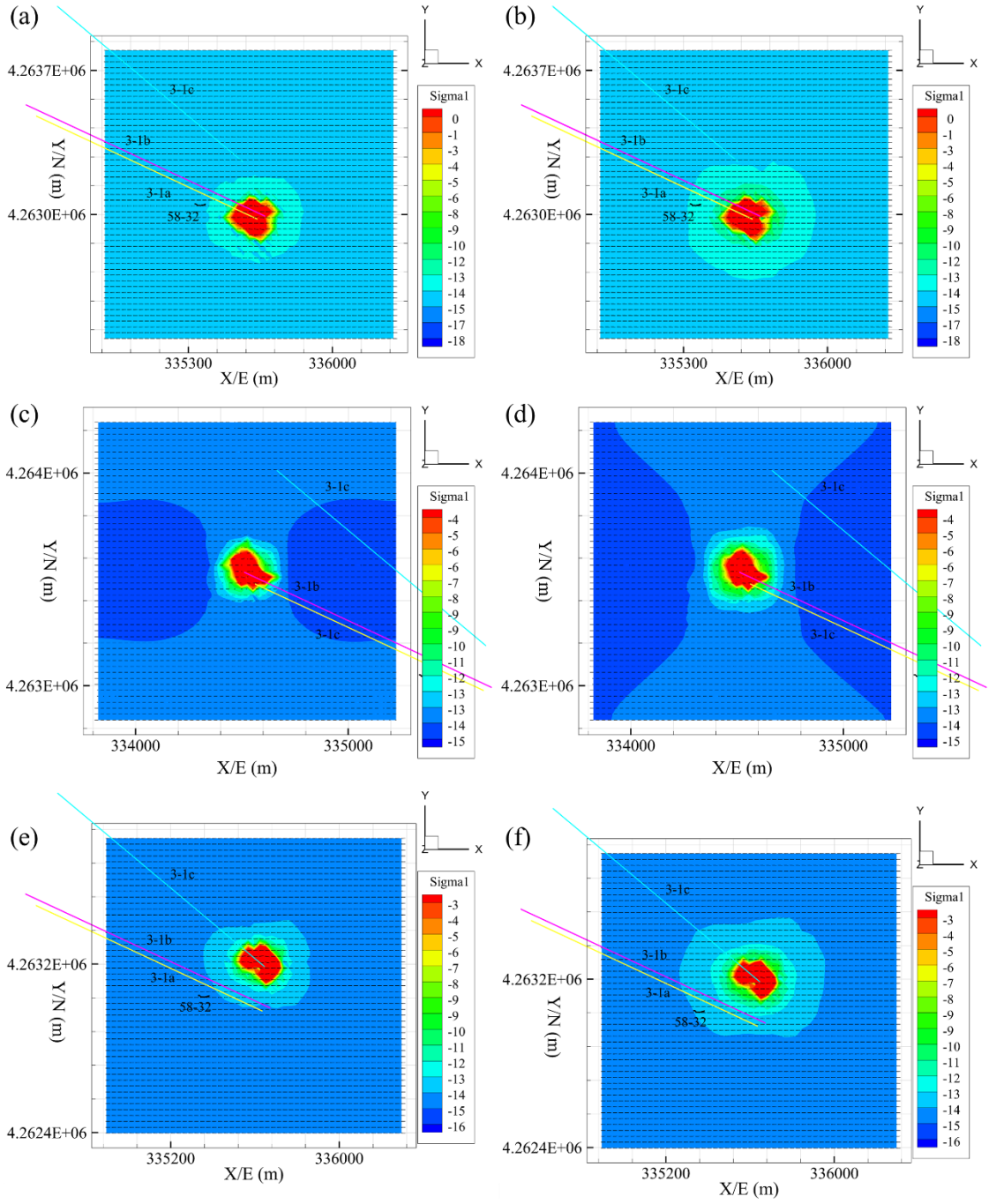

Figure 7.11 The evolution of minimum effective principle stress during the injection. (a) and (b) minimum effective principle stress due to well 3-1a injection at 3600 seconds and 6900 seconds, respectively. (c) and (d) minimum effective principle stress due to well 3-1b injection at 3600 seconds and 6900 seconds, respectively. (e) and (f) minimum effective principle stress due to well 3-1c injection at 3600 seconds and 6900 seconds, respectively.

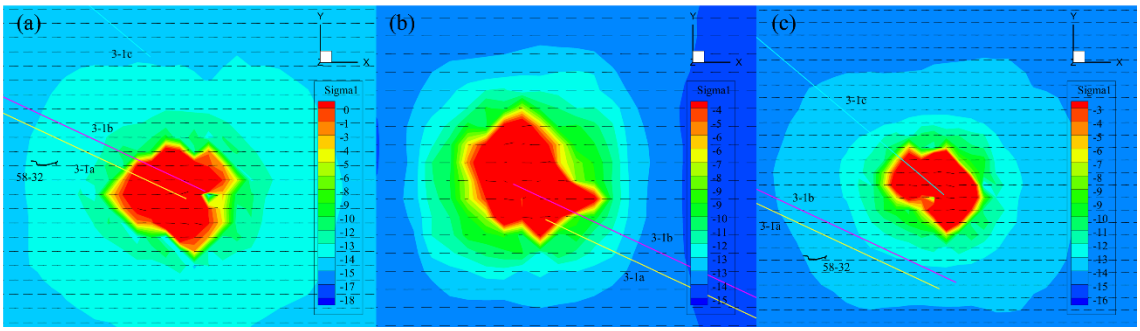

Figure 7.12 The direction of minimum effective principal stress during the injection. (a), (b) and (c) is the minimum effective principle stress due to well 3-1a, 3-1b and 3-1c injection at 6900 seconds, respectively.

7.3 Cyclic Hydraulic Stimulation of Utah FORGE

Hydraulic stimulation is necessary to create a connected fracture network for extracting geothermal energy by fluid circulation. A challenge in the EGS reservoir stimulation is creating a large stimulated volume without risk of seismic evets. In addition, often it is necessary in practice to stimulate "uncritical" zones which would require higher than expected pressures challenging available packer technology. The concept of cyclic injection has been used to help increase fracture complexity and lower the short-circuiting potential. The main idea is to inject the intended volume using several injection cycles of different duration to increase rock damage near and away from the wellbore (Figure 7.13). The concept of increasing fracture complexity by cyclic injection has been suggested in the past (Kiel 1977) and was believed to yield long, branching fractures in naturally fractured formations. Cyclic injection is known to reduce breakdown pressure (as well as lower the level of induced seismicity) via progressive rock fatigue. Hence some authors have called this procedure Fatigue Hydraulic Fracturing (Zang, Yoon et al. 2013). The approach has been recently attempted in Pocheon EGS site in Korea where a M_w 5.4 earthquake occurred in November 2017 (Grigoli, Cesca et al. 2018). The cyclic injection

schemes has been suggested as an alternative to lower seismicity risk (Zang, Yoon et al. 2013, Zang, Stephansson et al. 2016, Hofmann, Zimmermann et al. 2019). Studies have suggested that cyclic injection schemes can effectively reduce breakdown pressure and magnitude of the largest events and enhance the EGS reservoir (Hofmann, Zimmermann et al. 2018). Laboratory experiments were performed to investigate the effects of cyclic hydraulic stimulation on magnitude of induced seismicity (AE) and breakdown pressure (Patel, Sondergeld et al. 2017, Zhuang, Kim et al. 2017). They showed that the breakdown pressure and maximum magnitude of induced seismicity is decreased by 20% for a cyclic hydraulic stimulation compared to injection with constant rate, respectively. However, the effects of natural fracture network on breakdown pressure and induced seismicity has not been considered. Numerical modeling of the cyclic hydraulic stimulation could be a valuable tool for studying the injection designs.

In this section, we present two injection scenarios for the well 3-1c in Utah FORGE EGS. These injection scenarios are presented in Figure 7.13. The first injection scenario is a cyclic injection rate and the second injection scenario is a constant injection rate. The total injection volume of those two injection scenarios are both 3051 m^3 over a period of 35.8 hours. The maximum injection rate in cyclic injection and constant injection cases is 20 BPM and 9.1 BPM, respectively. The reservoir parameters in the simulations can be found in the previous section. Figure 7.14 shows the evolution of the fracture pressure during the two injection scenarios. The maximum pressure during the cyclic injection and constant injection is 38.6 MPa and 35.4 MPa, respectively. The value of the maximum pressure likely depends on the ratio between maximum injection rate and minimum injection rate in a cycle and the geometry of the fracture network. However, none of the

fractures start to propagate during those two injection scenarios. Figure 7.15 shows the evolution of SRV during the two injection scenarios. It seems that the SRV in the cyclic injection is larger than the SRV in constant injection during the first 1000 minutes of injection. After 1000 minutes, the SRV in both injection scenarios are almost the same because the entire fractured reservoir is stimulated in both scenarios. In addition, the number of MEQs from cyclic injection is larger than constant injection because of the high fracture pressure in cyclic injection (Figure 7.16). For instance, the maximum number of MEQs from the cyclic injection and constant injection cases is 3389 and 3115, respectively. Figure 7.17 shows the distribution of MEQs at injection 2125 minutes. The maximum magnitude of MEQs during the cyclic injection and constant injection is 1.2 and 1.3, respectively. Therefore, the cyclic injection scenario can reduce the maximum magnitude of MEQs and increase the SRV. Figure 7.18 shows the evolution of the fracture pressure during the cyclic injection and constant injection at 500 minutes and 2125 minutes, respectively. Figure 7.19 shows the evolution of matrix pressure during the cyclic injection and constant injection at 500 minutes and 2125 minutes, respectively. Figure 7.20 shows the evolution of fracture permeability during the cyclic injection and constant injection at 500 minutes and 2125 minutes, respectively. Figure 7.21 shows the evolution of matrix permeability during the cyclic injection and constant injection at 500 minutes and 2125 minutes, respectively.

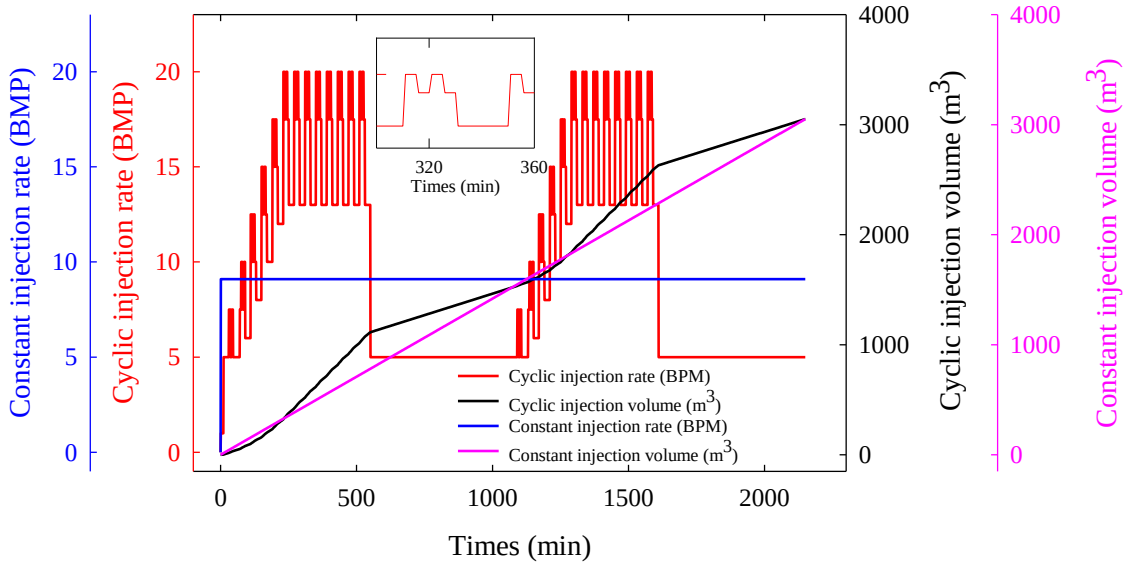

Figure 7.13 The summary of two injection scenarios. The first injection scenario is cyclic injection rate (red line) and the second injection scenario is constant injection rate (blue line). The total injection volume of those two injection scenarios are both 3051 m^3.

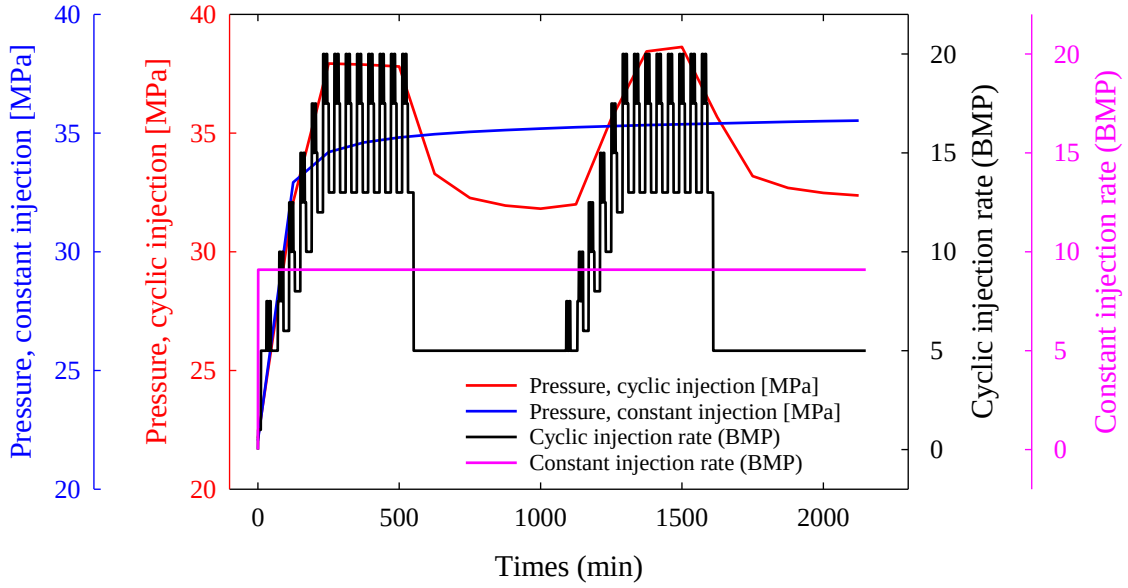

Figure 7.14 The evolution of fracture pressure during the two injection scenarios.

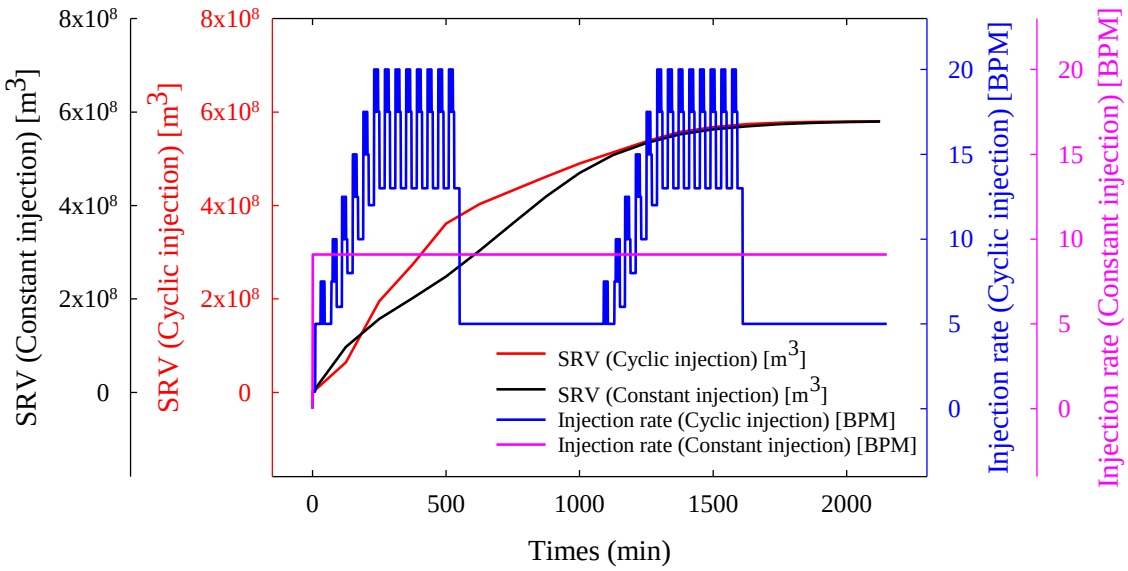

Figure 7.15 The evolution of SRV during the two injection scenarios. The SRV in the cyclic injection is larger than SRV in constant injection during the first 1000 minutes injection. After 1000 minutes, the SRV in those injection scenarios are almost the same because the entire fractured domain is pressurized in both scenarios.

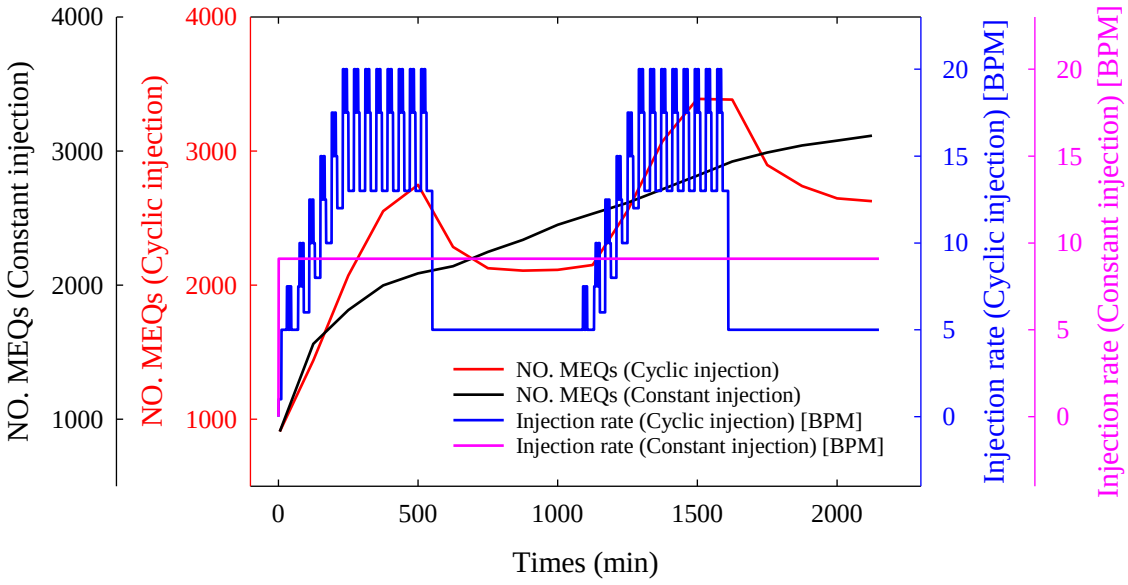

Figure 7.16 The evolution of number of MEQs during the two injection scenarios.

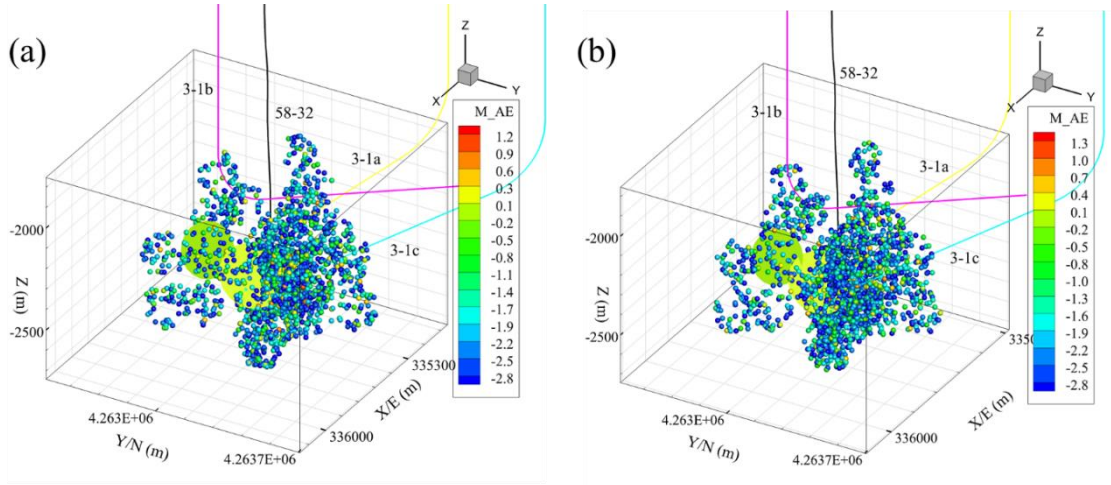

Figure 7.17 The distribution of MEQs during the two injection scenarios. (a) the distribution of MEQs during under cyclic injection at 2125 minute. (b) the distribution of MEQs during under constant injection at 2125 minute.

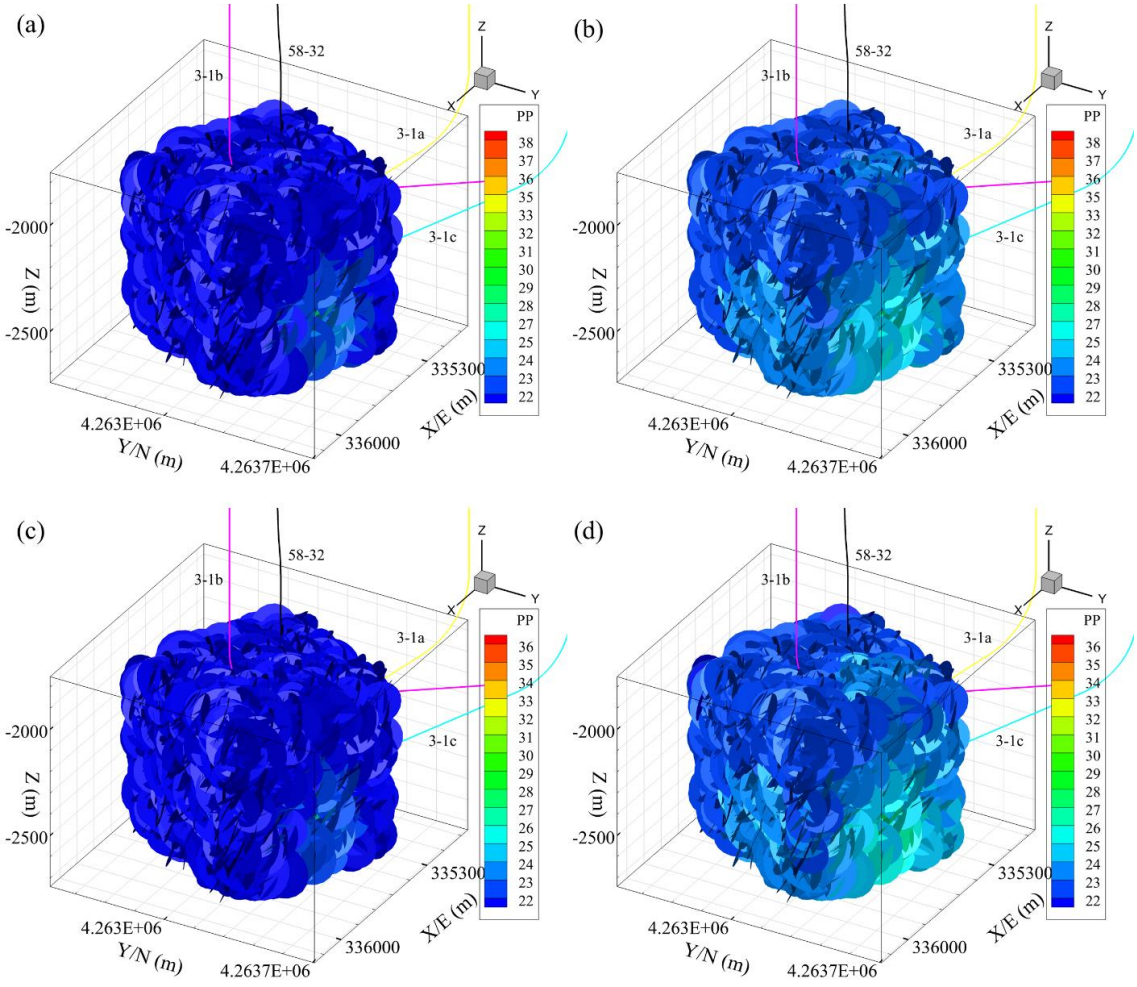

Figure 7.18 The evolution of fracture pressure during the two injection scenarios. (a) and (b) is the fracture pressure under cyclic injection at 500 minute and 2125 minute, respectively. (c) and (d) is the fracture pressure under constant injection at 500 minute and 2125 minute, respectively.

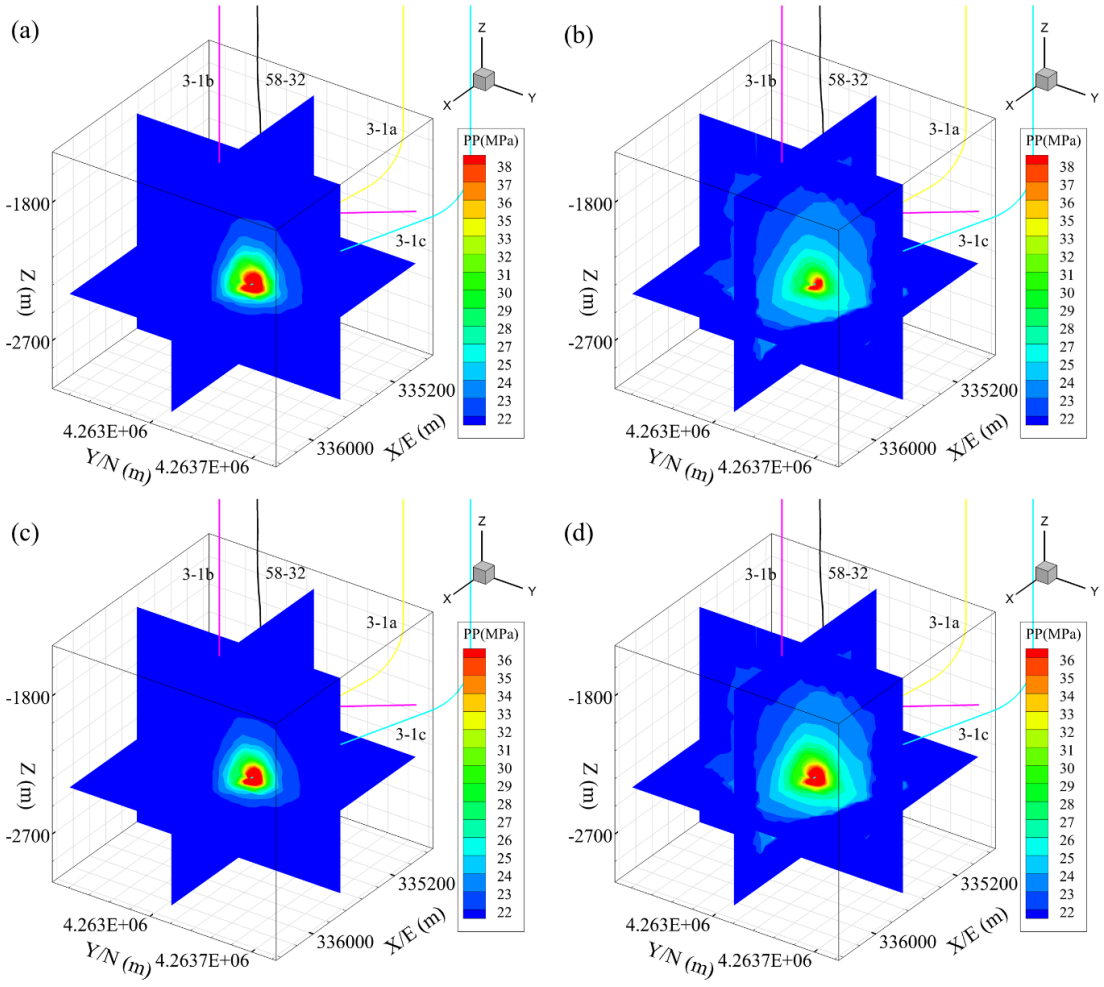

Figure 7.19 The evolution of matrix pressure during the two injection scenarios. (a) and (b) is the matrix pressure under cyclic injection at 500 minute and 2125 minute, respectively. (c) and (d) is the matrix pressure under constant injection at 500 minute and 2125 minute, respectively.

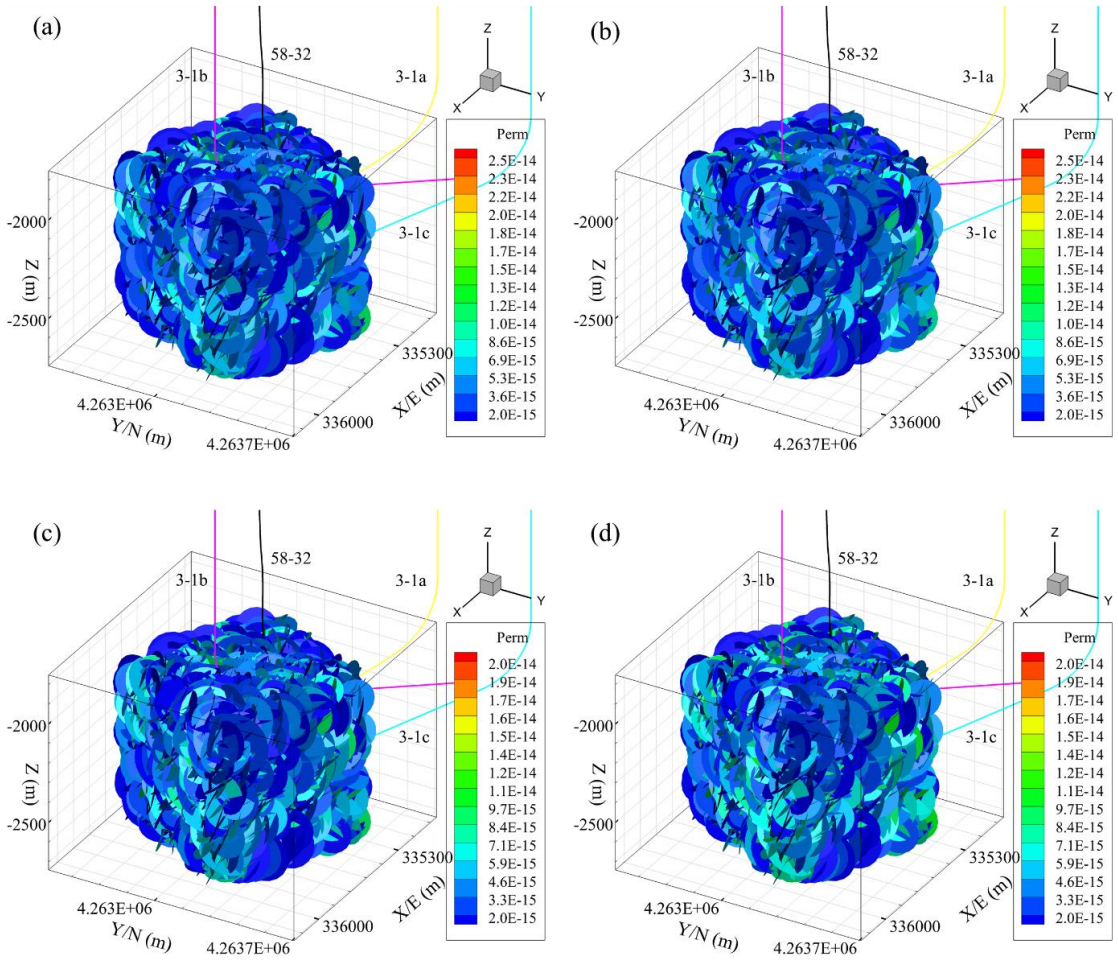

Figure 7.20 The evolution of fracture permeability during the two injection scenarios. (a) and (b) is the fracture permeability under cyclic injection at 500 minute and 2125 minute, respectively. (c) and (d) is the fracture permeability under constant injection at 500 minute and 2125 minute, respectively.

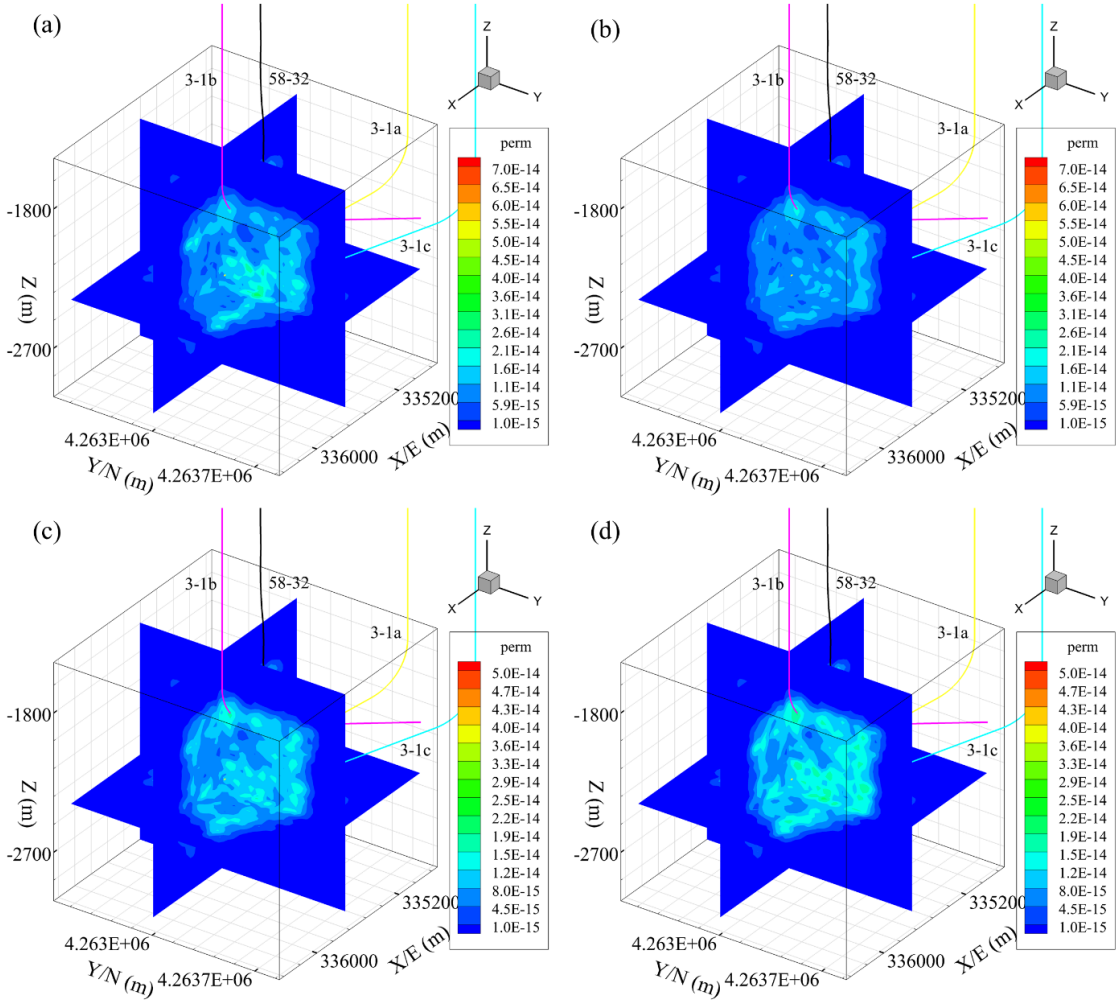

Figure 7.21 The evolution of matrix permeability during the two injection scenarios. (a) and (b) is the matrix permeability under cyclic injection at 500 minute and 2125 minute, respectively. (c) and (d) is the matrix permeability under constant injection at 500 minute and 2125 minute, respectively.

7.4 Conclusions

In this Chapter, the extended fracture network model is applied to Utah FORGE EGS to identify the best injection well trajectories. After comparison between the numerical results from well 3-1a, 3-1b and 3-1c, well 3-1c could be the best one for injection well of Utah FORGE EGS. Because the injection of well 3-1c generate the largest SRV and the maximum number of MEQs. Such extended fracture network model could be useful

in analyzing the EGS development. However, one limitation of this extended fracture network model is the fracture network pressure induced stress filed. The stress shadow is described by Eshelby solution which is currently not mapped induced stress field of fracture network. Advance methods need to propose to accurately calculate induced stress field of fracture network.

Chapter 8 Natural Fracture Orientations Using Geomechanics Based Stochastic Analysis of Microseismicity Related to Reservoir Stimulation

8.1 Introduction

Natural Fractures have a significant effect on the fluid transport capability of a reservoir. Properties commonly used to characterize natural fractures encompass frequency, persistence, size and orientation. The natural fracture orientations are a critical feature that exerts a large control over network permeability tensor. Despite their essential role in reservoir development, there are still large uncertainties regarding direct and indirect diagnostic technologies for characterizing natural fracture orientations in-situ away from the wellbore. In the last several decades, considerable effort has been made by researchers to refine many methods to constrain the uncertainty in measuring natural fracture orientations from seismic data (National Research Council 1996, Willis, Burns et al. 2006, de Figueiredo, Schleicher et al. 2012). In general, geophysical methods are expensive and tend to have a poor ability to spatially resolve the fracture network geometry resulting from stimulation (National Research Council 1996). Image logging is an attractive tool for detecting the orientations, however, coupled with the effects of stress redistribution around borehole, and spatial heterogeneity may lead to erroneous log interpretation (Fernández-Ibáñez, DeGraff et al. 2018). Furthermore, the description of natural fracture geometries obtained from local field surveys has to be scaled up to the entire reservoir, which can cause loss of geometric characteristics of the natural fractures. The question of how to establish the natural fracture pattern away from the borehole remains a challenging issue. Thus, natural fracture patterns in numerical analysis are

commonly treated in a stochastic framework (Bruel, Cacas et al. 1994, Willis-Richards, Watanabe et al. 1996, Rahman, Hossain et al. 2002, Tezuka, Tamagawa et al. 2005, Dershowitz, Cottrell et al. 2010, Wang and Ghassemi 2012, Rinaldi and Nespoli 2017). The uncertainties in natural fracture orientations challenge the reliability of numerical tools for optimizing completions, design and production assessment.

A source of data on the nature of the reservoir fracture network is microseismic data or microearthquakes (MEQs) generated during stimulation. Fluid injection perturbs the pore pressure and the in-situ stress state within the reservoir and leads to natural fracture reactivation, shear slip and possibly their propagation, which is often manifested as multiple MEQs. Interpretation of MEQs can illustrate the natural fracture geometry, stimulated volume distribution and also can provide data on the in-situ stress state (Pine and Batchelor 1984, Shapiro, Huenges et al. 1997, Warpinski, Wolhart et al. 2004, Kuang, Zoback et al. 2017). The generation of MEQs is believed to evolve from rock failure in shear, and shear slip on new or pre-existing fracture planes (Raleigh, Healy et al. 1976, Pearson 1981, Pine and Batchelor 1984) and fracture propagation (Kamali and Ghassemi 2017, Ye, Janis et al. 2017, Ye and Ghassemi 2018). Some reservoir properties such as permeability have been estimated using inverse modeling of microseismic observations. This inverse modeling is commonly referred to as seismicity based reservoir characterization (SBRC) and has been used to estimate the rock mass permeability that results from stimulation (Pearson 1981, Shapiro, Huenges et al. 1997, Ghassemi, Jafarpour et al. 2013). Also, a diagnostic technique has been proposed to estimate the reservoir permeability from MEQs (Shapiro, Huenges et al. 1997). A pore pressure diffusion model was used to link MEQs to equivalent permeability at the reservoir scale,

assuming the rock was in the limiting state. The hydraulic diffusivity was determined using the diffusion length-occurrence time curve fit for the onset of seismicity. However, this approach has limited application to hydraulic fracturing because the natural fractures are not considered explicitly in such diagnostic techniques (Shapiro, Patzig et al. 2003, Lee and Ghassemi 2011, Carcione, Currenti et al. 2018). This approach also lacks quantitative analysis of the relation between the field-observed MEQ distribution and the simulated MEQ distribution. This framework was therefore improved by combining a geomechanics model and Ensemble Kalman filter (EnKF) to infer reservoir permeability and geomechanical properties from field-observed MEQ distribution (Tarrahi and Jafarpour 2012, Ghassemi, Jafarpour et al. 2013, Tarrahi, Jafarpour et al. 2015). A Kernel Density Estimation (KDE) was used to smooth the MEQs as continuous seismicity density since EnKF is designed to integrate continuous data. However, a noticeable limitation of KDE is that it cannot capture the discrete quality of MEQs and compromises the value of discrete MEQs. There are also several other limitations for the EnKF as a tool for interpreting MEQs, including (a) EnKF in large data results in severe ensemble spread underestimation due to the model nonlinearity and model error (Nester, Komma et al. 2012, Rainwater and Hunt 2013). (b) EnKF is less likely to handle a highly nonlinear relation between the observations and unknown parameters that it may not converge (Sætrom and Omre 2011, Sarma and Chen 2011, Yang, Kalnay et al. 2012).

Other existing MEQs interpretations have relied on grouping MEQs based on graph operations that depend on the locations of the MEQs hypocenters (Fehler, House et al. 1987, Fehler and Johnson 1989, Fehler 1990, Jones and Stewart 1997). Another approach is to first group the MEQs within similar waveforms (e.g., focal mechanisms, ratio of S

wave to P wave amplitudes) and then search for self-similar MEQ clusters to define the fractures (Aster and Scott 1993, Roff, Phillips et al. 1996, Kuang, Zoback et al. 2017). So, sets of clusters are grouped into fault planes that can be defined as the best fit for each cluster. An objective function which is depending on the ratio of S wave to P wave amplitudes and maximum separation distance is used to measure the matching level between different MEQs (Roff, Phillips et al. 1996). A previous study suggests a multiple-term objective function that is much more complex (Kuang, Zoback et al. 2017). In these approaches, the optimized focal mechanism solution is associated with the extremum of the objective function. However, due to arbitrariness of the objective function and low magnitude of MEQs, those methods seem to be poorly constrained and contains large errors (Kuang, Zoback et al. 2017). In conclusion, these methods suffer from three limitations: (a) the objective function is complex and results in convergence difficulties; (b) the waveform of MEQs is probably disorganized and the amplitude is very low, so only very strong MEQs can be selected; (c) there is no general theoretical framework to quantitatively measure the matching level between the simulated MEQ distribution and the field-observed MEQ distribution.

In this work an alternative method is developed that can help in characterizing the natural fractures orientations in the reservoir. We use the concept of similarity measure to develop a stochastic framework called Geomechanics-Based Stochastic Analysis of Microseismicity (GBSAM) to integrate field-observed MEQ distribution as prior information to infer natural fracture orientations. The concept of similarity measure is commonly used in data sciences and is applied to quantify the similarity between two objects. The core of the similarity measure is to build the distance metrics between two

objects (Jarvis and Patrick 1973, Frey and Dueck 2007). For instance, the distance metrics are calculated from the center of one object to the center of another object. A forward model is used to generate a simulated MEQ distribution when the shear stress at the center of natural fractures is larger than the shear strength according to the Mohr-Coulomb failure criterion. When one natural fracture slips, the shear energy is calculated, and it is supposed that a certain part of the shear energy will be released as seismic energy. If the released seismic energy is larger than the threshold energy of MEQs, additional MEQs are generated on the natural fracture plane. This assumption may affect the distribution of simulated MEQs while having little effect on the final estimation of orientation of fracture network. The threshold seismic energy of MEQs can be defined as the minimum detection capacity of the sensors which is interpreted as minimum seismic moment magnitude inferred from the sensors. *Mahalanobis* distance (Mahalanobis 1936, De Maesschalck, Jouan-Rimbaud et al. 2000, Huberty 2005), a type of similarity measure technique, is then applied to measure the similarity between the simulated MEQ distribution and the field-observed MEQ distribution. Finally, the GBSAM is applied to a data sets of MEQs recorded during Phase 2.2 of the Newberry Volcano EGS demonstration project and the Fenton Hill HDR.

8.2 Methodology

8.2.1 Forward Model for Natural Fracture Slip

The reservoir is assumed to contain a number of natural fractures. The objective of the forward model is to analyze the natural fractures responses to pore pressure increase and stress variations associated with injection to generate simulated MEQ distribution. As a first approach, the injection problem can be approximated via a line injection source in a

porous rock without considering poroelastic effects, which is bounded by two semi-infinite impermeable layers (Figure 8.1). In the Newberry and Fenton Hill projects, often a long open interval is used for injection. Thus it is reasonable to adopt the line source to simulate pore pressure redistribution resulting from an injection. Point sources can also be easily implemented. The line injection source ($r = 0$) extends over the thickness of the permeable layer $2h$, and fluid is injected into the surrounding rock masses at a constant volumetric rate Q over the finite time interval. The natural fractures are stochastically distributed throughout the permeable layer with an assigned effective permeability. The permeability of the layer is assumed to be the effective permeability of the matrix/natural fracture system and thus fracture flow in fractures (Safari and Ghassemi 2016, Cheng and Ghassemi 2017)) is not explicitly considered. All these simplifications can be relaxed, however, the objective here is to test the inversion concept rather than to capture detailed physics of the process. Poroelastic and thermal effects (Ghassemi and Tao 2016) are neglected at this stage of our work. Initially ($t = 0$), all hydraulic and mechanical fields are assumed to be in equilibrium.

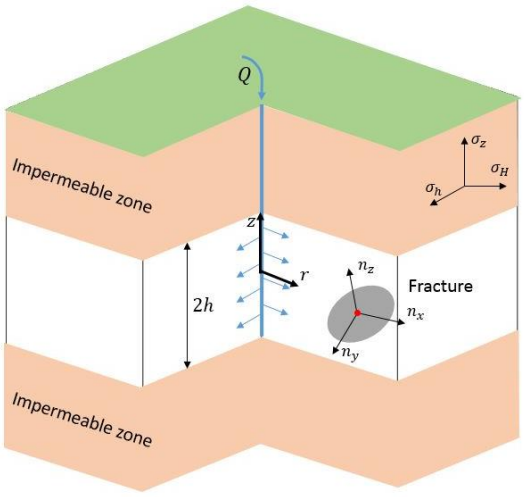

Figure 8.1 Geometry of the problem: a line injection source in a fractured zone.

This problem can be simplified by introducing the following dimensionless parameters.

$$r^* = \frac{r}{h}, \quad z^* = \frac{z}{h}, \quad t^* = \frac{t}{t_c}, \quad p^* = \frac{p}{p_c} \tag{8.1}$$

Where $p_c = Q/8\pi\kappa h$ is the characteristic pressure, κ is the permeabilityk[L^2] divided by fluid viscosity μ_f[Pa · s], p is the pore pressure[Pa], $t_c = h^2/4c$ is the characteristic time, t_s^* is the time when injection shut in and c is the diffusivity coefficient. The pore pressure field $p^*(r^*, t^*, t_s^*, z^*)$ at a certain point in time t^* and position in the reservoir (r^*, z^*) is given as (Marck, Savitski et al. 2015):

$$p^*(r^*, t^*, t_s^*, z^*) = \begin{cases} p_r^*(r^*, t^*, t_s^*, z^*), & |z^*| \le 1 \\ 0, & |z^*| > 1 \end{cases} \tag{8.2}$$

$p_r^*(r^*, t^*, t_s^*, z^*)$ is the pore pressure field in the reservoir and the gravity effects are neglected. To drive the analytical solutions for pore pressure generated by a uniform line source density over the thickness of the reservoir, the diffusion equation is:

$$\frac{\partial p}{\partial t} = c\nabla^2 p \tag{8.3}$$

The diffusion equation (8.3) can be re-written as:

$$\frac{\partial p_r^*}{\partial t^*} - \frac{\partial^2 p_r^*}{\partial (r^*)^2} - \frac{1}{r^*}\frac{\partial p_r^*}{\partial r^*} = 0, \qquad t^* > 0 \tag{8.4}$$

Equation (8.4) can be solved with the initial conditions and boundary conditions to get the pore pressure field $p_r^*(r^*, t^*, t_s^*, z^*)$ in which t_s^* is equal to t^*. The solution for equation (8.4) is $p_r^* = E_1((r^*)^2/t^*)$ (Theis 1935) and this solution is also given in (Jacob 1940, Carslaw and Jaeger 1959). E_1 is the exponential integral defined as given in equation (8.5).

$$E_1(x) = \int_x^\infty \frac{e^{-t}}{t} \mathrm{d}t \tag{8.5}$$

In this work, we consider constant volumetric rate Q over the finite time interval $t_s^* > 0$. This is simply achieved by superimposing the solution for injection rate Q starting at $t^* = 0$ with the solution for withdrawal rate Q beginning at $t^* = t_s^*$:

$$p_r^*(r^*, t^*, t_s^*, z^*) = \begin{cases} E_1\left(\frac{(r^*)^2}{t^*}\right), & 0 < t^* < t_s^* \\ E_1\left(\frac{(r^*)^2}{t^*}\right) - E_1\left(\frac{(r^*)^2}{t^* - t_s^*}\right), & t_s^* \le t^* \end{cases} \tag{8.6}$$

where E_1 is the exponential integral. Figure 8.2 shows a plot of equation (8.6) with $t_s^* = 10$. The pore pressure of the entire reservoir could be increased a short time period after shut-in before decreasing. The magnitude of the modified pore pressure Δp_r^* increases with distance r^* away from the injection source. After fluid injection is completed, the pore pressure in the neighborhood of the source remains higher and diffuses through the reservoir, which suggest that if Δp_r^* is sufficient large, then additional simulated MEQs may also be generated after cessation of injection.

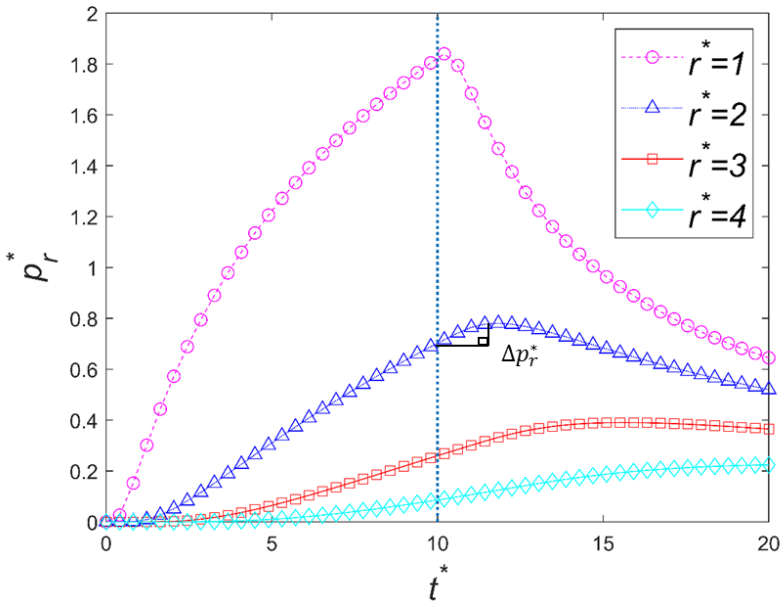

Figure 8.2 Pore pressure field p_r^* in the reservoir during finite duration injection at a constant volumetric rate, at $r^* = 1, 2, 3, 4$. Dotted vertical line indicates the shut-in time $t_s^* = 10$. Δp_r^* is

modified pore pressure due to shut-in. Note that the pore pressure still increases in a short time period after shut-in.

8.2.2 Generation of Simulated MEQ Distribution

In this work, the simulated MEQ distribution is generated when the natural fractures fail in shear. To determine fracture slip, the effective normal stress σ_n and shear stress σ_s acting on the plane whose unit normal is $[n_x, n_y, n_z]$ at the center of natural fracture (red point in Figure 8.1) are calculated. From the Cauchy's equation, the traction vector $\boldsymbol{t}^n$ on fracture is $\sigma'_{ij} n_j$, with σ'_{ij} as the effective stress. The normal stress on the natural fracture is $\sigma_n = \boldsymbol{t}^n \cdot n$ and shear stress σ_s is $\sqrt{|\boldsymbol{t}^n|^2 - \sigma_n^2}$. The Coulomb failure function (CFF) which describes the proximity of natural fracture to frictional slip is

$$\text{CFF}=\sigma_s - \mu_s \sigma_n - c' \tag{8.7}$$

where μ_s is the friction coefficient and c' is the cohesive strength. In this study of failure, the geometry of the natural fracture is treated as a mass point which inherits all the geometrical and mechanical properties of the natural fracture and is located at the center of the natural fracture. Each mass point has a theoretical fracture plane with a given orientation. The mechanics of the mass point represent the mechanics state of the entire natural fracture which can be derived from equation (8.7). Recently, different numerical methods such as discrete element method (Al-Busaidi, Hazzard et al. 2005, Zhao and Paul Young 2011), hybrid boundary element/finite element (Lee and Ghassemi 2011, Safari and Ghassemi 2016, Rinaldi and Nespoli 2017) are applied to generate simulated MEQ distribution. An essential limitation in current MEQ generation algorithms from aforementioned numerical methods is that if any physical point (e.g., element, node, seed or grain) on the fracture fails, exactly one simulated MEQ is generated. Thus, the

processes of generating simulated MEQ distribution have severe mesh-dependency issues in most numerical methods. Another limitation is that usually some heuristics are used to control the number of simulated MEQ distribution (Hazzard and Young 2004, Rinaldi and Nespoli 2017). From this aspect, numerical methods do not necessarily provide a significant advantage. To remedy the scale mismatch between the model elements and the natural fracture due to implicit fracture representation, we propose a new simple method to outline the location and the number of simulated MEQs that are generated on a fracture plane upon slip. If the Coulomb failure function (CFF) is larger than zero and the natural fracture is slipping, one simulated MEQs will be induced at the center of the natural fracture. In this configuration, the shear energy of the natural fracture is calculated by $\tau^2 \cdot A/2G$ where τ is the shear stress on the fracture and G is the shear modulus and A is the area of fracture plane. Stress drop varies from micro-earthquake to micro-earthquake and the stress drop estimation depends on the slip displacement on the fracture and corner frequency of the source spectrum. Previous studies (Allmann and Shearer 2007, Yamada, Mori et al. 2007, Goertz-Allmann, Goertz et al. 2011, Ye and Ghassemi 2018) suggested that the average stress drop is from 4 MPa to 10 MPa, approximately one third of the shear stress in our cases. So, due to the high uncertainty in stress drop estimation, we hypothesize that one third of the shear energy in the fracture surface is released in the form of seismic wave during the fracture slipping processes. If the seismic energy is larger than the threshold seismic energy of MEQs, additional simulated MEQs are generated. The threshold seismic energy of MEQs can be defined as the minimum detection capacity of the sensors, which is interpreted as the minimum seismic moment magnitude inferred from the sensors. There is an empirical formula to estimate the seismic

energy from seismic moment magnitude (Kanamori 1978, Goodfellow, Nasseri et al. 2015)

$$\log_{10}(E_R) = 4.8 + 1.5 \cdot M_w \tag{8.8}$$

E_R is the seismic energy and M_w is the seismic moment magnitude. In this study, the minimum seismic moment magnitude inferred from the sensors M_w is set to zero. Thus the threshold seismic energy of MEQs in this study is:

$$E_R = 10^{4.8+1.5 \cdot M_w} = 10^{4.8+1.5 \cdot 0} = 63096(J) \tag{8.9}$$

The number of additional simulated MEQs is the integer part of the ratio of the released seismic energy to the threshold seismic energy of MEQs. The released seismic energy is $(\Delta\tau)^2 \cdot A/(2G)$, where $\Delta\tau$ is the stress drop and G is shear modulus and A is the area of fracture slip area (assumed to equal the fracture surface). Specially, the locations of additional simulated MEQs are randomly distributed on the fracture plane.

8.2.3 Mahalanobis Distance

The concept of similarity is essential to pattern recognition problems and is applied to data classification and clustering in data sciences (Cha 2007). From the data scientist's perspective, similarity quantifies the degree (or the extent) to which two discrete or continuous objects are. Hence, the concept of similarity is appropriate for measuring the matching level between the simulated MEQ distribution and the field-observed MEQ distribution.

The natural fracture orientations in the forward model that have the smallest value of similarity would most likely be the best and will be considered to be the same as the true reservoir natural fracture orientations. Here, the Mahalanobis distance (MD), a concept of similarity, is used to quantify the matching level between the simulated MEQ

distribution and the field-observed MEQ distribution. MD is defined in terms of both the mean and variance of the variables (e.g., MEQ data) and the covariance matrix of all the variables, and therefore it takes advantage of the covariance among variables. For instance, suppose we have two data groups of MEQs and they are all two dimensional (Figure 8.3). Group 1 is $X(x_i^1, y_i^1)$ and group 2 is $Y(x_j^2, y_j^2)$ where i, j is the object number and superscripts $1,2$ are group index of MEQ data (Table 8.1).

Table 8.1 The two data group and the same data after centering

Object Number (i,j)	x^1	y^1	x^2	y^2	$\widehat{x^1}$	$\widehat{y^1}$	$\widehat{x^2}$	$\widehat{y^2}$
1	3.5	2	2	3.5	1.2	-0.025	-2.8	0.4
2	3	2	4.5	3	0.7	-0.025	-0.3	-0.1
3	2	4	4.5	2	-0.3	1.975	-0.3	-1.1
4	3	3	7	3	0.7	0.975	2.2	-0.1
5	4	2	6	4	1.7	-0.025	1.2	0.9
6	2	1.5			-0.3	-0.525		
7	1	1.5			-1.3	-0.525		
8	3	1.25			0.7	-0.775		
9	1	2			-1.3	-0.025		
10	0.5	1			-1.8	-1.025		
$\bar{X}, \bar{Y}$	2.3	2.025	4.8	3.1				

The number of MEQs in each group need not be the same. Prior to the analysis, data are often pre-processed which involves transforming the data into a suitable form for the inverse analysis. One of the most common operations is centering. The centered data matrix of each data group can be calculated as $\hat{X} = X - mean(X) = \mathrm{X} - \bar{X}$ and $\hat{Y} = Y - mean(Y) = Y - \bar{Y}$, respectively. The covariance matrix of each group is computed using the centered data matrix as follow:

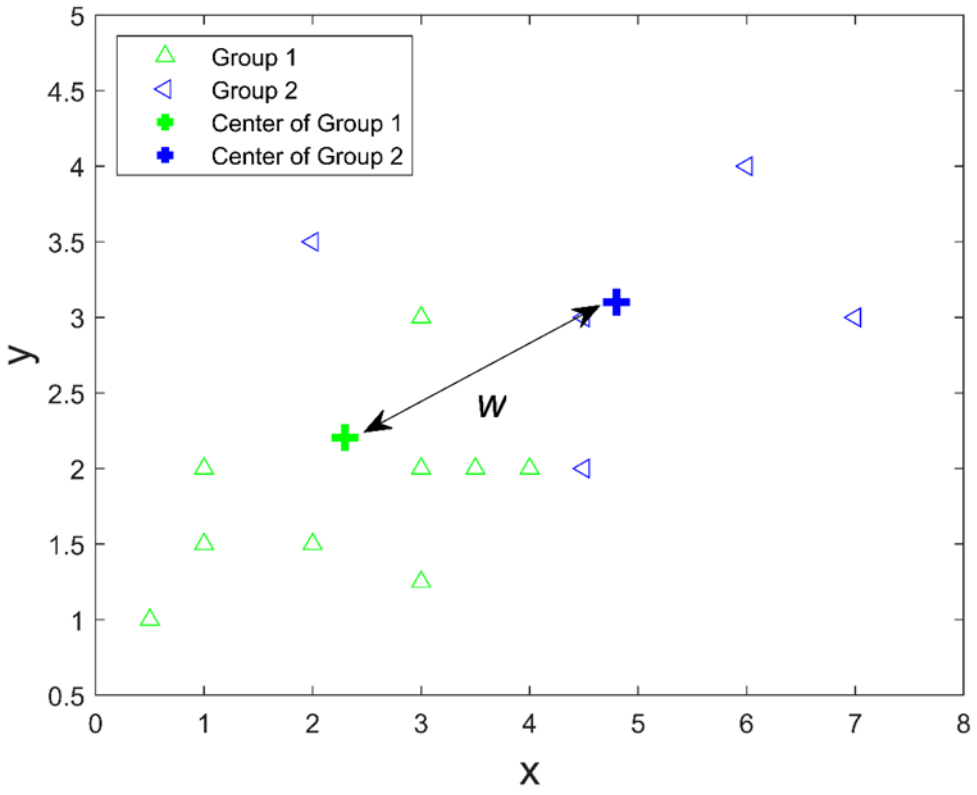

Figure 8.3 Mahalanobis distance *w* and the center of each group.

$$S_1 = \frac{1}{n_1}\hat{X}\cdot\hat{X} = \frac{1}{n_1}\begin{bmatrix}\widehat{x^1}\cdot\widehat{x^1} & \widehat{x^1}\cdot\widehat{y^1}\\ \widehat{y^1}\cdot\widehat{x^1} & \widehat{y^1}\cdot\widehat{y^1}\end{bmatrix} = \begin{bmatrix}1.26 & 0.22\\ 0.22 & 0.71\end{bmatrix} \tag{8.10}$$

$$S_2 = \frac{1}{n_2}\hat{Y}\cdot\hat{Y} = \frac{1}{n_2}\begin{bmatrix}\widehat{x^2}\cdot\widehat{x^2} & \widehat{x^2}\cdot\widehat{y^2}\\ \widehat{y^2}\cdot\widehat{x^2} & \widehat{y^2}\cdot\widehat{y^2}\end{bmatrix} = \begin{bmatrix}2.86 & 0.02\\ 0.02 & 0.44\end{bmatrix} \tag{8.11}$$

Where n_1 and n_2 represent the number of data in groups 1 and 2, respectively. $(x^1 \cdot y^1)$ is the dot product of two vectors. The pooled covariance matrix (integration of two covariance matrix into one covariance matrix of all data) S is calculated as:

$$S = \frac{n_1}{n_1+n_2}S_1 + \frac{n_2}{n_1+n_2}S_2 \tag{8.12}$$

The value of MD, $w(X,Y)$, is calculated as:

$$w(X,Y) = \sqrt{(\bar{X}-\bar{Y})^T S^{-1}(\bar{X}-\bar{Y})} = 2.172 \tag{8.13}$$

where S^{-1} is the inverse of the pooled covariance matrix. The value of w is larger than zero and represents the matching level between those two groups. If the value of w is smaller, the simulated data have higher matching level with the observed data.

8.2.4 Inverse Analysis GBSAM

To interpret field-observed MEQ distribution for natural fracture orientations, we propose a general inverse analysis named GBSAM. The main components of GBSAM include a forward model for pore pressure e.g., the finite duration line injection model, simulated MEQs generation model, and Mahalanobis distance. To simplify the analysis to estimate the natural fracture orientations from a highly complex reservoir system, the variables of the problem need to be reduced. Specifically, the number of natural fractures and their location, the natural fracture sets, as well as the shape of the natural fractures and their radius need be estimated to constrain the uncertainty before the inverse analysis starts. A field-observed seismic event is assumed to represent a natural fracture in the reservoir because the spatial distribution of field-observed MEQs are scattered in the reservoir (Fang, Elsworth et al. 2018). Thus the number of natural fractures in GBSAM is assumed to equal to the number of field-observed MEQs and the natural fractures in GBSAM have the same location as the field-observed MEQ distribution. The reservoir may have multiple natural fracture sets. In each iteration of the solution procedure, the natural fracture at the field-observed MEQ location could be from any of the multiple sets assumed. Before an iteration starts, the fracture at a point is randomly chosen from the total sample population (including all natural fracture sets). Each natural fracture set has the same number of the natural fractures. The natural fractures are assumed to be penny-shaped and their radii are pre-defined based on field studies. In each natural fracture set,

natural fracture orientations are assumed to be normal (other distributions can be considered but both groups should have identical distributions) (Long, Remer et al. 1982, Gutierrez and Youn 2015). These assumptions preserve the GBSAM characteristics while optimizing the inverse analysis. Here we need to point out that GBSAM is not intended to predict the orientation of individual natural fractures in a large set. It intends to find the likely orientation of each set.

The goal of this study is to identify the unknown natural fracture orientations $n = \{n_x, n_y, n_z\}$ or $\{dip, dip\ direction\}$ by performing inverse analysis. n is the normal direction of a fracture plane. It is more convenient to use a vector normal to the fracture plane in the computations. Here a simple example with synthetic data is used to illustrate the main steps of GBSAM. In this example, the reservoir has two sets of natural fractures and the fracture sets have identical distributions.

Step 1. Define all parameters, but the natural fracture orientations. In this example, all fractures in a set have the same orientation (although one could consider other distribution of orientations). The initial orientations of each set are the same and can be given by any value and we arbitrarily choose: $\{n_x^1, n_y^1, n_z^1\} = \{0.01, 0.01, \sqrt{1 - 0.01^2 - 0.01^2}\}$ and $\{n_x^2, n_y^2, n_z^2\} = \{0.01, 0.01, \sqrt{1 - 0.01^2 - 0.01^2}\}$. The number of natural fractures in each set is identical so as to exclude the influences of the difference between natural fractures density of each set. In the first solution step, we let the two sets be identical to ascertain if a single set of fractures fits the data.

Step 2. Compute the distribution of stress and pore pressure and shear energy on the fracture planes. The shear energy is $\tau^2 \cdot A/(2G)$, where τ is shear stress and G is shear modulus and A is the area of fracture plane. Step 2 is the start point of an iteration.

Step 3. Check whether the Coulomb failure function (CFF) of each fracture is larger than zero. If CFF is positive, frictional sliding occurs on a fracture and a simulated MEQs are generated at the center of the fracture. One third of shear energy is supposed to be released in the form of seismic waves during fracture slipping processes. If the seismic energy is larger than the pre-defined threshold energy of MEQs, additional simulated MEQs will be generated. The number of additionally generated MEQs is the integer part of the ratio of the released seismic energy to pre-defined threshold energy of MEQs. Those additional simulated MEQs are randomly distributed on the fracture plane.

Step 4. Compare the simulated MEQ distribution with the field-observed MEQ distribution via MD (for the overall sets). Calculate the value of MD w_i using equation (8.13) where i is the ith iteration. The calculation of MD w_i is dependent on the simulated MEQ distribution generated by the entire natural fracture population. Thus, MD is calculated for all natural fracture populations.

Step 5. Store the value of MD w_i, fracture orientations and the current number of iteration i. Calculate the average value of MD $v_i = \frac{\sum w_i}{i}$ (for all sets) and the sum ($\sum w_i$) is for the number of iteration. Step 5 is the end point of an iteration.

Step 6. Repeat calculation from step 2 to step 5 until the $|v_i - v_{i-1}| \leq \varepsilon$ (ε is a small number) to ensure stability. Store the average value of MD v_i and the number of iteration i. In each iteration the natural fracture at an MEQ location could belong to a different set than in the previous iteration so that v_i will change from iteration to iteration.

Step 7. Update the natural fracture orientations by increasing n_y^2 from 0.01 to 0.02. The strategy for updating the orientations is to try to test any combination of fracture orientations. Thus the fracture orientations starts from n_y or n_z or n_x without affecting

the final results. Now, the fracture orientations are: $\{n_x^1, n_y^1, n_z^1\} = \{0.01, 0.01, \sqrt{1-0.01^2-0.01^2}\}$ and $\{n_x^2, n_y^2, n_z^2\} = \{0.01, 0.02, \sqrt{1-0.01^2-0.02^2}\}$. The number of iteration i is restarted from one. Furthermore, there are formulas for converting from a fracture normal to dip and dip direction (Allmendinger, Cardozo et al. 2011).

Step 8. Repeat calculations from step 2 to step 7, i.e., the process of considering every combination of orientations exactly once via tree search algorithm.

Step 9. The natural fracture orientations yielding the minimum average value of MD v is assumed to represent the true reservoir conditions.

One needs to check whether the GBSAM has converged during the solution process. For instance, Figure 8.4(a) shows the evolution of the value of MD w, with the number of iteration when $\{n_x^1, n_y^1, n_z^1\} = \{0.1, 0.95, 0.31\}$ and $\{n_x^2, n_y^2, n_z^2\} = \{0.1, 0.96, 0.27\}$. The value of MD w seems disorganized, yet they still are distributed around a certain value 0.208. Figure 8.4(b) shows that, the average value of the MD v becomes smooth and constant when the number of iteration is larger than 600. Figure 8.4(c) is an error bar analysis which shows that the maximum value of the standard deviation is only 0.0002 when the number of iteration is 600. Thus GBSAM is considered to be stable and unique.

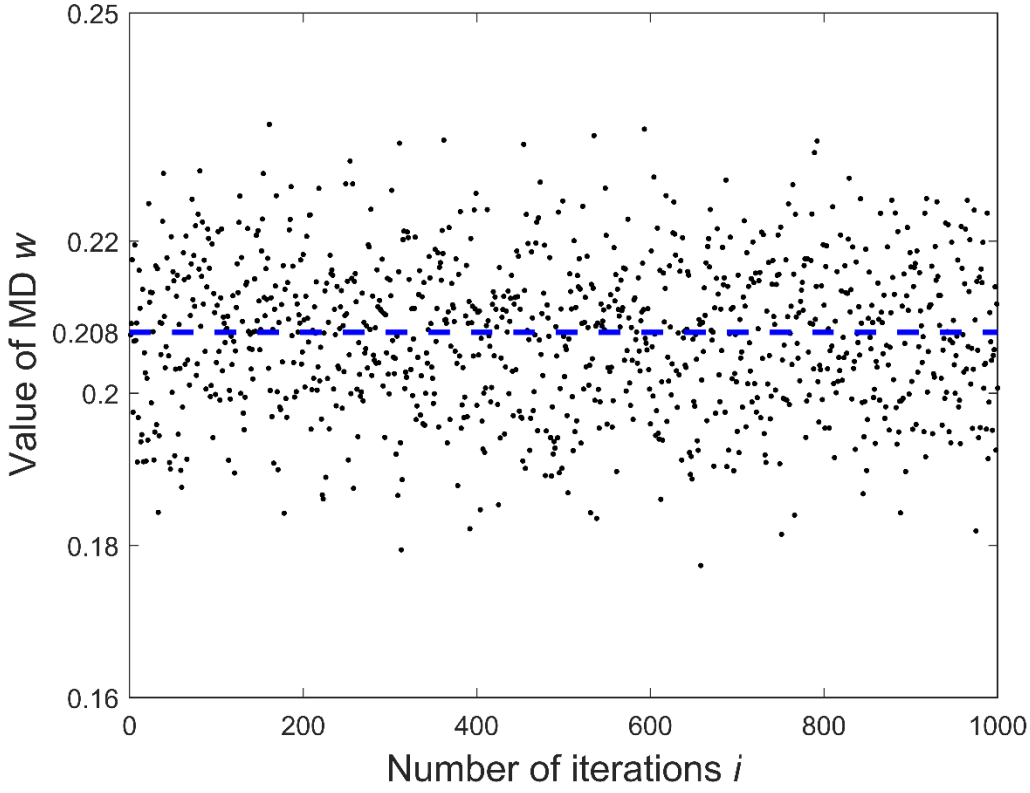
0.25
0.22
0.208
0.2
0.18
0.16
Value of MD w
0
200
400
600
800
1000
Number of iterations i

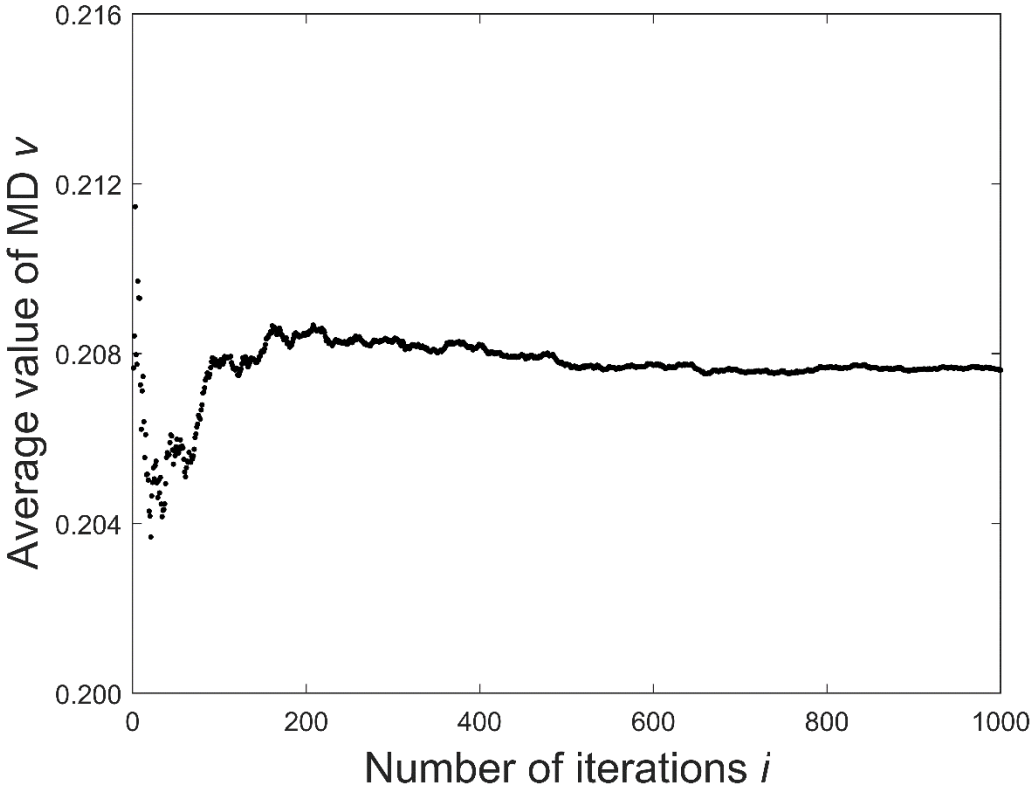
0.216
0.212
0.208
0.204
0.200
Average value of MD v
0
200
400
600
800
1000
Number of iterations i

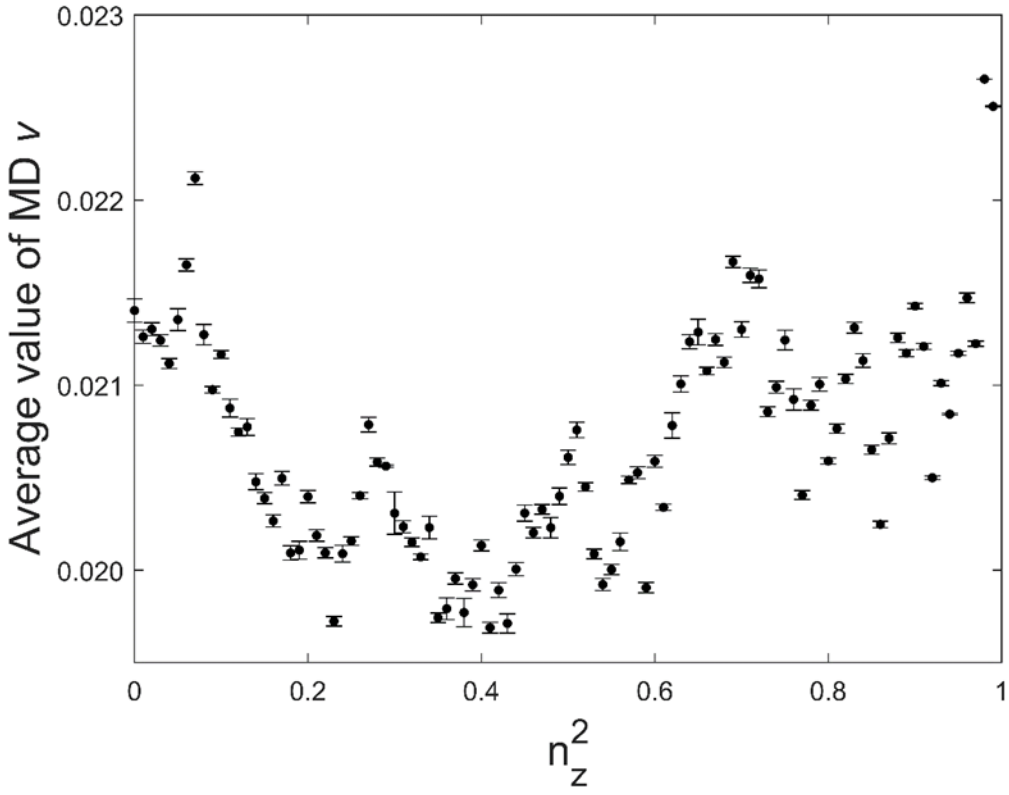

Figure 8.4 Results analysis of GBSAM: (a) the evolution of value of MD w with iterations with $n_z^1 = 0.31$ and $n_z^2 = 0.27$; (b) the evolution of average value of MD v with iterations $n_z^1 = 0.31$ and $n_z^2 = 0.27$; (c) the error bar analysis for GBSAM with $n_z^1 = 0.31$ and n_z^2 from 0 to 1.

From the above analysis, one needs to select an appropriate maximum iteration number to ensure GBSAM stability during the process.

8.3 Newberry EGS Example

In this section, GBSAM is applied to estimate the natural fracture orientations of Newberry Volcano EGS demonstration. Phase 2.2 of Newberry EGS stimulation lasted from September 23, 2014 to November 21, 2014. During this time period, about 2.5 million gallons (9464 m^3) of water were injected. A fall-off test was carried out from October 15 to November 10. During phase 2.2 stimulation, 344 field-observed MEQs were located and recorded. Borehole televiewer (BHTV) was used to map the natural

fractures and 399 fractures were recorded. Those fractures are intersecting the wellbore and do not necessarily correlate with the 344 field-observed MEQs. In order to predicate the natural fracture orientations of Newberry EGS, further assumptions are needed. The orientation of the natural fracture system is supposed to follow a normal distribution (Long, Remer et al. 1982, Gutierrez and Youn 2015). The standard deviation σ is kept constant while the mean μ varies during the inverse analysis.

In this example, we use a line source of length equal to the length of the open hole section of well NWG 55-29, with the same average inject rate $Q = \frac{0.063m^3}{s}$. The length of the open section of well NWG 55-29 is 906 m. The reservoir properties in GBSAM used are shown in Table 8.2. The permeability used in this example is the estimated value for the John Day formation (Cladouhos, Petty et al. 2015).

Table 8.2 Parameters used in this work for Newberry simulations.

Parameter	Variable	Value and unit
Vertical Stress (z direction)	σ_z	$67MPa$
Maximum Horizontal Stress(x direction)	σ_x	$46MPa$
Minimum Horizontal Stress(y direction)	σ_y	$30MPa$
Injection time	t	$58\ days$
Injection rate	Q	$0.0063\ m^3/s$
Shear modulus	G	$10GPa$
Fluid Viscosity	μ_f	$0.40 \cdot 10^{-3} Pa \cdot s$
Permeability	k	$1 \cdot 10^{-15} m^2$
Hydraulic diffusivity	c	$19 \cdot 10^{-2} m^2/s$

Cohesive strength	c'	0
Friction coefficient	μ_s	0.52
Total number of iterations		600
Permeability zone of thickness	$2h$	$906m$
Standard deviation for dip	Degree	$\sqrt{80}$
Standard deviation for dip direction	Degree	$\sqrt{160}$
Natural fracture radius		$60m$

We carry out the invers analysis which was mentioned in the chapter 7.2. The results from the GBSAM show that the fractures average dip is $\{\mu, \sigma\} = \left\{60^o, \sqrt{80}^o\right\}$ and the fracture dip direction are $\{\mu, \sigma\} = \left\{100^o, \sqrt{160}^o\right\}$ and $\{\mu, \sigma\} = \left\{270^o, \sqrt{160}^o\right\}$. Figure 8.5 shows the results from GBSAM and the results from BHTV. As can be observed from Figure 8.5(a), fracture dips from GBSAM are in good agreement with observations from BHTV while BHTV is not always available and it only represents the near wellbore region which may or may not reflect the reservoir. Figure 8.5(b) shows that the natural fractures dip directions from GBSAM are also in good agreement with observation from BHTV. The total number of simulated MEQ distribution is 370 indicating that some natural fractures may generate multiple MEQ events under the given conditions. For instance, if the fracture orientations are appropriately assigned and released seismic energy is high, hundreds of simulated MEQs may occur on the same natural fracture planes. As shown in Figures 8.5(c)-(e), the simulated MEQ distribution has a good match with the field-

observed MEQ distribution so that the fracture orientations in GBSAM have a good match with the fracture orientations in the reservoir.

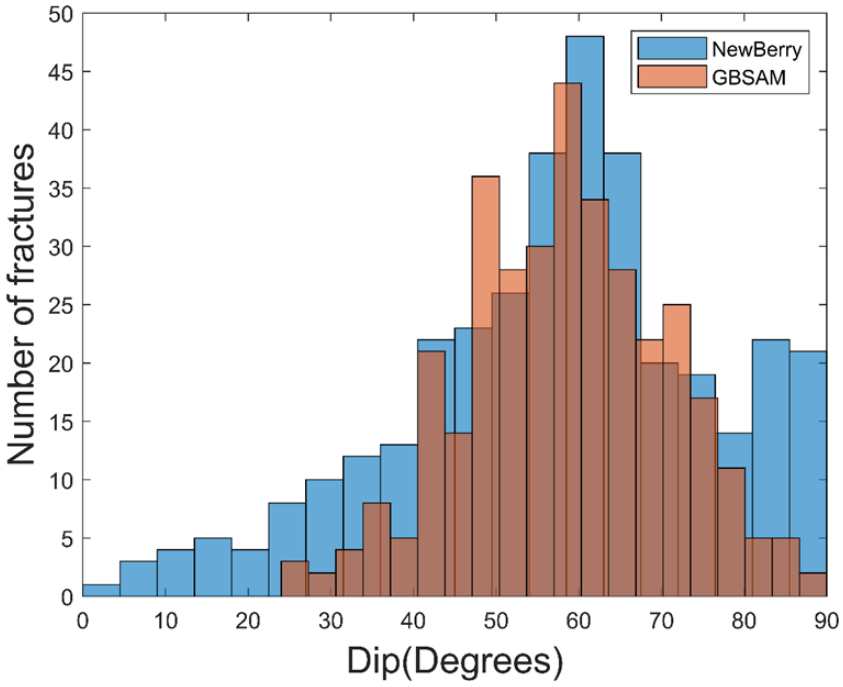

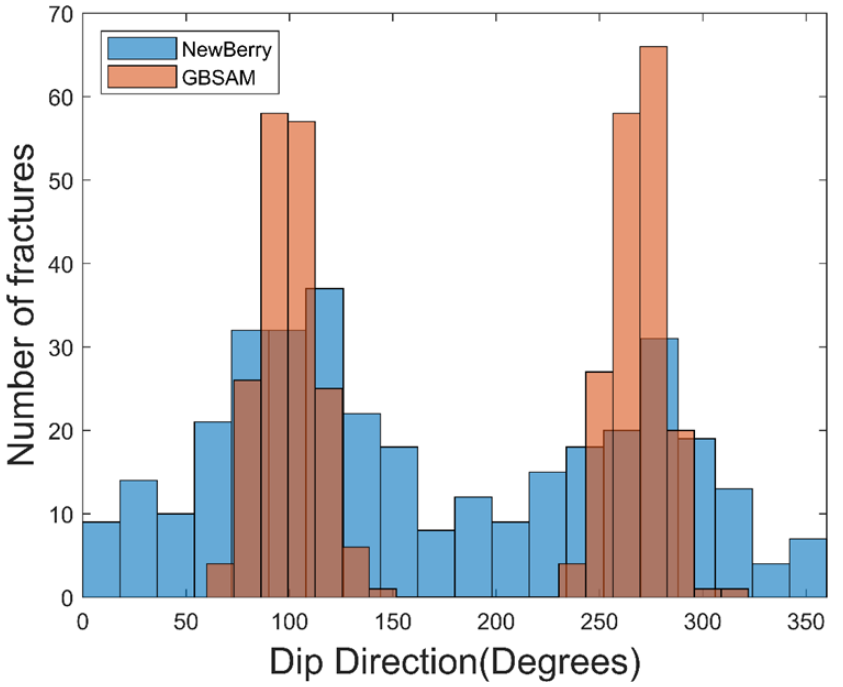

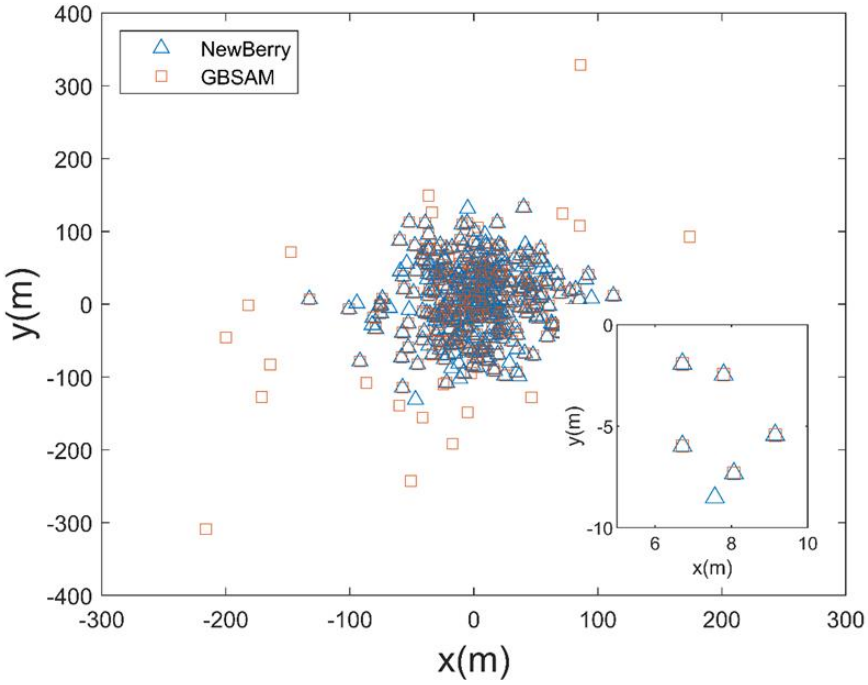
NewBerry
GBSAM
y(m)
x(m)
400
300
200
100
0
-100
-200
-300
-400
-300
-200
-100
0
100
200
300
0
-5
-10
6
8
10
y(m)
x(m)

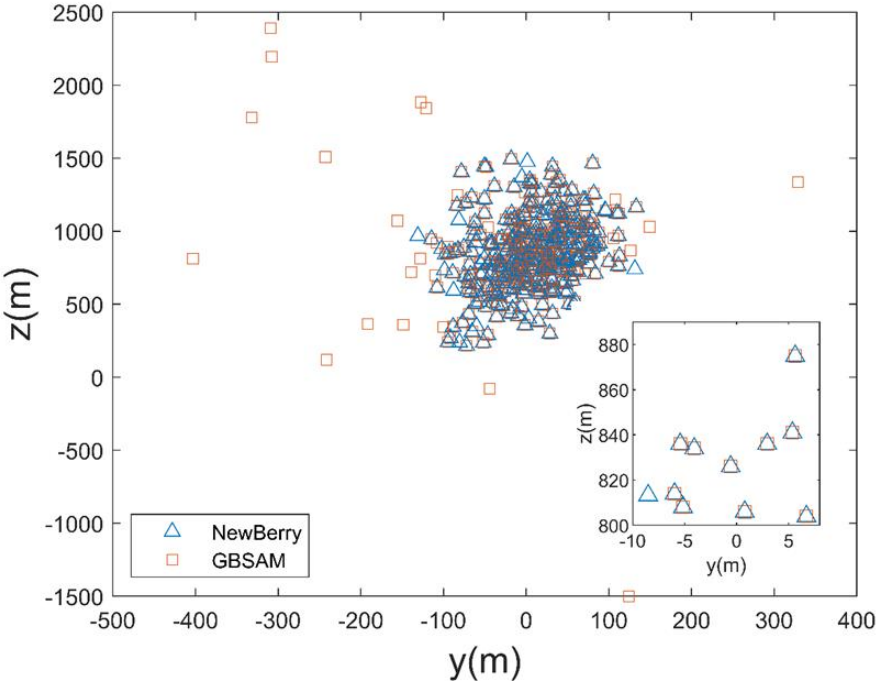
NewBerry
GBSAM
z(m)
y(m)
2500
2000
1500
1000
500
0
-500
-1000
-1500
-500
-400
-300
-200
-100
0
100
200
300
400
880
860
840
820
800
-10
-5
0
5
z(m)
y(m)

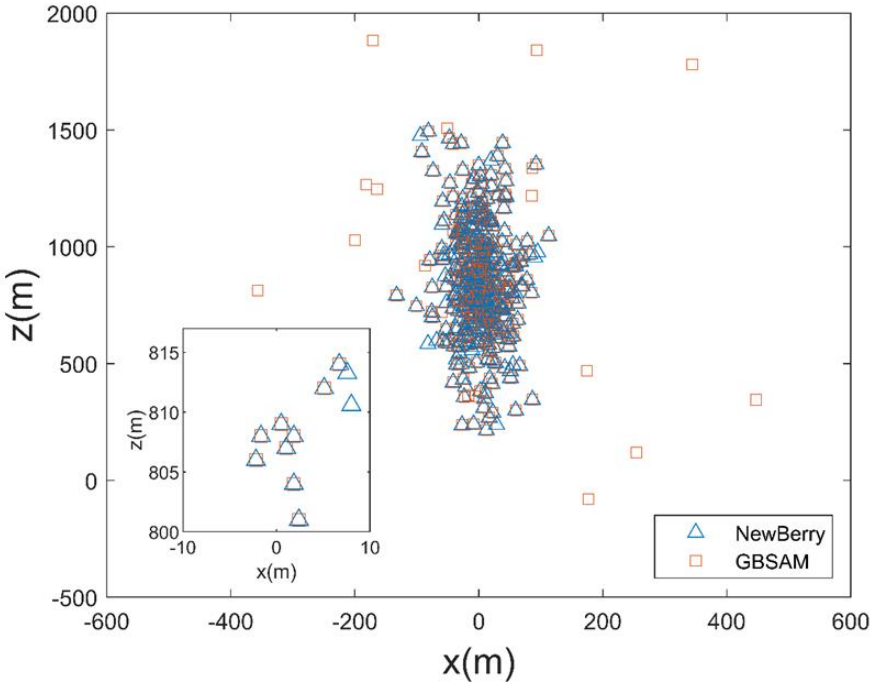

Figure 8.5 (a) Comparison between fracture dip from GBSAM and fracture dip from BHTV. (b) Comparison between fracture dip direction from GBSAM and fracture dip direction from BHTV. (c)~ (e) Map view of the simulated MEQ distribution and the field-observed MEQ distribution.

Note that the MEQ locations from the simulations and the data are not exactly the same since the model allows for multiple MEQs on a fracture. The figures only show that the overall populations are similar.

8.4 Fenton Hill HDR Example

The Fenton Hill HDR project was carried out from 1970 to 1995 at Fenton Hill, New Mexico. During this time period, the Los Alamos National Laboratory created and tested two reservoirs at depths in the range of 2.8-3.5 km. The first reservoir, named the Phase I reservoir, was created at a depth interval of 2800-2950m. The second reservoir, named the Phase II reservoir, was created at a depth of around 3500m. Figure 8.6 shows the location map of Fenton Hill HDR and a simplified geological map of the Jemez volcanic field and the Espanola Basin of the Rio Grande Rift in north-central New Mexico.

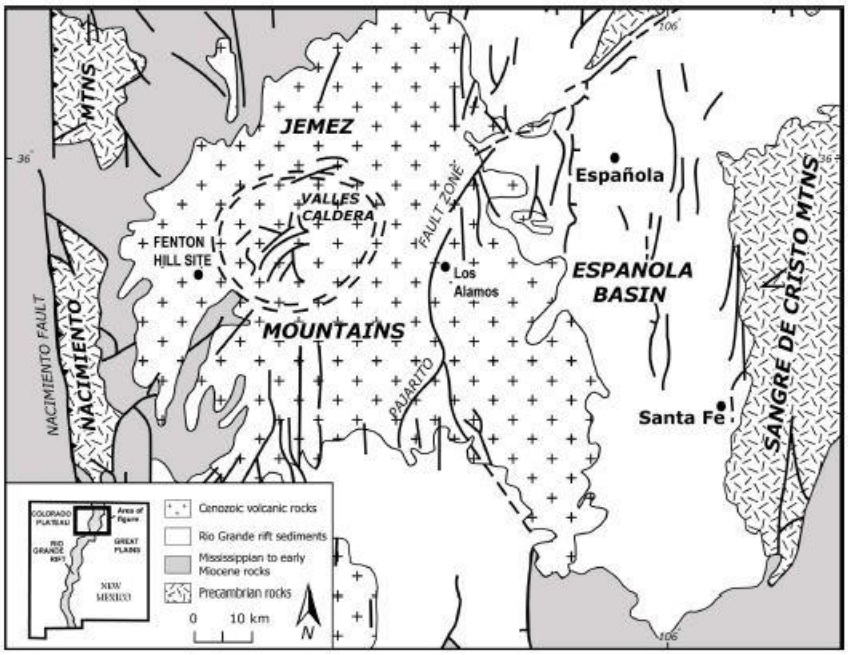

Figure 8.6 Location map of the Fenton Hill HDR site and simplified geological map of the Jemez volcanic field and the Espanola Basin of the Rio Grande Rift in north-central New Mexico (after Baldridge et al., 1995).

Downhole and surface geophones were installed in the vicinity of the experimental site for seismic monitoring. An on-line system for recording and locating 3886 field-observed MEQ distribution was developed and deployed. Table 8.3 lists the input parameters for GBSAM. Figure 8.7(a) and (b) show the results from the GBSAM. These results show that the natural fracture's dip is $\{\mu, \sigma\} = \left\{60^o, \sqrt{80}^o\right\}$ and the natural fracture dip directions are $\{\mu, \sigma\} = \left\{80^o, \sqrt{160}^o\right\}$. Figure 8.7(a) shows that the fracture dips from GBSAM are in good agreement with observations from the results in (Roff, Phillips et al. 1996) and Figure 8.7(b) shows that the fracture dip directions from GBSAM are also in good agreement with observation from Raff's results (Roff, Phillips et al. 1996). The total number of simulated MEQs is 4816 indicating that some natural fractures may generates multiple MEQ events under the given conditions. From Figure 8.7 (c)-(e), simulated MEQ distribution has a good match with field-observed MEQ distribution so that it is

likely that the fracture orientations in GBSAM reflect the fracture orientations in the reservoir.

Table 8.3 Parameters used in Fenton Hill HDR (Brown, Duchane et al. 2012)

Parameter	Variable	Value and unit
Vertical Stress (z direction)	σ_z	$90MPa$
Maximum Horizontal Stress(x direction)	σ_x	$45MPa$
Minimum Horizontal Stress(y direction)	σ_y	$30MPa$
Injection time	t	$2.5\ days$
Injection rate	Q	$0.0097\ m^3/s$
Shear modulus	G	$21GPa$
Fluid Viscosity	μ_f	$0.47 \cdot 10^{-3} Pa \cdot s$
Permeability	k	$0.9 \cdot 10^{-15} m^2$
Hydraulic diffusivity	c	$21 \cdot 10^{-2} m^2/s$
Cohesive strength	c'	$1MPa$
Friction coefficient	μ_s	0.50
Total number of iterations		600
Permeability zone of thickness	h	$1000m$
Standard deviation for dip	Degree	$\sqrt{80}$
Standard deviation for dip direction	Degree	$\sqrt{160}$
Natural fracture radius		$60m$

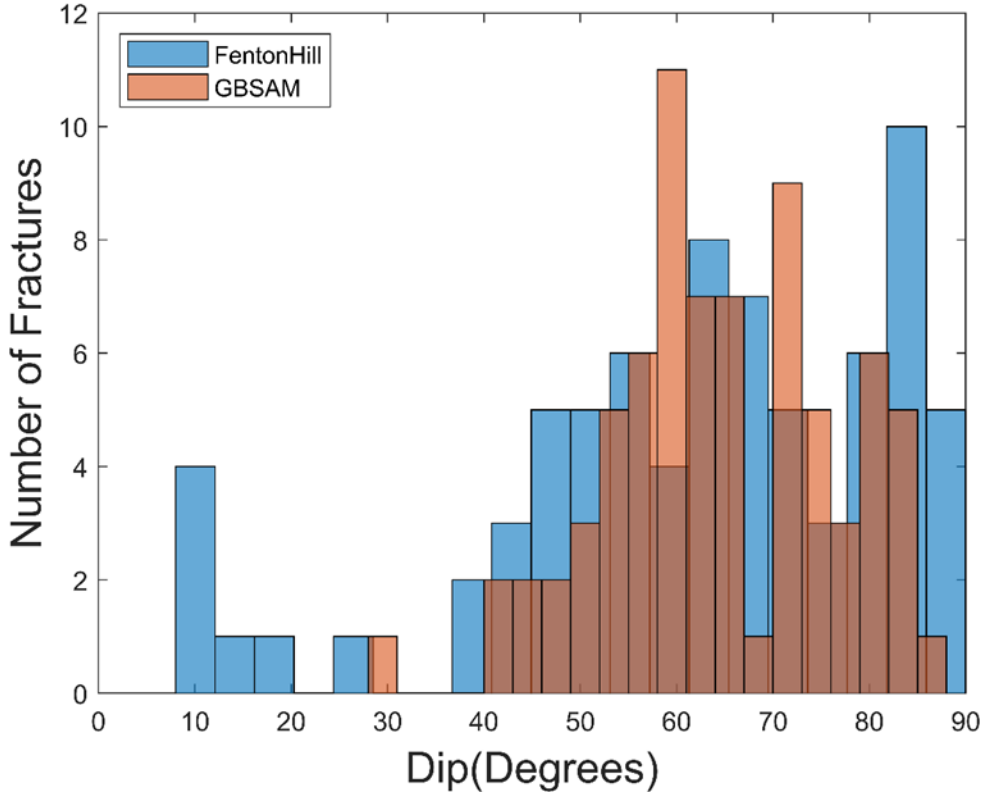
FentonHill
GBSAM
Number of Fractures
Dip(Degrees)
0
2
4
6
8
10
12
0
10
20
30
40
50
60
70
80
90

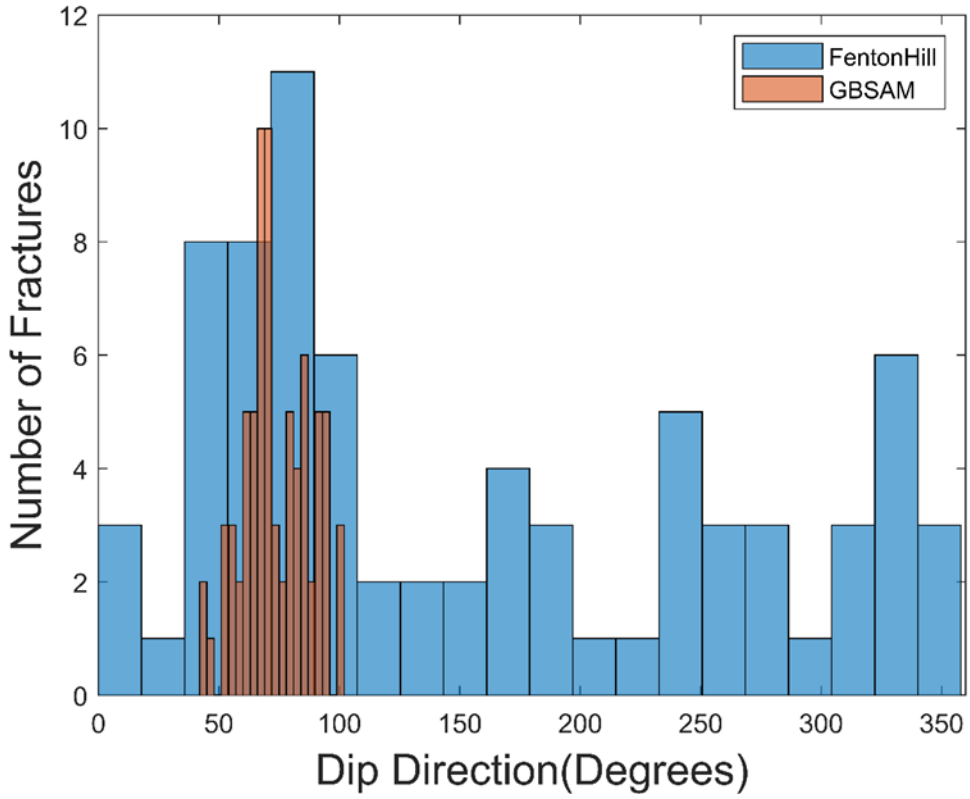
FentonHill
GBSAM
Number of Fractures
Dip Direction(Degrees)
0
2
4
6
8
10
12
0
50
100
150
200
250
300
350

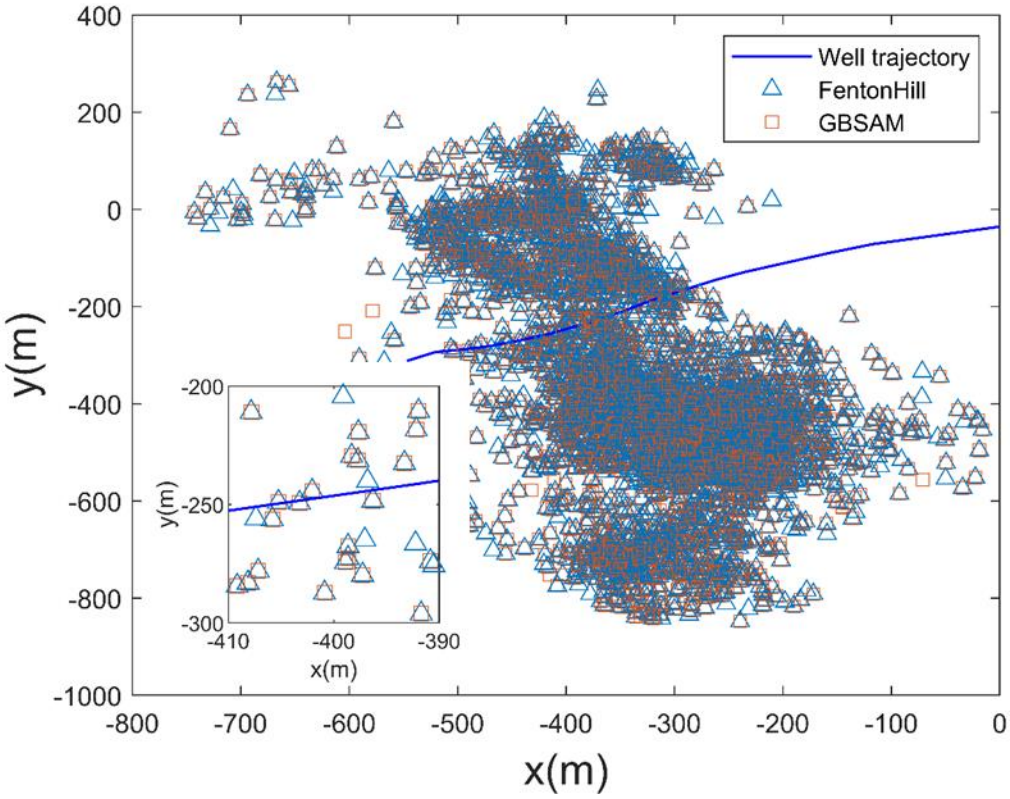
Well trajectory
FentonHill
GBSAM
y(m)
x(m)
400
200
0
-200
-400
-600
-800
-1000
-800
-700
-600
-500
-400
-300
-200
-100
0
-200
-250
-300
-410
-400
-390
y(m)
x(m)

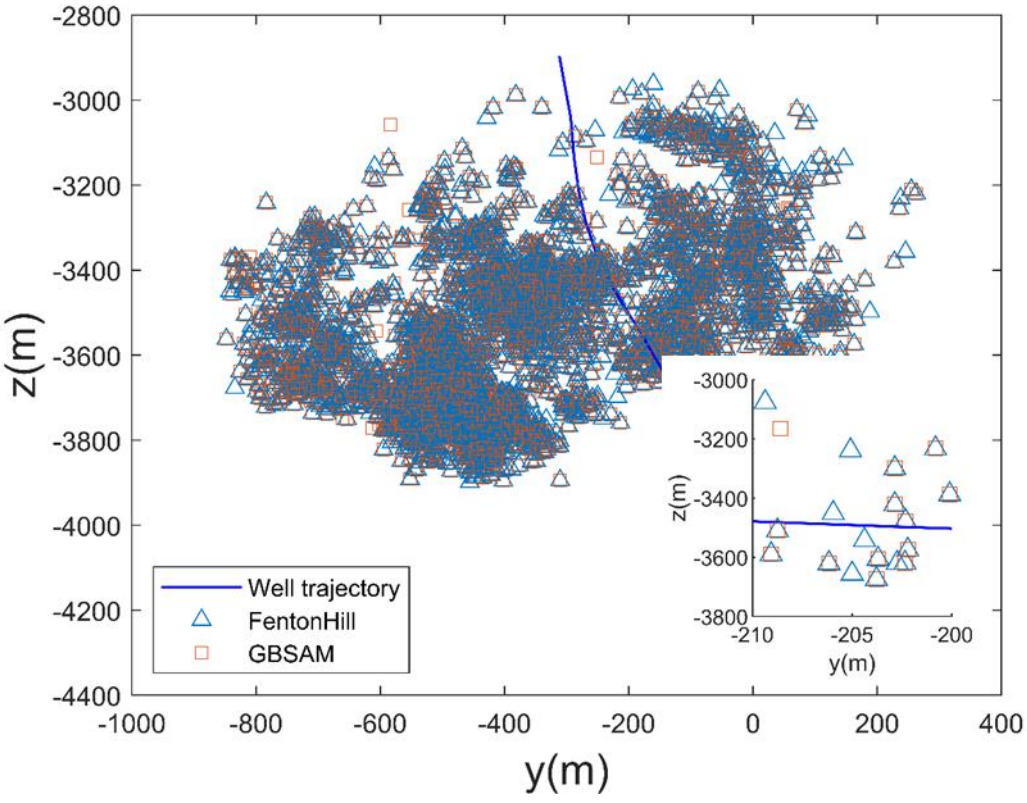
Well trajectory
FentonHill
GBSAM
z(m)
y(m)
-2800
-3000
-3200
-3400
-3600
-3800
-4000
-4200
-4400
-1000
-800
-600
-400
-200
0
200
400
-3000
-3200
-3400
-3600
-3800
-210
-205
-200
z(m)
y(m)

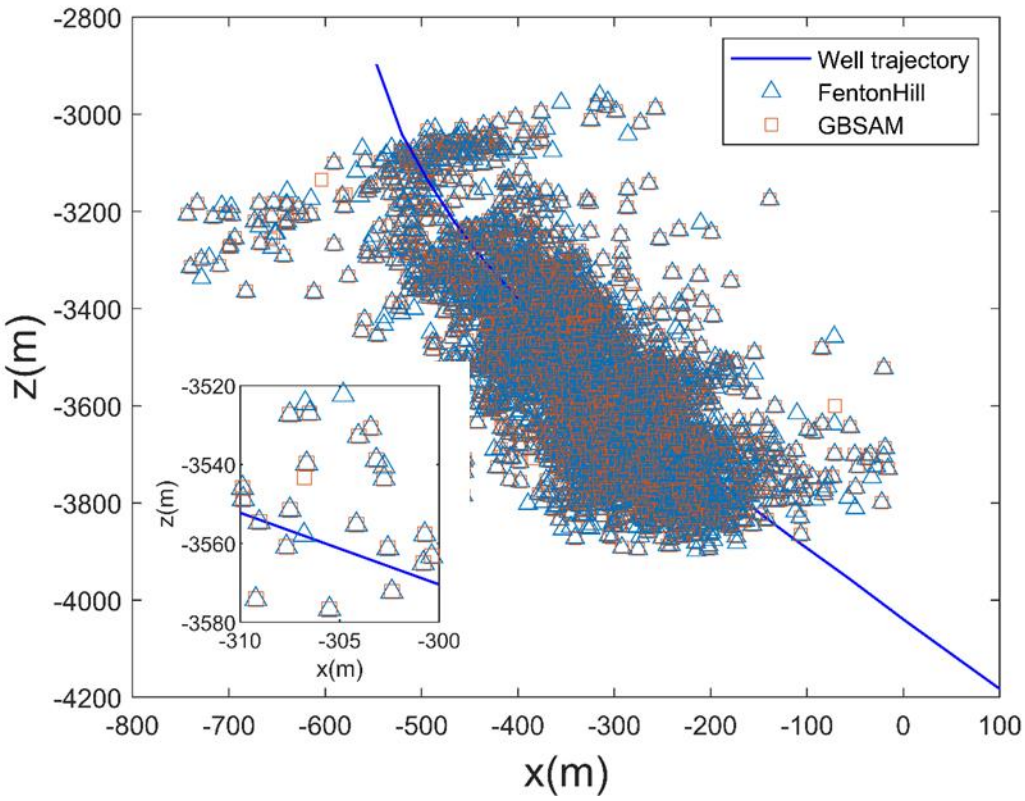

Figure 8.7 (a) Comparison between fracture dip from GBSAM and fracture dip from previous results (Roff et al., 1996). (b) Comparison between fracture dip direction from GBSAM and fracture dip direction from Raff's results. (c)~ (e) Map view of simulated MEQ distribution and field-observed MEQ distribution.

8.5 Discussion and Conclusion

Constraining the natural fracture orientations in reservoirs is of high interest to geothermal and petroleum industry. Natural fracture orientations are typically estimated from 1-D scan lines in outcrops and boreholes imaging logging, or 2D circular sampling in outcrops. Boreholes image logging provides critical data for measuring fracture orientations at applicable operational temperature of the tool. However, image logs provide fracture orientations at the wellbore scale and difficulties and uncertainties exist in upscaling the results to the field scale.

An effective method has to integrate tools from geology, geophysics, and geomechanics geostatistics to characterize the natural fracture orientations. In this work, we propose GBSAM to constrain the natural fracture orientations by combining a geomechanics and geostatistics model to interpret microseismic data. The pore pressure changes are modeled using a finite duration line source rather than a point source. The distribution of the simulated MEQ can be affected by the properties of the source model. The diffusion path of the pore pressure generated by a point source model is different from the diffusion path of the pore pressure generated by a line source model. The shape of MEQ cloud from those two can therefore be also different. This would depend on the reservoir structure and given such significant level of uncertainty and heterogeneity in geothermal reservoir permeability, the point source model is not pursued. The core steps in GBSAM are handling with discrete MEQs data and measuring similarity between the field-observed MEQ distribution and the simulated MEQ distribution. Here we have applied Mahalanobis distance, a common tool from data sciences to measure similarity between field-observed MEQ distribution and simulated MEQ distribution. The mechanism of generating simulated MEQ distribution has also been improved, allowing fracture to have multiple simulated MEQs. The number of additional simulated MEQs on a fracture is defined as the integer part of the ratio of released seismic energy to threshold seismic energy. In order to verify the model, GBSAM is applied to extract information about natural fracture orientations (dip and dip direction) in two case studies, Newberry EGS and the Fenton Hill HDR. Results from GBSAM are in good agreement with results from boreholes image logging or previous studies in those case studies. This inverse analysis

is the first of its kind and enables us to estimate natural fracture orientations using microseismic data.

Chapter 9 Conclusions and Future Work

9.1 Summary of the Dissertation and Original Contributions

A fully coupled thermo-hydro-mechanical-seismic (THMS) finite element model with a dynamic 3D fracture network has been developed. The model can consider fracture propagation and induced seismicity. Several verifications and general examples are presented for the THMS with a dynamic 3D fracture network. The fractur network model is applied to simulate the Collab testbed 1 (May 24, Stim-II HF@164 Notch). Numerical simulations show that the simulated fracture pressure profiles reasonably follow the trend observed in the field test. The simulations support the concept that a natural fracture was propagated from the injection well connecting with the production well via intersection and coalescence with other natural fractures consistent with plausible flow paths observed on the field. The distribution of simulated MEQs have good agreement with the field-observed MEQs.

Then the Coupled Thermo-Hydro-Mechanical-Seismic Model with the 3D fracture network (with rate state friction law) is used to assess the effects of fluid diffusion and poroelastic stress on induced seismicity. Two types of injection scenarios are designed in the numerical simulations to distinguish and to underscore the contributions of fluid diffusion and poroelastic stress to the fracture stability and induced seismicity. The poroelastic effects can perturb the stress field in the vicinity of the injection location and gives rise to extension/compression zones. The distribution of tensile and compressive stress state will be determined by the fracture location, orientation, injection location, as well as matrix diffusivity and fracture connectivity in the reservoir. In one injection scenario water is injected on the entire surface of the fracture and the diffusion time is

very small. As the fluid diffuses into the rock matrix, the poroelastic effect causes the total normal stress acting on the fracture to increase, contributing to fracture stability. This is because the surrounding zone of the fracture experiences compression due to the poroelastic effect in response to pore pressure buildup. In contrast, fracture pressure significantly increases when injecting into the fracture. Therefore, the effective normal stress is decreased. In a second scenario fluid is injected some distance away from the fracture and the diffusion time is relatively large. In this case, the poroelastic effect favors fracture slip due to increased poroelastic tensile stress ahead of the compression zone.

The model has the capability to consider the effects of fracture roughness on fracture failure and induced seismicity. The role of the spatial distribution of fracture roughness on seismic events pattern on the fracture plane is investigated. Such model is applied to a current laboratory test and the simulated seismicity generally matches the lab observation. The simulated results show that the lower JRC (roughness), the higher the likelihood seismicity occurs on the fracture when the length of unstable zone is larger than the nucleation length. The model is also applied to simulate the stimulation of a planned wellbore in the Utah FORGE EGS to help optimize the wellbore trajectory for best stimulation outcome. Finally, a Geomechanics-Based Stochastic Analysis of Microseismicity (GBSAM) method is developed to estimate fracture orientation from seismicity data. This GBSAM is applied to the Newberry EGS and Fenton Hill HDR experiment to characterize the natural fracture network. The results agree well with field data.

In summary, the original contributions of this dissertation are:

1. Mahalanobis distance, a type of similarity measure technique, is used to measure the similarity between the simulated MEQs distribution and the field-observed MEQs distribution to find the best natural fracture distribution that fits the field-observed MEQs data. The natural fractures orientations which correspond to the best simulated MEQs distribution in the GBSAM is a realistic realization of the subsurface conditions.

2. A dual-scale semi-deterministic fracture network model is developed that can combine data derived from image logs, foliations/micro fractures, core with fracture properties which follow a stochastic distribution. The variation of micro fracture/foliations away from the fracture follow a stochastic distribution (Lognormal distribution). An advantage of this fracture network model is that measurement data can be incorporated to constrain the uncertainties in the rock mass.

3. An ultrafast analytic approach for fracture propagation is presented using the maximum tensile stress criterion and the concept of dynamic fictitious plane. Both non-planar and planar propagation are considered in this approach. The fictitious plane is best fitted by the updated fracture tips and fracture process of propagation is performed on this fictitious plane.

4. Two prescribed conditions (threshold slip rate and threshold slip distance) are proposed to distinguish between the seismic and aseismic slip on a fracture. The Gutenberg-Richter law is employed to constrain the number and magnitude of MEQs by two prescribed conditions (energy conservation and magnitude of the background seismicity).

5. The spatial variability of JRC is obtained through the concept of stochastic partitioning of fracture plane. The spatial distribution of the fracture shear stiffness as a function of the effective normal stress is mapped based on the distribution of JRC. A critical velocity

as a function of fracture shear stiffness is defined to distinguish between the seismic/aseismic states. The effects of load rate on the transition between aseismic and seismic can be explored.

6. The extended Fourier transform method is presented to use two Hurst exponents in x- and y-directions, and the amplitude parameters (RMS) of scan points on the fracture are used to generate a self-affine anisotropic surface. The JRC- Hurst exponent relations can be estimated by performing the calculation of JRC over the self-affine synthetic isotropic/anisotropic roughness derived by two Hurst exponents H_x, H_y and RMS. The advantage of JRC- Hurst exponent relation over others is that the full spectrum of H with JRC are covered and effects of anisotropic roughness on JRC are also considered.

9.2 Recommendations for Future Work

The future work may include the flowing aspects:

1. Accurate numerical simulation of fracture network deformation and fluid flow is crucial to the assessment of the evolution of in-situ stress at field scale during the fractured reservoir stimulation. A linear complementarity problem (LCP) with regularized friction can be introduced for robustly handling the fracture network friction contact problems. Therefore, the friction contact problem can be set up as an LCP and the stability and accuracy of numerical program are enhanced.

2. The multiscale nature of the fracture surface on seismicity patterns, fracture deformation and fluid flow can be further studied. Roughness and planarity are the primary components of the fracture surface at small scale and large scale, respectively. At small scale, fracture roughness significantly contributes to the fracture shear strength. As the fracture size increases, both roughness and planarity components provide the shear

resisting during the fracture shear slip. Specifically, fracture planarity may cause the fracture to climb during the processes of shear slip. Fracture surface's gradual separation and shear strength should be decreased. As the fracture size continues to increase, both roughness and planarity components enter the problem, and the shear strength tend to stable over the fracture size. Therefore, fracture planarity needs to be considered in the procedure of upscaling JRC.

Additional model applications:

1. The evolution of in-situ stress at field scale during the fractured reservoir stimulation is of interest. Geomechanical modeling of 3D in-situ stress at field scale is essential to study the relative importance of stress source and assess the fault slip potential. However, the magnitude of maximum horizontal stress is needed to constrain to calibrate the geomechanical model. This can be achieved by combining the geomechanical model with source mechanisms of seismicity.
2. Integrated geomechanical modeling and distributed acoustic sensing can be used to advance the characterization of fractured reservoir stimulation. Distributed acoustic sensors (DAS) installed in boreholes provide continuous data on fracturing processes and induced seismicity. These sensors measure strain (or strain rate) with high spatial resolution (~ 1 m) along the fiber and can survive extreme conditions. DAS data must be well understood to avoid potential errors and inaccurate description. Geomechanical model is recommended to integrate the DAS measurement to better interpret the DAS data.

References

Acosta-Colon, A., L. J. Pyrak-Nolte and D. D. Nolte (2009). "Laboratory-scale study of field of view and the seismic interpretation of fracture specific stiffness." Geophysical Prospecting **57**(2): 209-224.

Akarapu, S., T. Sharp and M. O. Robbins (2011). "Stiffness of Contacts between Rough Surfaces." Physical Review Letters **106**(20): 204301.

Al-Busaidi, A., J. F. Hazzard and R. P. Young (2005). "Distinct element modeling of hydraulically fractured Lac du Bonnet granite." Journal of Geophysical Research: Solid Earth **110**(B6).

Alameda-Hernández, P., J. Jiménez-Perálvarez, J. A. Palenzuela, R. El Hamdouni, C. Irigaray, M. A. Cabrerizo and J. Chacón (2014). "Improvement of the JRC Calculation Using Different Parameters Obtained Through a New Survey Method Applied to Rock Discontinuities." Rock Mechanics and Rock Engineering **47**(6): 2047-2060.

Alghannam, M. and R. Juanes (2020). "Understanding rate effects in injection-induced earthquakes." Nature Communications **11**(1): 3053.

Allis, R., M. Gwynn, C. Hardwick, W. Hurlbut and J. Moore (2018). "Thermal characteristics of the FORGE site, Milford, Utah." Geothermal Resources Council Transactions **42**: 15.

Allmann, B. P. and P. M. Shearer (2007). "Spatial and temporal stress drop variations in small earthquakes near Parkfield, California." Journal of Geophysical Research: Solid Earth **112**(B4): n/a-n/a.

Allmendinger, R. W., N. Cardozo and D. M. Fisher (2011). Structural geology algorithms: Vectors and tensors, Cambridge University Press.

Amann, F., V. Gischig, K. Evans, J. Doetsch, R. Jalali, B. Valley, H. Krietsch, N. Dutler, L. Villiger, B. Brixel, M. Klepikova, A. Kittilä, C. Madonna, S. Wiemer, M. O. Saar, S. Loew, T. Driesner, H. Maurer and D. Giardini (2018). "The seismo-hydromechanical behavior during deep geothermal reservoir stimulations: open questions tackled in a decameter-scale in situ stimulation experiment." Solid Earth **9**(1): 115-137.

Anders, M. H., S. E. Laubach and C. H. Scholz (2014). "Microfractures: A review." Journal of Structural Geology **69**: 377-394.

Asadollahi, P. (2009). "Stability analysis of a single three dimensional rock block: effect of dilatancy and high-velocity water jet impact [Ph. D thesis]." USA: University of Texas at Austin.

Asadollahi, P., M. C. A. Invernizzi, S. Addotto and F. Tonon (2010). "Experimental Validation of Modified Barton's Model for Rock Fractures." Rock Mechanics and Rock Engineering **43**(5): 597-613.

Aster, R. C. and J. Scott (1993). "Comprehensive characterization of waveform similarity in microearthquake data sets." BULLETIN-SEISMOLOGICAL SOCIETY OF AMERICA **83**: 1307-1307.

Avouac, J.-P. (2015). "From Geodetic Imaging of Seismic and Aseismic Fault Slip to Dynamic Modeling of the Seismic Cycle." Annual Review of Earth and Planetary Sciences **43**(1): 233-271.

Baisch, S., R. Vörös, E. Rothert, H. Stang, R. Jung and R. Schellschmidt (2010). "A numerical model for fluid injection induced seismicity at Soultz-sous-Forêts." International Journal of Rock Mechanics and Mining Sciences **47**(3): 405-413.

Bakhtar, K. and N. Barton (1984). Large Scale Static And Dynahic Friction Experinents. The 25th U.S. Symposium on Rock Mechanics (USRMS). Evanston, Illinois, American Rock Mechanics Association**:** 10.
Barton, N. (1973). "Review of a new shear-strength criterion for rock joints." Engineering Geology **7**(4): 287-332.
Barton, N. and S. Bandis (1982). Effects Of Block Size On The Shear Behavior Of Jointed Rock. The 23rd U.S Symposium on Rock Mechanics (USRMS). Berkeley, California, American Rock Mechanics Association**:** 22.
Barton, N., S. Bandis and K. Bakhtar (1985). "Strength, deformation and conductivity coupling of rock joints." International Journal of Rock Mechanics and Mining Sciences & Geomechanics Abstracts **22**(3): 121-140.
Barton, N. and V. Choubey (1977). "The shear strength of rock joints in theory and practice." Rock mechanics **10**(1): 1-54.
Barton, N. and E. Quadros (2014). Most Rock Masses are likely to be Anisotropic. ISRM Conference on Rock Mechanics for Natural Resources and Infrastructure - SBMR 2014. Goiania, Brazil, International Society for Rock Mechanics and Rock Engineering**:** 8.
Beer, A. J., D. Stead and J. S. Coggan (2002). "Technical Note Estimation of the Joint Roughness Coefficient (JRC) by Visual Comparison." Rock Mechanics and Rock Engineering **35**(1): 65-74.
Brock, W. G. and T. Engelder (1977). "Deformation associated with the movement of the Muddy Mountain overthrust in the Buffington window, southeastern Nevada." GSA Bulletin **88**(11): 1667-1677.
Brown, D. W., D. V. Duchane, G. Heiken and V. T. Hriscu (2012). Mining the earth's heat: hot dry rock geothermal energy, Springer Science & Business Media.
Brown, S. R. (1987). "A note on the description of surface roughness using fractal dimension." Geophysical Research Letters **14**(11): 1095-1098.
Bruel, D. and M. Cacas (1992). "NUMERICAL MODELLING TECHNIOUE." Geothermal Energy in Europe: the Soultz Hot Dry Rock Project: 267-279.
Bruel, D., M. C. Cacas, E. Ledoux and G. de Marsily (1994). "Modelling storage behaviour in a fractured rock mass." Journal of Hydrology **162**(3): 267-278.
Candela, T., F. Renard, M. Bouchon, A. Brouste, D. Marsan, J. Schmittbuhl and C. Voisin (2009). "Characterization of Fault Roughness at Various Scales: Implications of Three-Dimensional High Resolution Topography Measurements." Pure and Applied Geophysics **166**(10): 1817-1851.
Candela, T., F. Renard, Y. Klinger, K. Mair, J. Schmittbuhl and E. E. Brodsky (2012). "Roughness of fault surfaces over nine decades of length scales." Journal of Geophysical Research: Solid Earth **117**(B8).
Carcione, J. M., G. Currenti, L. Johann and S. Shapiro (2018). "Modeling fluid injection induced microseismicity in shales." Journal of Geophysics and Engineering **15**(1): 234-248.
Carslaw, H. and J. Jaeger (1959). Conduction of heat in solids, Oxford University Press, Oxford.
Cavailhes, T., J.-P. Sizun, P. Labaume, A. Chauvet, M. Buatier, R. Soliva, L. Mezri, D. Charpentier, H. Leclère, A. Travé and C. Gout (2013). "Influence of fault rock foliation on fault zone permeability: The case of deeply buried arkosic sandstones (Grès d'Annot, southeastern France)." AAPG Bulletin **97**(9): 1521-1543.

Cha, S.-H. (2007). "Comprehensive survey on distance/similarity measures between probability density functions." International Journal Of Mathematical Models And Methods In Applied Sciences **1**(4): 300-307.
Chang, K. W. and P. Segall (2016). "Injection-induced seismicity on basement faults including poroelastic stressing." Journal of Geophysical Research: Solid Earth **121**(4): 2708-2726.
Cheng, A. H.-D. (2016). Poroelasticity, Springer.
Cheng, Q. and A. Ghassemi (2017). Numerical Modeling of Fluid Flow, Heat Transfer and Induced Mircoseismicity in Three Dimensional Fracture Networks. 51st U.S. Rock Mechanics/Geomechanics Symposium. San Francisco, California, USA, American Rock Mechanics Association.
Cheng, Q., X. Wang and A. Ghassemi (2019). "Numerical simulation of reservoir stimulation with reference to the Newberry EGS." Geothermics **77**: 327-343.
Choi, M.-K. (2013). Characterization of Fractures Subjected to Normal and Shear Stress. Doctor of Philosophy (PhD), Purdue University.
Cladouhos, T. T., S. Petty, M. W. Swyer, Y. Nordin, G. Garrison, M. Uddenberg, K. Grasso, P. Stern, E. Sonnenthal, G. Foulger and B. Julian (2015). Newberry EGS Demonstration: Phase 2.2 Report, AltaRock Energy, Seattle, WA (United States)**:** Medium: ED; Size: 138 p.
de Figueiredo, J. J. S., J. Schleicher, R. R. Stewart and N. Dyaur (2012). "Estimating fracture orientation from elastic-wave propagation: An ultrasonic experimental approach." Journal of Geophysical Research: Solid Earth **117**(B8).
De Maesschalck, R., D. Jouan-Rimbaud and D. L. Massart (2000). "The Mahalanobis distance." Chemometrics and Intelligent Laboratory Systems **50**(1): 1-18.
Delaney, P. T. (1982). "Rapid intrusion of magma into wet rock: Groundwater flow due to pore pressure increases." Journal of Geophysical Research: Solid Earth **87**(B9): 7739-7756.
Dershowitz, W. S., M. G. Cottrell, D. H. Lim and T. W. Doe (2010). A Discrete Fracture Network Approach For Evaluation of Hydraulic Fracture Stimulation of Naturally Fractured Reservoirs. 44th U.S. Rock Mechanics Symposium and 5th U.S.-Canada Rock Mechanics Symposium. Salt Lake City, Utah, American Rock Mechanics Association.
Dershowitz, W. S. and H. H. Einstein (1988). "Characterizing rock joint geometry with joint system models." Rock Mechanics and Rock Engineering **21**(1): 21-51.
Dieterich, J. H. (1992). "Earthquake nucleation on faults with rate-and state-dependent strength." Tectonophysics **211**(1): 115-134.
Dobroskok, A. and A. Ghassemi (2005). "Deformation and stability of a discontinuity in a geothermal system." Transactions - Geothermal Resources Council **29**: 349-352.
Du, S., H. Gao, Y. Hu, M. Huang and H. Zhao (2015). "A New Method for Determination of Joint Roughness Coefficient of Rock Joints." Mathematical Problems in Engineering **2015**: 634573.
EGS Collab Team (2020). DOE Geothermal Data Repository.
Eshelby, J. D. and R. E. Peierls (1957). "The determination of the elastic field of an ellipsoidal inclusion, and related problems." Proceedings of the Royal Society of London. Series A. Mathematical and Physical Sciences **241**(1226): 376-396.

Eshelby, J. D. and R. E. Peierls (1959). "The elastic field outside an ellipsoidal inclusion." Proceedings of the Royal Society of London. Series A. Mathematical and Physical Sciences **252**(1271): 561-569.
Fang, Y., D. Elsworth and T. T. Cladouhos (2018). "Reservoir permeability mapping using microearthquake data." Geothermics **72**: 83-100.
Fardin, N., O. Stephansson and L. Jing (2001). "The scale dependence of rock joint surface roughness." International Journal of Rock Mechanics and Mining Sciences **38**(5): 659-669.
Fehler, M. (1990). "Identifying the plane of slip for a fault plane solution from clustering of locations of nearby earthquakes." Geophysical Research Letters **17**(7): 969-972.
Fehler, M., L. House and H. Kaieda (1987). "Determining planes along which earthquakes occur: Method and application to earthquakes accompanying hydraulic fracturing." Journal of Geophysical Research: Solid Earth **92**(B9): 9407-9414.
Fehler, M. and P. Johnson (1989). "Determination of fault planes at Coalinga, California, by analysis of patterns in aftershock locations." Journal of Geophysical Research: Solid Earth **94**(B6): 7496-7506.
Fernández-Ibáñez, F., J. DeGraff and F. Ibrayev (2018). "Integrating borehole image logs with core: A method to enhance subsurface fracture characterization." AAPG Bulletin **102**(6): 1067-1090.
Ficker, T. (2017). "Fractal properties of joint roughness coefficients." International Journal of Rock Mechanics and Mining Sciences **94**: 27-31.
Finnila, A., B. Forbes and R. Podgorney (2019). Building and Utilizing a Discrete Fracture Network Model of the FORGE Utah Site. 44th Workshop on Geothermal Reservoir Engineering, Stanford University, Stanford, California.
Fournier, A., D. Fussell and L. Carpenter (1982). "Computer rendering of stochastic models." Commun. ACM **25**(6): 371–384.
Fournier, T. and J. Morgan (2012). "Insights to slip behavior on rough faults using discrete element modeling." Geophysical Research Letters **39**(12).
Frey, B. J. and D. Dueck (2007). "Clustering by passing messages between data points." science **315**(5814): 972-976.
Fu, P., H. Wu, X. Ju and J. Morris (2020). Analyzing Fracture Flow Channel Area in EGS Collab Experiment 1 Testbed, Lawrence Livermore National Lab.(LLNL), Livermore, CA (United States).
Ghanashyam, N., P. Robert, H. Hai and The EGS Collab Team (2019). EGS Collab Earth Modeling: Integrated 3D Model of the Testbed. GRC Transactions.
Ghassemi, A., B. Jafarpour and M. Tarrahi (2013). Geomechanical Reservoir Characterization with Microseismic Data. SPE Eastern Regional Meeting. Pittsburgh, Pennsylvania, USA, Society of Petroleum Engineers.
Ghassemi, A. and Q. Tao (2016). "Thermo-poroelastic effects on reservoir seismicity and permeability change." Geothermics **63**(Supplement C): 210-224.
Ghassemi, A. and Q. Zhang (2006). "Porothermoelastic Analysis of the Response of a Stationary Crack Using the Displacement Discontinuity Method." Journal of Engineering Mechanics **132**(1): 26-33.
Gilbert, J. R., G. L. Miller and T. Shang-Hua (1995). Geometric mesh partitioning: implementation and experiments. Proceedings of 9th International Parallel Processing Symposium.

Goebel, T. H. W., G. Kwiatek, T. W. Becker, E. E. Brodsky and G. Dresen (2017). "What allows seismic events to grow big?: Insights from b-value and fault roughness analysis in laboratory stick-slip experiments." Geology **45**(9): 815-818.
Goertz-Allmann, B. P., A. Goertz and S. Wiemer (2011). "Stress drop variations of induced earthquakes at the Basel geothermal site." Geophysical Research Letters **38**(9): n/a-n/a.
Goodfellow, S. D., M. H. B. Nasseri, S. C. Maxwell and R. P. Young (2015). "Hydraulic fracture energy budget: Insights from the laboratory." Geophysical Research Letters **42**(9): 3179-3187.
Grasselli, G. (2006). "Manuel Rocha Medal Recipient Shear Strength of Rock Joints Based on Quantified Surface Description." Rock Mechanics and Rock Engineering **39**(4): 295.
Grasselli, G. and P. Egger (2003). "Constitutive law for the shear strength of rock joints based on three-dimensional surface parameters." International Journal of Rock Mechanics and Mining Sciences **40**(1): 25-40.
Grigoli, F., S. Cesca, A. P. Rinaldi, A. Manconi, J. A. López-Comino, J. F. Clinton, R. Westaway, C. Cauzzi, T. Dahm and S. Wiemer (2018). "The November 2017 Mw 5.5 Pohang earthquake: A possible case of induced seismicity in South Korea." Science **360**(6392): 1003-1006.
Gu, H. and X. Weng (2010). Criterion For Fractures Crossing Frictional Interfaces At Non-orthogonal Angles. 44th U.S. Rock Mechanics Symposium and 5th U.S.-Canada Rock Mechanics Symposium. Salt Lake City, Utah, American Rock Mechanics Association**:** 6.
Gu, J.-C., J. R. Rice, A. L. Ruina and S. T. Tse (1984). "Slip motion and stability of a single degree of freedom elastic system with rate and state dependent friction." Journal of the Mechanics and Physics of Solids **32**(3): 167-196.
Guido, F. L., M. Antonellini and V. Picotti (2015). "Modeling ground displacement above reservoirs undergoing fluid withdrawal/injection based on an ellipsoidal inhomogeneity model." International Journal of Rock Mechanics and Mining Sciences **79**: 63-69.
Gutierrez, M. and D.-J. Youn (2015). "Effects of fracture distribution and length scale on the equivalent continuum elastic compliance of fractured rock masses." Journal of Rock Mechanics and Geotechnical Engineering **7**(6): 626-637.
Hanks, T. C. and H. Kanamori (1979). "A moment magnitude scale." Journal of Geophysical Research: Solid Earth **84**(B5): 2348-2350.
Harbord, C. W. A., S. B. Nielsen, N. De Paola and R. E. Holdsworth (2017). "Earthquake nucleation on rough faults." Geology **45**(10): 931-934.
Hazzard, J. F. and R. P. Young (2004). "Dynamic modelling of induced seismicity." International Journal of Rock Mechanics and Mining Sciences **41**(8): 1365-1376.
Hicks, T. W., R. J. Pine, J. Willis-Richards, S. Xu, A. J. Jupe and N. E. V. Rodrigues (1996). "A hydro-thermo-mechanical numerical model for HDR geothermal reservoir evaluation." International Journal of Rock Mechanics and Mining Sciences & Geomechanics Abstracts **33**(5): 499-511.
Hillers, G., Y. Ben-Zion and P. M. Mai (2006). "Seismicity on a fault controlled by rate-and state-dependent friction with spatial variations of the critical slip distance." Journal of Geophysical Research: Solid Earth **111**(B1).

Hofmann, H., G. Zimmermann, M. Farkas, E. Huenges, A. Zang, M. Leonhardt, G. Kwiatek, P. Martinez-Garzon, M. Bohnhoff, K.-B. Min, P. Fokker, R. Westaway, F. Bethmann, P. Meier, K. S. Yoon, J. W. Choi, T. J. Lee and K. Y. Kim (2019). "First field application of cyclic soft stimulation at the Pohang Enhanced Geothermal System site in Korea." Geophysical Journal International **217**(2): 926-949.
Hofmann, H., G. Zimmermann, A. Zang, J. S. Yoon, O. Stephansson, K. Y. Kim, L. Zhuang, M. Diaz and K. B. Min (2018). Comparison of Cyclic and Constant Fluid Injection in Granitic Rock at Different Scales. 52nd U.S. Rock Mechanics/Geomechanics Symposium. Seattle, Washington, American Rock Mechanics Association**:** 10.
Hsiung, S. M., A. Ghosh, M. P. Ahola and A. H. Chowdhury (1993). "Assessment of conventional methodologies for joint roughness coefficient determination." International Journal of Rock Mechanics and Mining Sciences & Geomechanics Abstracts **30**(7): 825-829.
Hu, L., A. Ghassemi, J. Pritchett and S. Garg (2020). "Characterization of laboratory-scale hydraulic fracturing for EGS." Geothermics **83**.
Huberty, C. J. (2005). Mahalanobis Distance. Encyclopedia of Statistics in Behavioral Science, John Wiley & Sons, Ltd.
Iio, Y. (2009). Earthquake Nucleation ProcessEarthquake nucleation process. Encyclopedia of Complexity and Systems Science. R. A. Meyers. New York, NY, Springer New York**:** 2538-2555.
Im, K., C. Marone and D. Elsworth (2019). "The transition from steady frictional sliding to inertia-dominated instability with rate and state friction." Journal of the Mechanics and Physics of Solids **122**: 116-125.
International Society for Rock Mechanics (1978). "International society for rock mechanics commission on standardization of laboratory and field tests: Suggested methods for the quantitative description of discontinuities in rock masses." International Journal of Rock Mechanics and Mining Sciences & Geomechanics Abstracts **15**(6): 319-368.
Interstate Technology & Regulatory Council (2017). Characterization and Remediation in Fractured Rocks. Washington, D.C.
Jacob, C. E. (1940). "On the flow of water in an elastic artesian aquifer." Eos, Transactions American Geophysical Union **21**(2): 574-586.
Jang, H.-S., S.-S. Kang and B.-A. Jang (2014). "Determination of Joint Roughness Coefficients Using Roughness Parameters." Rock Mechanics and Rock Engineering **47**(6): 2061-2073.
Jarvis, R. A. and E. A. Patrick (1973). "Clustering using a similarity measure based on shared near neighbors." IEEE Transactions on computers **100**(11): 1025-1034.
Jones, R. H. and R. C. Stewart (1997). "A method for determining significant structures in a cloud of earthquakes." Journal of Geophysical Research: Solid Earth **102**(B4): 8245-8254.
Kachanov, M. L., B. Shafiro and I. Tsukrov (2013). Handbook of elasticity solutions, Springer Science & Business Media.
Kamali, A. and A. Ghassemi (2017). Reservoir Stimulation in Naturally Fractured Poroelastic Rocks. 51st U.S. Rock Mechanics/Geomechanics Symposium. San Francisco, California, USA, American Rock Mechanics Association.

Kamali, A. and A. Ghassemi (2018). "Analysis of injection-induced shear slip and fracture propagation in geothermal reservoir stimulation." Geothermics **76**: 93-105.
Kamali, A. and A. Ghassemi (2020). "On the Role of Poroelasticity in the Propagation Mode of Natural Fractures in Reservoir Rocks." Rock Mechanics and Rock Engineering.
Kanamori, H. (1978). "Quantification of Earthquakes." Nature **271**(5644): 411-414.
Kaven, J. O., S. H. Hickman, N. C. Davatzes and O. Mutlu (2012). "Linear complementarity formulation for 3D frictional sliding problems." Computational Geosciences **16**(3): 613-624.
Kiel, O. M. (1977). The Kiel Process Reservoir Stimulation By Dendritic Fracturing, Society of Petroleum Engineers**:** 29.
Kneafsey, T. J., D. Blankenship, P. F. Dobson, J. P. Morris, M. D. White, P. Fu, P. C. Schwering, J. B. Ajo-Franklin, L. Huang and M. Schoenball (2020). The EGS Collab Project: Learnings from Experiment 1. 45th Workshop on Geothermal Reservoir Engineering, Stanford, California, PROCEEDINGS.
Kneafsey, T. J., P. Dobson, D. Blankenship, J. Morris, H. Knox, P. Schwering and M. White (2018). An Overview of the EGS Collab Project: Field Validation of Coupled Process Modeling of Fracturing and Fluid Flow at the Sanford Underground Research Facility, Lead, SD. PROCEEDINGS, 43rd Workshop on Geothermal Reservoir Engineering, Stanford University, Stanford, California.
Kneafsey, T. J., P. F. Dobson, J. B. Ajo-Franklin, Y. Guglielmi, C. A. Valladao, D. A. Blankenship, P. C. Schwering, H. A. Knox, M. D. White, T. C. Johnson, C. E. Strickland, V. R. Vermuel, J. P. Morris, P. Fu, E. Mattson, G. H. Neupane, R. K. Podgorney, T. W. Doe, L. Huang, L. P. Frash, A. Ghassemi and W. Roggenthen (2019). EGS Collab Project: Status, Tests, and Data. 53rd U.S. Rock Mechanics/Geomechanics Symposium. New York City, New York, American Rock Mechanics Association**:** 19.
Kneafsey, T. J., P. F. Dobson, J. B. Ajo-Franklin, C. Valladao, D. A. Blankenship, H. A. Knox, P. Schwering, J. P. Morris, M. Smith, M. D. White, T. Johnson, R. Podgorney, E. Mattson, G. Neupane, W. Roggenthen and T. Doe (2018). The EGS Collab Project: Stimulation and Simulation. 52nd U.S. Rock Mechanics/Geomechanics Symposium. Seattle, Washington, American Rock Mechanics Association**:** 10.
Kuang, W., M. Zoback and J. Zhang (2017). "Estimating geomechanical parameters from microseismic plane focal mechanisms recorded during multistage hydraulic fracturing." GEOPHYSICS **82**(1): KS1-KS11.
Kulatilake, P. H. S. W., G. Shou, T. H. Huang and R. M. Morgan (1995). "New peak shear strength criteria for anisotropic rock joints." International Journal of Rock Mechanics and Mining Sciences & Geomechanics Abstracts **32**(7): 673-697.
Kulatilake, P. H. S. W. and J. Um (1999). "Requirements for accurate quantification of self-affine roughness using the roughness–length method." International Journal of Rock Mechanics and Mining Sciences **36**(1): 5-18.
Kumar, D. and A. Ghassemi (2018). "Three-Dimensional Poroelastic Modeling of Multiple Hydraulic Fracture Propagation from Horizontal Wells." International Journal of Rock Mechanics and Mining Sciences **105**: 192-209.
Laubach, S. E., J. N. Hooker and R. Marrett (2014). "A universal power-law scaling exponent for fracture apertures in sandstones." GSA Bulletin **126**(9-10): 1340-1362.
Lee, S. H. and A. Ghassemi (2011). Three-Dimensional Thermo-Poro-Mechanical Modeling of Well Stimulation And Induced Microseismicity. 45th U.S. Rock Mechanics

/ Geomechanics Symposium. San Francisco, California, American Rock Mechanics Association.
Lee, Y. H., J. R. Carr, D. J. Barr and C. J. Haas (1990). "The fractal dimension as a measure of the roughness of rock discontinuity profiles." International Journal of Rock Mechanics and Mining Sciences & Geomechanics Abstracts **27**(6): 453-464.
Li, Y. and R. Huang (2015). "Relationship between joint roughness coefficient and fractal dimension of rock fracture surfaces." International Journal of Rock Mechanics and Mining Sciences **75**: 15-22.
Long, J. C. S., J. S. Remer, C. R. Wilson and P. A. Witherspoon (1982). "Porous media equivalents for networks of discontinuous fractures." Water Resources Research **18**(3): 645-658.
Lu, J. and A. Ghassemi (2019). Coupled Thermo-Hydro-Mechanical-Seismic Modeling of Fractured Reservoir Stimulation with Application to EGS Collab. Proceedings, 44th Workshop on Geothermal Reservoir Engineering, Stanford University, SGP-TR-214.
Lu, J. and A. Ghassemi (2019). Semi analytical 3D modleing of fracture propagation in a fractured rock. Reservoir Geomechancs & Seismicity Researc Group JIP Internal Report. Norman, Oklahoma.
Magsipoc, E., Q. Zhao and G. Grasselli (2020). "2D and 3D Roughness Characterization." Rock Mechanics and Rock Engineering **53**(3): 1495-1519.
Mahalanobis, P. C. (1936). "On the generalised distance in statistics." Proceedings of the National Institute of Sciences of India, 1936: 49-55.
Makedonska, N., E. Jafarov, T. Doe, P. Schwering, G. Neupane and C. T. EGS (2020). Simulation of Injected Flow Pathways in Geothermal Fractured Reservoir Using Discrete Fracture Network Model. 45th Workshop on Geothermal Reservoir Engineering.
Mandelbrot, B. (1967). "How Long Is the Coast of Britain? Statistical Self-Similarity and Fractional Dimension." Science **156**(3775): 636-638.
Mandelbrot, B. B. (1985). "Self-Affine Fractals and Fractal Dimension." Physica Scripta **32**(4): 257-260.
Marck, J., A. A. Savitski and E. Detournay (2015). "Line source in a poroelastic layer bounded by an elastic space." International Journal for Numerical and Analytical Methods in Geomechanics **39**(14): 1484-1505.
Marone, C. (2019). The spectrum of fault slip modes from elastodynamic rupture to slow earthquakes. Proceedings of the International School of Physics "Enrico Fermi" on Mechanics of Earthquake Faulting, Varenna, Italy.
Mastrojannis, E. N., L. M. Keer and T. Mura (1980). "Growth of planar cracks induced by hydraulic fracturing." International Journal for Numerical Methods in Engineering **15**(1): 41-54.
Maus, S. and V. Dimri (1996). "Depth estimation from the scaling power spectrum of potential fields?" Geophysical Journal International **124**(1): 113-120.
McClure, M. W. (2012). Modeling and characterization of hydraulic stimulation and induced seismicity in geothermal and shale gas reservoirs. PhD, Stanford University Stanford, California.
McClure, M. W. (2015). "Generation of large postinjection-induced seismic events by backflow from dead-end faults and fractures." Geophysical Research Letters **42**(16): 6647-6654.

McGarr, A., S. M. Spottiswoode, N. C. Gay and W. D. Ortlepp (1979). "Observations relevant to seismic driving stress, stress drop, and efficiency." Journal of Geophysical Research: Solid Earth **84**(B5): 2251-2261.
Mclaskey, G. C. and F. Yamashita (2017). "Slow and fast ruptures on a laboratory fault controlled by loading characteristics." Journal of Geophysical Research: Solid Earth **122**(5): 3719-3738.
McTigue, D. F. (1986). "Thermoelastic response of fluid-saturated porous rock." Journal of Geophysical Research: Solid Earth **91**(B9): 9533-9542.
Meng, C., W. Heltsley and D. D. Pollard (2012). "Evaluation of the Eshelby solution for the ellipsoidal inclusion and heterogeneity." Computers & Geosciences **40**: 40-48.
Meng, F., L. N. Y. Wong and H. Zhou (2019). "Power law relations in earthquakes from microscopic to macroscopic scales." Scientific Reports **9**(1): 10705.
Min, K. S., Z. Zhang and A. Ghassemi (2010). Numerical Analysis of Multiple Fracture Propagation In Heterogeneous Rock. 44th U.S. Rock Mechanics Symposium and 5th U.S.-Canada Rock Mechanics Symposium. Salt Lake City, Utah, American Rock Mechanics Association**:** 10.
Mitchell, T. M. and D. R. Faulkner (2009). "The nature and origin of off-fault damage surrounding strike-slip fault zones with a wide range of displacements: A field study from the Atacama fault system, northern Chile." Journal of Structural Geology **31**(8): 802-816.
Moore, D. E. and D. A. Lockner (1995). "The role of microcracking in shear-fracture propagation in granite." Journal of Structural Geology **17**(1): 95-114.
Moore, J., J. McLennan, K. Pankow, S. Simmons, R. Podgorney, P. Wannamaker, C. Jones, W. Rickard and P. Xing (2020). The Utah Frontier Observatory for Research in Geothermal Energy (FORGE): A Laboratory for Characterizing, Creating and Sustaining Enhanced Geothermal Systems PROCEEDINGS, 45th Workshop on Geothermal Reservoir Engineering
Stanford University, Stanford, California, February 10-12, 2020.
Moore, J. N. and S. F. Simmons (2013). "More Power from Below." Science **340**(6135): 933-934.
Mura, T. (1987). Micromechanics of Defects in Solids, Springer Netherlands.
Myers, N. O. (1962). "Characterization of surface roughness." Wear **5**(3): 182-189.
Nadimi, S., B. Forbes, J. Moore, R. Podgorney and J. D. McLennan (2020). "Utah FORGE: Hydrogeothermal modeling of a granitic based discrete fracture network." Geothermics **87**: 101853.
National Research Council (1996). Rock Fractures and Fluid Flow: Contemporary Understanding and Applications. Washington, DC, The National Academies Press.
Nester, T., J. Komma, A. Viglione and G. Blöschl (2012). "Flood forecast errors and ensemble spread—A case study." Water Resources Research **48**(10): n/a-n/a.
Patel, S. M., C. H. Sondergeld and C. S. Rai (2017). "Laboratory studies of hydraulic fracturing by cyclic injection." International Journal of Rock Mechanics and Mining Sciences **95**: 8-15.
Patton, F. D. (1966). Multiple Modes of Shear Failure In Rock. 1st ISRM Congress. Lisbon, Portugal, International Society for Rock Mechanics and Rock Engineering**:** 5.
Pearson, C. (1981). "The relationship between microseismicity and high pore pressures during hydraulic stimulation experiments in low permeability granitic rocks." Journal of Geophysical Research: Solid Earth **86**(B9): 7855-7864.

Phan, A.-V., J. A. L. Napier, L. J. Gray and T. Kaplan (2003). "Symmetric-Galerkin BEM simulation of fracture with frictional contact." International Journal for Numerical Methods in Engineering **57**(6): 835-851.
Pine, R. J. and A. S. Batchelor (1984). "Downward migration of shearing in jointed rock during hydraulic injections." International Journal of Rock Mechanics and Mining Sciences & Geomechanics Abstracts **21**(5): 249-263.
Prassetyo, S. H., M. Gutierrez and N. Barton (2017). "Nonlinear shear behavior of rock joints using a linearized implementation of the Barton–Bandis model." Journal of Rock Mechanics and Geotechnical Engineering **9**(4): 671-682.
Pruess, K. (1992). Brief guide to the MINC-method for modeling flow and transport in fractured media, Earth Sciences Division, Lawrence Berkeley National Laboratory. Berkeley CA USA.
Rahman, M. K., M. M. Hossain and S. S. Rahman (2000). "An analytical method for mixed-mode propagation of pressurized fractures in remotely compressed rocks." International Journal of Fracture **103**(3): 243-258.
Rahman, M. K., M. M. Hossain and S. S. Rahman (2002). "A shear-dilation-based model for evaluation of hydraulically stimulated naturally fractured reservoirs." International Journal for Numerical and Analytical Methods in Geomechanics **26**(5): 469-497.
Rainwater, S. and B. R. Hunt (2013). "Ensemble data assimilation with an adjusted forecast spread." Tellus A: Dynamic Meteorology and Oceanography **65**(1): 19929.
Raleigh, C. B., J. H. Healy and J. D. Bredehoeft (1976). "An Experiment in Earthquake Control at Rangely, Colorado." Science **191**(4233): 1230-1237.
Rashidian, S. and L. C. Chang (2012). Peak Shear Displacement of Rock Fractures. 46th U.S. Rock Mechanics/Geomechanics Symposium. Chicago, Illinois, American Rock Mechanics Association**:** 4.
Rawal, C. and A. Ghassemi (2014). "A reactive thermo-poroelastic analysis of water injection into an enhanced geothermal reservoir." Geothermics **50**: 10-23.
Renard, F., C. Voisin, D. Marsan and J. Schmittbuhl (2006). "High resolution 3D laser scanner measurements of a strike-slip fault quantify its morphological anisotropy at all scales." Geophysical Research Letters **33**(4).
Renshaw, C. E. and D. D. Pollard (1995). "An experimentally verified criterion for propagation across unbounded frictional interfaces in brittle, linear elastic materials." International Journal of Rock Mechanics and Mining Sciences & Geomechanics Abstracts **32**(3): 237-249.
Rice, J. R. and A. L. Ruina (1983). "Stability of Steady Frictional Slipping." Journal of Applied Mechanics **50**(2): 343-349.
Richards‐Dinger, K. and J. H. Dieterich (2012). "RSQSim Earthquake Simulator." Seismological Research Letters **83**(6): 983-990.
Rinaldi, A. P. and M. Nespoli (2017). "TOUGH2-seed: A coupled fluid flow and mechanical-stochastic approach to model injection-induced seismicity." Computers & Geosciences **108**: 86-97.
Roff, A., W. S. Phillips and D. W. Brown (1996). "Joint structures determined by clustering microearthquakes using waveform amplitude ratios." International Journal of Rock Mechanics and Mining Sciences & Geomechanics Abstracts **33**(6): 627-639.
Rubin, A. M. and J.-P. Ampuero (2005). "Earthquake nucleation on (aging) rate and state faults." Journal of Geophysical Research: Solid Earth **110**(B11).

Rudnicki, J. W. (1977). "The inception of faulting in a rock mass with a weakened zone." Journal of Geophysical Research (1896-1977) **82**(5): 844-854.
Sætrom, J. and H. Omre (2011). "Ensemble Kalman filtering for non-linear likelihood models using kernel-shrinkage regression techniques." Computational Geosciences **15**(3): 529-544.
Safari, R. and A. Ghassemi (2016). "Three-dimensional poroelastic modeling of injection induced permeability enhancement and microseismicity." International Journal of Rock Mechanics and Mining Sciences **84**: 47-58.
Sagy, A., Z. e. Reches and I. Roman (2001). "Dynamic fracturing: field and experimental observations." Journal of Structural Geology **23**(8): 1223-1239.
Sarma, P. and W. H. Chen (2011). Robust and Efficient Handling of Model Contraints with the Kernal-Based Ensemble Kalman Filter. SPE Reservoir Simulation Symposium. The Woodlands, Texas, USA, Society of Petroleum Engineers.
Sayles, R. S. and T. R. Thomas (1978). "Surface topography as a nonstationary random process." Nature **271**(5644): 431-434.
Scholz, C. H. (2019). The Mechanics of Earthquakes and Faulting. Cambridge, Cambridge University Press.
Schwartzkopff, A. K., C. Xu and N. S. Melkoumian (2016). "Approximation of mixed mode propagation for an internally pressurized circular crack." Engineering Fracture Mechanics **166**: 218-233.
Scotti, O. and F. H. Cornet (1994). "In-situ stress fields and focal mechanism solutions in central France." Geophysical Research Letters **21**(22): 2345-2348.
Segall, P. and S. Lu (2015). "Injection-induced seismicity: Poroelastic and earthquake nucleation effects." Journal of Geophysical Research: Solid Earth **120**(7): 5082-5103.
Sesetty, V. and A. Ghassemi (2018). "Effect of rock anisotropy on wellbore stresses and hydraulic fracture propagation." International Journal of Rock Mechanics and Mining Sciences **112**: 369-384.
Shapiro, S. A., E. Huenges and G. Borm (1997). "Estimating the crust permeability from fluid-injection-induced seismic emission at the KTB site." Geophysical Journal International **131**(2): F15-F18.
Shapiro, S. A., R. Patzig, E. Rothert and J. Rindschwentner (2003). "Triggering of Seismicity by Pore-pressure Perturbations: Permeability-related Signatures of the Phenomenon." pure and applied geophysics **160**(5): 1051-1066.
Simmons, S. F., S. Kirby, J. Bartley, R. Allis, E. Kleber, T. Knudsen, J. Miller, C. Hardwick, K. Rahilly and T. Fischer (2019). Update on the geoscientific understanding of the Utah FORGE site. PROCEEDINGS, 44th Workshop on Geothermal Reservoir Engineering
Stanford University, Stanford, California, February 11-13, 2019.
Sneddon, I. N. (1946). "The distribution of stress in the neighbourhood of a crack in an elastic solid." Proceedings of the Royal Society of London. Series A. Mathematical and Physical Sciences **187**(1009): 229-260.
Stanton W. Caddey, Richard L. Bachman, Thomas J. Campbell, Rolland R. Reid and R. P. Otto (1992). The Homestake Gold Mine: an early Proterozoic iron-formation-hosted gold deposit, Lawrence County, South Dakota, US Department of the Interior, US Geological Survey.

Stigsson, M. (2016). Parametrisation of Fractures – Methods and Evaluation of Fractal Surfaces.
Stigsson, M. and D. Mas Ivars (2019). "A Novel Conceptual Approach to Objectively Determine JRC Using Fractal Dimension and Asperity Distribution of Mapped Fracture Traces." Rock Mechanics and Rock Engineering **52**(4): 1041-1054.
Tal, Y., T. Goebel and J.-P. Avouac (2020). "Experimental and modeling study of the effect of fault roughness on dynamic frictional sliding." Earth and Planetary Science Letters **536**: 116133.
Tal, Y. and B. H. Hager (2018). "Dynamic mortar finite element method for modeling of shear rupture on frictional rough surfaces." Computational Mechanics **61**(6): 699-716.
Tal, Y., B. H. Hager and J. P. Ampuero (2018). "The Effects of Fault Roughness on the Earthquake Nucleation Process." Journal of Geophysical Research: Solid Earth **123**(1): 437-456.
Tarasovs, S. and A. Ghassemi (2011). Propagation of a System of Cracks Under Thermal Stress. 45th U.S. Rock Mechanics / Geomechanics Symposium. San Francisco, California, American Rock Mechanics Association**:** 6.
Tarrahi, M. and B. Jafarpour (2012). "Inference of permeability distribution from injection-induced discrete microseismic events with kernel density estimation and ensemble Kalman filter." Water Resources Research **48**(10): n/a-n/a.
Tarrahi, M., B. Jafarpour and A. Ghassemi (2015). "Integration of microseismic monitoring data into coupled flow and geomechanical models with ensemble Kalman filter." Water Resources Research **51**(7): 5177-5197.
Tatone, B. S. A. and G. Grasselli (2010). "A new 2D discontinuity roughness parameter and its correlation with JRC." International Journal of Rock Mechanics and Mining Sciences **47**(8): 1391-1400.
Tatone, B. S. A. and G. Grasselli (2013). "An Investigation of Discontinuity Roughness Scale Dependency Using High-Resolution Surface Measurements." Rock Mechanics and Rock Engineering **46**(4): 657-681.
Tezuka, K., T. Tamagawa and K. Watanabe (2005). Numerical simulation of hydraulic shearing in fractured reservoir. Proceedings World Geothermal Congress, Antalya, Turkey.
Tezuka, K. and K. Watanabe (2000). "Fracture network modeling of Hijiori hot dry rock reservoir by deterministic and stochastic crack network simulator (D/SC)."
Theis, C. V. (1935). "The relation between the lowering of the Piezometric surface and the rate and duration of discharge of a well using ground-water storage." Eos, Transactions American Geophysical Union **16**(2): 519-524.
Tuttle, O. F. (1949). "Structural Petrology of Planes of Liquid Inclusions." The Journal of Geology **57**(4): 331-356.
Ucar, E., I. Berre and E. Keilegavlen (2018). "Three-Dimensional Numerical Modeling of Shear Stimulation of Fractured Reservoirs." Journal of Geophysical Research: Solid Earth **123**(5): 3891-3908.
Ulrich, C., P. F. Dobson, T. J. Kneafsey, W. M. Roggenthen, N. Uzunlar, T. W. Doe, G. Neupane, R. Podgorney, P. Schwering, L. Frash and A. Singh (2018). the Distribution, Orientation, and Characteristics of Natural Fractures for Experiment 1 of the EGS Collab Project, Sanford Underground Research Facility. 52nd U.S. Rock

Mechanics/Geomechanics Symposium. Seattle, Washington, American Rock Mechanics Association**:** 8.
Ünlüsoy, D. and M. L. Süzen (2020). "A new method for automated estimation of joint roughness coefficient for 2D surface profiles using power spectral density." International Journal of Rock Mechanics and Mining Sciences **125**: 104156.
Valko, P. and M. J. Economides (1995). Hydraulic fracture mechanics, Wiley Chichester.
Wang, X. (2014). Three-Dimensional FEM Modeling of Geothermal Reservoir Stimulation Using Stochastic Fracture Networks and Continuum Damage Mechanics. Ph.D., The University of Oklahoma.
Wang, X. and A. Ghassemi (2012). A 3D Thermal-Poroelastic Model For Naturally Fractured Geothermal Reservoir Stimulation. 46th U.S. Rock Mechanics/Geomechanics Symposium. Chicago, Illinois, USA, American Rock Mechanics Association.
Wang, X. and A. Ghassemi (2013). "A threedimensional thermal-poroelastic model for natural fractured geothermal reservoir stimulation." GRC Transactions **37**: 871-878.
Warpinski, N. R., S. L. Wolhart and C. A. Wright (2004). "Analysis and Prediction of Microseismicity Induced by Hydraulic Fracturing." SPE Journal **9**(01): 24-33.
Willis-Richards, J., K. Watanabe and H. Takahashi (1996). "Progress toward a stochastic rock mechanics model of engineered geothermal systems." Journal of Geophysical Research: Solid Earth **101**(B8): 17481-17496.
Willis, M. E., D. R. Burns, R. Rao, B. Minsley, M. N. Toksöz and L. Vetri (2006). "Spatial orientation and distribution of reservoir fractures from scattered seismic energy." GEOPHYSICS **71**(5): O43-O51.
Wu, H., P. Fu, X. Yang, J. P. Morris, T. C. Johnson, R. R. Settgast and F. J. Ryerson (2019). "Accurate imaging of hydraulic fractures using templated electrical resistivity tomography." Geothermics **81**: 74-87.
Yamada, T., J. J. Mori, S. Ide, R. E. Abercrombie, H. Kawakata, M. Nakatani, Y. Iio and H. Ogasawara (2007). "Stress drops and radiated seismic energies of microearthquakes in a South African gold mine." Journal of Geophysical Research: Solid Earth **112**(B3): n/a-n/a.
Yang, S.-C., E. Kalnay and B. Hunt (2012). "Handling Nonlinearity in an Ensemble Kalman Filter: Experiments with the Three-Variable Lorenz Model." Monthly Weather Review **140**(8): 2628-2646.
Ye, Z. and A. Ghassemi (2018). Injection-induced Fracture Propagation and Coalescence Under Triaxial Loading. 52nd US Rock Mechanics / Geomechanics Symposium. Seattle, Washington
Ye, Z. and A. Ghassemi (2018). "Injection-Induced Shear Slip and Permeability Enhancement in Granite Fractures." Journal of Geophysical Research: Solid Earth **123**(10): 9009-9032.
Ye, Z. and A. Ghassemi (2019). Failure Behavior of the Poorman Schist and Its Fractures from the COLLAB Simulation Site. 44rd workshop on geothermal reservoir engineering, Stanford, California, USA.
Ye, Z. and A. Ghassemi (2019). "Injection-Induced Propagation and Coalescence of Preexisting Fractures in Granite Under Triaxial Stress." Journal of Geophysical Research: Solid Earth **124**(8): 7806-7821.
Ye, Z. and A. Ghassemi (2019). Investigation of Micro-Seismicity and Permeability Evolution in Shale Fractures During Stimulation. SPE/AAPG/SEG Unconventional

Resources Technology Conference. Denver, Colorado, USA, Unconventional Resources Technology Conference**:** 11.
Ye, Z. and A. Ghassemi (2020). "Heterogeneous Fracture Slip and Aseismic-Seismic Transition in a Triaxial Injection Test." Geophysical Research Letters **47**(14): e2020GL087739.
Ye, Z., A. Ghassemi and T. Kneafsey (2020). Deformation, Failure and Permeability Evolution of Sealed Fractures in EGS Collab Poorman Schist. 45th Workshop on Geothermal Reservoir Engineering.
Ye, Z., M. Janis and A. Ghassemi (2017). Injection-Driven Shear Slip and the Coupled Permeability Evolution of Granite Fractures for EGS Stimulation. 51st U.S. Rock Mechanics/Geomechanics Symposium. San Francisco, California, USA, American Rock Mechanics Association.
Yong, R., J.-B. Qin, M. Huang, S.-G. Du, J. Liu and G.-J. Hu (2019). "An Innovative Sampling Method for Determining the Scale Effect of Rock Joints." Rock Mechanics and Rock Engineering **52**(3): 935-946.
Yu, X. and B. Vayssade (1991). "Joint profiles and their roughness parameters." International Journal of Rock Mechanics and Mining Sciences & Geomechanics Abstracts **28**(4): 333-336.
Zang, A., O. Stephansson, L. Stenberg, K. Plenkers, S. Specht, C. Milkereit, E. Schill, G. Kwiatek, G. Dresen, G. Zimmermann, T. Dahm and M. Weber (2016). "Hydraulic fracture monitoring in hard rock at 410 m depth with an advanced fluid-injection protocol and extensive sensor array." Geophysical Journal International **208**(2): 790-813.
Zang, A., J. S. Yoon, O. Stephansson and O. Heidbach (2013). "Fatigue hydraulic fracturing by cyclic reservoir treatment enhances permeability and reduces induced seismicity." Geophysical Journal International **195**(2): 1282-1287.
Zhao, X. and R. Paul Young (2011). "Numerical modeling of seismicity induced by fluid injection in naturally fractured reservoirs." Geophysics **76**(6): WC167-WC180.
Zhou, X. and A. Ghassemi (2009). "Finite element analysis of coupled chemo-poro-thermo-mechanical effects around a wellbore in swelling shale." International Journal of Rock Mechanics and Mining Sciences **46**(4): 769-778.
Zhuang, L., K. Y. Kim, S. G. Jung, Y. J. Nam, K. B. Min, S. Park, A. Zang, O. Stephansson, G. Zimmermann and J. S. Yoon (2017). Laboratory Evaluation of Induced Seismicity Reduction and Permeability Enhancement Effects of Cyclic Hydraulic Fracturing. 51st U.S. Rock Mechanics/Geomechanics Symposium. San Francisco, California, USA, American Rock Mechanics Association**:** 7.

Appendix A

The Eshelby solution was first introduced to formulate the elastic stress field surrounding and inside an inclusion in an isotropic elastic infinite medium (Eshelby and Peierls 1957, Eshelby and Peierls 1959). Since 1960's, Eshelby solution has been applied to solve complicate problems, such as faulting (Rudnicki 1977), deformation in reservoir undergoing production (Guido, Antonellini et al. 2015). An inclusion is defined as subdomain Ω in a domain D. Eigenstrain ε_{kl}^{*} is load on the inclusion while is zero in $D-\Omega$. Both inclusion Ω and the matrix $D-\Omega$ are the same elastic moduli C_{ijkl}. The displacement u_j , strain ε_{ij} and stress σ_{ij} for both the inclusion and matrix are expressed as (Mura 1987):

$$u_i(X) = -C_{kjmn}\int_{\Omega} \varepsilon^{*}(x)G_{ij,k}(X-x)\mathrm{d}x \tag{A1}$$

$$\varepsilon_{ij}(X) = -\frac{1}{2}\int_{\Omega} C_{klmn}\varepsilon_{mn}^{*}(x)\left(G_{ik,lj}(X-x)+G_{jk,li}(X-x)\right)\mathrm{d}x \tag{A2}$$

$$\sigma_{ij}(X) = -C_{ijkl}\left(\int_{\Omega} C_{pqmn}\varepsilon_{mn}^{*}(x)G_{kp,ql}(X-x)\mathrm{d}x+\varepsilon_{kl}^{*}(X)\right) \tag{A3}$$

For isotropic matrix, Green's function $G_{ij}(X-x)$ is given by

$$G_{ij}(X-x) = \frac{1}{16\pi\mu(1-v)|X-x|}\left((3-4v)\delta_{ij}+\frac{(X_i-x_i)(X_j-x_j)}{|X-x|^2}\right) \tag{A4}$$

The induced strain in the inclusion ε_{ij} is uniform and can be linearly connected with eigenstrain ε_{kl}^{*}

$$\varepsilon_{ij} = S_{ijkl}\varepsilon_{kl}^{*} \qquad \text{for } X \in \Omega \tag{A5}$$

Where S_{ijkl} is the Eshelby tensor and ε_{kl}^{*} is the eigenstrain which is regarded as internal strains caused by various mechanisms, including poroelastic and thermal changes in a body free from external force and surface constraint (Guido, Antonellini et al. 2015). The

Eshelby tensor is the function of inclusion shape and elastic properties of the matrix. The expressions of Eshelby tensor S_{ijkl} can be expressed as:

$$S_{ijkl} = S_{jikl} = S_{ijlk} \tag{A6}$$

$$S_{1111} = \frac{3}{8\pi(1-v)} a_1^2 I_{11} + \frac{1-2v}{8\pi(1-v)} I_1 \tag{A7}$$

$$S_{1122} = \frac{1}{8\pi(1-v)} a_2^2 I_{12} - \frac{1-2v}{8\pi(1-v)} I_1 \tag{A8}$$

$$S_{1133} = \frac{1}{8\pi(1-v)} a_3^2 I_{13} - \frac{1-2v}{8\pi(1-v)} I_1 \tag{A9}$$

$$S_{1212} = \frac{a_1^2+a_2^2}{8\pi(1-v)} I_{12} + \frac{1-2v}{16\pi(1-v)} (I_1 + I_2) \tag{A10}$$

Where v is Poisson's ration; I_i and I_{ij} are the given by integrals

$$I_1 = 2\pi a_1 a_2 a_3 \int_0^\infty \frac{\mathrm{d}s}{(a_1^2+s)\Delta(s)} \tag{A11}$$

$$I_{11} = 2\pi a_1 a_2 a_3 \int_0^\infty \frac{\mathrm{d}s}{(a_1^2+s)^2 \Delta(s)} \tag{A12}$$

$$I_{12} = 2\pi a_1 a_2 a_3 \int_0^\infty \frac{\mathrm{d}s}{(a_1^2+s)(a_2^2+s)\Delta(s)} \tag{A13}$$

Where $\Delta(s) = (a_1^2 + s)^{1/2}(a_2^2 + s)^{1/2}(a_3^2 + s)^{1/2}$; s is the integration variable. a_1, a_2 and a_3 is the semi-axis of ellipsoid. For $a_1 > a_2 > a_3$, the I_i can be expressed by standard elliptical integrals,

$$I_1 = \frac{4\pi a_1 a_2 a_3}{(a_1^2-a_2^2)(a_1^2-a_3^2)^{1/2}} \big(F(\theta,k) - E(\theta,k)\big) \tag{A14}$$

$$I_3 = \frac{4\pi a_1 a_2 a_3}{(a_2^2-a_3^2)(a_1^2-a_3^2)^{1/2}} \left(\frac{a_2 (a_1^2-a_3^2)^{1/2}}{a_1 a_3} - E(\theta,k) \right) \tag{A15}$$

Where

$$F(\theta,k) = \int_0^\theta \frac{\mathrm{d}w}{(1-k^2 \sin^2 w)^{1/2}} \tag{A16}$$

$$E(\theta,k) = (1 - k^2 \sin^2 w)^{1/2} \mathrm{d}w \tag{A17}$$

$$\theta = \sin^{-1}\left(1 - \frac{a_3^2}{a_1^2}\right)^{1/2} \tag{A18}$$

$$k = \left(\frac{(a_1^2 - a_2^2)}{(a_1^2 - a_3^3)}\right)^{1/2} \tag{A19}$$

Here F and E is the incomplete elliptic integrals of the first and second kind, respectively. The definition of θ in F can be found in Figure A1.

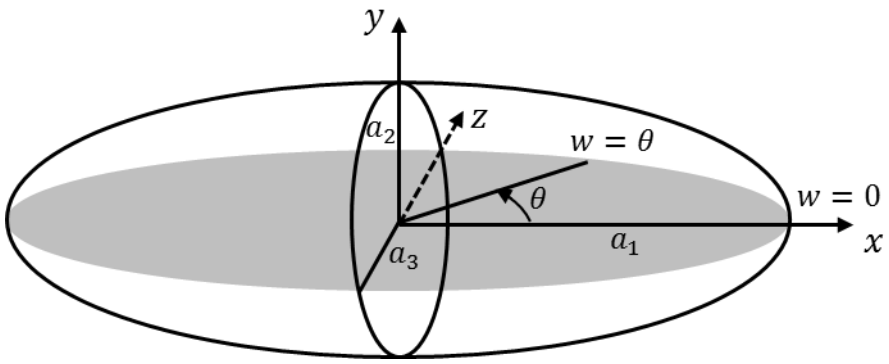

Figure A1 The definition of θ in F. a_1 , a_2, a_3 is the semi-axis of ellipsoid and $a_1 > a_2 > a_3$.

Among I_i and I_{ij} we have relations

$$I_1 + I_2 + I_3 = 4\pi \tag{A20}$$

$$3I_{11} + I_{12} + I_{13} = 4\pi/a_1^2 \tag{A21}$$

$$3a_1^2 I_{11} + a_2^2 I_{12} + a_3^2 I_{13} = 3I_1 \tag{A22}$$

$$I_{12} = (I_2 - I_1)/(a_1^2 - a_2^2) \tag{A23}$$

Mura 1987 provides the formulation for the exterior elastic strain due to eigenstrain

$$\varepsilon_{ij}(X) = D_{ijkl}(X)\varepsilon_{kl}^* \quad \text{for } X \in D - \Omega \tag{A24}$$

Where $D_{ijkl}(X)$ is the function of the location vector X relative to the inclusion center; $D_{ijkl}(X)$ are calculated as follows:

$$8\pi(1-v)D_{ijkl}(X) = 8\pi(1-v)S_{ijkl}(\lambda) + 2v\delta_{ij}X_iI_{,j}(\lambda) + (1-v)\left(\delta_{il}X_kI_{K,j}(\lambda) + \delta_{jl}X_kI_{K,i}(\lambda) + \delta_{ik}X_lI_{L,j}(\lambda) + \delta_{jk}X_lI_{L,i}(\lambda)\right) - \delta_{ij}X_k\left(I_K(\lambda) - a_1^2I_{KI}(\lambda)\right)_{,l} - \left(\delta_{ik}X_j + \delta_{jk}X_i\right)\left(I_j(\lambda) - a_1^2I_{Ij}(\lambda)\right)_{,l} - \left(\delta_{il}X_j + \delta_{jl}X_i\right)\left(I_j(\lambda) - a_1^2I_{Ij}(\lambda)\right)_{,k} - X_iX_j\left(I_J(\lambda) - a_1^2I_{IJ}(\lambda)\right)_{,lk} \quad \text{(A25)}$$

Where λ is the largest positive root of following equations:

$$\frac{X_1^2}{a_1^2+\lambda} + \frac{X_2^2}{a_2^2+\lambda} + \frac{X_3^2}{a_3^2+\lambda} = 1 \quad \text{(A26)}$$

To solve $D_{ijkl}(X)$, the $I_i(\lambda)$ and $I_{ij}(\lambda)$ and their first and second derivatives with respect to X_i are given as:

$$I_1(\lambda) = \frac{4\pi a_1a_2a_3}{(a_1^2-a_2^2)(a_1^2-a_3^2)^{1/2}}\left(F(\theta(\lambda),k) - E(\theta(\lambda),k)\right) \quad \text{(A27)}$$

$$I_3(\lambda) = \frac{4\pi a_1a_2a_3}{(a_2^2-a_3^2)(a_1^2-a_3^2)^{1/2}}\left(\frac{(a_2^2+\lambda)(a_1^2-a_3^2)^{1/2}}{\prod_k(a_k^2+\lambda)^{1/2}} - E(\theta(\lambda),k)\right) \quad \text{(A28)}$$

$$I_2(\lambda) = \frac{4\pi a_1a_2a_3}{\prod_k(a_k^2+\lambda)^{1/2}} - I_1(\lambda) - I_3(\lambda) \quad \text{(A29)}$$

$$I_{ij}(\lambda) = -\frac{I_i(\lambda)-I_j(\lambda)}{a_i^2-a_j^2} \text{ for } i \neq j \quad \text{(A30)}$$

$$I_{ii}(\lambda) = \frac{4\pi a_1a_2a_3}{3(a_i^2+\lambda)\prod_k(a_k^2+\lambda)^{1/2}} - \frac{\sum_j I_{ij}(\lambda)}{3} \quad \text{(A31)}$$

$$\theta = \sin^{-1}\left(\frac{a_1^2-a_3^2}{a_1^2+\lambda}\right)^{1/2} \quad \text{(A32)}$$

$$I_{i,j} = \frac{-2\pi a_1a_2a_3}{(a_i^2+\lambda)\prod_m(a_m^2+\lambda)^{1/2}}\lambda_{,j} \quad \text{(A33)}$$

$$I_{ij,j} = \frac{-2\pi a_1a_2a_3}{(a_i^2+\lambda)\left(a_j^2+\lambda\right)\prod_m(a_m^2+\lambda)^{1/2}}\lambda_{,k} \quad \text{(A34)}$$

$$I_{i,jk} = \frac{-2\pi a_1a_2a_3}{(a_i^2+\lambda)\prod_m(a_m^2+\lambda)^{1/2}}\left(\lambda_{,jk} - \left(\frac{1}{a_i^2+\lambda} + \frac{1}{2}\sum_n\frac{1}{a_n^2+\lambda}\right)\lambda_{,j}\lambda_{,k}\right) \quad \text{(A35)}$$

$$I_{ij,kl} = \frac{-2\pi a_1a_2a_3}{(a_i^2+\lambda)\left(a_j^2+\lambda\right)\prod_m(a_m^2+\lambda)^{1/2}}\left(\lambda_{,kl} - \left(\frac{1}{a_i^2+\lambda} + \frac{1}{a_j^2+\lambda} + \frac{1}{2}\sum_n\frac{1}{a_n^2+\lambda}\right)\lambda_{,k}\lambda_{,l}\right) \quad \text{(A36)}$$

We have the first and second order derivatives of $\lambda(X)$:

$$\lambda_{,i} = \frac{2X_i}{a_I^2+\lambda} \Big/ \frac{X_i X_j}{\left(a_J^2+\lambda\right)^2}, \lambda_{,ij} = \frac{F_{i,j-\lambda_{,i}C_{,j}}}{C} \tag{A37}$$

Where

$$F_i = \frac{2X_i}{a_I^2+\lambda}, C = \frac{X_i X_j}{\left(a_I^2+\lambda\right)^2} \tag{A38}$$

The $D_{ijkl}(X)$ can be calculated by submitting the Equation A27~A37 into Equation A25.

The displacement field $u_i(X)$ can be obtained by:

$$u_i(X) = \frac{1}{8\pi(1-v)}\left(\psi_{,jli}\varepsilon_{jl}^* - 2v\varepsilon_{mm}^*\phi_{,i} - 4(1-v)\varepsilon_{il}^*\phi_{,l}\right) \tag{A39}$$

Two integrals ϕ and ψ are given as:

$$\phi(X) = \int_\Omega |X - X'|\mathrm{d}X' \tag{A40}$$

$$\psi(X) = \int_\Omega \frac{1}{|X-X'|}\mathrm{d}X' \tag{A41}$$

Where Ω is the inclusion region; The function ϕ and $\psi_{,i}$ can be expressed in terms of $I_i(\lambda)$ and $I_{ij}(\lambda)$,

$$\phi = \frac{1}{2}\left(I(\lambda) - X_n X_n I_N(\lambda)\right) \tag{A42}$$

$$\psi_{,i} = \frac{1}{2}X_i\left(I(\lambda) - X_n X_n I_N(\lambda) - a_I^2\left(I_I(\lambda) - X_n X_n I_{lN}(\lambda)\right)\right) \tag{A43}$$

Where

$$I = \frac{4\pi a_1 a_2 a_3 F(\theta(\lambda),k)}{\left(a_1^2-a_3^2\right)^{1/2}} \tag{A44}$$

Finally, we express $\phi_{,i}$ and $\psi_{,ijl}$ in terms of I_i, I_{ij} and their first-order derivatives

$$\phi_{,i} = -X_i I_l(\lambda) \tag{A45}$$

$$\psi_{,ijl} = -\delta_{ij}X_l\left(I_L(\lambda) - a_I^2 I_{IL}(\lambda)\right) - X_i X_j\left(I_J(\lambda) - a_I^2 I_{IJ}(\lambda)\right)_{,l} - \left(\delta_{il}X_j + \delta_{jl}X_i\right)\left(I_J(\lambda) - a_I^2 I_{IJ}(\lambda)\right) \tag{A46}$$

The displacement fields $u_i(X)$ is calculated by substituting Equations A27~A37 and A46 into A39.

In our case, the elastic moduli of inclusion and matrix are different, for example, C^*_{ijkl} within inclusion Ω and C_{ijkl} with matrix $D-\Omega$. Eshelby 1957 suggested that the induced stress field due to an ellipsoidal inhomogeneity can be calculated by an inclusion problem when the eigenstrain is chosen properly. Such fictitious eigenstrain ε^*_{mn} can be calculated as (Meng, Heltsley et al. 2012):

$$\left(\Delta C_{ijkl}S_{klmn}-C_{ijkl}\right)\varepsilon^*_{mn}=-\Delta C_{ijkl}\varepsilon^{\infty}_{kl}-C^*_{ijkl}\varepsilon^P_{kl} \tag{A47}$$

Where $\Delta C_{ijkl}=C_{ijkl}-C^*_{ijkl}$ and remote strain $\varepsilon^{\infty}_{ij}$ and remote stress σ^{∞}_{ij} and their relationship :

$$\sigma^{\infty}_{ij}=C_{ijkl}\varepsilon^{\infty}_{ij} \tag{A48}$$

ε^P_{kl} is the initial eigenstrain of inhomogeneity. The stress and strain fields are given as:

$$\sigma_{ij}(X)=\begin{cases}\sigma^{\infty}_{ij}+C_{ijkl}(S_{klmn}\varepsilon^*_{mn}-\varepsilon^*_{mn}), & \text{interior}\\ \sigma^{\infty}_{ij}+C_{ijkl}D_{klmn}(X)\varepsilon^*_{mn}, & \text{exterior}\end{cases} \tag{A49}$$

$$\varepsilon_{ij}(X)=\begin{cases}\varepsilon^{\infty}_{ij}+S_{klmn}\varepsilon^*_{mn}, & \text{interior}\\ \varepsilon^{\infty}_{ij}+D_{klmn}(X)\varepsilon^*_{mn}, & \text{exterior}\end{cases} \tag{A50}$$

The first step is to construct the stiffness matrix C_{ijkl} and C^*_{ijkl} for given elastic moduli and Poisson ratio. We use Equation A48 to calculate σ^{∞}_{ij} or $\varepsilon^{\infty}_{ij}$, respectively. For example, remote strain $\varepsilon^{\infty}_{ij}$ is calculated by $\sigma^{\infty}_{ij}/C_{ijkl}$ where σ^{∞}_{ij} could be considered as applied far-field stress. In the next step, Equations A6~A23 are applied to construct the Eshelby tensor S_{ijkl} for a given ellipsoid (Poisson's ratio v and three semi-axis of ellipsoid a_1, a_2 and a_3). In the next step, the fictitious eigenstrain ε^*_{mn} is calculated by Equation A47 with C_{ijkl} and C^*_{ijkl}, $\varepsilon^{\infty}_{ij}$. In the next step, the tensor $D_{ijkl}(X)$ is constructed by

Equation A25~A38 with the given modulus of matrix, semi-axis and the coordinate of observer points. X_i. In the final step, the external strain and stress can be calculated by Equation A49 and A50. In general, the inhomogeneity problem (with different matrix and inclusion materials) can be solved by Equations A1~A50. The modulus and Poisson ratio of the inclusion is set as zero for representing the crack. Therefore, this is the limit of inhomogeneity problem. As for crack, C^*_{ijkl} is zero and then submit it to Equation A47 and fictitious eigenstrain ε^*_{mn} is calculated. So, the external stress field is given by Equation A49 and A50.

In this method, cracks is regarded as the limits of Eshelby inclusions and the elastic moduli inside the inclusion are set to zero. So, the inclusion is actually a hole and the strains and displacement on the boundary of the hole are useful for some problems. The crack is formed by collapsing one of the semi-axes of the ellipsoid to zero so that the crack opening displacement may be deduced from the displacement on the surface of the ellipsoid. However, it appears that the displacement filed of crack represented by an empty inclusion is not accurate; the issues occurs in the calculation of D_{ijkl} using Equation A25. Also, during the calculation of D_{ijkl}, the elliptical integrals A16 and A17 require much computation time. Therefore, the parallel algorithm is needed to be considered in future work. The pore pressure filed within the surrounding zone of a fracture is calculated by (Warpinski, Wolhart et al. 2004).

Appendix B

Here we give a detail describe of the flowchart (Figure B1) of our fully coupled thermo-hydro-mechanical-seismic (THMS) finite element model with 3D discrete fracture network.

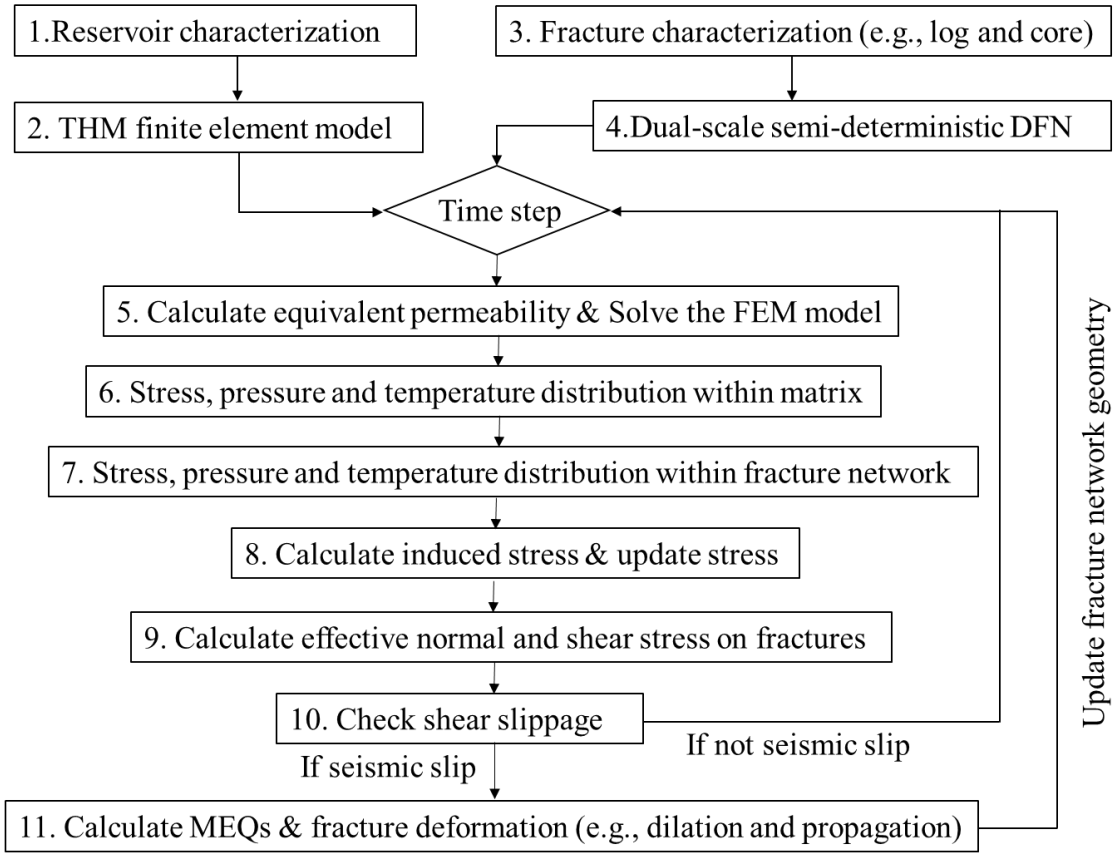

Figure B1 The flowchart of the integrated model.

In box 1, the focus of reservoir characterization is to define the mesh size and initial time step, the stochastic distribution of reservoir properties (e.g., modulus and permeability). In most cases, the mesh size and initial time step will be adjusted based on simulation results. For example, the time step will be reduced to capture the transition between aseismic and seismic. The time step is also reduced to possibly reflect the fracture

propagation. The best time step could be identified by try and error method. The mesh size in FEM need to be carefully addressed because our fracture network is embedded on mesh of FEM. However, we cannot dramatically refine the FEM mesh because our workstation cannot sustain it.

In box 2, the reservoir parameters are prepared in box 1. So those parameters are submitted into THM finite element method (Equation 2.9).

In box 3, core and outcrop from field project are examined. What is the foliation/micro-fracture distribution? In most cases, we do not know the distribution of foliation/micro-fracture at field scale. For example, the information of foliation/micro-fracture in Figure 2.1 is commonly available in lab. It seems that the density of foliation/micro-fracture is generally high, and those foliation/micro-fractures need to be considered into FEM. The major fracture can be obtained by the geophysical survey in small scale project (e.g., Collab). But other parameters of major fracture (e.g., aperture) is not available and is assumed to follow certain stochastic distribution. In large scale project (e.g., Utah FORGE), the fracture orientation in the surrounding zone of wellbore can be measured by imaging logs. Other parameters (e.g., aperture, fracture radius) are assumed to follow certain type of stochastic distribution.

In box 4, the geometry of major fracture and micro-fracture are defined by combining the data from imaging log, core and outcrop and stochastic distribution of fracture properties (e.g., aperture and location). Here the distribution of micro-fracture follows the power law (Pareto distribution, PDF $= a \cdot k^a / x^{a+1}$ and a and k are predefined based on estimation from box 3). Therefore, the distribution of micro-fracture population are defined in this box. The aperture of major fracture is followed the lognormal distribution.

In box 5, we use Equation 2.10 to calculate the equivalent permeability and solve the FEM model use Equation 2.9.

In box 6, pressure, stress distribution and temperature in FEM can be obtained based on the results from Equation 2.9.

In box 7, major fracture pressure, stress on fracture are calculated by interpolating the stress and pressure distribution on the finite elements.

In box 8, the induced stress field due to a fracture is measured by Eshelby solution (Appendix A). The total induced stress filed is obtained by superposition principle. The updated stress tensor is obtained by the sum of initial stress tensor and total induced stress field.

In box 9, the normal and shear stress of fracture are recalculated based on the updated stress tensor.

In box 10, check the fracture slippage.

If fracture is not slipped based on the failure criteria (Equation 2.11 and 2.12) and fracture deformation is not considered.

If fracture is slipped based on the failure criteria (Equation 2.11 and 2.12) and the slip rate (slip distance/time step) or slip distance (Equation 2.13) is not exceed the threshold slip rate (from Equation 2.28) and threshold slip distance (from Equation 2.30), respectively. Therefore, there is aseismic slip occurred on this fracture. Fracture aperture is updated by using Equation 2.14.

If fracture is slipped based on the failure criteria (Equation 2.11 and 2.12) and the slip rate (slip distance/time step) or slip distance (Equation 2.13) is exceed the threshold slip rate (from Equation 2.28) and threshold slip distance (from Equation 2.30), respectively.

Therefore, there is seismic slip occurred on this fracture. Fracture aperture is updated by using Equation 2.14. The number and magnitude of MEQs is constrained by using Equation 2.31~2.39. The CFF of each micro-fracture is calculated. The large CFF of micro-fracture, the larger magnitude of event occurs on this micro-fracture. Aseismic events occur on others failure micro-fractures.

In box 11, the distribution of MEQs is obtained in box 10. Fracture propagation is checked by using Equation 2.21. The equivalent stress intensity factor K_{eq} is calculated using Equation 2.21.

The properties of newly inserted penny fracture are assumed as the major fracture. Update the fracture network geometry for next time step.

Appendix C

A fracture surface is constructed from the scanning points using triangular mech. Previous works only calculate the JRC of the entire surface. However, the distribution of JRC on a fracture surface has a large influence on seismic patterns. In this appendix, a graph partition method is introduced to divide a surface into multiple patches. In this meshed, the fracture surface can be considered a graph and the fracture surface is subdivided into multiple patches by using the graph partition method and JRC values are calculated on each patch. Therefore, JRC is calculated locally. Graphs are often defined geometrically. Figure C1 shows a mesh of elements in 2D Euclidean space. The graph partitioning method partitions a *d*-dimensional mesh into multiple patches by finding a suitable sphere in *d*-space and dividing the vertices of the triangles mesh zone into those interior and exterior to the sphere. The cutting sphere is found by a randomized algorithm that involves a conformal mapping of the points on the surface of a sphere in *d*+1-space.

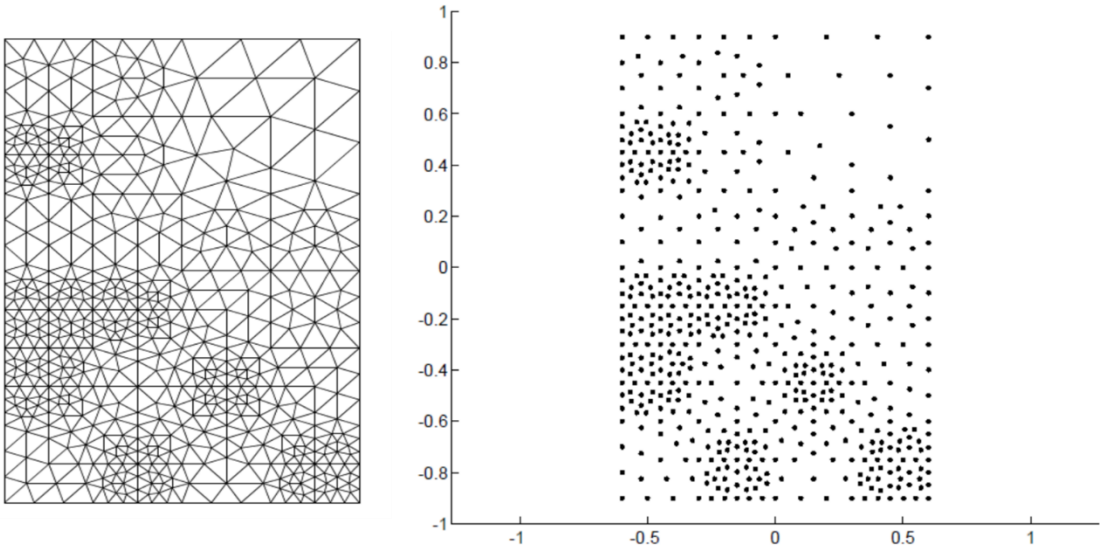

Figure C1 2D triangle mesh and points.

This graphs method generally involves six steps. Here a 2D example is introduced to illustrate how this method works.

Step 1. Project Up. Project the mesh points p stereographically from $\mathbb{R}^d$ to the unit sphere centered at the origin in $\mathbb{R}^{d+1}$. In the case of this example, d is 2. A point $p \in \mathbb{R}^2$ is projected to the sphere centered at the origin in $\mathbb{R}^3$ along the line through p and the (z) north direction [0 0 1] (Figure C2).

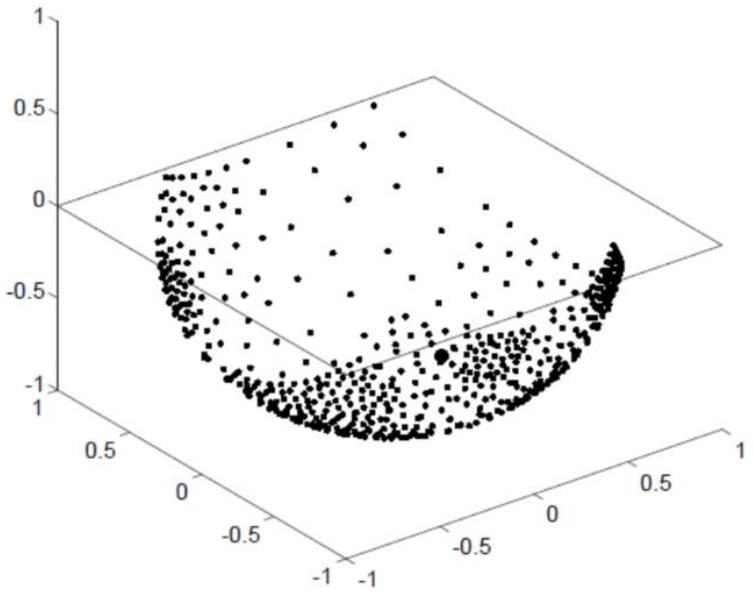

Figure C2 Projected mesh points. The large dot is the center points.

Step 2. Find CenterPoint. Computer a CenterPoint of the projected points in $\mathbb{R}^{d+1}$. This is a special point in the interior of the unit sphere. A CenterPoint of a given set of points is a point such that every hyperplane through the CenterPoint divides the given points approximately evenly (Figure C2).

Step 3. Conformal map: rotate and dilate. Move the projected points in $\mathbb{R}^{d+1}$. The surface of the unit sphere in two steps. First, rotate the projected points about the origin in $\mathbb{R}^{d+1}$ so that the CenterPoint becomes a point (0,0, r) on the $d+1$-st axis. Second, dilate the

points on the surface of the sphere so that the CenterPoint becomes the origin. The dilation can be described as a scaling in $\mathbb{R}^d$: project the rotated points stereographically down to $\mathbb{R}^d$; scale the points in $\mathbb{R}^d$ by a factor of $\sqrt{(1-r)/(1+r)}$; and project the scaled points up to the unit sphere in $\mathbb{R}^{d+1}$ again (Figure C3).

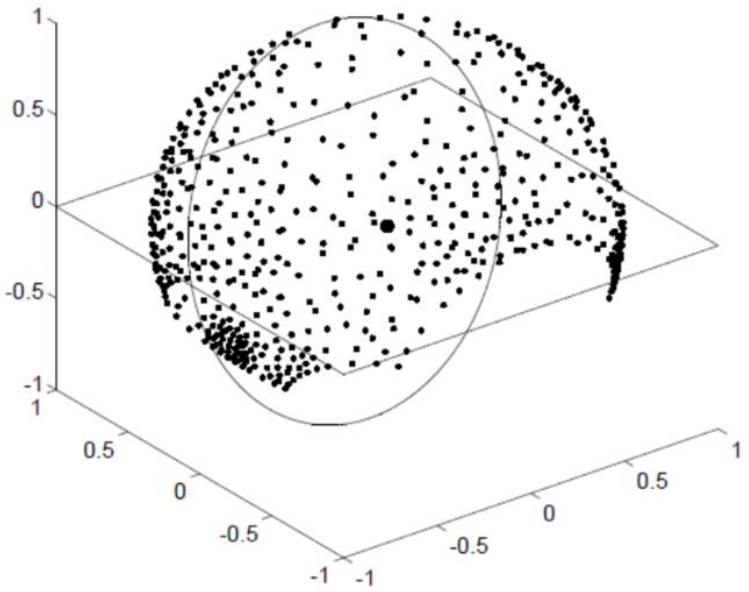

Figure C3 Conformally mapped points, with separating great circle. The CenterPoint is now at the origin.

Step 4. Find great circle. Choose a random great circle (i.e., d-dimensional unit sphere) on the unit sphere in $\mathbb{R}^{d+1}$ (Figure C3).

Step 5. Unmap and project Down. Transform the great circle to a circle in $\mathbb{R}^d$ by undoing the dilation, rotation, and stereographic projection (Figure C4).

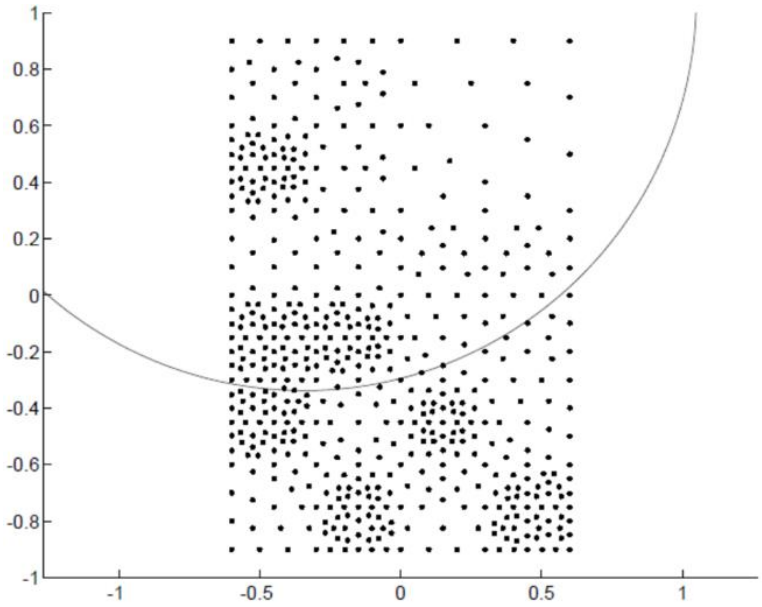

Figure C4 The separating circle projected back to the plane.

Step 6. Convert circle to separator. The vertex separator C is the vertices whose disks in the neighborhood representation (in $\mathbb{R}^d$) either (i) intersect the separating circle, or (ii) are smaller than the separating circle and would intersect it if magnified by a factor of α. The two sets A and B are the remaining vertices whose disks lie inside and outside the circle respectively (Figure C5).

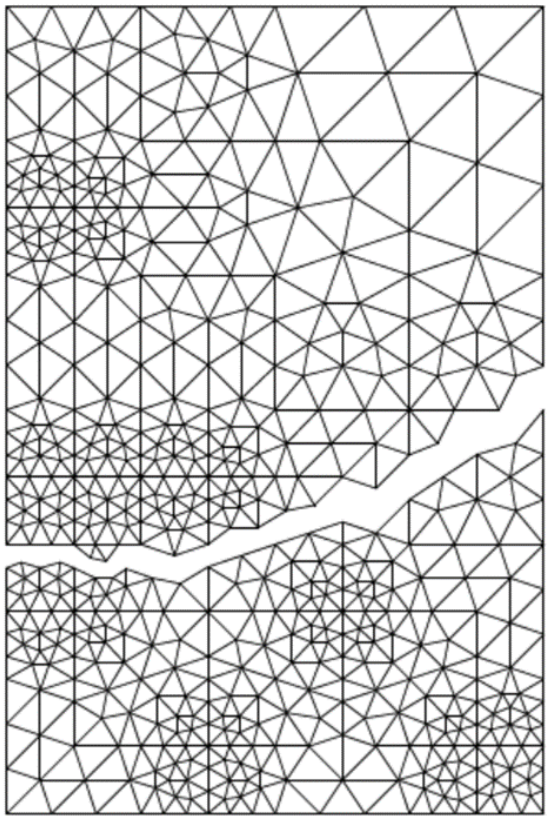

Figure C5 The edge separator induced by the separating circle. A vertex separator can also be extracted.

Appendix D

In this appendix, the MATLAB code for generating anisotropic surface is given as:

Main.m

```
% input: sigma, RMS of height of points on surface. Unit: m
%        H1, Hurst exponent in x direction
%        H2, Hurst exponent in Y direction
%        N, the number of points lay on an edge of surface is 2^(N+1)+1.
%        Lx, the length of edge of surface (square shape), unit: m
% output: F, the elements of meshed dimension anisotropic surface
%         V, the nodes of meshed dimension anisotropic surface, unit: m
%         nV, number of nodes of meshed dimension anisotropic surface
%         Z, the asperity of points on surface, unit: m
%         PixelWidth, samping interval or resolution, unit: m
%         Tapir, adjancy matrix for graph partition


sigma  = 2e-3; % m, RMS
H1     = 0.80; % Hurst exponent in x direction.
H2     = 0.60; % Hurst exponent in y direction.
N      = 9;     % the number of points lay on an edge of surface is 2^(N+1)+1.
Lx     = 0.5; % length of surface, unit: m
[F,V,nV,Z,PixelWidth,Tapir] = Anisurfmatrix(N,H1,H2,Lx,sigma);


function [F,V,nV,Z,PixelWidth,Tapir] = Anisurfmatrix(N,H1,H2,Lx,sigma)
% generate a dimension anisotropic surface (meshed surface)
% input: H1, Hurst exponent in x direction
%        H2, Hurst exponent in Y direction
%        N, the number of points lay on an edge of surface is 2^(N+1)+1.
%        Lx, the length of edge of surface (square shape), unit: m
%        sigma, RMS of height of points on surface. Unit: m
% output: F, the elements of meshed dimension anisotropic surface
%         V, the nodes of meshed dimension anisotropic surface, unit: m
%         nV, number of nodes of meshed dimension anisotropic surface
%         Z, the asperity of points on surface, unit: m
%         PixelWidth, sampling interval or resolution, unit: m
%         Tapir, adjancy matrix for graph partition

Z = Synthetic2DFault(N,H1,H2); % generate a dimensionless anisotropic surface

m = length(Z);
n = length(Z);
x = linspace(0,Lx,m);
y = linspace(0,Lx,n);
PixelWidth = Lx/(m-1);
[X,Y] = meshgrid(x,y);
Z = Z(:);
error = 1e-5;
scalefactor = 10;
id = 1;
temp = 1e10;

% re-scale the dimension anisotropic surface to enfore the RMS.
while abs(temp) > error
    Z_temp = rescale(Z,-scalefactor,scalefactor);
```

```
    temp = rms(Z_temp)-sigma;      % or RMS(Z) = sqrt(mean(Z.^2));
    if temp>0
       scalefactor = scalefactor/2;
    else
       scalefactor = scalefactor + error*2;
    end
    id = id + 1;
    if id>1000
       break
    end
end
%
Z = Z_temp;
Z = reshape(Z,m,n);
V = [X(:) Y(:) Z(:)];
nV = size(V,1);
% from point cloud to triangle mesh
F = delaunay(V(:,1),V(:,2)); %nodes(:,3) are elevation
% % partition mesh
% % adjancy matrix
edges = [F(:,1) F(:,2) ; F(:,2) F(:,3); F(:,3) F(:,1); ];
edges = sort( edges,2 );
edges = unique(edges,'rows');
edges = [edges(:,1) edges(:,2); edges(:,2) edges(:,1);(1:nV)' (1:nV)'];
values = ones(size(edges,1),1);
Tapir = sparse(edges(:,1),edges(:,2),values); % adjancey matrix
end

function RoughSurf = Synthetic2DFault(N,H1,H2)
% generate a dimensionless anisotropic surface
% input: H1, Hurst exponent in x direction
%        H2, Hurst exponent in Y direction
%        N, the number of points lie on an edge of surface
% output: RoughSurf, dimensionless anisotropic surface, RoughSurf(2^N+1,2^N+1).

l1 = 1/H1;
l2 = 1/H2;
x = (-2*2^N:2:2*2^N)/(2^(N+1));
x(2^N+1) = 1/2^N;
y = (-2*2^N:2:2*2^N)/(2^(N+1));
y(2^N+1) = 1/2^N;
[X,Y] = meshgrid(x,y); % mesh grid
%
rho = sqrt(abs(X).^(2/l1)+abs(Y).^(2/l2));
phi = rho.^(1 + (l1 + l2)/2); % scaled anisotropic matrix

Z=randn(2*2^N+1,2*2^N+1);   % random Gaussian noise
W=fftshift(fft2(Z))./phi;   % Gaussian noise is decomposed by Fourier transform
clear Z
T=real(ifft2(ifftshift(W))); % inverse Fourier transform is carried out to populate each coordinate of
surface.
RoughSurf = T -T(2^N+1,2^N+1);
End
```

Appendix E

Here we give a detail describe of the flowchart (Figure E1) of JRC-Hurst exponent relation and its application in our fully coupled thermo-hydro-mechanical-seismic (THMS) finite element model with 3D discrete fracture network.

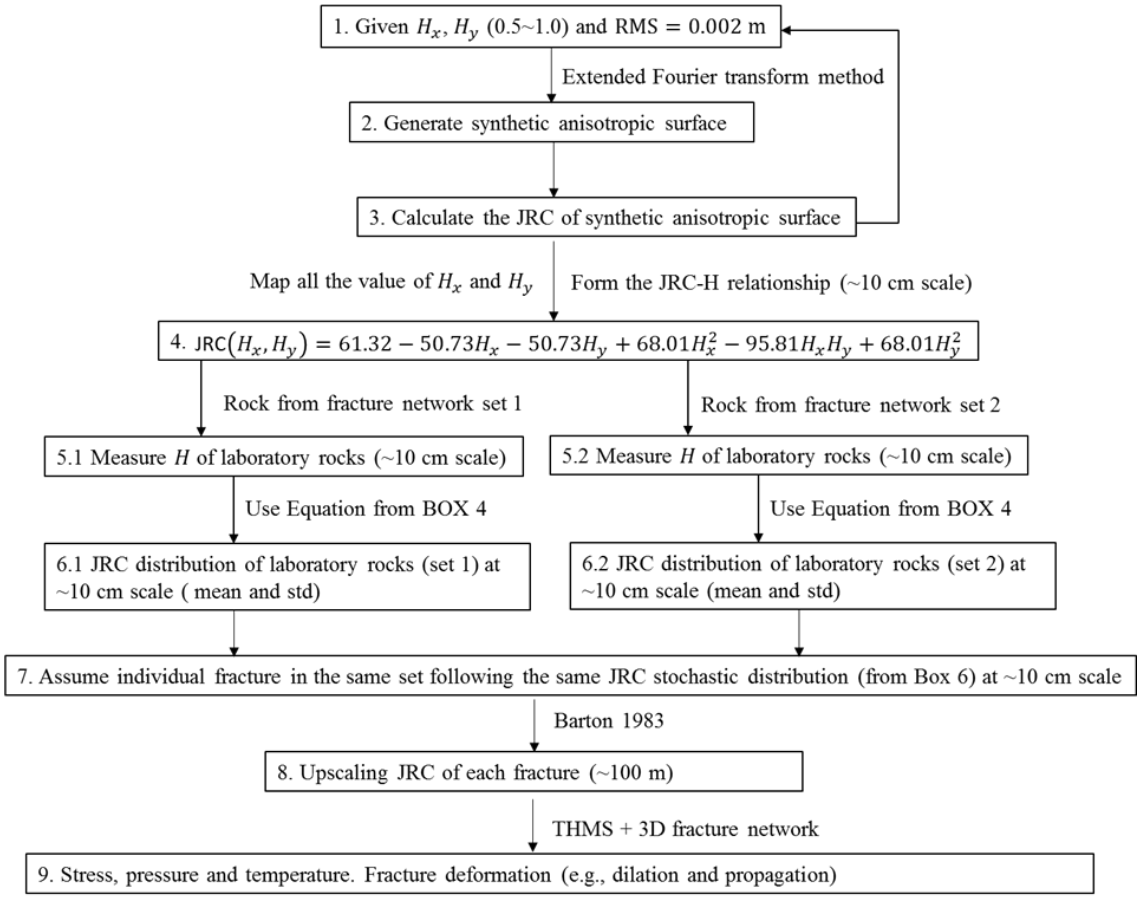

Figure E1 Flowchart of the integrated model.

In box 1, the range of Hurst exponent H_x and H_y is from 0.5 to 1.0 and RMS of height of points on surface is fixed at 0.002 m.

In box 2, the H_x and H_y and RMS are submitted into extend Fourier transform method (Chapter 5.2) to synthetic anisotropic surface.

In box 3, the JRC of entire synthetic anisotropic surface is calculated by JRC-Z_2 relationship.

$$\mathrm{JRC}=51.16\cdot(\mathrm{Z}_2)^{0.531}-11.44 \quad \text{(E1)}$$

We repeat the box 1 to box 3 with changing the value of H_x and H_y . RMS is fixed. Now multiple pairs of JRC and Hurst exponents are generated.

In box 4, the JRC-H relationship is formed by fitting the multiple pairs of JRC and Hurst exponents.

$$\mathrm{JRC}(H_x,H_y)=61.32-50.73H_x-50.73H_y+68.01H_x^2-95.81H_xH_y+68.01H_y^2 \quad \text{(E2)}$$

In box 5.1 and 5.2, measure H of laboratory rocks (~10 cm scale) at different fracture set. It is supposed that there are many rock samples from each set. For example, Figure E2 is one of laboratory rock sample from Utah FORGE site. The Hurst exponent is 0.61 based on Figure E2c.

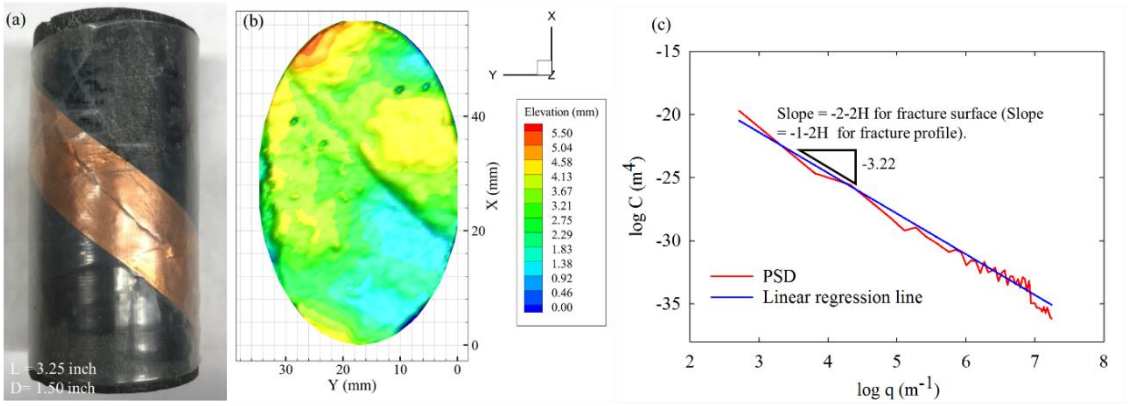

Figure E2 Rock sample in laboratory scale. The Hurst exponent is calculated by PSD analysis.

In box 6.1 and 6.2, we use Equation E2 from box 4 to calculate JRC of the laboratory rock (e.g., Figure E2). Therefore, the JRC of the laboratory rock (e.g., Figure E2) is 16.1 based on the Equation E2 from box 4. It is supposed that each fracture site may have

many rock samples (e.g., 5) and each rock sample have a JRC value. So, stochastic distribution (e.g., Lognormal) is applied to fix those JRC values. The mean and std of the Lognormal distribution could be treated as the JRC distribution of this fracture set at ~10 cm scale.

In box 7, assume individual fracture in the same set following the same JRC distribution (Lognormal) at ~10 cm scale. Such Lognormal distribution is derived in box 6.1 and 6.2.

In box 8, upscaling he JRC of each fracture (~100 m). Here we use approach from Barton 1983.

$$\mathrm{JRC}_n = \mathrm{JRC}_0 \left(\frac{L_n}{L_0}\right)^{-0.02\mathrm{JRC}_0} \tag{E3}$$

$$\mathrm{JCS}_n = \mathrm{JCS}_0 \left(\frac{L_n}{L_0}\right)^{-0.03\mathrm{JRC}_0} \tag{E4}$$

Where JRC_n is the JRC value of fracture at length scale L_n. JRC_0 is the JRC value of fracture at length scale L_0 (~10 cm).

In box 8, we submit the fracture with JRC into the THMS with a dynamic 3D fracture network to calculate the stress, pressure, temperature and fracture deformation.

Appendix F

In general, fracture rupture can be simulated by spring-slider system. Further, the rate-state friction law can be included in spring-slide system. In this model, fracture or even large-scale fault could be represented by a 1D slider. In a one-dimensional spring-slider system, the Newtonian force balance governing motion is defined as:

$$M\ddot{u} = K_s(u_{lp} - u) - \mu\sigma_n \tag{F1}$$

Where u_{lp} is the displacement of a load point, u is the displacement of the slider and μ is the friction coefficient between the slider and the surface; M is mass per unit area at facture depth ($\mathrm{kg/m^2}$); K_s is fracture shear stiffness. The evolution law of state variable θ is defined as:

$$\frac{\mathrm{d}\theta}{\mathrm{d}t} = 1 - \frac{V\theta}{D_c} \tag{F2}$$

Where V is slip velocity. Rate and state friction law is defined as:

$$\mu = \mu_0 + a\ln\left(\frac{V}{V_0}\right) + b\ln\frac{V_0\theta}{D_c} \tag{F3}$$

Here, the initial displacement is u_{ini} and velocity V_{ini}. The solution of Equation F1 is given as

$$u(t) = (u_{ini} - F)\cos(\omega t) + \frac{V_{ini}}{\omega}\sin(\omega t) + F \tag{F4}$$

Where $\omega = \sqrt{K_s/M}$ is angular velocity and $F = u_{lp} - \mu\sigma_n/K_s$. The solution Equation F4 can be discretized in time Δt by updating u and V in each time step as

$$u^{i+1} = \left[u^i - \left(u_{lp}^{i+1} - \mu^{i+1}\sigma_n/K_s\right)\right]\cos(\omega\Delta t) + \frac{V^i}{\omega}\sin(\omega\Delta t) + \left(u_{lp}^{i+1} - \mu^{i+1}\sigma_n/K_s\right) \tag{F5}$$

The acceleration between time steps i and $i + 1/2$ is:

$$a = \frac{V^{i+1/2} - V^i}{\Delta t/2} \tag{F6}$$

Where $V^{i+1/2} = \left(u^{i+1} - u^{i}\right)/\Delta t$. Thus, the velocity at time steps $i+1$ is given as:

$$V^{i+1} = V^{i} + a\Delta t = 2\frac{u^{i+1} - u^{i}}{\Delta t} - V^{i} \tag{F7}$$

The evolution law of state variable θ can be discretize as:

$$\theta^{i+1} = \theta^{i} + \left(1 - \frac{V^{i+1}\theta^{i}}{D_c}\right)\Delta t \tag{F8}$$

Rate and state friction can be discretized as:

$$\mu^{i+1} = \mu_0 + a\ln\left(\frac{V^{i+1}}{V_0}\right) + b\ln\left(\frac{V_0\theta^{i+1}}{D_c}\right) \tag{F9}$$

The Equation F8, F9, F5 and F7 are coupled and need be solved by Newton-Raphson method until the velocity V^{i+1} converges. The procedure of this approach could be followed:

Step 1: define the initial friction using Equation F9 with $i = 0$. Thus, the initial friction $\mu^1 = \mu_0 + a\ln\left(\frac{V^1}{V_0}\right) + b\ln\left(\frac{V_0\theta^1}{D_c}\right) = \mu_0 + a\ln\left(\frac{V^1}{V_0}\right) + b\ln\left(\frac{V_0\theta^1}{D_c}\right)$.

Here, $\mu_0, a, b, V_0, V^1, D_c$ and θ^1 are all predefined.

Step 2: calculate the displacement of an initial load point: $X_i = \mu^1\sigma_n/K_s$. As for a micro-fracture, the load point is itself because micro-fracture is treated as mass point. For a major fracture. The load points are the scanned points on the surface. The mechanical interaction between the points are not considered.

Step 3: The displacement of load point at time step $i+1$: $X_{i+1} = X_i + \Delta t \cdot V_l$

Step 4: Use F8 to calculate the state variable θ^{i+1}

Step 5: With Equation F9 and θ^{i+1} and the current slip rate V^{i+1} calculate the μ^{i+1}.

Step 6: With Equation F5, V^{i+1}, μ^{i+1} calculate the displacement u^{i+1}.

Step 7: Update the current slip rate V^{i+1} using Equation F7.

Step 8: Recalculate the current slip rate V^{i+1} using Equation F9, F5 and F7

Step 9: If the current slip rate V^{i+1} during the iteration meets the convergence criterion ((abs (V^{i+1} of previous iteration /V^{i+1} of current iteration)-1) < $1x10^{-7}$). The iteration has converged.

Step 10: Start next time step. The input parameters for next time step are friction coefficient μ^{i+1}, and slip rate V^{i+1} and state variable θ^{i+1} and displacement of load point X_{i+1}.